Film Dynamics and Deposit Formation in Evaporating Multi-Component Liquids

Dissertation

Achim Bender

TECHNISCHE
UNIVERSITÄT
DARMSTADT

Filmdynamik und Ablagerungsbildung in verdunstenden mehrkomponentigen Flüssigkeiten

Film Dynamics and Deposit Formation in Evaporating Multi-Component Liquids

Doctoral thesis
by Achim Bender

submitted in fulfillment of the requirements for the
degree of Doktor-Ingenieur
(Dr.-Ing.)

at the Department of Mechanical Engineering
of the Technical University of Darmstadt

First Examiner:	Apl. Prof. Dr. Tatiana Gambaryan-Roisman
Second Examiner:	Dr. Prashant Valluri
Third Examiner:	Prof. Dr.-Ing. Peter Stephan

Darmstadt 2020

Danksagung

Diese Dissertationsschrift entstand während meiner Anstellung als wissenschaftlicher Mitarbeiter am Fachgebiet für Technische Thermodynamik der Technischen Universität Darmstadt. Bei Herrn Prof. Peter Stephan möchte ich mich herzlich für die Möglichkeit bedanken, die Promotion an seinem Fachgebiet durchzuführen. Das positive Arbeitsklima am Institut und die eingeräumte Freiheit bei der wissenschaftlichen Arbeit habe ich als äußerst angenehm und wichtig empfunden. Bei Frau Apl. Prof. Tatiana Gambaryan-Roisman bedanke ich mich für die exzellente Betreuung. Ihr stets offenes Ohr bei auftretenden Schwierigkeiten und ihre wertvollen Impulse haben sehr zum Gelingen der Arbeit beigetragen.

Ich möchte mich bei all jenen bedanken, die meine Tätigkeit am Fachgebiet während des Studiums betreut haben. Durch Hiwi-Jobs und die Masterarbeit wurde in dieser Zeit mein Interesse an der Thermodynamik sowie der analytischen und numerischen Arbeit geweckt und ich konnte vieles lernen, was über den Vorlesungsstoff hinausgeht. Besonders gilt mein Dank Herrn Dr. Stefan Batzdorf für die Betreuung meiner Masterarbeit.

Für die bereits angesprochene gute Arbeitsatmosphäre am Institut gilt mein herzlicher Dank allen Kolleginnen und Kollegen am TTD. Niklas Preußer und Thomas Antritter möchte ich außerdem für die sorgfältige Durchsicht des Manuskriptes danken.

Ausdrücklich bedanken möchte ich mich bei meinen Eltern und bei meinem Bruder für die vielfältige Unterstützung während des gesamten Studiums. Mein besonderer Dank gilt meiner Frau Irini. Ihre Unterstützung, aufmunternden Worte in Zeiten des Zweifelns und gelegentlich der ein oder andere sanfte Schubs in die richtige Richtung haben zur Fertigstellung dieses Werkes wesentlich beigetragen.

Darmstadt, den 4. November 2019

Achim Bender

Abstract

Abstract

Deposit formation from evaporating liquid films and drops is an important phenomenon in many industrial applications. In internal combustion engines, deposits form from fuel films on ports, cylinder walls, and pistons. In the exhaust gas treatment, deposits form from the urea-water solution, which is injected into the exhaust pipe to reduce nitrogen oxide emissions. In both cases, the deposit formation has a negative influence on the process efficiency and increases the emission of pollutants.

The influence of physical parameters on the evaporation and deposition process is not understood. While some individual aspects of the evaporation and deposit formation process have been addressed numerically in the literature, the influence of some key phenomena remain unknown. Furthermore, a single multiscale model, taking all relevant physical processes and their interactions into account, is not available. Such a model would be important in order to gain a basic understanding of the process and to deduce strategies to avoid deposit formation in the future. This thesis is a first step in the development of such a model. Based on the analysis of previous investigations, it is concluded that the process can be separated into two stages.

In the first stage, a thin liquid film, which is influenced by evaporation, turbulent shear stress, and chemical reactions, is present on a structured wall. This liquid film ruptures at some time during the process and then continues to

Zusammenfassung

Ablagerungsbildung von verdunstenden Flüssigkeitsfilmen und Tropfen ist ein wichtiges Phänomen in vielen industriellen Anwendungen. In Verbrennungsmotoren bilden sich Ablagerungen aus Kraftstofffilmen auf Ventilen, Zylinderwänden und Kolben. Bei der Abgasnachbehandlung bilden sich Ablagerungen von Harnstoff-Wasser-Lösungen, die in den Abgasstrang eingespritzt werden, um Stickoxidemissionen zu reduzieren. In beiden Fällen haben die Ablagerungen einen negativen Einfluss auf die Effizienz des Prozesses und sie erhöhen den Schadstoffausstoß.

Der Einfluss von physikalischen Parametern auf den Verdunstungs- und Ablagerungsprozess ist nicht ausreichend verstanden. Obwohl mittels numerischer Simulation einzelne Aspekte des Verdunstungsprozesses und der Ablagerungsbildung in der Literatur behandelt wurden, bleibt die Rolle einiger bedeutender Phänomene bisher unklar. Weiterhin gibt es bislang kein einzelnes Multiskalen-Modell, welches alle relevanten physikalischen Phänomene und deren Interaktionen berücksichtigt. Ein solches Modell wäre wichtig, um ein grundlegendes Verständnis für den Prozess zu entwickeln und daraus Strategien zur Vermeidung von Ablagerungen abzuleiten. Diese Arbeit ist ein erster Schritt in der Entwicklung eines solchen Modells. Aus der Analyse von früheren Untersuchungen kann abgeleitet werden, dass sich der Prozess in zwei Stufen aufteilen lässt.

In der ersten Stufe existiert ein dünner Flüssigkeitsfilm auf einer strukturierten Wand, der von Verdunstung, der turbulenten Scherströmung und chemischen Reaktionen beeinflusst wird. Dieser Flüssigkeitsfilm reißt im weiteren Prozessverlauf auf und tritt in die zweite

evaporate in the second stage in which the deposits form.

Long-wave theory is used to derive various models to investigate the evolution and stability of thin liquid films. These models consider a film on a heated or cooled structured wall evaporating into a pure vapor atmosphere or into an ambient gas, a liquid film with a time-dependent chemical reaction subject to a laminar shear flow, and a liquid film sheared by a turbulent shear stress from the gas flow. The resulting evolution equations are solved with a finite difference solver developed in this work. The linear stability of the solution is addressed and parametric studies are conducted. It is shown that the investigated physical phenomena have a big influence on the film stability and evolution and that there are strong interactions between the individual phenomena. This makes a full numerical simulation of the film development necessary.

Evaporation and deposit formation from sessile binary drops are investigated with an arbitrary Lagrangian-Eulerian method. The mesh is deformed to follow the shape of the evaporating drop and the deposit shape. The developed model is validated against a correlation and experimental data. The results show that ring shaped deposits occur in the vicinity of the three-phase contact line in the absence of Marangoni flow. A parametric study for urea-water drops is conducted. The temperature of the wall, initial composition of the drop, and drop size influence the evaporation of the drop, the time of first deposit formation, and the deposit growth rate, as well as the resulting deposit shape. The deposit shape changes from a ring-shaped to a cap-shaped pattern with increasing importance of thermocapillarity.

Stufe ein, in der er weiter verdunstet und Ablagerungen bildet.

Die *Long-Wave Theory* wird verwendet, um mehrere Modelle herzuleiten, mit denen die Entwicklung und Stabilität von dünnen Flüssigkeitsfilmen untersucht wird. Diese Modelle berücksichtigen verdampfende oder verdunstende Filme auf beheizten oder gekühlten strukturierten Wänden, einen Flüssigkeitsfilm mit einer zeitlich veränderlichen chemischen Reaktion, geschert von einer laminaren Schubspannung, und einen Flüssigkeitsfilm, der von einer turbulenten Schubspannung geschert wird. Die resultierenden Evolutionsgleichungen werden von einem Finite-Differenzen-Löser gelöst, der in dieser Arbeit entwickelt wurde. Die lineare Stabilität der Lösung wird betrachtet und Parameterstudien werden durchgeführt. Es wird gezeigt, dass die untersuchten physikalischen Phänomene einen großen Einfluss auf die Stabilität und Entwicklung des Films haben und dass es starke Wechselwirkungen zwischen den einzelnen Phänomenen gibt. Dies macht eine volle numerische Simulation der Filmentwicklung notwendig.

Die Verdunstung und Ablagerungsbildung aus aufgesetzten binären Tropfen wird mithilfe einer *Arbitrary Lagrangian-Eulerian* Methode untersucht. Das Gitter wird verformt, um der Form des verdunstenden Tropfens und der Form der Ablagerung zu folgen. Das entwickelte Modell wird mit Hilfe von einer Korrelation und experimentellen Daten validiert. Die Ergebnisse zeigen, dass sich ringförmige Ablagerungen in der Nähe der Dreiphasenkontaktlinie bilden, wenn der Marangoni-Effekt vernachlässigt werden kann. Eine Parameterstudie für Harnstoff-Wasser Tropfen wird durchgeführt. Die Wandtemperatur, die initiale Zusammensetzung des Tropfens und die Tropfengröße beeinflussen die Tropfenverdunstung, die Zeit, zu der sich die ersten Ablagerungen bilden, die Wachstumsrate der Ablagerungen sowie deren resultierende Form. Die Form der Ablagerungen ändert sich von ringförmig zu kappenförmig, wenn Thermokapillarität berücksichtigt werden muss.

Contents

Nomenclature

Latin Symbols

Symbol	Description	Unit
a	thermal diffusivity	$\mathrm{m^2\,s^{-1}}$
A, B	non-dimensional amplitude	-
c	film length	m
c_p	specific heat capacity	$\mathrm{J\,kg^{-1}\,K^{-1}}$
$\mathscr{C}$	correlation function	-
d	characteristic length/thickness	m
D	density ratio	-
D_{bin}	binary diffusion coefficient	$\mathrm{m^2\,s^{-1}}$
$\mathbf{e}$	unit vector	-
E	non-dimensional evaporation rate	-
$\mathscr{E}$	activation energy	$\mathrm{J\,mol^{-1}}$
f	condensation coefficient	-
$\mathbf{F}$	non-dimensional shear stress vector	-
F	average non-dimensional shear stress	-
$\mathbf{g}$	gravitational acceleration vector	$\mathrm{m\,s^{-2}}$
g	gravitational acceleration	$\mathrm{m\,s^{-2}}$
G	non-dimensional gravity	-
h	film/drop height	m
h_{ls}, h_{lv}	enthalpy of solidification/vaporization	$\mathrm{J\,kg^{-1}}$
H	non-dimensional film height	-
i	imaginary number	-
$\mathbf{I}$	identity tensor	-
j	mass flux	$\mathrm{kg\,m^{-2}\,s^{-1}}$
J	non-dimensional interfacial mass flow	-
k	thermal conductivity	$\mathrm{W\,m^{-1}\,K^{-1}}$
k_{wave}	wavenumber	$\mathrm{m^{-1}}$
K	non-dimensional wavenumber	-
l	substrate height	m
L	non-dimensional substrate height	-
M	molar mass	$\mathrm{kg\,mol^{-1}}$
$\mathbf{n}$	normal vector	-
$\mathscr{O}$	order of magnitude	various
p	pressure	$\mathrm{N\,m^{-2}}$
P	non-dimensional pressure	-

q	heat per volume	$\mathrm{J\,m^{-3}}$
$\dot{q}$	heat flux	$\mathrm{W\,m^{-2}}$
r	radial coordinate	m
r_{react}	reaction rate	$\mathrm{s^{-1}}$
R	radius	m
$\mathscr{R}$	universal gas constant	$\mathrm{J\,mol^{-1}\,K^{-1}}$
s	small distance	m
S	non-dimensional surface tension	-
$\mathbf{t}$	tangential vector	-
t	time	s
$\mathbf{T}$	stress tensor	$\mathrm{N\,m^{-2}}$
T	temperature	K
$\mathbf{u}$	velocity vector	$\mathrm{m\,s^{-1}}$
u, v, w	velocity component in x-, y-, z-direction	$\mathrm{m\,s^{-1}}$
U, V, W	non-dimensional velocity component in X-, Y-, Z-direction	-
V	volume	$\mathrm{m^3}$
$\dot{V}$	volume rate of change	$\mathrm{m^3\,s^{-1}}$
$\mathscr{W}$	mesh deformation energy	$\mathrm{m^3}$
$\mathbf{x}$	coordinate vector	m
x, y, z	Cartesian coordinates	m
X, Y, Z	non-dimensional Cartesian coordinates	-

Greek Symbols

Symbol	Description	Unit
α	heat transfer coefficient	$\mathrm{W\,m^{-2}\,K^{-1}}$
β	mass transfer coefficient	$\mathrm{m\,s^{-1}}$
γ	resistance to evaporation	$\mathrm{kg^{-1}\,m^2\,s\,K}$
Γ	non-dimensional resistance to evaporation	-
δ	length scale	m
ϵ	perturbation parameter	-
ε	relative error	-
ζ	small parameter	-
θ	contact angle	deg
Θ	non-dimensional temperature	-
κ	curvature	$\mathrm{m^{-1}}$
λ	porosity	-
Λ	non-dimensional wavelength	-
μ	dynamic viscosity	$\mathrm{kg\,m^{-1}\,s^{-1}}$
ν	kinematic viscosity	$\mathrm{m^2\,s^{-1}}$
ξ	mass fraction	$\mathrm{kg\,kg^{-1}}$

Ξ	normalized concentration	-
ρ	density	$kg\,m^{-3}$
σ	surface tension / interfacial tension	$N\,m^{-1}$
Σ	source term	$W\,m^{-3}$ or s^{-1}
τ	non-dimensional time	-
τ_{int}	interfacial shear stress	$N\,m^{-2}$
χ	mole fraction	$mol\,mol^{-1}$
ω	frequency	s^{-1}
Ω	non-dimensional growth rate	-

Subscripts

Subscript	Description
0	initial or reference condition / order 0
1, 2	order 1, order 2
A	species A
air	air
bin	binary
c	convection
crit	critical
dep	deposit
e	energy
g	gas
H2O	water
i	index
ind	grid independent
int	interface
l	liquid
ls	liquid-solid or crystallization
lv	liquid-vapor or evaporation
mat	material frame
max	maximal
mesh	mesh frame
min	minimal
react	reaction
rms	root mean square
rup	rupture
s	solid
sat	saturation
u	urea
v	vapor

w	wall
wave	wave
ν	viscous
τ	friction / non-dimensional time
∞	far field value

Superscripts

Superscript	Description
$+$	viscous units
$'$	disturbed state or fluctuation
T	transposed

Accents

Accent	Description
$\bar{}$	average
$\tilde{}$	varied definition of non-dimensional parameter
$\hat{}$	varied definition of non-dimensional parameter

Abbreviations

Abbreviation	Description
ALE	Arbitrary Lagrangian-Eulerian
CFD	Computational Fluid Dynamics
DNS	Direct Numerical Simulation
FDM	Finite Difference Method
FEM	Finite Element Method
LES	Large Eddy Simulation
LWT	Long-Wave Theory
RANS	Reynolds-Averaged Navier-Stokes
SCR	Selective Catalytic Reduction
SGS	Subgrid Scale
UWS	Urea-Water Solution
VOF	Volume Of Fluid

Non-dimensional Groups

Symbol	Description	Definition
Bi	Biot number	$\alpha\, d/k$
Bo	Bond number	$\rho\, g\, d^2/\sigma$
Ca	Capillary number	$\mu\, u/\sigma$
Da	Damköhler number	$d^2\, r_{\text{react},0} \exp[-\mathscr{E}/(\mathscr{R}\, T)]/\nu$
Ma	Marangoni number	$-(\partial\sigma)/(\partial T)(\Delta T\, d)/(2\,\mu\, a)$
Pe	Péclet number	$Re\, Sc = d\, u/D_{\text{bin}}$
Pr	Prandtl number	ν/a
Re	Reynolds number	$d\, u/\nu$
Re_τ	friction Reynolds number	$d\, u_\tau/\nu$
Sc	Schmidt number	ν/D_{bin}

Chapter 1

Introduction

1.1 Motivation and Relevance

Evaporation and deposit formation from multi-component liquid films and drops is an often encountered and important topic. Everyone is probably familiar with the stains left behind on the kitchen counter after some of the morning coffee spilled or with the deposits on the stove after the pasta water has boiled over. Deposit formation, however, also has various impacts in industrial applications, ranging from deposition in membrane distillation processes [90], improving inkjet printing quality [63], and fouling in heat exchangers [212], to new medical diagnostics from structures in dried blood samples [38, 237].

Another large industrial branch where film evaporation and deposit formation is an important object of research and development is the automotive industry. Here, deposit formation can be found both in the combustion chamber of internal combustion engines [246] and in the exhaust gas treatment system [41]. Despite the increased speed of development of electrical cars in recent years, big challenges remain for this engine concept ranging from expensive (both financially and in terms of environmental impact) resources necessary for the batteries [158] to the setup of an electrical grid, which can handle charging a large number of cars with electricity from renewable energy sources [56]. For trucks or heavy building machinery, current electrical engine concepts often cannot provide the required range, yet [60]. This is why it is unlikely that the electrical engine will replace the internal combustion engine completely within the next years.

However, due to a tightening of emission laws in several countries around the world and to an increase in awareness that man-made climate change has to be kept under control, the internal combustion engine has to be made more efficient and the exhaustion of environmentally harmful or greenhouse gases has to be reduced [153]. Additionally, the increased use of fuels synthesized from plants or from water and carbon dioxide with the use of electrical energy (so called e-fuels) affect the combustion process [101]. Deposit formation from thin liquid films is highly relevant in this context for both the combustion chamber and the exhaust gas treatment, as it affects the engine efficiency, the emission of pollutants, and the lifetime of the engine in a negative way.

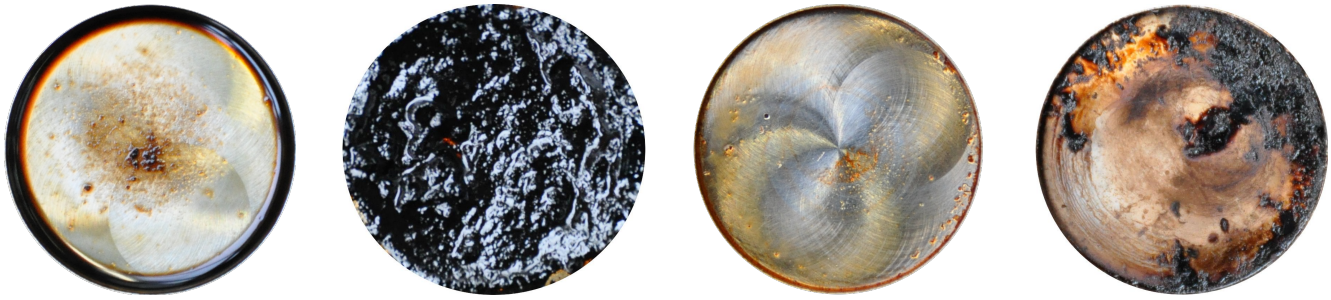

gasoline diesel benzene methylnaphthalene

Figure 1.1: Combustion chamber deposits for different fuel types found after repeated drop evaporation (adapted from [97]).

1.1.1 Combustion Chamber Deposits

Fuel and engine oils in the combustion chamber of internal combustion engines are known to form wall films through drop-wall interaction on ports, cylinder walls, and pistons after injection [67, 180, 190, 246]. Fuel components with lower boiling points mostly evaporate, while heavier components remain in the film and undergo cross linking and chemical reactions [89, 157, 245]. The deposits can be found on the hot walls after a sufficient residence time [67, 97, 190, 246]. Fuel components with higher boiling temperatures are more likely to form deposits [91, 92, 120]. The deposits have a negative influence on the combustion cycle [91, 92] and lead to increased particle and NO_x emissions as well as misfire and reduced engine torque [246]. Direct injection gasoline engines, which are superior to port fuel injection engines in terms of environmental impact [187], tend to lead to more deposits than port fuel injection engines [19]. Furthermore, it has been shown that deposits on the injector lead to pre-ignition, increased fuel consumption, as well as higher carbon monoxide, hydrocarbon, and particle emissions and, in the worst case, even to engine malfunction [18, 234].

The structure and composition of the hydrocarbon fuel components influence deposit formation [97, 119] (see Fig. 1.1). Bio-diesel fuels have been found to lead to increased deposit formation compared to regular diesel fuels [142], which poses a challenge for further development. Guthrie [93] reviewed relevant literature and found deposit formation in gasoline engines to be influenced by the chemical structure of the substances, the fuel and engine oil properties, residence times of the film, and the wall temperature. Furthermore, it was found that the wall temperature is the most important influence on deposit formation [52].

On the one hand, it was found that under engine operating conditions, higher wall temperatures lead to an increase of the deposit formation [13, 127], while, on the other hand, it was established that in the presence of wall films, which usually lead to a decrease of the wall temperature, the formation of deposits increases [93]. The wall film is influenced by the turbulent gas flow. It was also shown that already formed deposit structures are preferably wetted [96], which might lead to an acceleration of the deposition process at these locations. The roughness [74] and thermal properties [106, 230] of the deposits influence the heat transfer characteristics of the overall process.

The deposition process itself takes much longer than the evaporation of an individual fuel film formed during one injection cycle. Singer and Rühe [206] showed that the cross-linking of components of diesel and bio-diesel fuels, which eventually lead to deposits, is slow compared to the evaporation of the low boiling fraction components. Due to this, experimental investigations of deposit formation in combustion chambers are usually long-term experiments, ranging over a multitude of injection cycles. The engine run times, before deposit samples are taken, range from two hours [51, 125] to up to 70 hours [181]. It has been found that repeated wetting and dryout of the walls leads to deposit formation, as deposit precursors from previous cycles remain on the surface after the dryout [20].

Deposit formation from diesel, bio-diesel, and other hydrocarbon drops, which repeatedly impinge on a hot substrate, have been investigated [15, 16, 17, 97]. Depending on the liquid, several hundred [97] to up to 1000 drops [16] are necessary to reach considerable deposit structures. The deposit formation was found to take place close to the edge of the wetted surface, as deposit precursors, which formed through autoxidation of fuel components, are transported through the liquid to the edge of the wetted area where they deposit [97]. In some cases, if it was possible to place the successive drops on the same spot, ring-shaped deposits were observed. These were found in the region of the three-phase contact line of the drops, which is the location where liquid, gas, and solid meet.

1.1.2 Deposits in DeNO$_x$ Exhaust Gas Treatment

Selective catalytic reduction (SCR) is used in the exhaust system of diesel engines to reduce nitrogen oxide emissions. A urea-water solution (UWS) with 32.5 weight percent urea (also referred to by its brand name AdBlue) is injected into the hot exhaust gas. Here, the urea decomposes to ammonia, which reacts with the nitrogen oxides and reduces them to nitrogen and water [130].

However, ensuring high reduction rates of the nitrogen oxides requires high dosing rates of the solution. This leads to the impingement of solution onto the exhaust pipe and the formation of liquid films [34, 41]. The occurrence of this phenomenon is enhanced at low exhaust temperatures shortly after engine start-up, due to the low evaporation rates of the drops [37]. The existence of a wall film has been found to be a crucial factor for the formation of deposits in SCR-systems [196, 207]. Both in experimental investigations of a laboratory exhaust system and in generic experiments of evaporating urea-water drops on a heated surface in a controlled environment, the deposits were found to form primarily at the three-phase contact line [39, 192]. The addition of surface active agents (surfactants) to AdBlue is now considered in order to influence the wetting characteristic of the solution with the goal of reducing deposition [138]. The deposits are formed on the exhaust pipe walls and lead to performance loss of the system, as well as higher engine back pressure [243]. The deposition rate increases with higher injection rates and lower wall temperatures [216]. In these cases, experimental investigations report formation of deposit structures covering up to 60 % of the channel height depending on the temperatures and flow velocities [37] (see Fig. 1.2). The turbulent gas flow affects the evaporation process of the film and the shape of the final deposit structure.

The composition of the formed deposit depends strongly on the wall temperature. Water evaporates from the liquid film much faster than urea [33, 34]. Kinetic models of the decomposition of solid urea

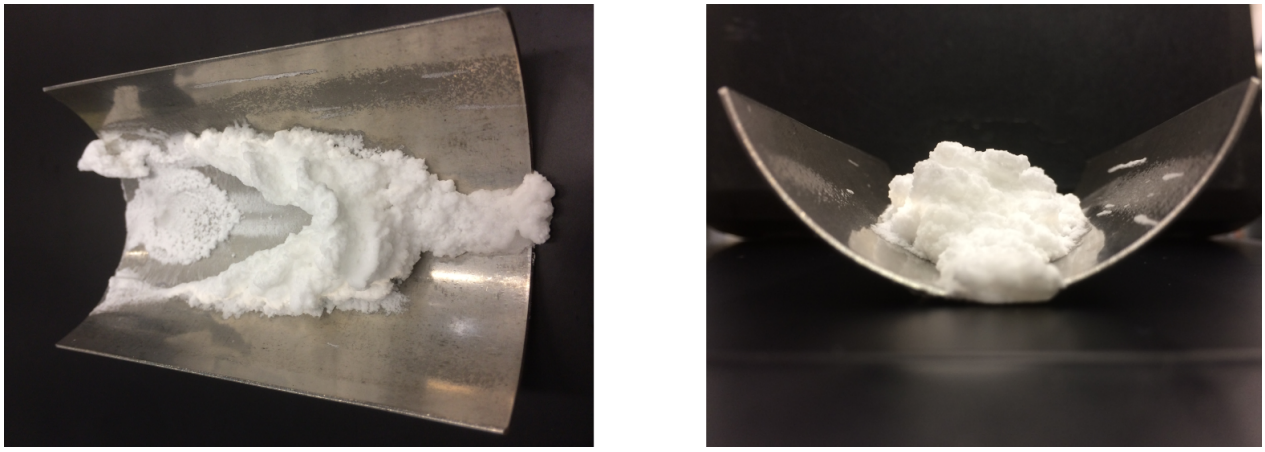

Figure 1.2: Deposits found on the channel wall after evaporation of urea-water solutions. [I]

have been proposed [40] and applied to predict various decomposition stages of urea and the amount of deposits [41, 175]. The kinetic model predicts that the rate of urea decomposition is low at temperatures below 200 °C. Similarly, experimental studies saw that the formed deposit consists primarily of crystalline urea at wall temperatures below the urea melting point of around 133 °C [207, 243]. Other research has confirmed that urea is the main component of the formed deposits even at higher temperatures up to 150 °C [41] or 220 °C [37]. At higher temperatures, the urea decomposition through chemical reactions becomes more important and urea bi-products such as biuret, triuret, ammelide, ammeline, and cyanuric acid are increasingly found in the deposits [37, 41].

The time scales of water evaporation were found to be much smaller than the time scales of urea decomposition [196]. This leads to an increase of the urea concentration over time inside the film and to urea crystallization [192]. Experimental investigations further confirm that industrially relevant deposit amounts are found over a multitude of injection periods. The time scale of the deposit formation has been found to be around 600 s for temperatures below 220 °C [207]. Lab experiments of exhaust treatment systems have been conducted for between 100 hours [243] and 200 hours [25] to obtain industrially relevant deposit structures. In these cases, the already formed deposit influences the film evolution of the following injection cycles.

1.2 Deduction of the Modeling Concept and Outline of the Thesis

As the previous section has shown, the description of multi-component films evaporating on heated structured walls and the formation of deposits from these films is a complex chemical-physical process. A single complete model to describe the process and to enhance the basic knowledge is necessary to deduct strategies to control or avoid deposit formation in the future. However, there are plenty of sub-processes and physical phenomena involved, covering many different time and length scales. Furthermore, the individual phenomena influence and interact with each other. This makes the formulation of a complete detailed model very challenging and is the reason that no such model can be found in the literature.

[I] I would like to thank Dr. Marion Börnhorst from Karlsruhe Institute of Technology for supplying me with these pictures and allowing me to use them in this thesis.

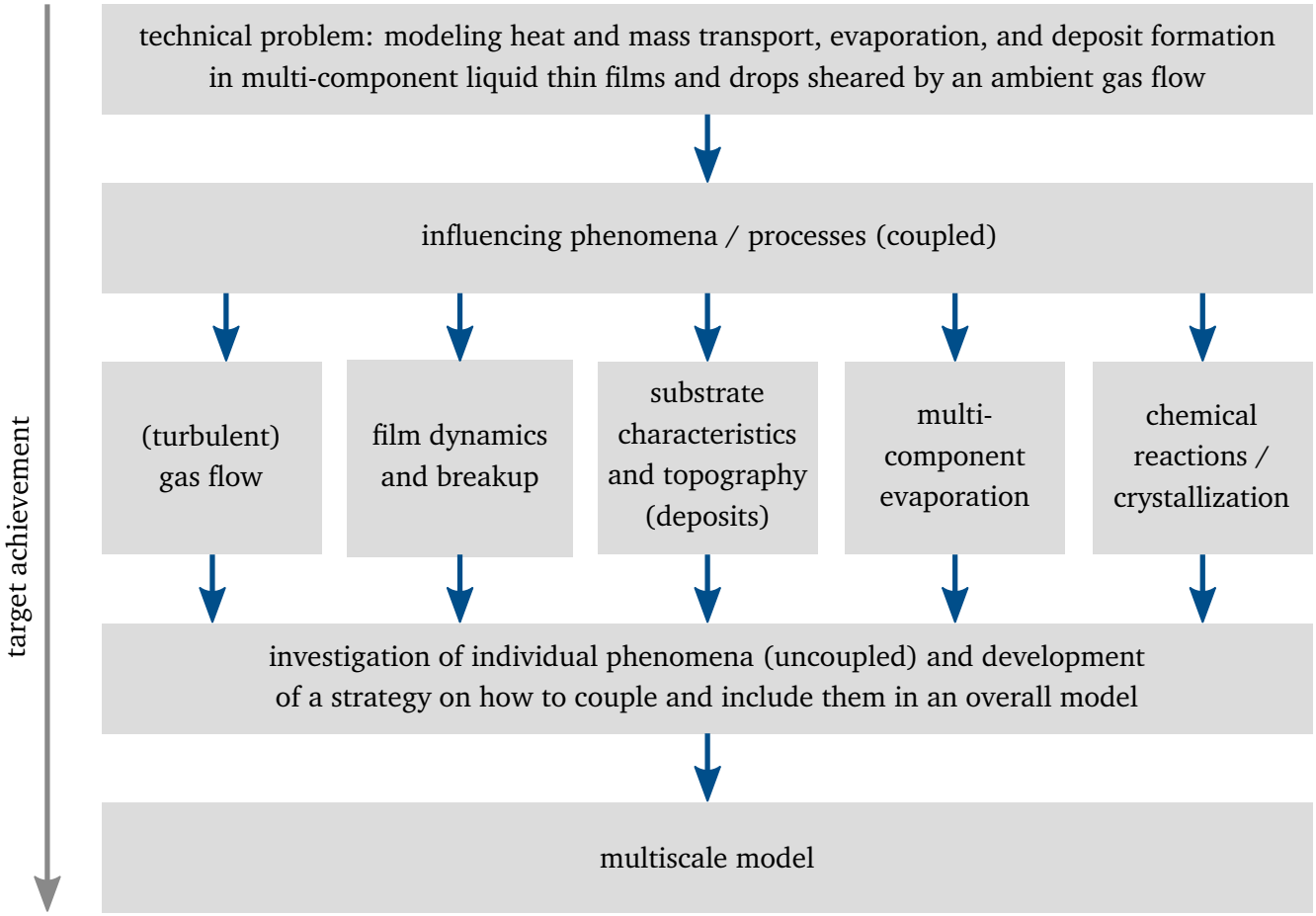

Figure 1.3: Schematic of the development process for the multiscale numerical model.

Existing modeling approaches, which are discussed in detail in the next chapter, cover selected individual phenomena and their effects on the process. Additionally, due to the mentioned length and time scales and the multitude of relevant physics, it is difficult to gain experimental access to the process. Laboratory scale experiments of engines and exhaust pipes have led to the identification of some influencing parameters on the process. However, it is usually not possible to measure all relevant physical parameters with a high enough spatial and temporal resolution to deduce a fundamental understanding of the involved processes and their dynamics. This means that, despite their practical importance, the sequence of the process and the dependence on different parameters remain unknown.

This thesis is one step to overcome these challenges and eventually obtain a multiscale model that can describe the entire process of the multi-component film evaporation on heated structured walls and the formation of deposits. The pathway from the technical problem to the multiscale model is shown in Fig. 1.3. The development starts at the technical problem of modeling the heat and mass transport, evaporation, and deposit formation in multi-component liquid thin films and drops sheared by an ambient gas flow. The target is to eventually develop a multiscale model for the entire process. As a first step towards the target, the key phenomena and processes of the problem, which influence the heat and mass transfer, have been identified. These are, firstly, the flow in the gas phase, which may be turbulent and influences the liquid dynamics and affects the transport in the gas phase. Secondly, various important influences on the film stability and breakup can be identified. The characteristics and topography of the

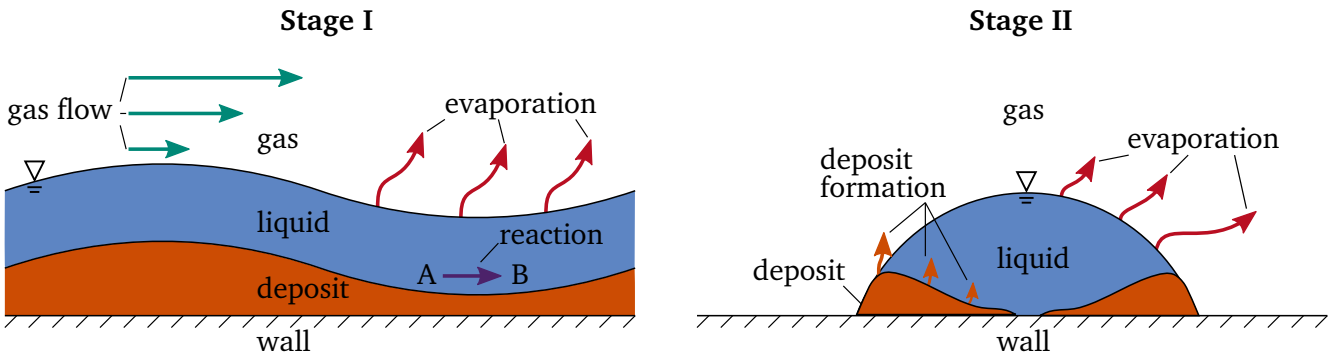

Figure 1.4: Overview over the two stages of the problem. Initially, a liquid film is present, which is influenced by the formed deposit, evaporation, chemical reactions, and the gas flow (left). After the film breakup, drops evaporate on the wall and deposit is formed (right).

substrate, which can be the deposit, have to be considered. The deposits can result from crystallization of a diluted component of the liquid or through chemical reactions of one or several species. The evaporation dynamics of the multi-component liquid has to be studied. Lastly, the chemical reactions in the liquid and the gas phase are of interest. In a later step, these identified key phenomena are investigated separately or with selected important interactions to determine their influence for the overall process. From these investigations, a strategy for the coupling of the physics can be deduced, which eventually leads to the multiscale model.

This thesis is the result of research in a subproject embedded in the "Collaborative Research Center/Transregio 150" [55], which aims at gaining a fundamental understanding of turbulent, chemically reactive multiphase flows near walls and to develop models to describe the complex industrial processes. The relevant influences on film dynamics and breakup, which are identified by the literature review, as well as the interaction of a turbulent gas flow with the liquid film are analytically and numerically investigated in this work. Furthermore, a model to simulate multi-component evaporation in connection with deposit formation is developed. The interplay between the deposit and the liquid is considered, as well. The porosity of the deposits and complex chemical reactions inside the fluid are not investigated in detail in this work.

As shown in the previous section, it can be concluded that the time scales of the film evolution and breakup are much smaller (in the range of milliseconds to several seconds) than the time scales of the deposit formation (dozens of seconds to hours). Additionally, various authors [30, 39, 97, 192] suggest that the deposit formation starts in the vicinity of the three-phase contact line, which means that film breakup has occurred before the deposit formation starts. From this, the following general scenario is identified: the liquid film initially present on the substrate ruptures at some point before deposit formation can be observed near the now formed contact lines. The time scale of deposit formation is slow compared to the time scale of the film rupture. These considerations lead to the separation of the process into two distinct stages for the scope of this thesis, as shown in Fig. 1.4. In the first stage, the thin liquid film evolution and stability is investigated. This film is primarily influenced by evaporation, chemical reactions, the ambient gas flow, and the formed deposit. The interaction of these phenomena eventually lead to film

breakup. In the second stage, the liquid film has been reduced to individual drops, which evaporate on the hot surface. Deposits form in this second phase from the evaporating drops.

The approach taken in this thesis is to first investigate the identified key phenomena, which are typical for the industrial applications and likely to influence the film evolution and rupture, as well as the deposit formation, individually. This allows for the selection of different methods best suited for the specific case. From the results gathered by these investigations, the importance of the individual phenomena and the relevant time and length scales can be derived. Conclusions on how to implement them into an overall simulation model are drawn. In future work, the relevant phenomena and interactions can then be included into this model.

The rest of the thesis is structured as follows: in the next chapter, the state of the art of liquid film evolution and breakup (stage I) and of deposit formation from evaporating drops (stage II) is summarized. The most important influencing phenomena and their interactions are identified, which primarily affect the film rupture and the formation of deposits, and which have to be understood to develop the multiscale model. Furthermore, important open questions are deduced from the literature survey, which are addressed in the thesis. In the third chapter, models for investigation of the film evolution and breakup for evaporating films on structured walls, films with chemical reactions, and films sheared by a turbulent gas flow are derived and important results are analyzed. The numerical model to simulate deposit formation from evaporating drops is presented in chapter four. Following validation, the results of this model are reported and the influence of various parameters on the deposit formation process and the resulting deposit shape is discussed. The results of both stages (film evolution and breakup, as well as deposit formation from drops) are summarized and discussed in chapter five and conclusions are drawn concerning the development of the multiscale model. Finally, the thesis closes with an outlook on suggested future investigations.

Chapter 2

State of the Art

The literature relevant for the two stages of deposit formation from evaporating liquids identified in chapter 1 is reviewed in this chapter. Firstly, film dynamics and stability of a thin liquid film (stage I) are addressed. After that, important contributions regarding drop evaporation and deposit formation from drops (stage II) are reviewed. Finally, the state of the art is summarized and important open research questions are deduced, which are addressed in this thesis.

2.1 Stage I – Film Evolution and Stability

This section gives a review of the experimental and numerical investigations of the evolution and stability of thin liquid films. First, important mechanisms determining the film stability are summarized and a widely used modeling approach is shown. Thereafter, existing work on the physical processes, which were identified as key influencing factors on film stability in the internal combustion engine and the exhaust pipe scenario (see Fig. 2.1), are discussed in separate sections.

The stable or unstable behavior of a liquid film is influenced by an interplay of various forces acting on the film and its interface. A more in-depth discussion of the instability mechanisms discussed in this section can be found, for example, in the textbooks [54, 68, 205] and the references therein. Firstly and intuitively, gravity has a major influence on film stability. If the film rests on the ceiling, meaning the

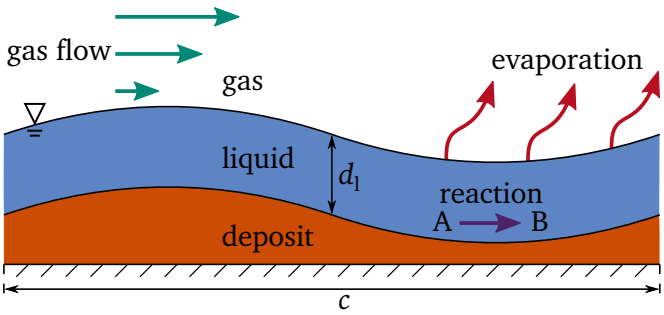

Figure 2.1: Important physical effects influencing evolution and stability of thin liquid films.

gravity vector points from the wall into the liquid, gravity contributes to an unstable behavior of the film and every infinitesimal film disturbance will grow and lead to film breakup (Rayleigh-Taylor instability). In contrast, if the gravity vector points from the liquid phase to the wall on which the film rests, the resulting volume force has a stabilizing effect on the film and the film surface is forced towards a flat interface shape. Gravity also plays an important role for the buoyancy-driven formation of convection cells (Bénard cells) observed in a thin liquid film resting on a heated wall. If the temperature-induced density gradients in the liquids are sufficiently large, convection cells form in the film. The resulting flow pattern is often referred to as Rayleigh-Bénard convection.

Secondly, surface tension always acts to minimize the surface energy, which means that, in the case of a constant surface tension, the film interface area is minimized. Neglecting effects at the three-phase contact line (assuming the film is unbounded), surface tension acts towards a flat interface shape and, thus, has a stabilizing effect on the film.

An important mechanism contributing to film instability and breakup is the Marangoni effect. Named after the Italian physicist Carlo Marangoni, it describes the transport of mass along a fluid-fluid interface due to surface tension gradients. The liquid is convected from regions with low surface tension towards areas with higher surface tension. Surface tension gradients on the interface can arise through temperature gradients or concentration gradients. The resulting Marangoni flow is called thermocapillarity or thermal Marangoni effect and solutocapillarity or solutal Marangoni effect, when it is caused by temperature gradients or concentration gradients, respectively. In the case of thermocapillarity, the surface tension reduces with temperature for most liquids. Considering a liquid film wetting a heated wall, this effect can lead to different instability mechanisms.

In the short scale instability (or short-wave instability), an arbitrary point of the interface becomes warmer than the surrounding area (e.g. by a random fluctuation). This leads to a local minimum of the surface tension and to an outward flow of liquid. Warmer liquid flows up to fill the void, which leads to a further increase of the interface temperature and to an enhancement of the flow. The feedback mechanism eventually results in vortex-shaped convective structures in the liquid film if the non-dimensional Marangoni number

$$Ma = \left| \frac{\partial \sigma}{\partial T} \right| \frac{\Delta T \, d}{2 \, \mu_\mathrm{l} \, a_\mathrm{l}} \tag{2.1}$$

exceeds a critical value ($Ma > Ma_\mathrm{crit}$). In the above, $\frac{\partial \sigma}{\partial T}$ is the gradient of the surface tension σ with respect to the temperature T, ΔT is a characteristic temperature difference of the problem (in this case the temperature difference between the wall and the ambient gas), the characteristic length scale d is the film thickness d_l for an infinite film, μ_l is the dynamic viscosity, and a_l the thermal diffusivity of the liquid. The length scale of the vortices is the length scale of the film height, which leads to a flow pattern similar to the Rayleigh-Bénard convection (sometimes called Marangoni-Bénard instability).

The long scale (or long-wave) instability is typically observed if the height of the film resting on the hot wall is small compared to the film length. If an arbitrary point of the interface has a higher temperature

than the surrounding interface as a result of fluctuation, a local minimum of the surface tension is the consequence and flow of liquid away from the hot point parallel to the interface results. Consequently, a film height minimum develops. Since, at the point of the film height minimum, the interface is closer to the hot wall, the interface temperature increases further, leading to a stronger sideways flow of liquid and to a further film height decrease. Eventually, this instability mechanism can lead to film breakup. A more complex instability mechanism called hydrothermal wave instability can be observed if the film is heated from one side and cooled from the other side [208]. Additionally, it is possible that short-wave and long-wave instability overlap, which can lead to a range of different flow patterns.

An ambient gas flow can affect the evolution and stability of liquid films as is familiar from the formation of water waves on a lake surface due to wind. Generally, the velocity of the liquid film will be lower than the velocity of the gas flow if the liquid film is set in motion through the shear stress of the gas at the liquid-gas interface. A disturbance (e.g. a wave) of the liquid-gas interface influences the shear flow in the gas phase. The gas flow has to move around the disturbance, leading to an increase of the local gas velocity and a decrease in the pressure above the wave. The minimum of the pressure field in turn leads to a further growth of the waves. This mechanism is called Kelvin-Helmholtz instability. Furthermore, in case of a turbulent gas flow, solely the local shear stress and pressure fluctuations, which result from the turbulent flow structures, can generate surface disturbances. The space- and time-dependent shear stress, for example, leads to film deformation traveling at different speeds. Over time, these waves grow as they merge with each other, which influences the film evolution and can lead to film breakup.

Lastly, evaporation influences the film dynamics and breakup. The influence of evaporation is threefold. Firstly, if the evaporative mass flux is not constant across the interface, it can lead to Marangoni convection either through temperature gradients at the interface from evaporative cooling or through concentration gradients in multi-component systems. Secondly, evaporation will generally reduce the mass of the liquid film and decrease the film height, which will eventually lead to breakup. Finally, the fluid leaving the liquid due to evaporation causes a recoil force on the interface, which pushes the interface towards the liquid. This so called vapor recoil is caused by the sudden decrease in density as the fluid transforms from liquid to vapor, which results in an expansion of the gas and a force on the interface.

A widely used approach to investigate the stability and evolution of thin liquid films is the so called long-wave theory (LWT) [57, 163]. Generally, it is assumed that the film thickness is much smaller than the length scale of the film thickness variation. The parameter ϵ, which is the film height divided by the length scale of the film thickness variation, is consequently much smaller than unity ($\epsilon \ll 1$). Using this assumption, the relevant governing equations (e.g. continuity equation, Navier-Stokes equation, and energy equation for a film governed by surface tension, gravity, and thermocapillarity) and associated boundary conditions are non-dimensionalized. Additionally, it is required that convective terms in the governing equations are small compared to diffusive terms. Employing a perturbation analysis in the parameter ϵ yields an evolution equation for the film height. For a two-dimensional film, the evolution equation can have the following exemplary structure:

$$H_\tau + \left[H^3 \left(S\, H_{XXX} - \frac{G}{3} H_X \right) - \widehat{Ma}\, H_X\, H^2 \right]_X = 0\,, \tag{2.2}$$

where H is the non-dimensional film height, τ is the non-dimensional time, X the non-dimensional spatial coordinate, S the non-dimensional surface tension, G the non-dimensional gravitational acceleration, and $\widehat{Ma}$ is a modified Marangoni number.

Depending on the investigated scenario, the definition of the non-dimensional parameters might vary or additional terms can appear. As can be seen from Eq. (2.2), the evolution equation is a fourth order partial differential equation in space and time. However, the big advantage of this approach is that only one equation has to be solved and that the importance of individual physical phenomena can be studied separately from each other by manipulating the non-dimensional parameters. This is why LWT is widely used to investigate stability and evolution of thin liquid films. A shortcoming of this method is that there is a direct assignment of one film thickness to each point of the film surface, which means that drop detachment and breaking of waves cannot be modeled. In addition, the inertia effect cannot be taken into account in the leading order. These limitations are often acceptable for thin films.

2.1.1 Films Driven by Evaporation and Marangoni Effect

Evaporating Films

Thin liquid films evaporating on planar or structured surfaces have been studied by various authors. The heat supply for evaporation can be provided either from a heated wall or from a hot ambient gas phase [226]. Furthermore, evaporation into a pure vapor atmosphere has to be distinguished from evaporation into a mixture of vapor and ambient non-condensable gas. In the former, the evaporative mass flux is determined by the heat transport to the interface [24]. In the latter, diffusive and convective vapor transport in the gas phase also influences the evaporation mass flux [132]. It is often assumed that the interface temperature is equal to the saturation temperature (for evaporation into a pure vapor atmosphere) or that the interface is saturated with vapor in the gas phase (for evaporation in the presence of non-condensable gas), which means a local equilibrium is achieved. However, in some cases (e.g. for thin films [195]), the assumption does not hold true, which is then called non-equilibrium evaporation.

Evaporation of a liquid film on a plane wall into a pure vapor atmosphere was considered by Burelbach *et al.* [48] using LWT. The effects of evaporative mass loss, vapor recoil, surface tension, viscous forces, and thermocapillarity on the film stability are discussed. Each parameter is varied individually to determine its influence on the film dynamics. Thermocapillary forces result from non-equilibrium evaporation, with the temperature of the interface depending on the heat fluxes from the wall to the interface and on evaporative cooling. Thus, local film height minima have a higher temperature than the surrounding interface, which results in film instability. For a condensing film (where the wall is cooled), thermocapillarity was found to delay the rupture time.

The so called disjoining pressure [109] arises due to attractive forces between liquid and substrate molecules. It leads to the presence of a thin adsorbed liquid film with a thickness of a few molecular layers in the region of the three-phase contact line, which influences the heat and mass transfer. This effect can be included into the long-wave evolution equation to investigate evaporating films with a three-phase contact line. This approach has been used to predict the dynamics and stability, as well as the heat and

mass transfer for both perfectly wetting liquids [129] and partially wetting liquids [3, 4, 162] evaporating into a pure vapor atmosphere.

Haut and Colinet [98] numerically studied evaporation of a thin liquid layer into a mixture of the vapor of the liquid and an additional non-condensable gas. An analytical expression for the evaporation rate was derived and a one-sided model for the process was obtained. Furthermore, it was shown that surface tension driven instability (Marangoni effect) is enhanced by the presence of the non-condensable component in the gas phase. A similar approach was taken by Dondlinger *et al.* [64] to study the linear and weakly nonlinear stability of a liquid film evaporating into an inert gas with neglectable interface deformation. Pattern formation inside the liquid film was found as a result of thermocapillarity above a linear stability limit.

A model for the description of film dynamics, as well as heat and mass transfer in a gas-driven film in a micro channel was developed by Kabova *et al.* [116] using the lubrication approximation. The film is locally heated from the lower wall and evaporates into the surrounding gas phase. Convective transport is taken into account in both the liquid and the gas phase. This allows the investigation of the development of the concentration and thermal boundary layers in the liquid film and the gas phase, as well as their influence on the evaporation rate and surface tension gradients. It has been found that diffusion in the gas phase is the limiting factor for evaporation at low gas flow rates. The influence of both the Marangoni effect and evaporation on the film deformation was quantified.

An evaporating liquid layer bounded on both sides by walls with different temperatures was considered by Sáenz *et al.* [185]. It had previously been shown that the horizontal temperature gradient along the interface leads to Marangoni convection and so called hydrothermal waves. The investigation of evaporation of the liquid into the ambient gas revealed that evaporative cooling of the interface, on the one hand, inhibits the wave formation, but, on the other hand, the thinning of the liquid layer due to evaporative mass loss enhances the effect. Furthermore, it was shown that the evaporation rate cannot be correctly predicted from vapor diffusion in the gas phase alone. The convective flow in the gas phase due to the Marangoni effect influences the concentration profile in the gas and the local evaporation rates.

Non-Evaporating and Evaporating Films on Structured Walls

The structure of the wall can have an important effect on the film dynamics and evaporation through the uneven heating of the liquid film, which in turn can result in thermal Marangoni convection and film instability. Deposit structures below the liquid film will consequently influence film evaporation as they considerably contribute to wall roughness. The stability, dynamics, and heat transfer of liquid films on structured walls have also received considerable attention in theoretical and numerical investigations.

Using a one-sided LWT model, it was shown that grooves in the flow direction of a falling liquid film have a stabilizing influence on the flow [81]. The evaporation of the falling film into a pure vapor atmosphere while flowing along a grooved wall was investigated. For low liquid mass flow rates, the grooves are only partially filled with the liquid film, leaving the groove crests dry. In this case, the presence of the three-phase contact line leads to a substantial increase of the overall heat transfer due to the high evaporation rates in the vicinity of the three-phase contact line (the so called micro-region evaporation

[214]). Similarly, observations were made with a model describing liquid films driven along the grooved surface by the gas flow and compared to experimental data [100].

The thermocapillary induced deformation and rupture of a thin liquid film resting on a heated structured wall was investigated by Gambaryan-Roisman *et al.* [83] and Kabova *et al.* [117, 118] using LWT. The thickness of the film is not uniform due to the sinus-shaped wall structures, which leads to a non-uniform temperature distribution at the liquid-vapor interface. The local temperature maxima at the interface are found above the locations of the film structure crests and the temperature minima correspond to the locations of the structure troughs. The temperature differences lead to thermocapillary stresses, which result in liquid Marangoni flow from the film height minima to the film height maxima and consequently enhance film deformation. It was found that the evolution equation of the film height can posses stable stationary solutions or describe the local film thinning and rupture. This depends both on the parameters of the surface structure (amplitude and wavelength of the grooves) and on the values of the governing parameters of the film flow, which reflect the relative importance of surface tension, gravity, and Marangoni stresses.

LWT was also used to study the stability of a falling liquid film on a grooved surface evaporating into a mixture of vapor and a non-condensable gas [82]. It was assumed that the heat transfer between the liquid and the ambient gas phase is determined by a constant heat transfer coefficient. In the limit of small surface groove amplitudes compared to the average liquid film thickness (a so called microstructured surface), the dynamics of a resting evaporating film has been investigated. It was shown that the film dynamics are either dominated by the Marangoni effect or evaporation during different stages of film thinning. The amplitude of the film height deformation increases in the stages, which are governed by the Marangoni convection. The work focuses on cases where the Marangoni effect is the major driving force for the rupture of the liquid film.

Eres *et al.* [73] modeled a coating process of a two-component liquid where one component evaporates into the ambient gas phase with a prescribed evaporation rate. This leads to thinning of the liquid film and varying species concentrations in the film. The governing equations are reduced to a pair of coupled, nonlinear partial differential equations using lubrication approximation. Surface tension forces arise from gradients of the solvent concentrations at the interface and lead to oscillatory motions of the free surface. Gaskell *et al.* [84] built on this model and investigated the flow of an evaporating two-component film flowing down an inclined and structured wall. The surface tension force was kept constant in this research, but the viscosity of the liquid changes as a function of the solvent concentration and may lead to deformations of the free surface. It was shown that local wall topographies can lead to an uneven distribution of the volatile component in the liquid film.

There is increasing interest in the literature in liquid film evaporation and into controlling the associated Marangoni effect [80]. However, the simultaneous influence of evaporation and the Marangoni effect on the dynamics and stability of the liquid film on a heated structured wall has not been systematically studied. Furthermore, the review reveals that the effect of the Marangoni convection on an evaporating liquid film where the heat for evaporation is provided from a hot gas phase has not been investigated numerically.

2.1.2 Reactive Films

Despite the extensive interest in the stability of thin liquid films and its frequent appearance in industrial applications, the influence of a chemical reaction inside the film on film dynamics and stability has not received much attention. The first analytical and numerical contribution found in this area is the work of Dagan and Pismen [59], who investigated the impact of a multistable kinetic system on the film dynamics using a long-wave model. Concentration gradients at the interface lead to a solutal Marangoni effect, which can cause the development of film height disturbances. A linear stability analysis for a reversible interfacial reaction of two semi-infinite liquid phases was conducted [229]. The reaction was assumed to take place at the interface of the two liquids, where a solute of the one liquid rapidly reacts with a solute of the other liquid to form a product species. Oscillatory instabilities are obtained in a small concentration range.

A reactive falling film was studied by Qi and Johnson [176] with viscosity being a function of the film composition. The reaction order was found to influence the linear stability of the flow system. Braun *et al.* [42] examined the influence of solutocapillarity on the spreading of a drop on a solid plate using lubrication approximation. An isothermal chemical reaction inside the drop leads to surface tension driven flows, which affect the flow patterns during early stages of the drop spreading.

The influence of a chemical reaction of an insoluble surfactant on the dynamics and breakup of a thin liquid film on a solid substrate was investigated by Gallez *et al.* [79]. The chemical reaction leads to variation of the surfactant concentration at the interface and, consequently, to surface tension gradients. This gives rise to Marangoni convection and causes film dynamics, which cannot be found from the pure hydrodynamic model of the film surface. Reacting surfactants at the interface of thin horizontal liquid films were also considered in the work of Pereira *et al.* [167, 168]. The surfactant reacts with a second species adsorbed at the interface. The long-wave approximation was used to derive three coupled equations for the film height and the two species concentrations at the interface. The chemical reaction of the surfactant was found to have a destabilizing effect on the liquid film and to give rise to solitary pulses at the interface.

A vertically falling liquid film in contact with a wall of constant temperature was considered by Trevelyan *et al.* [222]. A first order chemical reaction was present in the film following an Arrhenius equation for the reaction rate r_{react}

$$r_{\mathrm{react}} = r_{\mathrm{react},0}\, e^{-\mathscr{E}/(\mathscr{R}\,T)}, \tag{2.3}$$

where $r_{\mathrm{react},0}$ is the pre-exponential factor, $\mathscr{E}$ is the activation energy, and $\mathscr{R}$ the universal gas constant. The chemical reaction was assumed to be slow, leading to small values of the dimensionless Damköhler number

$$Da = \frac{d^2\, r_{\mathrm{react}}}{\nu_{\mathrm{l}}}, \tag{2.4}$$

where the characteristic length d is again the film thickness d_{l}, ν_{l} is the kinematic viscosity of the liquid, and r_{react} is evaluated for a characteristic temperature.

The liquid-gas interface was assumed to be adiabatic and having a constant concentration of reactant. This assumption leads to an unlimited supply of the reactant from the interface into the film through diffusive mass transport. After an initial transient phase, a stationary concentration distribution of reactant in the film is established. Consequently, the investigation focuses on the behavior of the film when small deviations from the stationary state occur. The lubrication approximation and a double perturbation analysis lead to the deduction of an evolution equation for the film height. The analysis of the basic state revealed that, as long as the surface tension decreases with increasing temperature, exothermic reactions have a stabilizing effect on the liquid film. Furthermore, exothermic reactions were found to decrease the mass transport inside the film. If, however, the chemical reaction is endothermic, the reaction destabilizes the liquid film and can lead to film rupture.

This analysis was extended by Trevelyan and Kalliadasis [221] to large values of the non-dimensional Péclet number, which means that convective transport in the film is important. The Péclet number for mass transport problems is defined as the product of the non-dimensional Reynolds number and the Schmidt number

$$Pe = Re\,Sc = \frac{d\,u}{\nu_\mathrm{l}}\,\frac{\nu_\mathrm{l}}{D_\mathrm{bin}} = \frac{d\,u}{D_\mathrm{bin}}\,, \tag{2.5}$$

where u is a characteristic velocity and D_bin is the binary diffusion coefficient. To include convective terms into the evolution equation, higher order terms were kept in the derivation of the equation, which allowed the investigation of the whole feedback cycle of the problem. The temperature gradients at the interface resulting from the chemical reaction lead to surface tension gradients, which affect the evolution of the liquid film. The evolution of the liquid film, however, alters the reaction rate through convective heat and mass transport and therefore has an effect on the release of heat from the chemical reaction. A summary of the works of this research group is given in [223].

The effect of the energy release from an exothermic reaction on the temperature and concentration-dependent viscosity and density of the liquid was considered for a thin liquid film bounded from above and below by an inviscid fluid with constant density and temperature [149]. The liquid film was so thin that gravitational effects were neglected. The influence of gravitational forces compared to surface tension forces is captured in the non-dimensional Bond number

$$Bo = \frac{\rho_\mathrm{l}\,g\,d^2}{\sigma}\,, \tag{2.6}$$

where ρ_l is the density of the liquid and g is the gravitational acceleration. If the Bond number is small, $Bo \ll 1$, gravitational forces can be neglected compared to surface tension forces. As density and viscosity of the liquid decreased with increasing temperature, the exothermic chemical reaction leads to decreasing film density and viscosity and, additionally, gives rise to thermocapillary effects. It was found that the density reduction has a stabilizing effect on the film evolution, while the thermocapillary effect and the decrease of the viscosity of the liquid are destabilizing.

No investigations were found considering the effect of the limited supply of reactant in the film on the film dynamics. In the industrial applications mentioned in the previous chapter, the reactants (educts) are components of the liquid forming the thin wall films. This means that the reactant cannot be supplied by mass transfer with the ambient gas phase and the amount of reactant in the film decreases over time as the chemical reaction consumes it.

2.1.3 Shear-Driven Films

In single-phase flows, the Reynolds number is the important non-dimensional number used to characterize the flow and predict flow patterns. It is defined as the ratio of inertia and viscous forces

$$Re = \frac{u\,d}{\nu}\,, \tag{2.7}$$

where d is the characteristic length of the problem (e.g. the channel height for gas flows or the film thickness for thin liquid films). If the Reynolds number is increased sufficiently (past a critical Reynolds number Re_{crit}), an initially laminar flow becomes unstable and transitions to a turbulent flow. The critical Reynolds number depends on the geometry of the flow problem [172].

An important characteristic of turbulent flows is that the flow velocity varies drastically and irregularly in both space and time. The velocity field can be divided into a statistically stationary mean velocity and velocity fluctuations [172]. An often used measure for the shear stress applied by a turbulent flow on a wall or a fluid interface is the non-dimensional friction Reynolds number

$$Re_\tau = \frac{u_\tau\,\delta}{\nu}\,, \tag{2.8}$$

where $u_\tau \equiv \sqrt{\overline{\tau}_{\mathrm{int}}/\rho}$ is the friction velocity, $\overline{\tau}_{\mathrm{int}}$ is a temporal and spatial average of the wall shear stress component in the main flow direction, and the length scale δ follows as $\delta = d/2$ for channel flows.

The evolution and stability of liquid films sheared by an ambient gas flow has been investigated both experimentally and numerically. An overview of both approaches for liquid films sheared by laminar and turbulent gas flows is given below.

Experimental Investigations

As the modeling of turbulent two-phase flows is very challenging, this area has received considerable experimental attention applying various different measuring techniques [103]. Many experimental investigations consider falling films accompanied by a co- or counter-current turbulent gas flow, motivated from the industrial applications in thin film evaporators or condensers [9, 10, 23, 47, 104]. The film stability limit is substantially reduced for falling films compared to horizontal films [114, 115]. The influence of gravity outweighs the shear stress influence for falling films in many cases, which is why flow regime maps generated for falling films cannot be transferred to horizontal films. Isothermal horizontal

liquid films sheared by an ambient turbulent gas have been the subject of many experimental investigations [22, 43, 111, 112, 113, 164], while evaporating horizontal liquid films sheared by a turbulent gas flow were considered in [99, 100, 112, 114, 184, 231].

Ayati *et al.* [22] imposed waves into the liquid film by an oscillating plate at the liquid-gas interface near the entrance section of the two-phase channel. For the wave frequencies generated, the influence of the turbulent gas flow on the wave shape could not be quantified. Flow regime maps show the expected shape of the liquid-gas interface as a function of the Reynolds number of the liquid film flow and the Reynolds number of the gas flow. For a perfluorohexane (FC-72) film, such flow regime maps were obtained for moderate Reynolds numbers for non-evaporating [113], as well as for heated and evaporating liquid films (with the wall heat flux as an additional parameter) [114]. Depending on the liquid and gas Reynolds number, a smooth interface, two-dimensional waves, three-dimensional waves or a breakdown of the film flow are observed. Similar flow diagrams have also been obtained for water [43] with the velocity and the length scale of the expected film structures as input parameters. Furthermore, two separate deformation regimes of the liquid-gas interface were identified by Paquier *et al.* [164]. The first regime corresponds to low gas velocities and shows that the film surface is dominated by seemingly randomly distributed wrinkles, which propagate downstream and are elongated in streamwise direction. The amplitude of the film height disturbance increases approximately linearly with the gas velocity in this regime. Above a threshold in the wind speed, in the second regime, well organized gravity capillary waves were observed. The amplitude of the film height disturbances was then found to increase stronger than linearly with increasing gas velocity.

The gas flow rate was found to influence the occurrence of film breakup [104], as well as the frequency, wavelength, and velocity of the film height disturbances. With increasing gas Reynolds number, the frequency and velocity of the film height disturbances increase, while the spacing between the waves decreases [9, 23, 47, 231]. Additionally, the disturbance growth rates and life times depend on the gas flow direction and Reynolds number [7, 10]. Furthermore, it was found that the velocity profile inside the film is similar to the laminar velocity profile due to the high viscosity of the liquid [164, 231] and that the turbulent boundary layer above the film behaves similarly to a boundary layer above a dry wall [184].

As the film behavior strongly depends on the liquid and gas Reynolds number, the used fluids, and the experimental conditions, a quantitative comparison between different works is difficult.

Analytical Investigations and Numerical Modeling

Theoretical and numerical modeling of the evolution and stability of co-flowing or counter-flowing two-phase laminar flows revealed that the interfacial shear stress can lead to film deformation, traveling waves, development of ligaments, instabilities, and three-dimensional surface structures using approximate methods [36, 137, 193, 241] and numerical solution of the full equation system [75, 225].

However, in the case of a turbulent gas flow, the modeling of the system is much more challenging. A review on different approaches for numerical simulations of the problem can be found in [14]. It has been shown numerically that the mean velocity field of the turbulent gas flow influences the evolution of the liquid-gas interface [213].

An often used simplification for the treatment of turbulent flows is the use of Reynolds-averaged Navier-Stokes (RANS) models in which the main velocity field of the flow is obtained from solving the Reynolds equations [172, 191]. Turbulence models (such as the often used k-ϵ model) are used to determine the Reynolds stresses, which appear as unknowns in the Reynolds equations. The benefit of this type of modeling lies in the relatively low computational cost. However, the quality of the results depends on the used turbulence model and its suitability to the individual flow problem. Furthermore, only average values for the velocity field and the resulting interfacial shear stresses in a two-phase flow problem can be obtained.

Using RANS models in the gas phase, a linear stability analysis of a thin liquid film sheared by a turbulent gas flow has been conducted by Ó Náraigh *et al.* [159]. A base-state model for steady and fully developed flow fields was derived using a mixing-length theory and an interpolation function for the eddy viscosity. It was shown that the flow field in the liquid is quasi laminar and that destabilization of the interface can result from the big difference in the viscosity of the two fluids. The resulting pattern is referred to as interfacial modes, while internal Tollmien-Schlichting modes could also be predicted. By modifying the formulation of the eddy viscosity, the effect of interfacial roughness, which corresponds to the wave amplitude for a disturbed film, was approximated. For large interfacial roughness, a competition between the two modes was demonstrated. A similar work from the same research group focused on the effect of the Reynolds stresses induced in the gas flow by interfacial waves [160]. Using various RANS turbulence models, it was shown that these wave-induced stresses do not affect the flow for low Reynolds numbers. But at higher Reynolds numbers they had to be considered to obtain good agreement with experimental values. For small wave amplitudes, however, good agreement can be reached even for larger Reynolds numbers ($Re = \mathcal{O}(10^5)$). An Orr-Sommerfeld stability analysis of the problem showed that the film flow is unstable to linear perturbations due to the large difference in viscosity between the liquid and the gas for high Reynolds numbers.

The influence of a turbulent gas flow on the stability of an isothermal [8] and condensing [5] liquid film flowing down an inclined plane has been considered. The effect of the gas flow on the film was described by a constant interfacial shear stress. Tseluiko and Kalliadasis [224] used separate models for the liquid and the gas problem for a falling film with a counter-flowing turbulent gas. By taking advantage of the large difference in viscosity between the liquid and the gas phase and using the assumption that the turbulent fluctuations in the gas phase decay towards the interface similarly as towards a solid wall, the two problems have been solved independently from each other. A RANS model was solved in the gas phase to obtain the average turbulent flow field, while LWT was used in the liquid phase. This model was later extended to co-flowing liquid and gas flows [227]. The interfacial shear stress gathered from the solution of the flow problem in the gas phase was used for the solution of the liquid flow problem. Using an integral boundary layer (IBL) method, the effect of the turbulent gas flow on a single-hump wave of the liquid film was analyzed. Additionally, the work of Tseluiko and Kalliadasis [224] has been extended to the investigation of the linear stability of the system [228]. Convective instabilities, meaning that local disturbances grow by traveling downstream with the film, were found at low flow rates of the gas phase, while initially localized instabilities spread across the entire domain at higher gas flow rates and were then referred to as absolute instabilities. However, as mentioned before, the results for falling films cannot be directly transferred to horizontal films since gravity severely influences the results [115].

A combination of a volume of fluid method (VOF) with RANS modeling and a k-ϵ turbulence model was used to study the effect of turbulence on a liquid-gas interface [147, 148]. A strong gas flow has shown to cause instabilities in the film, which in turn induces the formation of wave patterns and disengagement of drops from the film. It was found that surface waves enhance heat transfer from the film to the gas phase. This approach is also widely used in other works for isothermal or evaporating falling and horizontal films for industrial applications, due to the easy setup of the problem in commercial computational fluid dynamics (CFD) codes and the limited computational cost [58, 85, 135].

A similar modeling idea (RANS and VOF) was pursued in the work of Shirani *et al.* [204], where a VOF equation for turbulent flows was obtained, which included an additional term named the volume fraction velocity term. This term takes the influence of the fluctuating velocity field on the interface into account and is modeled using the turbulent kinetic viscosity. Additionally, a scaling factor is needed, which has to be adjusted to the specific scenario. Another approach to improve the results of RANS calculations in two-phase flows was to analyze the results of direct numerical simulations (DNS) and experimental investigations and to deduce a specialized turbulence model for interfacial flows [155]. It was found that this model can account for the reduction of the eddy viscosity near the free surface and that the movement of the free surface can be included by deriving a transport equation for the surface position. However, the effect of the locally fluctuating turbulent fields on the free surface cannot be accurately described with these models.

Since RANS models yield an average velocity field, they are not capable of modeling the effect of the fluctuating turbulent shear stresses on the interface evolution. Large eddy simulations (LES) have been used in various works to capture the turbulent shear stress influence on the interface in two-phase flows. Compared to RANS approaches, LES is computationally more expensive. In a typical LES approach, the large scale structures, containing about 80 percent of the turbulent energy, are resolved. The contributions of the smaller motions, in the so called subgrid scale (SGS), are modeled. Several models exist for different applications and a free surface requires a specialized treatment of the SGS motions. Two of such specialized SGS models for free surface turbulent flows have been developed based on the analysis of DNS results and using the assumption that the surface fluctuations are small [203]. This is done to more accurately calculate the turbulent field in the gas phase, while its effect on the surface movement is not considered. If surface movement is included, additional SGS terms appear [154]. Ketterl and Klein [124] reviewed various SGS models for multiphase flows and compared them with DNS data of spray breakup. It is concluded through correlation and a magnitude analysis that the correct treatment of the interface remains challenging.

A review of LES methods used for free surface flows with an emphasis on applications in engineering can be found in [152]. LES has been combined with a VOF method for interface capturing to describe cavitation of a turbulent flow around an airfoil [183]. Comparison of RANS and LES results revealed that the RANS model gave poor results for the two-phase flow problem. A drop sheared by a turbulent gas flow was investigated with LES and VOF by Rettenmaier [179]. Adaptive mesh refinement at the liquid-gas interface was used to resolve the turbulent velocity field down to the level of a direct numerical simulation, while further away from the interface a standard LES is conducted. This idea has been previously formulated by Herrmann and Gorokhovski [102]. However, the interface area for films is much

larger than for drops and no works have been found applying this method to the dynamics of a liquid film on a wall.

The most accurate numerical representation of turbulent flows can be achieved with direct numerical simulations (DNS) in which all eddies are resolved down to the Kolmogorov length scale. This makes DNS very costly in terms of computational effort, which is why it is rarely used for multiphase flows or complex geometries. Some approaches considered two-phase flows with DNS under the assumption that the interface is flat [145] or that the amplitude of the interface deformations are at least two orders of magnitude smaller than the wavelength of the waves [143]. Using a DNS and a boundary-fitting method, the turbulence characteristics of a counter-current gas-liquid flow were analyzed and compared to an open-channel flow [78]. The method focused on the characteristics of the gas flow and was restricted to small changes in the topology of the interface and the absence of drop separation. It was shown that the lighter phase (the gas phase) perceives the interface similarly to a flexible solid surface. The method has later been extended to condensing films [134].

A direct numerical simulation of a counter-current air-water flow down an inclined plane has been performed by Zonta *et al.* [247, 248]. A boundary-fitting method is used for the interface representation, and the domain is mapped from the deformed geometry (due to liquid wave formation) to a reference domain. The growth and decay of waves are studied under the combined effects of gravity, turbulent shear stress, and pressure fluctuations. However, due to the high computational costs, this analysis was conducted for a relatively low friction Reynolds numbers ($Re_\tau = 170$).

Recently, the effect of a turbulent gas flow on a liquid surface below the onset of wave generation (in the so called wrinkle regime [164]) was studied numerically [169]. Time-averaged shear stress and pressure fluctuation fields from a DNS of a single-phase channel flow are used to calculate the surface displacement for a simplified liquid layer. To enable the coupling, it has been assumed that the surface structures are small enough to not influence the turbulent gas flow, i.e. the structures are within the viscous boundary layer. The liquid layer was assumed to be of infinite depth and at rest despite the shear from the gas flow. Additionally, the effect of surface tension on film stability was neglected. The results indicate that, in this configuration, the surface wrinkles, which are elongated in streamwise direction, are largely dominated by pressure fluctuations at the interface. It is concluded that larger surface waves form when the amplitude of the wrinkles becomes so large that the roughness effect on the turbulent boundary layer cannot be neglected.

No studies were found investigating the effect of the fully resolved turbulent shear stress data on the film dynamics of a horizontal liquid film taking the surface tension and movement of the liquid layer into account. The high gas Reynolds numbers of $\mathcal{O}(10^4 - 10^5)$ in the industrial applications considered are particularly problematic for a full DNS of a turbulent two-phase channel flow. However, the effect of the time-dependent shear stress structures on the thin film should be considered as they affect film evolution and stability, as well as heat and mass transfer phenomena.

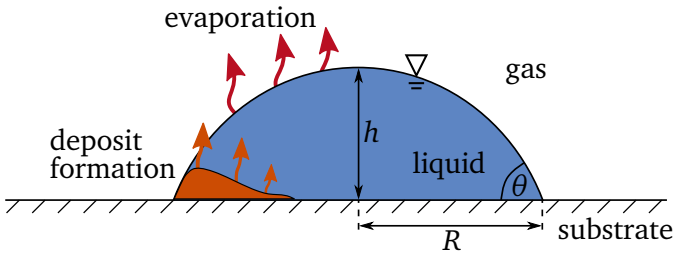

Figure 2.2: Deposit formation from an evaporating suspended drop.

2.2 Stage II – Deposit Formation from Evaporating Drops

This section summarizes experimental and numerical investigations of drop wetting, evaporation, and deposit formation. Following a brief overview on the influencing factors on the drop shape, the drop evaporation process is discussed. Afterwards, the works devoted to the deposit formation process from evaporating drops are reviewed.

2.2.1 Drop Hydrodynamics

A drop sitting on a substrate forms a contact angle θ at the three-phase contact line where liquid (index l), gas (g) and the solid substrate (s) meet (see Fig. 2.2). The contact angle follows from a balance of the line forces at the contact line (Young's equation) to

$$\cos\theta = \frac{\sigma_{\mathrm{sg}} - \sigma_{\mathrm{ls}}}{\sigma_{\mathrm{lg}}}, \tag{2.9}$$

with the interfacial tension at the solid-gas interface σ_{sg}, at the liquid-solid interface σ_{ls}, and at the liquid-gas interface σ_{lg} (thereafter denoted as surface tension and abbreviated with σ). Equation (2.9) assumes that there is a thermodynamic equilibrium between all three phases. The surface tension forces prevent further spreading of the drop and the interfacial forces between substrate and liquid prevent contraction of the drop [35]. The drop is in a state of minimal energy, which means that an external energy supply is necessary to increase or decrease the wetted substrate area. Thus, the resulting contact angle is often called equilibrium contact angle. It can be seen from Young's equation that the equilibrium contact angle depends on the solid-liquid-gas pairing. An equilibrium contact angle of $\theta = 0°$ is often referred to as complete wetting, $0° < \theta < 90°$ is called partial wetting (or hydrophilic if the liquid is water), $90° < \theta < 180°$ is partial non wetting (or hydrophobic for water), and $\theta = 180°$ is complete non wetting.

If a drop is evaporating and the volume of liquid in the drop reduces with time, one often finds experimentally that the wetted area remains unchanged initially and the contact angle of the drop decreases. The drop is not in an equilibrium with its surrounding and the receding of the contact line is actively prevented. Chemical imperfections of the substrate (locally varying wetting characteristics) or physical

imperfections (surface roughness or grooves) are responsible for this phenomenon. The drop is then referred to as a pinned drop.

Usually, a drop is not pinned for all contact angles. If the contact angle falls below the so called receding contact angle, the contact line recedes and the wetted area decreases. If the contact angle is higher than the advancing contact angle, the contact line will advance. The difference between advancing and receding contact angle is called contact angle hysteresis. The contact angle hysteresis depends strongly on the liquid-solid pairing, as well as on the chemical and physical properties of the substrate.

If a liquid drop on an impermeable substrate is small enough, the influence of gravity on the drop can be neglected. This influence is assessed with the non-dimensional Bond number, which is defined similarly to section 2.1.2. The characteristic length is defined based on the height of the drop apex h and the drop radius R ($d^2 = Rh$). If $Bo \ll 1$, the influence of gravity on the drop shape is negligible. For higher Bond numbers, gravity leads to a reduction of the drop height. Furthermore, the drop shape can be influenced by viscous forces arising from velocity fields inside the drop (e.g. caused by Marangoni convection). The effect of this velocity u inside the drop on the drop shape is assessed with the non-dimensional capillary number

$$Ca = \frac{\mu_l u}{\sigma}, \tag{2.10}$$

which compares viscous forces to surface tension forces. For $Bo \ll 1$ and $Ca \ll 1$ the drop shape can be assumed to resemble a spherical cap and one finds

$$h = R \tan\left(\frac{\theta}{2}\right). \tag{2.11}$$

Additionally, the drop volume V is then given from the relation

$$V = \frac{1}{6}\pi h\left(3R^2 + h^2\right). \tag{2.12}$$

2.2.2 Drop Evaporation

The evaporation of free drops with no contact line is a one-dimensional problem governed by the diffusion of vapor in the gas phase (see section 2.1.1). In contrast, the evaporation of a suspended drop on a heated substrate is a complex and at least two-dimensional phenomenon. Picknett and Bexon [170] found that drops evaporate either in the constant contact angle mode, where the contact angle stays constant and the wetted area decreases over time, or in the constant contact radius mode, in which the contact angle decreases and the drop is pinned.

However, it was found experimentally that a drop usually does not evaporate in just one of the two modes. After the suspension of the drop on the substrate, the drop spreads until it reaches a maximum diameter. After that, the drop evaporates in the constant contact radius mode until the contact angle falls below the

receding contact angle. When this point is reached, the contact angle remains at a fixed value, while the wetted area decreases [44, 211]. In the last phase, just before the drop is completely evaporated, both contact angle and wetted area decrease simultaneously [215]. Surface roughness or deposits on the wall can lead to additional cases, which are discussed in the next section along with the deposit formation.

The local evaporation rate of a suspended drop is generally not uniform across the interface, even if the interface has a homogeneous temperature and diffusion is the only transport mechanism in the gas phase. Only in the special case of a contact angle of 90° is the evaporative mass flux uniform across the liquid-gas interface and can be calculated analytically. If the contact angle is lower than 90°, the evaporative mass flux has a maximum at the three-phase contact line [72]. This can be explained intuitively with the larger amount of space per interface length at the contact line, which means that a vapor molecule is more likely to diffuse away from the interface at this position. This leads to higher concentration gradients at the three-phase contact line compared to the drop apex and consequently to higher evaporation rates [174]. It has been shown that the evaporation time of a drop decreases with increasing hydrophilicity (decreasing equilibrium contact angle) [202]. If the contact angle is higher than 90°, the evaporation rate has a minimum at the three-phase contact line and increases towards the drop apex.

Based on the solution of the Laplace equation for the vapor concentration in the gas phase, which is valid for quasi-stationary situations (see [215]), an expression of the evaporation rate as a function of the contact angle was first derived by Picknett and Bexon [170]. Hu and Larson [107] solved the evaporation problem numerically for arbitrary drops and contact angles between zero and 90 degrees. A correlation for the change of the drop volume $\dot{V}$ of the drop was derived from the results, which states

$$\dot{V} = -\frac{\pi M R D_{\mathrm{bin}}}{\rho_{\mathrm{l}} \mathscr{R} T} \left[p_{\mathrm{int}}(T) - p_{\mathrm{v},\infty} \right] \left(0.27\,\theta^2 + 1.30 \right) . \tag{2.13}$$

Here, θ is in radians, M is the molar mass, p_{int} is the saturation pressure of vapor in the gas phase at the position of the liquid-gas interface, and $p_{\mathrm{v},\infty}$ is the partial pressure of vapor in the gas phase far away from the interface. If the drop is small and evaporating in the constant contact angle mode, the drop volume over time can be derived analytically using Eqs. (2.11), (2.12), and (2.13). However, if the drop is evaporating in a constant contact radius mode, the volume evolution over time has to be obtained numerically or with an approximate solution given by Schönfeld *et al.* [194]. A more general expression for the evaporation rate, which is valid for arbitrary contact angles, was derived analytically by Popov [173]. However, it has been shown that the easier expression by Hu and Larson given in Eq. (2.13) captures the evaporation process very well for contact angles below 90° [209].

The evaporation rate increases with decreasing relative humidity (or decreasing partial pressure of the vapor) far away from the interface. It can be easily seen from Eq. (2.13) that the temperature influences the evaporation rate. The evaporation rate increases with temperature because the saturation pressure of the vapor increases stronger than linearly with temperature. However, the choice of temperature in this correlation is not trivial. The easiest thing is to assume that the drop has the same temperature as the heated wall or as the gas phase (if the wall is not heated). However, in this approach, the effect of evaporative cooling at the interface and the heat transport through the liquid or gas phase to the interface

are neglected. Additionally, thermal effects of the substrate might influence the temperature profile inside the drop and consequently the evaporation rate. In a typical diffusion driven drop evaporation case and assuming the substrate has a uniform temperature (an infinitely high thermal conductivity), the temperature field inside the drop is governed by the thermal conductivity of the liquid [215]. In this case, a drop resting on a heated wall has the maximum interface temperature at the contact line, leading to high evaporation rates at this position and the temperature minimum at the drop apex. However, it was shown that for substrates of considerable thickness or with a low thermal conductivity, the heat transport through the substrate can be the limiting mechanism [69, 136]. In this case, the contact line has the minimum temperature inside the liquid and the maximum temperature is observed at the drop apex. Numerical investigations demonstrated that a drop evaporates slower on a substrate with higher thermal resistance, independently from the source of this high thermal resistance, which can be its extensive thickness or its low thermal conductivity [2]. It was shown experimentally that the temperature differences between the apex and the contact line reduce with time for a pinned drop as the drop height decreases [87].

The thermal effects of the substrate (namely the thermal resistance) and evaporative cooling at the liquid-gas interface were included into the correlation for the evaporation rate of pinned drops by Sefiane and Bennacer [198]. These effects have also been considered experimentally for the evaporation of water drops [210]. It was found that for wall temperatures considerably higher than the ambient temperature, the thermal effusivity $\sqrt{k\,\rho\,c_p}$ (with the thermal conductivity k and the specific heat capacity at constant pressure c_p) is the major influencing factor. This is confirmed by numerical finite element investigations conducted by Lopes *et al.* [146]. Furthermore, they reported that the local temperature distribution at the liquid-gas interface is governed by the transient heat transport.

Convective transport phenomena associated with drop evaporation can be separated into convection in the liquid and in the gas phase. The evaporation itself induces a convective flow in the gas phase, the so called Stefan flow. This flow is induced by the different densities of liquid and vapor. If a certain mass of liquid evaporates at the interface and becomes vapor, the density suddenly decreases so that the newly created vapor drives out the already existing vapor boundary layer in the gas phase. In this case, the convective mass transport in the gas phase might become important. The significance of this (and other) convective mass transfer mechanism can be assessed with the non-dimensional Péclet number, as described in section 2.1.2 (with the characteristic length being the drop radius in this case). It has been reported that the maximum velocity of the Stefan flow is of the order $\mathcal{O}(10^{-3}\,\mathrm{m/s})$ [201], which makes Pe of $\mathcal{O}(10^{-2})$ for drop radii around 1 mm. In this case, the convective transport can be neglected compared to the diffusive transport. However, these estimations were based on contact angles of about 90° and low substrate temperatures. In the case of a heated wall, the Stefan flow can become important [215].

Additionally, buoyancy can lead to convective vapor transport in the gas phase. Ait Saada *et al.* [1] used numerical simulations to show the importance of buoyancy flow in the gas phase for the evaporation rate of drops at substrate temperatures higher than the ambient temperature. In another work, it was shown experimentally that alcohol drops evaporate faster for higher wall temperature than a pure diffusion driven model predicts, and it was shown numerically that the evaporation rate of alcohol drops only agrees with the pure diffusion driven model if gravity is neglected [49]. An empirical model for the contribution of the convective transport was derived. It was shown that, for hydrocarbon fluids, the evaporation rate

can be predicted with acceptable accuracy if an effective diffusion rate is defined, incorporating the effect of molecular diffusion and convective transport [97].

An important convective effect inside pinned partially wetting evaporating drops is the so called Deegan flow [61]. The maximum evaporation rate at the three phase contact line (for $\theta < 90°$) leads to a flow from the bulk of the drop towards the three-phase contact line. The flow velocity inside the drop increases along the drop radius and the Deegan flow becomes more pronounced with decreasing contact angle [62]. Typical flow velocities of the Deegan flow were given as $\mathcal{O}(10^{-5}\,\mathrm{m/s})$ [215].

The temperature differences along the liquid-gas interface of an evaporating drop can result in thermocapillary convection inside the drop. The non-dimensional Marangoni number is used to estimate the influence of the surface tension forces compared to viscous forces (see section 2.1) where the characteristic length of the problem is the drop height). It has been found that for typical temperature differences inside a millimeter sized drop on a substrate with high thermal conductivity, the thermocapillary induced flow velocity is $\mathcal{O}(10^{-1}\,\mathrm{m/s})$ and can, thus, outweigh the influence of the Deegan flow [215]. Semenov *et al.* [201] report based on numerical calculations that above a drop radius of $R = 10^{-5}\,\mathrm{m}$, the Marangoni convection inside a water drop should be considered. Yang *et al.* [239] modeled evaporation of a single-component drop using an arbitrary Lagrangian-Eulerian (ALE) method. The liquid is heated from below by a hot substrate. The temperature distribution in the substrate was solved for. Additionally, thermocapillarity is included in the model. It was shown that the Marangoni convection leads to a higher average temperature in the drop and to higher evaporation rates compared to a case in which thermocapillarity is neglected.

However, thermocapillarity is often neglected in the simulation of evaporating water drops. Hu and Larson [108] found no thermocapillary induced convection in water and explained the lack of Marangoni flow with the high affinity of water to be contaminated with surfactants in the experiment. A matching of the theoretical flow field with experimental data could only be achieved by reducing the Marangoni number by a factor of 100 [108, 136]. Girard *et al.* [86] concluded that the influence of the Marangoni flow on the evaporation of water drops is negligible. This was confirmed by comparing pure water with binary mixtures drops, with only Deegan flow being observable in the case of pure water drops [53]. It was, however, possible to induce thermal Marangoni convection inside a pure water drop by locally heating the substrate on which the drop was resting with a laser beam [128]. It can be concluded that the importance of the thermal Marangoni effect in water drops remains an open question and seems to depend strongly on the purity of the water and other experimental conditions.

Additional effects are encountered if the evaporating drop is a (binary) liquid mixture instead of a pure liquid. The liquid mixture inside the drop is not homogeneous if one of the components acts like a surfactant (e.g. water-alcohol mixtures), even in the absence of evaporation [215]. For an evaporating water-alcohol drop, an alcohol with low molar mass (e.g. ethanol or methanol) is the component with the higher vapor pressure for most compositions and is consequently expected to evaporate more strongly than water. Additionally, the surface tension of such alcohols is lower than the one of water. Consequently, the drop does not follow the four evaporation stages described above for a pure fluid. Instead, the concentration field inside the drop leads to a behavior in between the one expected for a pure water and a pure alcohol drop [144, 200]. It was found that the evaporation process of such a drop can be

divided into three stages [199]. Initially, the contact line is rich of alcohol due to its surfactant behavior. Consequently, the contact angle that can be observed is close to the equilibrium contact angle of alcohol. Since alcohol evaporates faster than water from the drop and the diffusive mass transport from the drop bulk to the interface is not fast enough to keep the concentration of alcohol at the contact line constant, the interface contains mostly water in the second stage of evaporation. The resulting contact angle was found to be similar to the contact angle expected for a water drop. As the wetting characteristics of the substrate result in a higher contact angle for water than for alcohol, the contact angle increased and the wetted area decreased. In the final phase, alcohol has diffused to the interface again and the contact angle decreases again. These changes in contact angle could be observed since the drop was not pinned. For pinned drops, the composition at the interface cannot be deduced so easily from the contact angle evolution.

Hamamoto *et al.* [95] describe the solutal Marangoni effect in an evaporating water-alcohol mixture. Initially, alcohol is uniformly distributed along the interface but, as the drop evaporates, the concentration of alcohol at the drop apex is reduced. The concentration near the three-phase contact line remains relatively stable despite the stronger evaporation in this region, due to the replenishing effect of the Deegan flow. This leads to a higher surface tension at the drop apex compared to the contact line and results in a Marangoni flow from the contact line towards the drop apex.

A numerical model to describe the evaporation process of an ouzo drop (a mixture of water, alcohol and oil) was developed [218]. An axisymmetric lubrication approximation is used to derive a height function for the interface position. The functionality between the liquid and vapor composition is formulated using Raoult's law that gives the vapor-liquid equilibrium for a multi-component mixture, which varies from the one of a pure fluid. The evaporation rate is limited by diffusion in the gas phase. Interfacial concentration gradients lead to solutal Marangoni effects, which in turn affect the heat and mass transport inside the drop.

Most studies investigating the evaporation of urea-water solution drops considered free drops with no contact line. Birkhold *et al.* [33] modeled the evaporation of free urea-water drops assuming rapid diffusion inside the drop. It was found that the vapor pressure decreases with increasing urea concentration at the interface, leading to a continuous decrease of the evaporation rate and an increase of the drop temperature over time. A detailed kinetic model of the evaporation and thermal decomposition of the UWS in SCR systems was used by Ebrahimian *et al.* [70]. They found that the vapor pressures of urea are so small compared to water that a pure evaporation of water can be assumed. Urea was found to melt and eventually decompose inside the drop at higher temperatures. Similar results were obtained from a reduced model, which separated the evaporation and decomposition of free urea-water drops into three distinct stages. In the first stage, the water evaporates from the drop, while urea decomposes in the second stage, which leads to chemical reactions in the gas phase in a third stage.

Evaporating free fuel drops have been considered by Ra and Reitz [178]. The drop was treated as spherical and the concentration inside the drop was assumed to be uniform to simplify the evaporation modeling for the complex liquid mixture. In later works, the diffusion inside the drop was taken into account, but the drop was still considered to be free and spherical [6, 188]. No studies could be found modeling the evaporation of UWS or fuel drops on heated substrates. However, similar effects as the ones

observed for water-alcohol drops are expected for such complex multi-component mixtures. The influence of the different evaporation rates of the components and the Marangoni flow on deposit formation are assessed more closely in the following section.

Most numerical simulations and experimental investigations consider axisymmetric drops for simplicity. A numerical study of three-dimensional elliptical and irregular drops has shown that a wide variety of three-dimensional flow phenomena are triggered by the irregular drop shape [186].

2.2.3 Deposit Formation

Deposition from evaporating drops has received considerable attention throughout the last two decades. Deegan *et al.* [61] showed that a sessile drop, which contains particles, leaves behind a ring-shaped deposit after the liquid is evaporated (often referred to as the "coffee ring effect"). The study of this phenomenon led to the deduction of the Deegan flow described in the previous section. The particles are transported towards the three-phase contact line where they accumulate at the interface of the pinned drop and form the deposition ring. The presence of the deposit was found to influence the drop hydrodynamics. An initially pinned drop is expected to experience transition to a constant contact angle mode after the contact angle falls below a threshold value (receding contact angle). The presence of deposits at the contact line, however, lead to a prolongation of the pinning phase, called self-pinning [62]. In some situations a stick-slip movement of the interface was observed, which means that the drop repeatedly switches between the pinning and receding of the contact line [161]. Concentric deposit rings result as the deposit pattern of a particle laden drop, in this case. A ring forms at each position where the contact line was pinned [220].

Controlling the deposit pattern is a very challenging task [45, 166]. It has been shown that necessary conditions for a coffee ring effect are the presence of particles in the drop, a pinned contact line, and a peak of the evaporation rate at the contact line [136, 197]. However, various other factors such as humidity, particle composition, size, concentration, shape, and interactions with the substrate influence the deposit pattern [197, 215, 242].

Additionally, it was found that convective effects inside the drop strongly influence the deposition pattern. Hu and Larson [108] showed that the presence of the Marangoni flow can outweigh the effect of the Deegan flow inside an evaporating drop and reverse the coffee ring effect. Thermocapillary flow transports the particles away from the three-phase contact line along the liquid-gas interface towards the drop apex, from where the particles are transported down towards the substrate at the center of the drop and deposit there. The direction and magnitude of the Marangoni flow was later shown to be sensitive to the ratio of the thermal conductivity of the substrate and the liquid, to the substrate thickness, and to the contact angle [182, 235]. It was concluded that the shape of the resulting deposit depends on the intensity of the Marangoni flow but is not influenced by its direction. In the absence of the Marangoni flow, a ring-shaped deposit is expected, while for increasing thermocapillarity, a uniform deposit layer can be found, and a cap-shape deposit with a maximum at the center of the wetted area is observed for strong Marangoni flow [197, 215].

Parsa *et al.* [165] experimentally investigated pattern formation from drying water-butanol drops. It was found that, in the initial stage of evaporation, local concentration gradients lead to solutal Marangoni flow inside the drop and a chaotic movement of the particles inside the drop. At later times, most of the volatile component has evaporated from the drop and the particle deposition patterns are governed by capillary and thermocapillary flow. A uniform deposit pattern was found on an unheated substrate and a dual-ring deposit shape (where the inner ring results from thermocapillarity) on a heated substrate. If the substrate temperature was increased further, a stick-slip behavior of the drop occurred leading to concentric rings.

So far in this section, only deposition of particles from the drop was considered. Another deposit formation mechanism is crystallization of an initially dissolved component. It was found that the deposit formation starts at locations of the substrate where the saturation concentration is exceeded [123, 141]. Convective effects influence the final deposit shape similarly to the deposit formation of particles [197]. Furthermore, it was shown that the evaporation rate of water drops with dissolved salt decreases with increasing salt concentration [244]. The deposit patterns from crystallization depend on the wettability of the substrate. Altering the substrate wettability leads to different crystal shapes [217]. Yakhno *et al.* [238] showed that water drops with dissolved sodium chloride leave behind ring-shaped deposits. However, the deposition pattern changes if an additional component is added to the liquid. A wide variety of deposition patterns was observed from drops of polystyrene and sodium chloride including concentric rings, needle-shaped crystals, and chains of triangular-shaped crystals [123]. It was found that the humidity of the gas phase and the composition of the liquid influence the observed deposit structures. Crystallization from drops of water and calcium sulfate were experimentally investigated [150]. The ring-shaped deposits were found to form from pinned drops in hydrophilic situations. Crystallization initiated at the three-phase contact line after a drop evaporation time of about 10 s on a hot surface. Afterwards, the crystals grow in all directions. Furthermore, evaporation on superhydrophobic and liquid-impregnated surfaces was investigated. It was found that impregnating the surface can prevent nucleation of crystals and self-pinning of the drop, which delays deposition and might be used to control the deposit formation process. Leiterer *et al.* [139] investigated the crystallization of caffeine from water drops. The crystallization starts at the three-phase contact line where the highest evaporation rates are observed and, thus, the concentration of caffeine has its maximum, if thermocapillary effects can be neglected. It was observed that the crystals grow from the three-phase contact line in all directions, meaning that deposits are encountered outside of the wetted area. This can be explained by the porosity of the crystal structures, which sucks liquid toward the outer region of the crystal.

Several works are devoted to the deposit formation from biological liquids. A simple baseline solution of a biological liquid containing the protein lysozyme and sodium chloride was investigated by Gorr *et al.* [88]. It was concluded that the deposition pattern depends strongly on the salt concentration. Experimental investigations of drying blood drops are conducted in hopes that the investigation of the resulting deposit pattern might open up new opportunities for diagnostics [46, 236]. It was found that the deposit formation begins at the drop edge and continues inwards from there. The Marangoni flow drives the red blood cells to the contact line. The control of the environmental conditions is essential as it was found that humidity influences the observed deposit patterns [38].

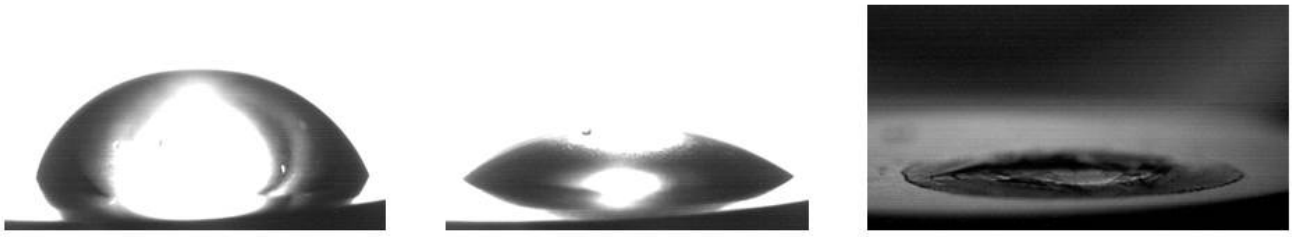

0 s 145 s 290 s

Figure 2.3: Evaporation and deposit formation from a urea-water drop on a heated wall (adapted from [30]).

Deposit formation from fuel drops was investigated by Arifin *et al.* [15, 16, 17] and Hänichen *et al.* [97]. In these works, a considerable number of drops (several hundred) were necessary before deposit formation could be observed. A difficulty arising from the highly complex liquid is that the deposit formation process is not entirely clear. Additionally, the multitude of drop evaporation events necessary to observe a deposit shape makes it difficult to asses the point at which the deposit formation starts. However, it was concluded that at substrate temperatures below the boiling point, an irregular deposit shape close to the substrate edge can be found, while the deposit formation was concentrated at the substrate center for higher temperatures [97].

The crystallization process of urea from drops of UWS was investigated experimentally by Schmid *et al.* [192]. Using optical and thermal measuring techniques, it was found that the deposit formation process starts at the three-phase contact line for all investigated substrate materials and temperatures. It was further shown that the deposit formation starts when the saturation concentration of urea inside the drop is exceeded. A maximum of the deposit growth rate was identified at the liquid-gas interface for hydrophilic substrates throughout the evaporation process. Additionally, a very pronounced peak in the drop temperature at the position of the deposit formation can be observed for the moment at which the first deposit is formed. The temperature increases by up to 40 K and then decreases again within a time frame of about 0.2 s, leading to large temperature gradients of $\mathcal{O}(10^2\,\mathrm{K/s})$. This is explained by the heat released from the crystallization of urea. Interestingly though, this temperature increase is only observed at the moment of initial deposit formation and not throughout the entire deposition process. The initiation of deposit formation at the three-phase contact line for evaporating urea-water drops was also found experimentally in [30]. In order to get a clearer view on the deposit formation process, the urea mass fraction was reduced to 2 % (compared to 32.5 % for AdBlue). Snapshots of the drop evaporation and the resulting deposit shape from this investigation are depicted in Fig. 2.3. It was concluded that the drop is pinned throughout the evaporation process (despite the low urea concentration) and that the deposit formation was limited to the area around the contact line.

Modeling of the deposit formation process is a challenging task due to the large number of influencing factors discussed above. Popov [173] developed an approximate model to investigate deposit formation of colloid particles at the contact line of drying drops due to capillary flow. Karapetsas *et al.* [121] used lubrication theory and the assumption of a homogeneous concentration over the drop height to derive a numerical model for particle transport in thin drops. It was found that, as the particle concentration at the

contact line increases, the evaporation rate decreases. Similarly, it was found from a long-wave simulation that an evaporating thin film with receding contact line leaves behind rings of deposits due to the stick-slip motion of the film [76, 77]. Similar investigations have been performed for the self-organization in thin liquid films of a volatile solute and a non-volatile component taking into account the solutal Marangoni effect [66]. A level-set method has been utilized to track a growing deposit layer from sedimentation at the base of a liquid film [140].

An approximate expression for the deposit height and slope formed by nanoparticles at the contact line of an evaporating drop was derived by Askounis *et al.* [21] based on the results of experimental investigations. It was found that an increase of the evaporation rate leads to a decreased slope of the deposit. Recently, Kolegov and Barash [131] developed a simplified model to compute the particle transport inside a pinned drop accounting for diffusion, advection and capillary forces between the particles. The particles are transported towards the three-phase contact line due to Deegan flow. In the final stages of evaporation (when the drop is very thin), particle chains are formed stretching from the contact line towards the drop center originating from capillary attraction between the particles.

No studies could be found considering a full numerical model for the deposit formation of pinned drops where the temperature and concentration fields inside the drop are resolved in both vertical and radial direction. Furthermore, the effect of the formed deposit on the heat and mass transfer inside the drop has never been considered.

2.3 Conclusions from the State of the Art and Goals of the Thesis

The objective of this thesis is to numerically investigate film stability and breakup, as well as deposit formation from evaporating drops, which are the two stages of the problem identified in section 1.2. From the developed models, the important physical parameters and their interactions are deduced with the help of parametric studies. The long-term target, which is not in the scope of this thesis, is to obtain an overall multiscale model (see Fig. 1.3) for film evaporation and deposit formation in inner-engine and exhaust pipe conditions.

The literature review shows that there is a substantial amount of research in each of the particular aspects of the problem. However, several important issues remain open. These can be summarized as follows:

- The film evaporation and film stability on a structured wall have each been investigated individually. The interplay of these phenomena on each other has, however, not been addressed.
- A number of research has dealt with chemical reactions in a thin liquid film. An underappreciated topic is the effect of the decaying reaction rate over time, which is expected to severely influence the film stability limit.
- A large amount of studies focuses on the effect of a turbulent gas flow on a liquid film, but resolved direct numerical simulations of the shear stress fields are commonly not considered. It remains an open question how these time and space varying shear stress fields affect the liquid-gas interface and how this complex phenomenon can be appropriately modeled numerically.

- Deposit formation from evaporating drops has been extensively studied experimentally for both particle laden drops and deposition through crystallization. However, no detailed numerical models of crystallization-driven deposition from a drying drop exist. The effect of several important parameters (such as wall temperature, concentration, and thermocapillarity) on the time and position of the first deposit formation, as well as the deposit growth rates and the influence of the deposit on the drop evaporation process have not been investigated numerically.

Based on these open topics, research questions have been derived that are addressed in this thesis. These can be separated into the derived two stages of the problem as follows:

Stage I – Film Evolution and Stability

- Which of the identified important phenomena (evaporation, chemical reactions, (turbulent) gas flow, Marangoni effect) influence the film stability and lead to film breakup and how can they be appropriately modeled?
- How do these phenomena interact with and influence each other?
- What are the relevant time scales of the growth of the film height disturbances and film breakup?

Stage II – Drop Evaporation and Deposit Formation

- What is the influence of key parameters (wall temperature, initial composition, drop radius, wettability) and the Marangoni effect on deposit formation?
- Where does the deposit form, what are the deposit growth rates, and what is the shape of the deposit structure?
- How does the formed deposit structure influence the drop evaporation?
- What are the relevant time scales of the evaporation and deposit formation process?

The film stability and evolution is discussed in the next chapter. LWT is the method chosen to investigate the thin liquid film due to its advantages mentioned in section 2.1. The chosen fluid is hexane as an exemplary fluid for inner-engine conditions. Chapter 4 numerically investigates drop evaporation and deposit formation using a finite element method (FEM) with a moving mesh. This method is chosen to accurately resolve the liquid-gas interface. Urea-water solution is the chosen binary-component liquid in this chapter due to its use in exhaust gas treatment. The advantage of this liquid compared to fuels is that the mechanism of deposit formation (crystallization of the urea on the wall) is known. All models and methods developed in this thesis can, however, be used to investigate other fluids. So, for example, as soon as the mechanism of deposit formation is known for a fuel, it can be incorporated into the FEM model.

Chapter 3

Film Dynamics and Film Stability

3.1 Modeling Approach

The governing equations and boundary conditions of any multiphase flow problem (including film dynamics) can be solved directly using various interface tracking or interface capturing approaches [233]. However, the computational costs for the investigation of film dynamics and stability are high. The reason for this lies in the fine computational grid necessary to track or capture the interface position. Additionally, a number of coupled governing equations have to be solved to cover the relevant transport processes.

This is why approximate approaches for the simulation of thin liquid films have been developed. One of the most widely used approaches for theoretical and numerical description of dynamics and stability of thin liquid films is the long-wave theory (LWT) (see section 2.1). The advantage of this approximate method is that only a single equation needs to be solved to investigate the film dynamics and stability, which greatly reduces the computational cost. Another benefit of this method is that different physical parameters of the problem appear as separate terms in the evolution equation, which makes it easy to study their influence on the overall problem.

3.1.1 Governing Equations

In this chapter, thin liquid films experiencing physical phenomena and interactions, which are expected to influence the film evolution and stability, are investigated. The governing equations are formulated for the incompressible liquid phase. Phenomena occurring at the liquid-gas interface (e.g. evaporation or Marangoni stresses) are represented as boundary conditions. Consequently, the continuity equation and Navier-Stokes equations are given by

$$\nabla \cdot \mathbf{u} = 0\,, \tag{3.1}$$

$$\rho\left[\frac{\partial \mathbf{u}}{\partial t}+(\mathbf{u}\cdot\nabla)\,\mathbf{u}\right]=\rho\,\mathbf{g}+\nabla\cdot\mathbf{T}, \tag{3.2}$$

where $\mathbf{u}$ is the velocity vector with the components u, v, and w in x-, y-, and z-direction, t the time, $\mathbf{g}=\{0,0,g\}$ is the gravitational acceleration, and $\mathbf{T}$ is the stress tensor. Under the assumption that liquid and gas are incompressible Newtonian liquids and using Stokes' hypothesis, the stress tensor can be written as

$$\mathbf{T}=-p\,\mathbf{I}+\mu\left[\nabla\mathbf{u}+(\nabla\mathbf{u})^{\mathrm{T}}\right], \tag{3.3}$$

with the identity tensor $\mathbf{I}$. The energy conservation equation is written in temperature form using Fourier's law and given by

$$\frac{\partial\left(\rho\,c_p\,T\right)}{\partial t}+\nabla\cdot\left(\mathbf{u}\,\rho\,c_p\,T\right)=\nabla\cdot(k\,\nabla T)+\Sigma_{\mathrm{e}}\,, \tag{3.4}$$

where Σ_{e} represents source terms to account for the latent heat of chemical reactions in the film. In the solid phase, no convection or source terms are present so that the energy equation reduces to the heat conduction equation

$$\frac{\partial\left(\rho\,c_p\,T\right)}{\partial t}=\nabla\cdot(k\,\nabla T)\,. \tag{3.5}$$

Lastly, the species transport equation for the mass fraction of component A of a binary mixture is given by

$$\frac{\partial\,\xi_{\mathrm{A}}}{\partial t}+\nabla\cdot(\mathbf{u}\,\xi_{\mathrm{A}})=\nabla\cdot(D_{\mathrm{bin}}\,\nabla\xi_{\mathrm{A}})+\Sigma_{\mathrm{react}}\,, \tag{3.6}$$

where ξ is the mass fraction and Σ_{react} represents reactive source terms.

Throughout this chapter, it is assumed that the film is so thick at any position that van der Waals forces can be neglected but so thin that buoyancy does not play a role ($Bo\ll 1$). It is assumed that temperature differences within the liquid film are so small that all material parameters, except for the surface tension, are calculated for an average temperature. The surface tension of typical pure fluids decreases with increasing temperature and vanishes at the critical point. It is assumed that the surface tension σ is solely a linear function of temperature ($\partial\sigma/\partial T=\mathrm{d}\sigma/\mathrm{d}T=\text{const.}=\sigma_T<0$). This leads to

$$\sigma=\sigma_0+\sigma_T\,(T-T_0)\,, \tag{3.7}$$

with the surface tension σ_0 at reference temperature T_0 [71]. The Marangoni effect is then modeled under the assumption that temperature gradients at the interface will lead to tangential stresses. The remaining material properties are evaluated for an average temperature and are not a function of position or time.

3.1.2 Solver Development

The evolution equations derived using the LWT are fourth order partial differential equations in time and space (see for example Eq. (2.2)). Three evolution equations capturing different key influencing phenomena are derived in the following sections of this chapter. The setup of the solver for all three cases is similar, which is why this description of the solver development is valid for all cases. The evolution equations are solved numerically based on the finite difference method (FDM). The solver was developed in this work in the program *MATLAB* for both two-dimensional and three-dimensional problems.

Second order central differences are utilized for spatial discretization. The temporal discretization is done using a second order accurate Crank-Nicolson method for two-dimensional problems and first order accurate explicit Euler method for three-dimensional problems [189]. This is due to the fact that the matrices in the equation system are much larger for three-dimensional problems and exceed the available working memory if a Crank-Nicolson method is used. The time-step size has been evaluated separately for each problem discussed in the following section to ensure independence of the results from the time integration. Furthermore, a mesh refinement study has been conducted. It has been found that 300 grid points are sufficient to ensure the calculation of the correct film shape even for highly disturbed films for two-dimensional problems. The associated figures can be found in appendix A.2. The calculation is terminated if the film height at any point is lower than 1 % of the initial height, since the developed models do not account for contact line dynamics. It is assumed that film rupture occurs at the point where the film height falls below this threshold.

3.2 Evaporation and Wall Structure

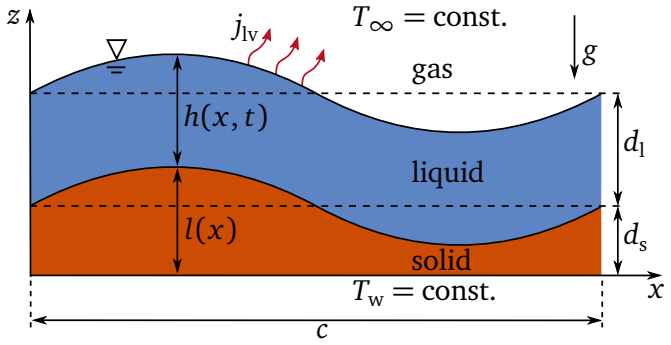

Figure 3.1: Domain for the simulation of an evaporating thin film on a structured wall.

A thin liquid film evaporating on a heated or cooled structured wall is investigated in this section. The wall structure can be thought of as an existing deposit structure on the substrate. Evaporation leads to a thinning of the liquid film and eventually to film rupture. However, uneven heating of the liquid through the structured wall leads to temperature gradients at the liquid-gas interface, which give rise to the thermal Marangoni effect. This also has an influence on the time at which film rupture occurs. The importance and interactions of the two mentioned factors is not yet understood and is considered here. Some of the derivations, discussions, and results given in this section have been published by Bender *et al.* in [29, 31].

3.2.1 Derivation of the Evolution Equation for Evaporating Films on Structured Walls

The sketch of the problem is shown in Fig. 3.1. The setup is two-dimensional, periodic, and consists of a thin liquid film of thickness $h(x,t)$ and length c, which rests on a rigid, impermeable, and structured wall of variable thickness $l(x)$. The film length c is also the length scale of the film thickness variation in this case. The initial average film thickness is denoted as d_l and the average wall thickness is d_s. The gas phase far away from the interface is kept at a constant ambient temperature T_∞ and the lower side of the wall is at a constant wall temperature T_w. The liquid evaporates into the gas phase, which can consist of the pure vapor of the liquid or of a mixture of vapor and ambient non-condensable gas. This leads to a decrease of the film thickness over time.

The continuity, Navier-Stokes, and energy equation (Eqs. (3.1) - (3.4)) in the liquid film and the energy equation in the solid (Eq. (3.5)) are rewritten for a two-dimensional domain. For the solid ($z < l$, index s) this leads to

$$T_{\mathrm{s},t} = a_\mathrm{s}\left(T_{\mathrm{s},xx} + T_{\mathrm{s},zz}\right). \tag{3.8}$$

In the liquid film ($l \le z \le l+h$, index l) one finds

$$u_x + w_z = 0\,, \tag{3.9}$$

$$u_t + u\,u_x + w\,u_z = -\frac{1}{\rho_\mathrm{l}} p_x + \nu_\mathrm{l}\left(u_{xx} + u_{zz}\right), \tag{3.10}$$

$$w_t + u\,w_x + w\,w_z = -\frac{1}{\rho_\mathrm{l}} p_z + \nu_\mathrm{l}\left(w_{xx} + w_{zz}\right) - g\,, \tag{3.11}$$

$$T_{\mathrm{l},t} + u\,T_{\mathrm{l},x} + w\,T_{\mathrm{l},z} = a_\mathrm{l}\left(T_{\mathrm{l},xx} + T_{\mathrm{l},zz}\right). \tag{3.12}$$

The lower side of the wall ($z = 0$) has a constant temperature

$$T_\mathrm{s} = T_\mathrm{w}\,. \tag{3.13}$$

The boundary conditions on the solid-liquid interface $z = l$ are the no-slip and no-penetration conditions for the flow field. Furthermore, the temperature equality and a continuous heat flux has to be fulfilled

$$u = 0\,, \qquad w = 0\,, \qquad T_\mathrm{s} = T_\mathrm{l}\,, \qquad k_\mathrm{s}\left(T_{\mathrm{s},z} - l_x\,T_{\mathrm{s},x}\right) = k_\mathrm{l}\left(T_{\mathrm{l},z} - l_x\,T_{\mathrm{l},x}\right). \tag{3.14}$$

At the liquid-gas interface ($z = l + h$), the mass balance can be written with the following equation

$$j_{\mathrm{lv}} = \rho_{\mathrm{l}} \left(\mathbf{u}_{\mathrm{l}} - \mathbf{u}_{\mathrm{lg}} \right) \cdot \mathbf{n} = \rho_{\mathrm{v}} \left(\mathbf{u}_{\mathrm{g}} - \mathbf{u}_{\mathrm{lg}} \right) \cdot \mathbf{n}, \tag{3.15}$$

where j_{lv} is the evaporative mass flux normal to the interface (with $j_{\mathrm{lv}} < 0$ for condensation and $j_{\mathrm{lv}} > 0$ for evaporation), $\mathbf{u}_{\mathrm{lg}}$ is the velocity vector of the liquid-gas interface, and $\mathbf{n}$ is the unit normal vector on the interface.

The momentum balance at the interface is formulated as a normal and tangential stress balance

$$j_{\mathrm{lv}} \left(\mathbf{u}_{\mathrm{l}} \cdot \mathbf{n} - \mathbf{u}_{\mathrm{g}} \cdot \mathbf{n} \right) = \mathbf{T}_{\mathrm{l}} \cdot \mathbf{n} \cdot \mathbf{n} + \sigma \nabla \cdot \mathbf{n}, \tag{3.16}$$

$$j_{\mathrm{lv}} \left(\mathbf{u}_{\mathrm{l}} \cdot \mathbf{t} - \mathbf{u}_{\mathrm{g}} \cdot \mathbf{t} \right) = \mathbf{T}_{\mathrm{l}} \cdot \mathbf{n} \cdot \mathbf{t} - \nabla \sigma \cdot \mathbf{t}, \tag{3.17}$$

where the viscous stress tensor of the gas has been neglected compared to the liquid. This assumption is valid as long as the system is far from the critical point so that $\rho_{\mathrm{v}} \ll \rho_{\mathrm{l}}$ and $\mu_{\mathrm{v}} \ll \mu_{\mathrm{l}}$.

The normal $\mathbf{n}$ and tangential $\mathbf{t}$ vectors at the liquid-gas interface can be expressed as

$$\mathbf{n} = \frac{-(h_x + l_x)\, \mathbf{e}_x + \mathbf{e}_z}{\left[1 + (h_x + l_x)^2\right]^{\frac{1}{2}}}, \qquad \mathbf{t} = \frac{\mathbf{e}_x + (h_x + l_x)\, \mathbf{e}_z}{\left[1 + (h_x + l_x)^2\right]^{\frac{1}{2}}}, \tag{3.18}$$

using the unit vectors in x-direction $\mathbf{e}_x$ and z-direction $\mathbf{e}_z$. Equation (3.15) is used to approximate the first term in Eq. (3.16)

$$j_{\mathrm{lv}} \left(\mathbf{u}_{\mathrm{l}} \cdot \mathbf{n} - \mathbf{u}_{\mathrm{g}} \cdot \mathbf{n} \right) \approx -\frac{j_{\mathrm{lv}}^2}{\rho_{\mathrm{v}}}. \tag{3.19}$$

Using the continuity equation (3.9), the momentum balance at the interface $z = h + l$ follows to

$$\frac{j_{\mathrm{lv}}^2}{\rho_{\mathrm{v}}} - p + 2\mu_{\mathrm{l}} \frac{u_x \left[(h_x + l_x)^2 - 1\right] - (h_x + l_x)(u_z + w_x)}{1 + (h_x + l_x)^2} = \sigma \frac{(h_{xx} + l_{xx})}{\left[1 + (h_x + l_x)^2\right]^{\frac{3}{2}}}, \tag{3.20}$$

$$\mu_{\mathrm{l}} \frac{\left[1 - (h_x + l_x)^2\right](u_z + w_x) - 4\,(h_x + l_x)\, u_x}{\left[1 + (h_x + l_x)^2\right]^{\frac{1}{2}}} = \frac{\partial \sigma}{\partial T} \left[T_x + (h_x + l_x)\, T_z \right]. \tag{3.21}$$

The boundary condition for the energy equation at the liquid vapor interface ($z = l + h$) depends on if the evaporation is happening into a pure vapor atmosphere or into an ambient non-condensable gas and is assessed below.

Lastly, the kinematic boundary condition at the interface has to be fulfilled, which states:

$$\frac{j_{\mathrm{lv}}}{\rho_{\mathrm{l}}} + \frac{h_t + u\,(h_x + l_x) - w}{\left[1 + (h_x + l_x)^2\right]^{\frac{1}{2}}} = 0\,. \tag{3.22}$$

Evaporation into Pure Vapor

In the case of evaporation into a pure vapor atmosphere, the interfacial mass flux through the interface ($z = l + h$) is calculated using the interface temperature

$$j_{\mathrm{lv}} = \frac{T_{\mathrm{l}} - T_\infty}{\gamma}\,, \tag{3.23}$$

where γ is the resistance to evaporation at the interface, which can be defined using molecular kinetic theory [195]

$$j_{\mathrm{lv}} = \frac{T_{\mathrm{l}} - T_\infty}{\gamma} = \frac{2f}{2-f} \frac{h_{\mathrm{lv}}\,\rho_{\mathrm{v}}\,M^{0.5}}{T_\infty\,(2\,\pi\,\mathscr{R}\,T_\infty)^{0.5}}\,(T_{\mathrm{l}} - T_\infty)\,, \tag{3.24}$$

where f is the condensation coefficient and h_{lv} the enthalpy of evaporation. Using the heat transfer coefficient α, the resistance to evaporation follows to $\gamma = h_{\mathrm{lv}}/\alpha$. Typically, the molecular kinetic resistance to evaporation at the interface is low, which will lead to high Biot numbers [82]. The Biot number Bi is defined as the ratio of the conductive thermal resistance inside the fluid and the thermal resistance across the interface. Consequently, a high Biot number means that the thermal resistance inside the film plays a more important role than the thermal resistance at the interface. The boundary equation for the energy equation is then written as

$$j_{\mathrm{lv}}\,h_{\mathrm{lv}} + k_{\mathrm{l}} \frac{T_{\mathrm{l},x}\,(h_x + l_x) + T_{\mathrm{l},z}}{\left[1 + (h_x + l_x)^2\right]^{\frac{1}{2}}} = 0\,. \tag{3.25}$$

The governing equations and boundary conditions can be non-dimensionalized using the viscous velocity scales based on the velocity of the liquid $\nu_{\mathrm{l}}/d_{\mathrm{l}}$ in x-direction and $\nu_{\mathrm{l}}\epsilon/d_{\mathrm{l}}$ in z-direction, the viscous time scale $d_{\mathrm{l}}^2/(\nu_{\mathrm{l}}\,\epsilon)$ and the characteristic temperature difference $\Delta T = T_{\mathrm{w}} - T_\infty$. The dimensionless variables are then defined as

$$\epsilon = \frac{d_{\mathrm{l}}}{c}\,, \qquad H = \frac{h}{d_{\mathrm{l}}}\,, \qquad L = \frac{l}{d_{\mathrm{l}}}\,, \qquad X = \frac{x\,\epsilon}{d_{\mathrm{l}}}\,, \qquad Z = \frac{z}{d_{\mathrm{l}}}\,, \qquad U = \frac{u\,d_{\mathrm{l}}}{\nu_{\mathrm{l}}}\,, \qquad W = \frac{w\,d_{\mathrm{l}}}{\epsilon\,\nu_{\mathrm{l}}}\,,$$

$$\tau = \frac{t\,\nu_{\mathrm{l}}\,\epsilon}{d_{\mathrm{l}}^2}\,, \qquad \Theta = \frac{T - T_\infty}{T_{\mathrm{w}} - T_\infty}\,, \qquad P = \frac{\epsilon\,p\,d_{\mathrm{l}}^2}{\mu_{\mathrm{l}}\,\nu_{\mathrm{l}}}\,, \qquad J = \frac{j_{\mathrm{lv}}\,h_{\mathrm{lv}}\,d_{\mathrm{l}}}{k_{\mathrm{l}}\,(T_{\mathrm{w}} - T_\infty)}\,,$$

where U and W are the non-dimensional velocity components in the non-dimensional coordinates X and Z. Additionally, L, Θ, P, and J are the non-dimensional substrate height, temperature, pressure, and interfacial mass flux, respectively.

The non-dimensional parameters of the problem can be defined as

$$S = \frac{\sigma\, d_\mathrm{l}}{3\,\mu_\mathrm{l}\,\nu_\mathrm{l}}\,, \qquad G = \frac{d_\mathrm{l}^3\, g}{\nu_\mathrm{l}^2}\,, \qquad Ma = -\frac{\sigma_T\,(T_\mathrm{w} - T_\infty)\, d_\mathrm{l}}{2\,\mu_\mathrm{l}\, a_\mathrm{l}}\,,$$

$$Pr = \frac{\nu_\mathrm{l}}{a_\mathrm{l}}\,, \qquad Pr_\mathrm{s} = \frac{\nu_\mathrm{l}}{a_\mathrm{s}}\,, \qquad E = \frac{k_\mathrm{l}\,(T_\mathrm{w} - T_\infty)}{\mu_\mathrm{l}\, h_\mathrm{lv}}\,, \qquad D = \frac{3}{2}\frac{\rho_\mathrm{v}}{\rho_\mathrm{l}}\,, \qquad \Gamma = \frac{\gamma\, k_\mathrm{l}}{h_\mathrm{lv}\, d_\mathrm{l}}\,.$$

The non-dimensional surface tension S and gravity G is worked out by dividing the stresses arising from surface tension by viscous stresses and gravitational forces by viscous forces, respectively. The Marangoni number Ma is defined using the characteristic difference between the wall temperature and the temperature in the gas phase far away from the interface $(T_\mathrm{w} - T_\infty)$. The Prandtl number Pr is obtained by comparing viscous momentum transfer to conductive heat transfer. It should be noted that Pr_s is defined by comparing viscous momentum transfer of the liquid to conductive heat transfer in the solid. Typically it is found that this number is much smaller than the Prandtl number of the liquid ($Pr_\mathrm{s} \ll Pr$). Comparing the heat transport by conduction to evaporative heat transport gives the non-dimensional evaporation rate E. Finally, D is defined by the density ratio between liquid and vapor and the non-dimensional resistance to evaporation is denoted as Γ. It can be easily shown that $\Gamma = k_\mathrm{l}/(\alpha\, d_\mathrm{l}) = Bi^{-1}$ for evaporation into the pure vapor atmosphere.

After plugging these non-dimensionalizations into the governing equations and boundary conditions, a perturbation analysis can be performed to obtain an evolution equation for the film thickness. It is assumed that the film is thin, meaning that the characteristic film thickness d_l is much smaller than the length scale of the film thickness variation (see [57, 163]). The length scale of the film thickness variation, in this case, is in the order of the film length c, which is also the length scale of the variation of the wall topology.

This leads to the condition

$$\epsilon = d_\mathrm{l}/c \ll 1\,. \tag{3.26}$$

All dependent variables are then extended depending on the order of ϵ as shown exemplarily for the dimensionless velocity component U

$$U = U_0 + \epsilon\, U_1 + \epsilon^2\, U_2 + \mathcal{O}\left(\epsilon^3\right). \tag{3.27}$$

It is assumed that surface tension effects are strong $\mathcal{O}\left(\epsilon^{-3}\right)$ so that the surface tension term appears in the equation in the zeroth order $\mathcal{O}(0)$. Typically, the ratio of the liquid and vapor densities is large $\rho_\mathrm{v} \ll \rho_\mathrm{l}$ so that D is $\mathcal{O}\left(\epsilon^3\right)$. It is further assumed that the non-dimensional evaporation rate E is small – $\mathcal{O}(\epsilon)$ – leading to its appearance in the zeroth order. These considerations lead to the following reformulations:

$$\widetilde{S} = S\,\epsilon^3\,, \qquad \widetilde{G} = G\,\epsilon\,, \qquad \widetilde{Ma} = Ma\,\epsilon\,, \qquad \widetilde{E} = E/\epsilon\,, \qquad \widetilde{D} = D/\epsilon^3\,.$$

The problem is solved for the zeroth order of ϵ and the kinematic boundary condition at the interface (Eq. (3.22)) is used to obtain the following zeroth order evolution equation for the dimensionless film thickness H

$$H_\tau + \frac{\widetilde{E}}{\Gamma + \mathscr{H}} + \left\{ \left[\frac{\widetilde{E}^2 \mathscr{H}_X}{\widetilde{D}\left(\Gamma + \mathscr{H}\right)^3} + \widetilde{S}\left(H_{XXX} + L_{XXX}\right) - \frac{\widetilde{G}}{3}\left(H_X + L_X\right) \right] H^3 \right\}_X + \frac{\widetilde{Ma}}{Pr} \left[\frac{\Gamma \mathscr{H}_X}{\left(\Gamma + \mathscr{H}\right)^2} H^2 \right]_X = 0 , \tag{3.28}$$

with the substitution

$$\mathscr{H} = H + \frac{k_\mathrm{l}}{k_\mathrm{s}} L .$$

The terms of the evolution equation can be identified as the effects of different physical phenomena. The second term of Eq. (3.28) captures the effect of mass loss in the liquid due to evaporation. The third term represents the influence of the vapor thrust exerted by the density change associated with the phase change from liquid to vapor. The fourth term is the influence of surface tension and the fifth term represents the effect of gravity on the film surface. The last term on the left hand side of Eq. (3.28) represents the Marangoni stresses due to non-homogeneous interface temperature. For negligible evaporation, this evolution equation collapses to the equation given by Kabova *et al.* [118] for non-evaporating films on structured walls.

Evaporation into Ambient Gas and Heat Transport in Gas

If evaporation is governed by diffusive and convective transport of vapor in the gas phase, the interfacial mass flux can be calculated using the mass transfer coefficient β

$$j_\mathrm{lv} = \rho_\mathrm{v} \beta \left(\xi_\mathrm{sat,int} - \xi_\infty \right) , \tag{3.29}$$

where $\xi_\mathrm{sat,int}$ is the saturation concentration of vapor at the interface and ξ_∞ is the vapor mass fraction in the gas phase far from the interface. The saturation concentration at the interface can be approximated using the saturation concentration corresponding to the temperature T_∞ in the far field $\xi_\mathrm{sat,\infty}$

$$\xi_\mathrm{sat,int} = \xi_\mathrm{sat,\infty} + \frac{\mathrm{d}\xi_\mathrm{sat}}{\mathrm{d}T} \left(T_\mathrm{l} - T_\infty \right) . \tag{3.30}$$

The boundary condition for the energy equation at the liquid-gas interface ($z = h + l$) includes evaporative cooling, convective transport in the gas phase, and conductive transport in the liquid and can be written as

$$j_{\mathrm{lv}} h_{\mathrm{lv}} + \alpha (T_{\mathrm{l}} - T_{\infty}) + k_{\mathrm{l}} \frac{T_{\mathrm{l},x} (h_x + l_x) + T_{\mathrm{l},z}}{\left[1 + (h_x + l_x)^2\right]^{\frac{1}{2}}} = 0 . \tag{3.31}$$

Plugging Eq. (3.29) and Eq. (3.30) in Eq. (3.31) leads to

$$(T_{\mathrm{l}} - T_{\infty}) = \frac{-k_{\mathrm{l}} \frac{T_{\mathrm{l},x} (h_x + l_x) + T_{\mathrm{l},z}}{\left[1 + (h_x + l_x)^2\right]^{\frac{1}{2}}} - h_{\mathrm{lv}} \rho_{\mathrm{v}} \beta \left(\xi_{\mathrm{sat},\infty} - \xi_{\infty}\right)}{h_{\mathrm{lv}} \rho_{\mathrm{v}} \beta \frac{\mathrm{d}\xi_{\mathrm{sat}}}{\mathrm{d}T} + \alpha} . \tag{3.32}$$

If one assumes that the concentration far away from the interface is equal to the saturation concentration of the far field temperature ($\xi_{\infty} = \xi_{\mathrm{sat},\infty}$), the interfacial mass flux follows as

$$j_{\mathrm{lv}} = \rho_{\mathrm{v}} \beta \frac{\mathrm{d}\xi_{\mathrm{sat}}}{\mathrm{d}T} (T_{\mathrm{l}} - T_{\infty}) = -\rho_{\mathrm{v}} \beta \frac{\mathrm{d}\xi_{\mathrm{sat}}}{\mathrm{d}T} \frac{k_{\mathrm{l}} \left[T_{\mathrm{l},x} (h_x + l_x) + T_{\mathrm{l},z}\right]}{\left(h_{\mathrm{lv}} \rho_{\mathrm{v}} \beta \frac{\mathrm{d}\xi_{\mathrm{sat}}}{\mathrm{d}T} + \alpha\right) \left[1 + (h_x + l_x)^2\right]^{\frac{1}{2}}} , \tag{3.33}$$

and the boundary condition for the energy equation at $z = h + l$ becomes

$$j_{\mathrm{lv}} \left(h_{\mathrm{lv}} + \frac{\alpha}{\rho_{\mathrm{v}} \beta \frac{\mathrm{d}\xi_{\mathrm{sat}}}{\mathrm{d}T}} \right) + k_{\mathrm{l}} \frac{T_{\mathrm{l},x} (h_x + l_x) + T_{\mathrm{l},z}}{\left[1 + (h_x + l_x)^2\right]^{\frac{1}{2}}} = 0 . \tag{3.34}$$

Using the same viscous time and velocity scales as in the case of evaporation into pure vapor and applying the same analysis, one arrives at the same evolution equation (3.28). The non-dimensional parameters also stay the same except for J, E, and Γ, which change to

$$J = \frac{j_{\mathrm{lv}} \left(h_{\mathrm{lv}} + \frac{\alpha}{\rho_{\mathrm{v}} \beta \frac{\mathrm{d}\xi_{\mathrm{sat}}}{\mathrm{d}T}} \right) d_{\mathrm{l}}}{k_{\mathrm{l}} (T_{\mathrm{w}} - T_{\infty})} , \qquad E = \frac{k_{\mathrm{l}} (T_{\mathrm{w}} - T_{\infty})}{\mu_{\mathrm{l}} \left(h_{\mathrm{lv}} + \frac{\alpha}{\rho_{\mathrm{v}} \beta \frac{\mathrm{d}\xi_{\mathrm{sat}}}{\mathrm{d}T}} \right)} , \qquad \Gamma = \frac{k_{\mathrm{l}}}{d_{\mathrm{l}} \left(\rho_{\mathrm{v}} \beta \frac{\mathrm{d}\xi_{\mathrm{sat}}}{\mathrm{d}T} h_{\mathrm{lv}} + \alpha \right)} .$$

3.2.2 Results for Evaporating Films on Structured Walls

The simulations are conducted for a hexane film as an exemplary fluid for inner-engine conditions (material properties can be found in appendix A.1.1) with an initial average film thickness $d_l = 50\,\mu m$ and a film length of $c = 1\,cm$ covering an aluminum wall and evaporating into an atmosphere of air and hexane vapor. The characteristic temperature difference is $(T_w - T_\infty) = 5\,K$ and the heat and mass transfer coefficients have been calculated as $\alpha = 64.23\,W\,m^{-2}\,K^{-1}$ and $\beta = 0.014\,m\,s^{-1}$ employing a Nusselt and Sherwood correlation for forced convection with a gas Reynolds number of $Re = 1000$ [226].

The values of the non-dimensional parameters in the evolution equation (3.28) are as follows:

$$\epsilon = 5 \cdot 10^{-3}, \qquad \widetilde{S} = 3.165 \cdot 10^{-4}, \qquad \widetilde{G} = 3.679 \cdot 10^{-2}, \qquad \widetilde{Ma} = 3.327, \qquad Pr = 5.378,$$

$$\widetilde{E}_0 = 0.956, \qquad \widetilde{D} = 6.171 \cdot 10^4, \qquad \Gamma = 7.788, \qquad k_l/k_s = 4.843 \cdot 10^{-4}.$$

These parameters are used for the following investigations unless explicitly stated otherwise. It can be deducted from these parameters that even for high values of the non-dimensional evaporation rate compared to the reference value ($\widetilde{E} = 10 \cdot \widetilde{E}_0$), the third term in the evolution equation, which is governed by $\widetilde{E}^2/\widetilde{D}$ and represents the influence of the vapor thrust, is small. It can be concluded that the vapor thrust does not influence the film evolution. However, as this term does not affect the simulation time, it is retained in the solved equation. Temporal evolution of the film height is shown for the non-dimensional time τ. For the chosen parameters, $1\,\tau$ corresponds to $1.225\,s$.

Throughout this chapter, the non-dimensional parameters are varied independently from each other to investigate the influence of the different physical phenomena. In reality it would be quite challenging to change the evaporation rate, for example, without influencing the temperature field in the film and affecting the Marangoni effect. LWT allows this kind of separation of physical properties to gain insight into the influences and interactions of different physical parameters. In this section, the evaporation rate is varied, while the other non-dimensional parameters are kept constant.

The structure of the wall $L(X)$ is described by a sinusoidal function

$$L(X) = A\left[\cos\left(\frac{2\,\pi\,X}{\Lambda_s}\right) + 1\right], \tag{3.35}$$

where A is the amplitude and Λ_s the wavelength of the wall structure. The amplitude of the wall structure has been chosen to $A = 0.1$ throughout this section, while the wavelength of the structure is varied. This structured wall may represent the shape of an already formed deposit layer on the substrate. The influence of the deposit topography on the film evolution and breakup can consequently be addressed with this setup. An initial disturbance of the film interface with a sinusoidal shape, an amplitude of 0.1, and a wavelength of $\Lambda_l = 1$ is prescribed and kept constant in this section.

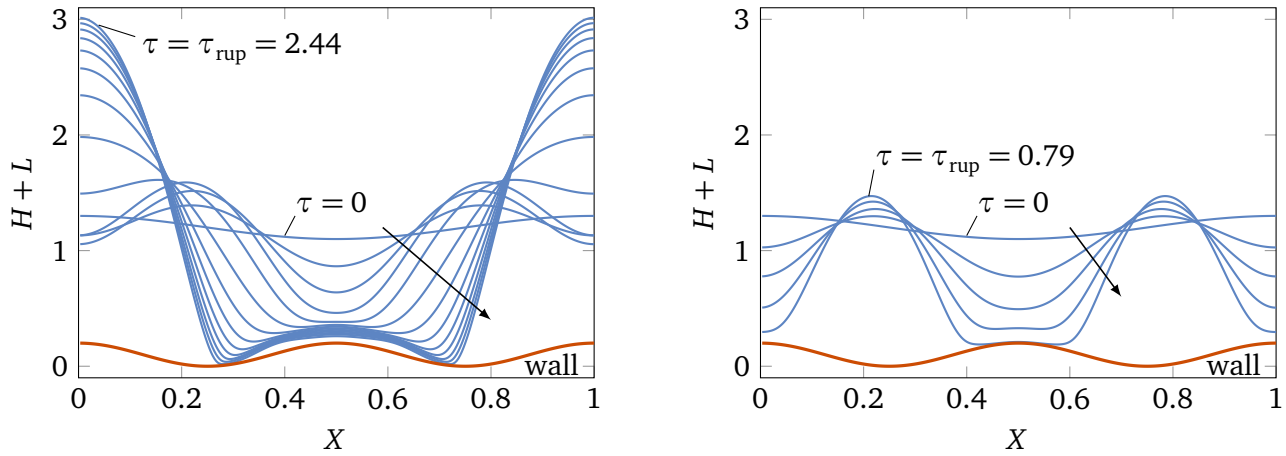

Figure 3.2: Time evolution of the film evaporating on a heated structured wall for two different evaporation rates of $\widetilde{E} = 0.5 \cdot \widetilde{E}_0$ (left) and $\widetilde{E} = 5.0 \cdot \widetilde{E}_0$ (right). The arrow points in the direction of increasing τ.

Film Heated by the Wall

The evolution of the film interface over time for two different evaporation rates and the same wall structure is shown in Fig. 3.2. The wall structure has a wavelength of $\Lambda_s = 0.5$. The time difference between the plotted interface shapes is identical in both plots. An increase of the initial disturbance with time can be seen for both evaporation rates. Initially, the sinusoidal shape of the liquid-gas interface is retained, while the amplitude of the film height disturbance increases. For larger times, the film deformation diverges from the sinusoidal shape and film rupture can be identified in both cases. The time to rupture τ_{rup} is approximately three times higher for the low evaporation rate compared to the high evaporation rate.

In the case of the low evaporation rate in the left of Fig. 3.2, the decrease in liquid volume due to evaporation is about 11.9 % of the initial liquid volume. From this it can be concluded that the Marangoni effect is the main driving force of the local thinning of the film and its rupture. For the high evaporation rate in Fig. 3.2 (right), the evaporative mass loss at the moment of rupture is 39.9 % of the initial film volume and the substantial decrease of the film volume can be seen in the figure. With increasing evaporation rate, the evaporative mass loss becomes more important for the determination of the rupture time. However, in both cases presented in Fig. 3.2, the Marangoni effect is concluded to be the main driving force of film rupture.

Moreover, it is illustrated in Fig. 3.2 that the point on the wall at which the rupture occurs is different in both cases. For the low evaporation rate, the point of rupture is close to the trough of the wall structure and two points at which the film ruptures simultaneously can be observed. In contrast, for the higher evaporation rate only one rupture point can be found, which is located at the crest of the wall structure. Generally, in the case of high evaporation rates, a rupture point at each crest of the topology is observed, whereas this is not true for lower evaporation rates due to the influence of the Marangoni effect.

The evolution of the non-dimensional temperature field Θ inside the film and the wall is shown in Fig. 3.3. No temperature gradient can be identified inside the wall since the thermal conductivity of the wall is

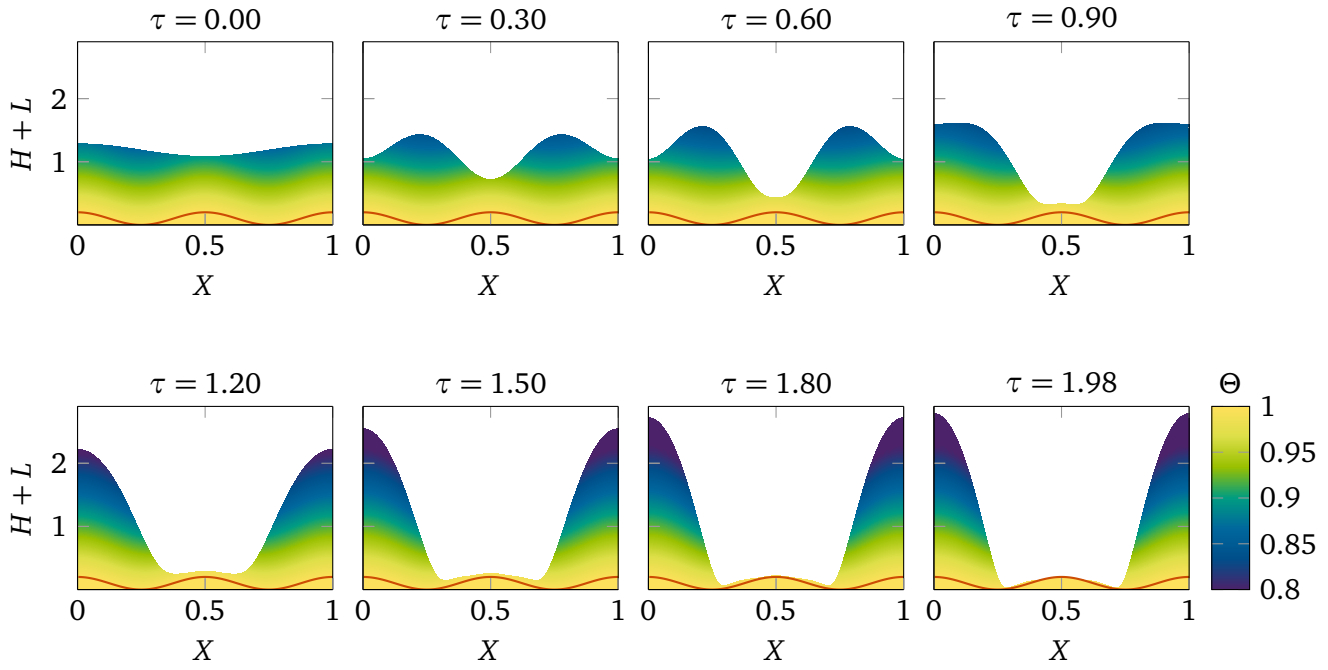

Figure 3.3: Time evolution of the non-dimensional temperature field inside the evaporating film on a structured wall.

more than 2000 times larger than the thermal conductivity in the film. The liquid film has its maximum temperature close to the wall structure, since it is heated from the structured wall and a decrease of the temperature with height can be observed. This is due to the cooling of the liquid-gas interface caused by evaporation into the ambient gas. The temperature of the liquid-gas interface is not uniform. The film troughs are warmer than the film crests, which show the lowest temperatures in the entire system.

The temperature gradients at the liquid-gas interface give rise to the Marangoni convection, which leads to liquid flow from the film troughs to the film crests. Consequently, the film crests become higher and the film troughs lower with increasing time. This, in turn, increases the temperature gradient at the interface and amplifies the Marangoni effect, until film rupture occurs.

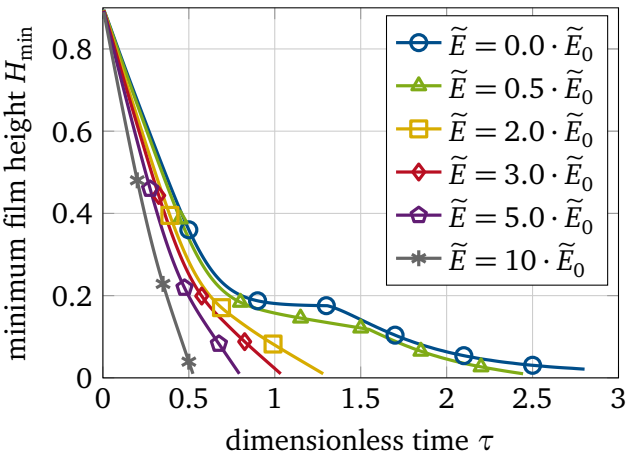

Figure 3.4: Time evolution of the minimum film height for different evaporation rates.

The minimum film height $H_{\min}$ over non-dimensional time for various evaporation rates is depicted in Fig. 3.4. For low evaporation rates, the film height decreases non-linearly with time. In the absence of phase change ($\widetilde{E} = 0.0 \cdot \widetilde{E}_0$), for example, the film height decreases fast initially until it reaches a plateau at $H_{\min} \approx 0.2$, where the minimum film height stays approximately the same between $\tau = 0.9$ and $\tau = 1.4$. Then, the minimum film height decreases again until film rupture is observed for $\tau \approx 2.8$. In the absence of evaporation, the film evolution is governed by the Marangoni effect. It has been shown that, even in the absence of evaporation, a film on a flat surface (without any wall topology) is unstable when subject to Marangoni stresses if the wavelength of the film disturbance is higher than the cut-off wavelength $\Lambda_{\mathrm{l,crit,0}}$ [163] defined as

$$\Lambda_{\mathrm{l,crit,0}} = 2\,\pi \left[\frac{\widetilde{Ma}}{Pr\,\widetilde{S}} \frac{\Gamma}{(\Gamma+1)^2} - \frac{\widetilde{G}}{3\,\widetilde{S}} \right]^{-\frac{1}{2}} . \tag{3.36}$$

For the parameters chosen in this section, one obtains $\Lambda_{\mathrm{l,crit,0}} = 0.50$. In the case of structured walls, the substrate topology leads to film destabilization so that the critical wavelength decreases $\Lambda_{\mathrm{l,crit}} < \Lambda_{\mathrm{l,crit,0}} = 0.50$ [83, 117]. As discussed previously, the initial disturbance of the film in this section was set to $\Lambda_{\mathrm{l}} = 1 > \Lambda_{\mathrm{l,crit}}$, which means that the film is unstable and the Marangoni effect causes film rupture even in the absence of evaporation. Since the total volume of the liquid over time is constant in this case, the decrease of the minimum film height corresponds to an increase of the film height deformation amplitude. The wall structure and the resulting Marangoni effect, consequently, have a non-linear effect on the film height evolution. This effect becomes less pronounced with increasing evaporation rate.

For large evaporation rates ($\widetilde{E} = 10 \cdot \widetilde{E}_0$), an almost linear decrease of the film thickness with time can bee seen in Fig. 3.4. The film evolution at each position of the domain is then strongly influenced by the evaporative mass loss, which is given by the second term of the evolution equation (3.28). For very high evaporation rates, the film evolution does not depend on gravity, surface tension, the wall topology or the Marangoni effect but is influenced solely by evaporation. The rupture times τ_{rup} obtained for different evaporation rates is investigated more closely in the following paragraph.

The time to rupture τ_{rup} is an important parameter since it has been shown that deposit formation occurs in the vicinity of the three-phase contact line. The dependence of the rupture time on the evaporation rate can be seen for wall topologies of different wavelength Λ_{s} in Fig. 3.5. For all investigated wall structures, the rupture time sharply decreases with increasing evaporation rate. For high evaporation rates, when the evaporative film thinning governs the film height evolution, the influence of the wall structure is less important and the rupture times are similar for all wall structures. The effect of the wall structure on the time to rupture is not monotonous. For low evaporation rates, the film on a wall with a wavelength of $\Lambda_{\mathrm{s}} = 0.25$ shows higher rupture times than the film on the other wall structures. However, for higher evaporation rates, the rupture times are shortest for $\Lambda_{\mathrm{s}} = 0.5$, longest for $\Lambda_{\mathrm{s}} = 0.125$, and $\Lambda_{\mathrm{s}} = 0.25$ lies in between. It can be concluded that there exists a critical wavelength, leading to the fastest rupture times. This critical wavelength depends on the evaporation rate. For $\widetilde{E}/\widetilde{E}_0 > 1.5$ this critical wavelength lies between $\Lambda_{\mathrm{s}} = 0.5$ and $\Lambda_{\mathrm{s}} = 0.25$. This behavior can be explained with the interaction of the imposed

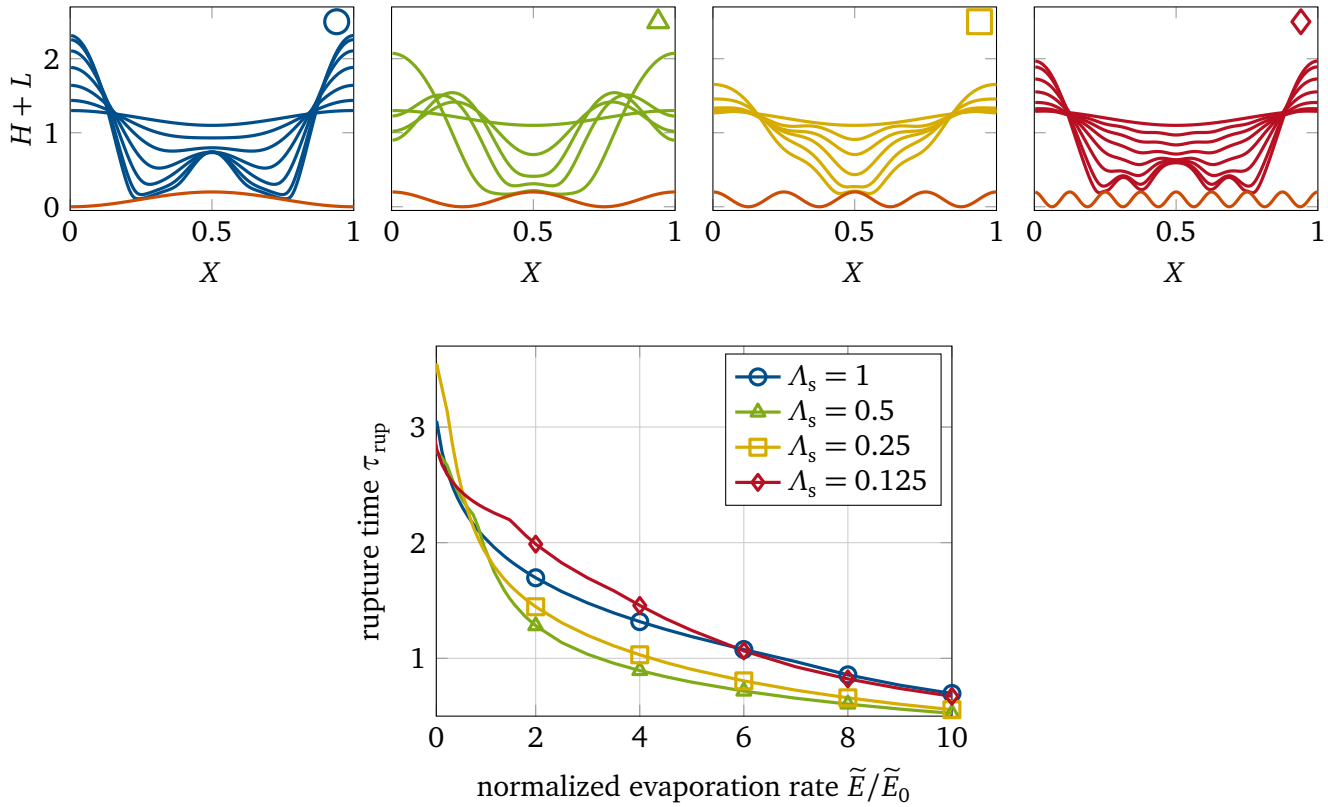

Figure 3.5: Rupture time over evaporation rate for different wall structures. The exemplary plots for the different wall structures are for $\widetilde{E} = 2.0 \cdot \widetilde{E}_0$.

disturbance of the film with the wavelength $\Lambda_l = 1$ and the evolution of the disturbance prompted by the wavelength of the wall structure Λ_s. Interactions give rise to a fast decrease of the minimum film height, when the amplitudes of the disturbances become similar to the film thickness. This makes it difficult to predict the rupture times without the full numerical simulation of the problem. The length scale of the film thickness variation follows from Fig. 3.5 to $\Lambda_s c$. It is worth pointing out that, even for $\Lambda_s = 0.125$, one finds $\epsilon/\Lambda_s = 0.04 \ll 1$ so that the approximations made in the derivation of the evolution equation stay valid.

Furthermore, it is presented in Fig. 3.5 that the point at which rupture occurs depends on the wall structure. For the lowest investigated wavelength of the wall structure, two rupture points between the crest and the trough are found. With increasing wavelength Λ_s the rupture points move towards the crest of the wall structure, until one rupture point is observed for $\Lambda_s = 0.25$. Finally, for $\Lambda_s = 0.125$, two rupture points are found for low evaporation rates, but four rupture points can be observed for $\widetilde{E}/\widetilde{E}_0 > 1.5$, leading to the sudden decrease of the rupture times in this area of Fig. 3.5.

Film Heated by the Ambient Gas

The liquid film can be heated either by the wall or by the ambient gas phase. If the film is heated by the ambient gas, the interface temperature increases with increasing thickness of the film if the wall temperature is kept constant. This leads to higher surface tension at the film crests compared to the film troughs and to a Marangoni flow from the film height maxima to the film height minima. Consequently,

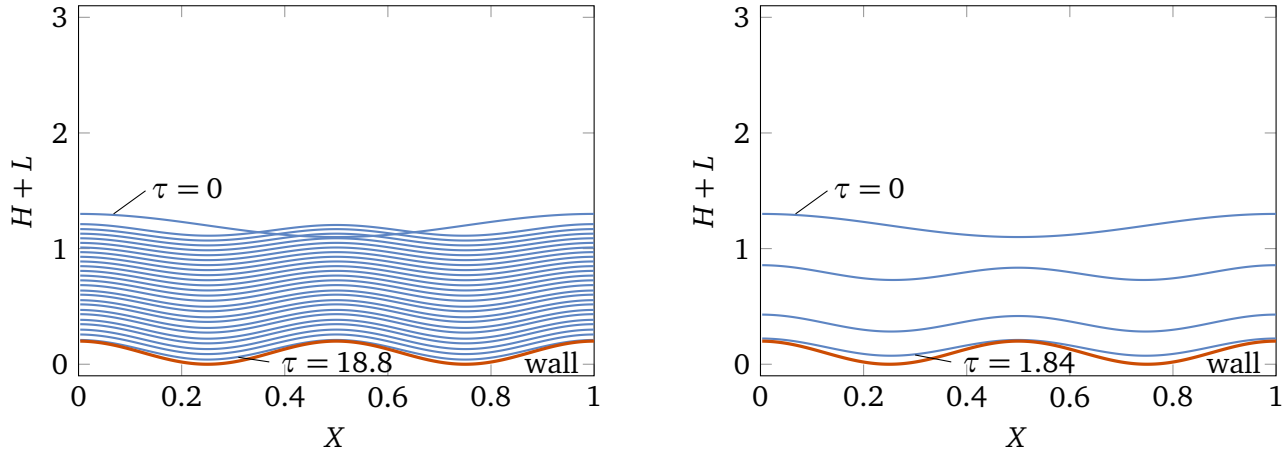

Figure 3.6: Time evolution of the film evaporating on a cooled structured wall for two different evaporation rates of $\widehat{E} = 0.5 \cdot \widehat{E}_0$ (left) and $\widehat{E} = 5.0 \cdot \widehat{E}_0$ (right).

the Marangoni effect acts to level out film height differences and the only remaining driving force of film rupture in Eq. (3.28) is the evaporative mass loss and the accompanying film thinning. As shown above, the evaporation rate depends on the temperature difference between the wall T_w and the ambient temperature in the gas phase T_∞. The definition of the non-dimensional evaporation rate given there was valid for a film heated by the wall. With the chosen definition of the evaporation rate, a wall temperature lower than the ambient gas temperature leads to condensation of liquid at the interface.

However, the developed model is also applicable to investigation of an evaporating film with the heat supplied by a hot ambient gas phase and where the wall is colder than the ambient gas. In this case, the definition of the non-dimensional evaporation rate $\widetilde{E}$ in the evolution equation (3.28) has to be changed to

$$\widehat{E} = \frac{k_l |T_w - T_\infty|}{\epsilon\, \mu_l\, \Delta h_{lv}} \quad \text{and} \quad \widehat{E} = \frac{k_l\, |T_w - T_\infty|}{\epsilon\, \mu_l \left(h_{lv} + \dfrac{\alpha}{\rho_v\, \beta\, \frac{d\xi_{sat}}{dT}} \right)},$$

for a film evaporating into pure vapor and into an ambient gas phase, respectively.

For the following investigation, a temperature difference of $T_w - T_\infty = -5\,K$ is assumed leading to identical non-dimensional parameters as in section 3.2.2, except that the sign of $\widetilde{Ma}$ is changed and $\widetilde{E}_0 = \widehat{E}_0$.

The evolution of the film height with time for two different evaporation rates is illustrated in Fig. 3.6. The parameter values in this figure are identical to the ones shown in Fig. 3.2 except that the direction of the Marangoni flow is reversed in the case of the heat supplied by the gas phase. It is easily seen that the initial film disturbance decays quickly due to the action of the Marangoni effect and a film with uniform film thickness is established. The interface shape follows the wall structure and remains almost unchanged throughout the evaporation process. Evaporation leads to a thinning of the film over time and film rupture in both cases. The rupture times observed increase almost linearly with decreasing

evaporation rate. The rupture times in Fig. 3.6 are much larger than in Fig. 3.2, where the Marangoni effect was the main driver of film rupture. The rupture point is identical for both evaporation rates if the film is heated by the gas phase and is located at the crests of the wall structure.

An approximate analytical solution of the problem of an evaporating thin film on a structured wall and heated by a hot ambient gas can be derived to further evaluate the film evolution. It is assumed that the thermal conductivity in the solid is much larger than the thermal conductivity in the liquid $k_\mathrm{l} \ll k_\mathrm{s}$. With the additional assumption that the amplitude of the film deformation at every location is much smaller than the film thickness, the evolution equation can be linearized. To do this, the film thickness and the wall structure are expressed as

$$H = H_0(\tau) + \zeta H_1(X,\tau), \qquad L = \zeta L_1(X) = \zeta \cos(K_\mathrm{s} X) = \zeta \cos\left(\frac{2\pi X}{\Lambda_\mathrm{s}}\right),$$

with the parameter $\zeta \ll 1$ and the non-dimensional wavenumber of the wall structure K_s. Plugging these expressions into the evolution equation (3.28) and arranging the terms depending on the order of ζ leads to

$$\begin{aligned} H_{0,\tau} + \frac{\widehat{E}}{\Gamma + H_0} + \zeta \Bigg[H_{1,\tau} - \frac{\widehat{E} H_1}{(\Gamma + H_0)^2} + \frac{\widehat{E}^2 H_0^3 H_{1,XX}}{\widetilde{D}(\Gamma + H_0)^3} + \widetilde{S} H_0^3 \left(H_{1,XXXX} + L_{1,XXXX}\right) \\ - \frac{\widetilde{G}}{3} H_0^3 \left(H_{1,XX} + L_{1,XX}\right) + \frac{\widetilde{Ma}\, \Gamma H_0^2 H_{1,XX}}{Pr(\Gamma + H_0)^2} \Bigg] + \mathcal{O}(\zeta^2) = 0 . \end{aligned} \tag{3.37}$$

The zeroth order equation in ζ follows as

$$H_{0,\tau} + \frac{\widehat{E}}{\Gamma + H_0} = 0 . \tag{3.38}$$

Equation (3.38) can be solved analytically and one finds

$$H_0(\tau) = -\Gamma + \sqrt{-2\widehat{E}\,\tau + [\Gamma + H_0(0)]^2} = -\Gamma + \sqrt{-2\widehat{E}\,\tau + (\Gamma + 1)^2}, \tag{3.39}$$

where $H_0(0) = 1$ is the initial average film thickness.

Equation (3.39) describes the decrease of the average film thickness with time. It can be concluded that the average film thickness in the linearized approximation depends only on the non-dimensional evaporation rate $\widehat{E}$, the non-dimensional resistance to evaporation Γ, and the time, which is consistent with the observations from Fig. 3.6.

Equation (3.37) can be solved in the first order in ζ assuming that H_1 varies slowly with time, which makes the first term in the square brackets of Eq. (3.37) negligible. The solution is sought based on a sinusoidal form of the film height and the wall structure in first order

$$H_1 = B\cos(K_\mathrm{s} X) \quad \text{and} \quad L_1 = \cos(K_\mathrm{s} X) .$$

From this, an expression for the dimensionless amplitude of the film thickness variation B is derived, which depends on the non-dimensional parameters of the problem $\widehat{E}$, $\widetilde{D}$, Γ, $\widetilde{S}$, $\widetilde{G}$, $\widetilde{Ma}$, and Pr, as well as the average film thickness H_0 and the dimensionless wavelength of the wall structure K_s

$$B = \frac{-\widetilde{S}K_s^2 - \widetilde{G}/3}{-\dfrac{\widehat{E}}{K_s^2 H_0^3 (\Gamma + H_0)^2} - \dfrac{\widehat{E}^2}{\widetilde{D}(\Gamma + H_0)^3} + \widetilde{S}K_s^2 + \dfrac{\widetilde{G}}{3} - \dfrac{\widetilde{Ma}\,\Gamma}{Pr H_0 (\Gamma + H_0)^2}}. \tag{3.40}$$

If evaporation is negligible ($\widehat{E} = 0$), Eq. (3.40) shows that the amplitude of the deformation of the liquid-gas interface is determined by the opposite effects of the Marangoni effect, on the one hand, and the surface tension and hydrostatic pressure, on the other hand. The amplitude can then be written as

$$B = \frac{1}{\Psi - 1}, \quad \text{with} \quad \Psi = \frac{\widetilde{Ma}\,\Gamma}{Pr H_0 (\Gamma + H_0)^2 \left(\widetilde{S}K_s^2 + \widetilde{G}/3\right)}. \tag{3.41}$$

If the substitution $\Psi \ll 1$, surface tension and hydrostatic pressure suppress the Marangoni effect and Eq. (3.41) simplifies to $B = -1$. In this case, the amplitude of the film thickness variation has the same value but opposite sign of the amplitude of the wall structure. The amplitudes level each other out and the liquid-gas interface remains flat. If, on the other hand, $\Psi \gg 1$, the Marangoni effect dominates and one finds $B < 0$ with $|B| \ll 1$. Then the amplitude of the film thickness variation is negligibly small and the shape of the liquid-gas interface follows the shape of the wall structure.

Therefore, the Marangoni effect makes the liquid-gas interface follow the structure of the wall, while surface tension and gravity act towards a flat interface. Consequently, for fluids with low surface tension or when gravitational forces are negligible, the interface is more likely to follow the wall structure. For typical fluid parameters and applications, the film shape will lie between the two scenarios, similar to the shape seen in Fig. 3.6

If evaporation is strong, however, the first term in the denominator of Eq. (3.40) has to be considered. In cases where, additionally, the vapor thrust cannot be neglected, the second term of the denominator is important. Both terms act to reduce the film thickness above the crests of the wall structure. If the interface shape would be dominated by the Marangoni effect in the absence of evaporation (in which case the interface follows the wall structure, as discussed above), the evaporation terms will act towards a flat interface. In contrast, if surface tension or gravity would determine the interface shape in the absence of evaporation (flat interface), the evaporation leads to a deformation of the flat interface and film thickness minima develop above the maxima of the wall structures and vice versa.

Typically, the first term in the denominator on the left hand side of Eq. (3.40), capturing the effect of evaporative film thinning, is much larger than the second term, which arises from the vapor thrust. This means that the amplitude of the film thickness variation depends on the wavelength of the wall structure K_s. For smaller wavelengths K_s the influence of evaporation on the amplitude B is more pronounced.

3.3 Chemical Reactions and Laminar Shear Flow

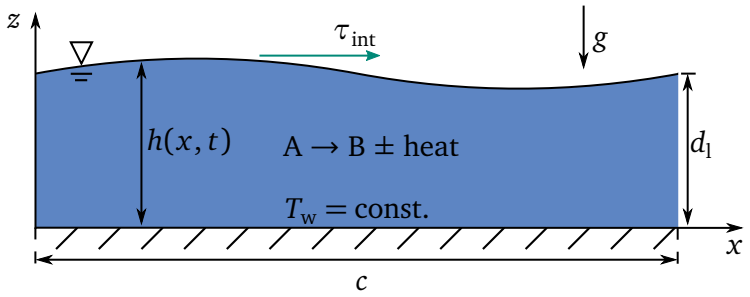

Figure 3.7: Domain for the simulation of a reacting thin film sheared by a constant shear stress.

In this section, a reactive thin liquid film on a wall with constant temperature and sheared at the liquid-gas interface with a constant shear stress is investigated. The reaction in the film leads to temperature gradients in the film and at the interface, which in turn give rise to thermal Marangoni effects. The reaction rate decreases as more and more reactant is consumed so that the importance of the Marangoni effect is time-dependent. Furthermore, the shear stress at the interface, exerted by a co-flowing gas flow, influences the film dynamics. Some of the derivations, discussions, and results given in this section have been published by Bender *et al.* in [28].

3.3.1 Derivation of the Evolution Equation for Laminar Shear-Driven Reactive Films

A sketch of the problem is depicted in Fig. 3.7. The two-dimensional, periodic setup corresponds to the thin liquid film of thickness $h(x,t)$ (average thickness d_l) and length c on a rigid, impermeable, and planar wall with constant wall temperature T_w. The interface is assumed to be adiabatic, meaning that heat exchange with the gas phase is neglected. The film consists initially solely of species A, which reacts in a first order decay to species B. This reaction can be endothermic or exothermic, leading to heat consumption or release in the film, respectively. It is assumed that evaporation or condensation of any species is negligible so that the sum of mass of the two species is constant over time. Both species are further assumed to be passive, meaning that the concentration profile does not influence the flow field, and the material properties of the film are independent of the composition of the film. At the interface, the film is sheared by the constant shear stress τ_int. The continuity equation and Navier-Stokes equations for this case are identical to section 3.2 (Eqs. (3.9) - (3.11)). The energy equation in the film now includes an additional term capturing the heat of reaction

$$T_t + u\,T_x + w\,T_z = a_\mathrm{l}\,(T_{xx} + T_{zz}) + r_\mathrm{react}\frac{q\,\xi_\mathrm{A}}{\rho_\mathrm{l}\,c_{p,\mathrm{l}}}\,, \tag{3.42}$$

where q is the heat per volume consumed ($q<0$) or released ($q>0$) by the endothermic or exothermic reaction, respectively.

Additionally, a transport equation for the mass fraction of species A – ξ_A – is solved

$$\xi_{A,t} + u\,\xi_{A,x} + w\,\xi_{A,z} = D_{bin}\left(\xi_{A,xx} + \xi_{A,zz}\right) - r_{react}\,\xi_A\,. \tag{3.43}$$

The reaction rate r_{react} is calculated using an Arrhenius equation for a first order decay

$$r_{react} = r_{react,0}\,e^{-\mathscr{E}/(\mathscr{R}\,T)}\,, \tag{3.44}$$

where $r_{react,0}$ is the pre-exponential factor and $\mathscr{E}$ is the activation energy. It can be seen that the reaction rate increases with temperature $r_{react} = r_{react}(T)$.
At the wall ($z = 0$) no-slip and no-penetration conditions for the velocity field, as well as a constant wall temperature and no species flux through the wall are prescribed, which is formulated as

$$u = 0\,, \qquad w = 0\,, \qquad T = T_w\,, \qquad \xi_{A,z} = 0\,. \tag{3.45}$$

The momentum balance at the interface ($z = h$) for a non-evaporating fluid with constant external shear stress follows as

$$\mathbf{T}_l \cdot \mathbf{n} \cdot \mathbf{n} + \sigma \nabla \cdot \mathbf{n} = 0\,, \tag{3.46}$$

$$\mathbf{T}_l \cdot \mathbf{n} \cdot \mathbf{t} - \nabla\sigma \cdot \mathbf{t} - \tau_{int} = 0\,. \tag{3.47}$$

Using the normal and tangential vectors defined in Eq. (3.18) in the limit of a flat wall ($l_x = 0$) and employing the continuity equation, one obtains for the normal and tangential stress balance at the interface

$$-p + 2\mu_l \frac{u_x\left(h_x^2 - 1\right) - h_x\left(u_z + w_x\right)}{\left(1 + h_x^2\right)} = \sigma \frac{h_{xx}}{\left(1 + h_x^2\right)^{\frac{3}{2}}}\,, \tag{3.48}$$

$$\mu_l \frac{\left(1 - h_x^2\right)\left(u_z + w_x\right) - 4\,h_x\,u_x}{\left(1 + h_x^2\right)^{\frac{1}{2}}} = \frac{\partial\sigma}{\partial T}\left(T_x + h_x\,T_z\right) + \tau_{int}\left(1 + h_x^2\right)^{\frac{1}{2}}\,. \tag{3.49}$$

It should be noted that, as stated in Eq. (3.7), the surface tension is assumed to be not dependent on the liquid composition. Additionally, the interface is adiabatic and no species transport across the interface is assumed so that the effect of the chemical reaction can be separated from other transport processes

$$-T_x\,h_x + T_z = 0\,, \tag{3.50}$$

$$-\xi_{A,x}\,h_x + \xi_{A,z} = 0\,. \tag{3.51}$$

Lastly, the kinematic boundary condition at the interface yields

$$h_t + u\,h_x - w = 0\,. \tag{3.52}$$

The governing equations and boundary conditions are non-dimensionalized. The velocities are non-dimensionalized with a velocity scale based on the interfacial shear stress, and time is non-dimensionalized with the reaction time scale based on the wall temperature. The characteristic temperature difference $\Delta T = (q\,\xi_{\mathrm{A},0})/(\rho_\mathrm{l}\,c_{p,\mathrm{l}})$ can be understood as the change in temperature in the film in the absence of heat transport after all educt has reacted and the reaction rate has decreased to zero. $\xi_{\mathrm{A},0}$ is the initial mass fraction of species A in the film and is set to $\xi_{\mathrm{A},0} = 1$ throughout this section. Consequently, the non-dimensional parameters read

$$\epsilon = \frac{d_\mathrm{l}}{c}\,, \qquad H = \frac{h}{d_\mathrm{l}}\,, \qquad X = \frac{x}{c} = \frac{x\,\epsilon}{d_\mathrm{l}}\,, \qquad Z = \frac{z}{d_\mathrm{l}}\,, \qquad U = \frac{\mu_\mathrm{l}\,u}{\tau_\mathrm{int}\,d_\mathrm{l}}\,, \qquad W = \frac{\mu_\mathrm{l}\,w}{\tau_\mathrm{int}\,d_\mathrm{l}\,\epsilon}\,,$$

$$\tau = r_{\mathrm{react},0}\,e^{-\mathscr{E}/(\mathscr{R}\,T_\mathrm{w})}\,t\,, \qquad \Theta = \frac{T - T_\mathrm{w}}{\frac{|q|\,\xi_{\mathrm{A},0}}{\rho_\mathrm{l}\,c_{p,\mathrm{l}}}}\,, \qquad P = \frac{p}{\tau_\mathrm{int}}\,, \qquad \Xi_\mathrm{A} = \frac{\xi_\mathrm{A}}{\xi_{\mathrm{A},0}}\,,$$

where Ξ_A is the normalized mass fraction of species A. The governing non-dimensional parameters of the problem are the non-dimensional surface tension force S and gravity G, as well as the Marangoni number Ma, the Prandtl number Pr, the dimensionless interfacial shear stress F, the Damköhler number Da, and the Schmidt number Sc, defined as

$$S = \frac{\sigma\,d_\mathrm{l}}{3\,\mu_\mathrm{l}\,\nu_\mathrm{l}}\,, \qquad G = \frac{d_\mathrm{l}^3\,g}{\nu_\mathrm{l}^2}\,, \qquad Ma = -\frac{\sigma_T\,\frac{q\,\xi_{\mathrm{A},0}}{\rho_\mathrm{l}\,c_{p,\mathrm{l}}}\,d_\mathrm{l}}{2\,\mu_\mathrm{l}\,a_\mathrm{l}}\,, \qquad Pr = \frac{\nu_\mathrm{l}}{a_\mathrm{l}}\,,$$

$$F = \frac{d_\mathrm{l}^2\,\tau_\mathrm{int}}{\mu_\mathrm{l}\,\nu_\mathrm{l}}\,, \qquad Da = \frac{d_\mathrm{l}^2\,r_{\mathrm{react},0}\,e^{-\mathscr{E}/(\mathscr{R}\,T_\mathrm{w})}}{\nu_\mathrm{l}}\,, \qquad Sc = \frac{\nu_\mathrm{l}}{D_\mathrm{bin}}\,.$$

Non-dimensional surface tension and gravity, as well as the Prandtl number are identical to the definitions given in section 3.2.1. The Marangoni number Ma is defined using the characteristic temperature difference $(q\,\xi_{\mathrm{A},0})/(\rho_\mathrm{l}\,c_{p,\mathrm{l}})$ described above. The dimensionless interfacial shear stress F is computed comparing the interfacial shear stress to viscous stresses in the film. The Damköhler number Da represents the ratio between the viscosity time scale and the reactive time scale. The Schmidt number Sc describes the ratio between viscous momentum transfer and diffusive mass transfer. In the following, a rapid mass diffusion in Z-direction is assumed ($\Xi_{\mathrm{A},ZZ} = 0$), which leads to a constant species concentration over the film height. This assumption is sometimes called "well-mixed" and is valid for thin films [84].

The dimensionless variables are plugged back into the governing equations and boundary conditions. A double perturbation analysis is carried out in the parameter ϵ and the Damköhler number Da to derive an evolution equation for the film height (see [222]). As in the previous section, it is assumed that the characteristic film thickness is small compared to the length scale of the film thickness variation ($\epsilon \ll 1$). Additionally, the chemical reaction is slow ($Da \ll 1$), but it is required that $\epsilon < Da \ll \epsilon^{\frac{1}{2}}$. Using these relations, all dependent variables can be expanded depending on the order of ϵ and Da as shown exemplarily for the dimensionless temperature

$$\Theta \propto \Theta_{00} + Da\,\Theta_{01} + \epsilon\,\Theta_{10} + Da^2\Theta_{02} + \epsilon\,Da\,\Theta_{11} + \epsilon^2\,\Theta_{20} + \mathcal{O}\left(Da^3\right). \tag{3.53}$$

As before, strong surface tension effects of $\mathcal{O}\left(\epsilon^{-2}\right)$ are assumed so that the surface tension term enters the equation in the zeroth order $\mathcal{O}(0)$. The tangential shear stress, which arises from the Marangoni forces, is found in $\mathcal{O}(\epsilon)$. Thus, it is required that $(\epsilon\,\mathrm{sgn}(q)Ma\,\Theta_X)/(Pr\,F)$ is $\mathcal{O}(\epsilon)$ with Θ_X of $\mathcal{O}(Da)$ and Pr of $\mathcal{O}(1)$, which leads to Ma in the order of $\mathcal{O}(Da^{-1})$. For convenience, the substitutions $\widetilde{S} = \epsilon^3 S$, $\widetilde{G} = \epsilon\,G$, and $\widetilde{Ma} = \epsilon\,Ma$ are utilized similarly to section 3.2. The problem is solved for $\mathcal{O}(0)$, $\mathcal{O}(Da)$, and $\mathcal{O}(\epsilon)$ and plugged into the kinematic boundary condition at the interface (Eq. (3.52)). This leads to the order ϵ evolution equation for the non-dimensional film height

$$H_\tau + \frac{\epsilon}{Da}\left[\frac{1}{2}F\,H^2 + H^3\left(\widetilde{S}\,H_{XXX} - \frac{\widetilde{G}}{3}H_X - \widetilde{Ma}\,Da\,H_X\,e^{-\tau}\right)\right]_X = 0\,. \tag{3.54}$$

The influence of the interfacial shear stress is found in the second term of the evolution equation. The third term captures the surface tension and the fourth term the gravitational effect. Finally, the last term on the left hand side of Eq. (3.54) includes the Marangoni effect.

3.3.2 Linear Stability Analysis for Laminar Shear-Driven Reactive Films

To gain further insight into the problem and to examine the film stability, the evolution equation (3.54) is linearized around the base state. The dimensionless film height H can be written as

$$H(X,\tau) = 1 + \zeta\,H_1(X,\tau), \tag{3.55}$$

with $\zeta \ll 1$, which assumes that the film height shows only small fluctuations around the undisturbed state. Equation (3.55) is substituted into the evolution equation (3.54). Neglecting terms that depend on ζ in a higher order than unity, leads to a linear partial differential equation

$$H_{1,\tau} + \frac{\epsilon}{Da}\left[F\,H_{1,X} + \widetilde{S}\,H_{1,XXXX} - \frac{\widetilde{G}}{3}H_{1,XX} - \widetilde{Ma}\,Da\,e^{-\tau}\,H_{1,XX}\right] = 0\,. \tag{3.56}$$

This linear equation, however, does not have constant coefficients because of the term depending on time in the form of $e^{-\tau}$. For large times, the change in $e^{-\tau}$ is much smaller than the change in τ so that

$$e^{-\tau} \approx \text{constant} \tag{3.57}$$

can be used for the scope of the linear analysis. For small times, this can still be applied if the perturbation growth rates Ω are large. Implicitly this was already required in the derivation of the evolution equation where $Da \ll 1$ was assumed. This assumption, namely that the time scale of the growth of the film thickness disturbance is small compared to the reactive time scale, is suitable for slow chemical reactions as found in many industrial applications. Now, the solutions of Eq. (3.56) can be sought using the normal mode approach

$$H_1(X,\tau) \propto e^{\Omega\tau + iKX}\,, \tag{3.58}$$

with the wavenumber K and the growth rate Ω of the perturbations. This leads to an expression for the disturbance growth rate as function of the wavenumber

$$\Omega = \frac{\epsilon}{Da}\left\{-i\,F\,K - K^2\left[K^2\,\widetilde{S} + \frac{\widetilde{G}}{3} + \widetilde{Ma}\,Da\,e^{-\tau}\right]\right\}. \tag{3.59}$$

The perturbations decay over time if the real part of the growth rate in Eq. (3.59) is smaller than zero ($\mathrm{Re}(\Omega) < 0$), which corresponds to a stable situation. If $\mathrm{Re}(\Omega) > 0$, the perturbations grow and the film is unstable. Consequently, surface tension has a stabilizing effect on the film. The surface tension term depends on K^4, which means that it is highly dependent on the wavenumber. Looking at terms of order K^2 (ignoring the influence of surface tension), one finds a stable film as long as

$$\frac{\widetilde{G}}{3} + \widetilde{Ma}\,Da\,e^{-\tau} > 0\,. \tag{3.60}$$

In the absence of gravitational forces ($\widetilde{G} = 0$), any endothermic reaction ($\widetilde{Ma} < 0$) leads to film destabilization, while an exothermic reaction leads to a stable behavior. As expected, gravity ($\widetilde{G} > 0$) has a stabilizing effect on the film as long as the gravity vector points from the interface to the wall. In this case, the stability condition for endothermic reactions follows as $\widetilde{G} > 3\,|\widetilde{Ma}|\,Da\,e^{-\tau}$. Because of the time dependency of this expression, a primarily unstable film becomes stable with sufficiently increasing time τ. Under the assumption that the linear approximation of the evolution equation stays valid, meaning that the initial disturbance did not grow magnificently, the disturbance grows, while τ satisfies the condition

$$\ln\left(\frac{3\,|\widetilde{Ma}|\,Da}{\widetilde{G}}\right) > \tau\,. \tag{3.61}$$

When this inequality is not true any more, the disturbances decay leading to a flat film. This behavior is independent of the film height.

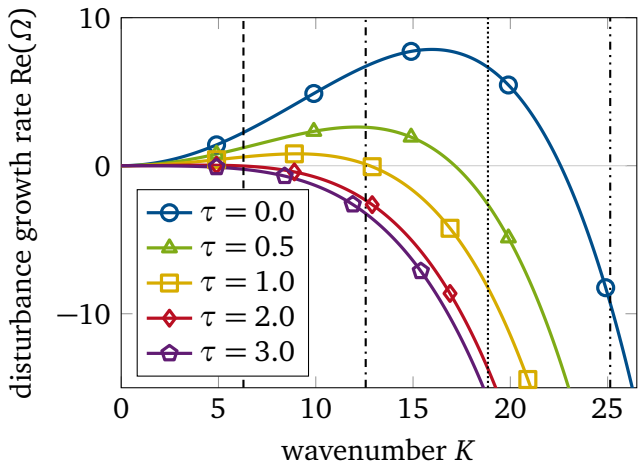

Figure 3.8: Development of the disturbance growth rate over the wavenumber for different time instances.

A critical wavenumber can be identified from Eq. (3.59) for which a maximum growth rate Ω can be found. This is the wavenumber K_{crit}, which fulfills the condition

$$\frac{\partial \text{Re}(\Omega)}{\partial K} = 0\,, \tag{3.62}$$

leading to

$$K_{\text{crit}} = \sqrt{\frac{3\widetilde{Ma}\,Da + \widetilde{G}}{-6\,\widetilde{S}}}\,. \tag{3.63}$$

The real part of the disturbance growth rate over the wavenumber is plotted for different times in Fig. 3.8 for an endothermic reaction. For a wavenumber of zero, the growth rate is zero, meaning an initial disturbance of the film is necessary. For small times, the growth rate increases with increasing wavenumber until a maximum value is reached, after which the growth rate decreases and becomes negative. A strong influence of the time τ on the shape of the curve can be observed. As time increases, the maximum growth rate decreases because the reaction rate decreases. Additionally, with increasing time, the maximum growth rate and the cutoff wavenumber, which corresponds to $\text{Re}(\Omega) = 0$, can be observed for lower wavenumbers. For large times corresponding to the reaction being finished, the linear stability is determined by the stabilizing effect of gravity and surface tension and the growth rate is negative for all wavenumbers. As discussed above, the analysis in this section is strictly justified for a fast growth of the disturbance in comparison to the reaction time. As a result, the validity condition for Eq. (3.59) is $\Omega \gg 1$, which means that this analysis is valid far from the neutral stability region. From Fig. 3.8 it can be seen that this condition is true for $10 \lesssim K \lesssim 20$ for $\tau = 0$, for example. Further insight can be gathered from the full numerical simulation.

It can bee seen in Eq. (3.59) that the interfacial shear stress F appears in the imaginary term. Consequently, this term does not affect the linear stability analysis and is not expected to influence the film height evolution in the linear approximation. However, outside the linear approximation, the interfacial shear stress affects the film stability and evolution, which is discussed in the next section.

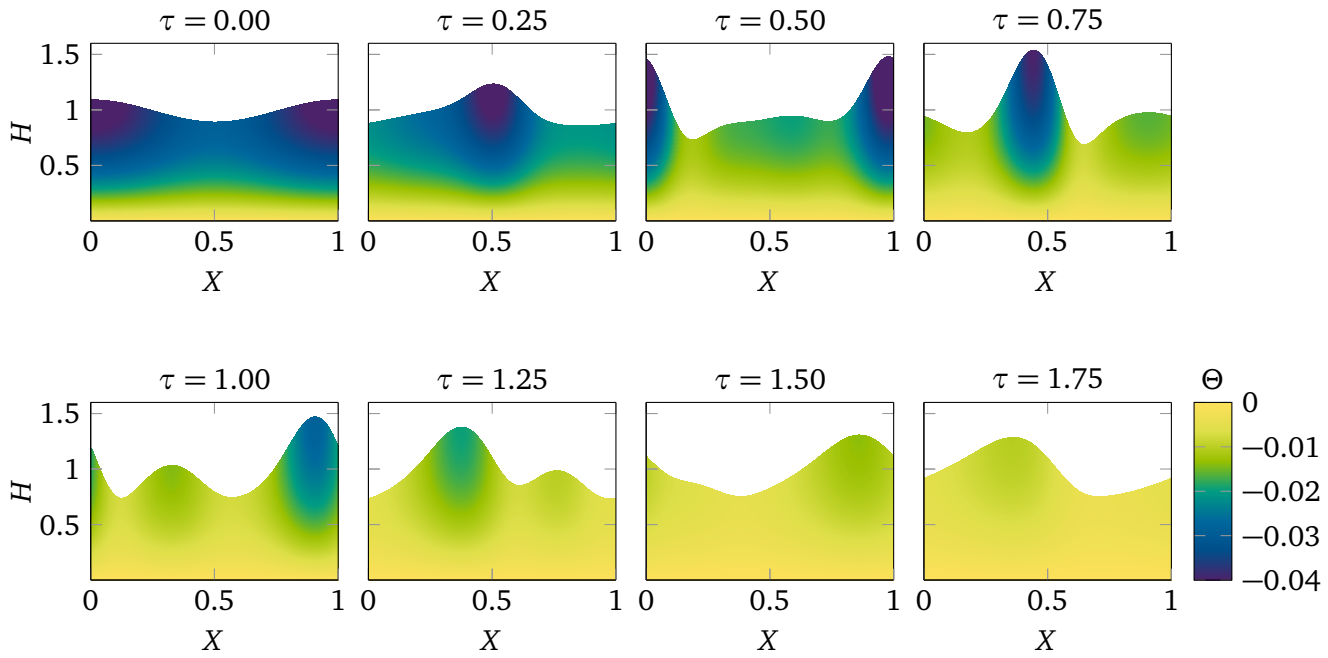

Figure 3.9: Time evolution of the non-dimensional temperature field inside the reactive, shear-driven film in the case of an endothermic reaction.

3.3.3 Results for Laminar Shear-Driven Reactive Films

Similarly to section 3.2.2, the simulations in this section are conducted for a hexane film with a film thickness $d_l = 50\,\mu\text{m}$ and a film length of $c = 1\,\text{cm}$ on a wall with a constant temperature of $T_w = 313.15\,\text{K}$ and sheared by a moderate interfacial shear stress. The chosen exemplary endothermic chemical reaction in the film leads to a characteristic temperature difference of $\Delta T = (q\,\xi_{A,0})/(\rho_l\,c_{p,l}) = -20\,\text{K}$. For the chosen parameter set, $1\,\tau$ corresponds to $0.453\,\text{s}$. The resulting reference values of the non-dimensional parameters in the evolution equation (3.54) are

$$\epsilon = 5 \cdot 10^{-3}\,, \qquad \widetilde{S} = 3.165 \cdot 10^{-4}\,, \qquad \widetilde{G} = 3.679 \cdot 10^{-2}\,,$$

$$\widetilde{Ma}_0 = -13.259\,, \qquad F_0 = 4.661\,, \qquad Da = 1.130 \cdot 10^{-2}\,.$$

The Marangoni number and the non-dimensional shear stress are varied in this section, while the other non-dimensional parameters are kept constant. Unless specified otherwise, the reference values are used.

The evolution of the non-dimensional temperature field Θ inside a film with an initial disturbance wavenumber $K = 2\,\pi$ is depicted in Fig. 3.9. It can be seen that the initial film height crest travels through the domain as a result of the interfacial shear stress. The reaction rate has its maximum value for $\tau = 0$ and then decreases with time as the educt concentration is reduced. The endothermic chemical reaction leads to temperature gradients at the liquid-gas interface, which result in a Marangoni flow. As the minimum interface temperature can be observed at the film crest, the resulting Marangoni flow drives the

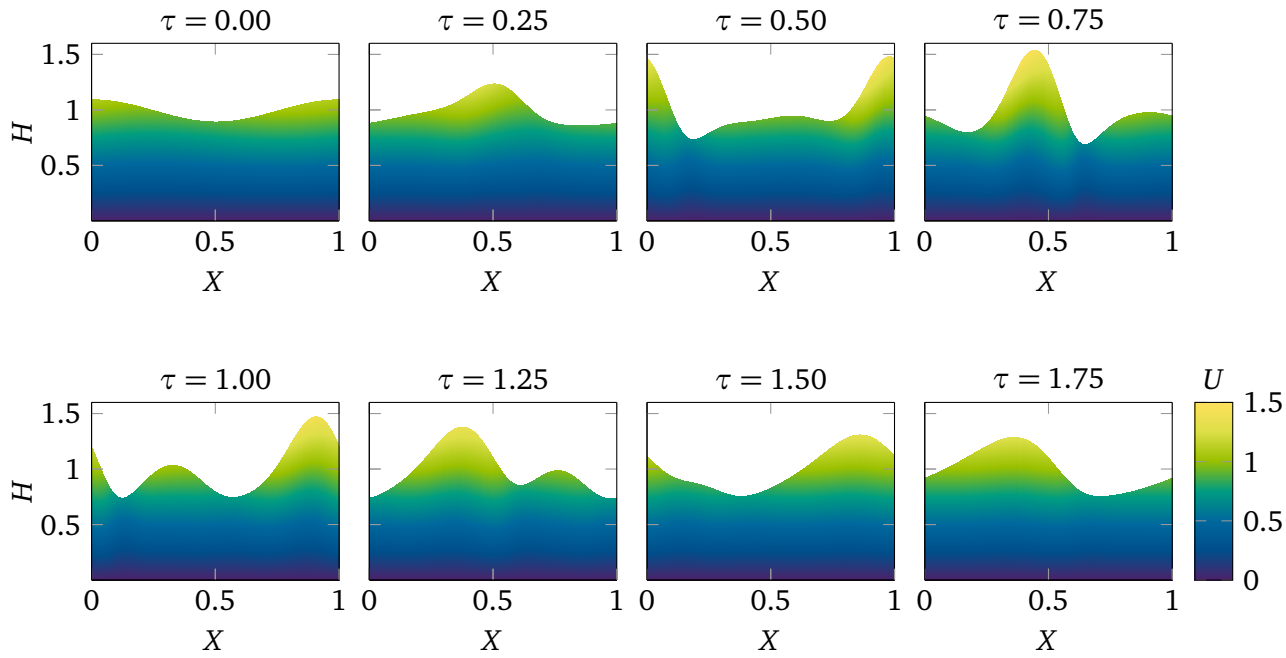

Figure 3.10: Time evolution of the non-dimensional horizontal velocity field inside the reactive, shear-driven film in the case of an endothermic reaction.

liquid from the troughs to the crest, leading to an increase of the film crest height for $\tau \leq 0.75$. It can be seen that the average temperature in the film rises with increasing time because the heat consumed by the chemical reaction decreases and heat conduction eventually leads to an almost homogeneous temperature in the film (for $\tau \geq 1.5$), which corresponds to the wall temperature. Consequently, as the temperature gradients at the liquid-gas interface reduce over time, the driving force of the film instability is reduced. The stabilizing effect of surface tension and gravity then lead to a decrease of the peak height over time (for $\tau > 0.75$) and eventually to a flat film interface.

The corresponding non-dimensional horizontal velocity field U in the film is shown in Fig. 3.10. The velocity is zero at the wall due to the no-slip condition and increases with the distance to the wall. The maximum velocity can be observed at the upstream side of the film crest. This leads initially to an increase of the peak's height and a decrease of the peak's thickness over time (for $\tau \leq 0.75$). Additionally, the evolution of a side maximum next to the highest peak can be observed starting from $\tau = 0.75$. This side maximum has a lower velocity than the highest peak. Consequently, the distance between the peaks decreases until the peaks merge at $\tau \approx 1.5$, again leading to one film height maximum in the film.

It had been shown in earlier works that, when the surface tension of a fluid decreases with increasing temperature, endothermic reactions have a destabilizing effect on the film, while exothermic reactions are stabilizing [221, 222]. This can be observed in Fig. 3.11 where Marangoni numbers, which correspond to an endothermic reaction ($0.4 \cdot \widetilde{Ma}_0$ - $1.2 \cdot \widetilde{Ma}_0$), lead to an increase of the maximum film height with time. It can be seen from the figure that the film is sensitive to the reaction parameters. A slight increase in the heat consumed by the chemical reaction (leading to a higher magnitude of the Marangoni number) yields a strong increase in the growth rate of the maximum film height. As discussed previously, when the reaction slows down over time, surface tension and gravity lead to a decrease of the maximum film

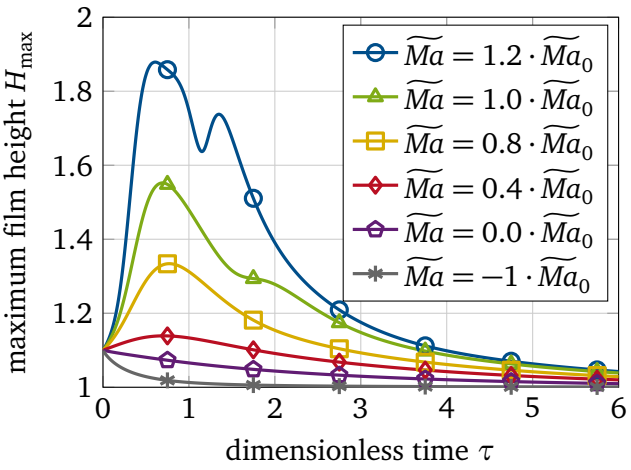

Figure 3.11: Time evolution of the film height maximum for varying reaction parameters. Note that $\widetilde{Ma}_0 < 0$ so that positive prefactors correspond to endothermic reactions and negative prefactors to exothermic reactions.

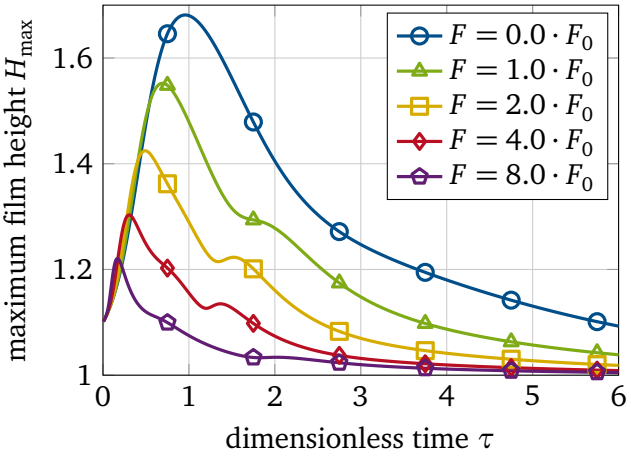

Figure 3.12: Time evolution of the film height maximum for varying interfacial shear stress.

height and eventually to a flat film in all scenarios. However, if the magnitude of the Marangoni number is increased a little further than the values shown in Fig. 3.11, film rupture occurs before the reaction rate has declined. Additionally, for $\widetilde{Ma} = 1.2 \cdot \widetilde{Ma}_0$, the film height reaches a maximum value, starts to decrease and then increases again to reach another peak, before it eventually decreases towards a flat film. This effect can be attributed to the influence of the shear stress, which leads to the merger of the highest film peak with a side peak at $\tau \approx 1.2$ (see Fig. 3.10). This results in the second increase of the maximum film height despite the continuously decreasing reaction rate.

Furthermore, it can bee seen from Fig. 3.11 that, in the absence of a chemical reaction ($\widetilde{Ma} = 0.0 \cdot \widetilde{Ma}_0$), no growth of the film height maximum is observed and surface tension and gravitational forces lead to a flat film. The stabilization is enhanced by an exothermic reaction ($\widetilde{Ma} = -1 \cdot \widetilde{Ma}_0$). Here, the heat released by the reaction causes temperature maxima at the film crests and minima at the film troughs so that the resulting Marangoni effect leads to a convection from the crests to the troughs, which decreases film height maxima. It can be seen that this stabilizing effect of the exothermic reaction decreases with time, too, as the reaction rate decreases.

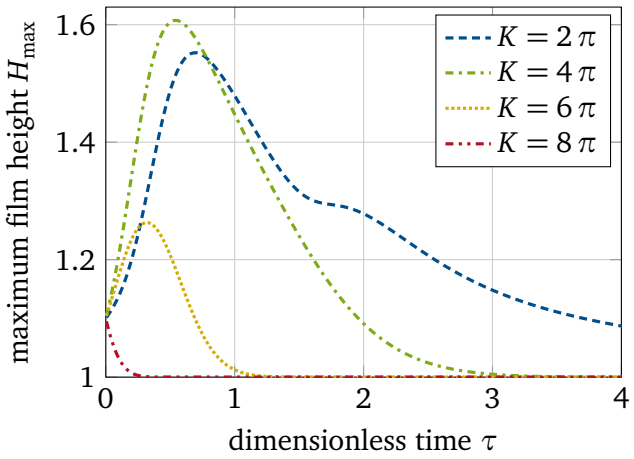

Figure 3.13: Time evolution of the film height maximum for different wavenumbers of the initial disturbance.

The evolution of the maximum film height for varying interfacial shear stress values is depicted in Fig. 3.12. The peak of the maximum film height decreases with increasing shear stress. One can conclude that in this case the shear stress acts to reduce existing film height maxima and consequently has a stabilizing effect on the film. This result could not be obtained from the linear stability analysis in section 3.3.2 and can only be found from solving the nonlinear evolution equation.

Additionally, it follows from Fig. 3.12 that the peak of the maximum film height is reached earlier and that the initial growth of the maximum film height is higher for higher shear stress magnitudes. This behavior can be explained by looking at the velocity field depicted in Fig. 3.10. The velocity on the upstream side of the peak is higher than on the downstream side, which leads to the development of a thin and high peak over time. Increasing shear stress enhances this phenomenon. However, as the peak becomes thinner, the interface curvature is increased, which leads to an increase of the surface tension force. The destabilizing effect of the reaction rate and the stabilizing effect of the surface tension have a competing effect on the film. With the increase of the surface tension force due to the thinner peaks for higher shear stress magnitudes, the maximum disturbance is reached for earlier times and the decrease of the film disturbance is enhanced as the reaction rate decays, which is evident from Fig. 3.12.

The real part of the disturbance growth rate as a function of the wavenumber of the initial film disturbance K is plotted in Fig. 3.8. The vertical lines correspond to four wavenumbers, which are now investigated more closely. The evolution of the maximum film height for these different values of the initial disturbance wavenumber K but with the same disturbance amplitude is displayed in Fig. 3.13. In the case of the low wavenumber $K = 2\,\pi$ the magnitude of the growth rate is relatively low for all times (see Fig. 3.8). This leads to both a moderate initial increase of the maximum film height and a moderate decrease of the film height when the reaction has slowed down.

If the wavenumber of the initial disturbance is increased to $K = 4\,\pi$, the growth rates are higher, especially at lower times, compared to $K = 2\,\pi$, which leads to a faster initial increase of the film height maximum and a higher peak value. It follows from Fig. 3.8 that the growth rate becomes negative for $\tau \approx 1.5$, which leads to a decrease of the maximum film height. It can be seen that this decrease is faster than for $K = 2\,\pi$ (Fig. 3.13). In the case of $K = 6\,\pi$, the initial growth of the film disturbance is similar to $K = 4\,\pi$. This

makes sense since the growth rates for $\tau = 0$ are almost identical in the two cases (Fig. 3.8). However, the maximum film disturbance is much higher for $K = 4\,\pi$ than for $K = 6\,\pi$, which is due to the faster decrease of the disturbance growth rate with time for $K = 6\,\pi$. This also leads to a faster decrease of the maximum film height after the peak value is reached. It can be shown that the highest crests are observed in the film for $K \approx 4\,\pi$ for the chosen parameters, despite the fact that the maximum growth rate for $\tau = 0$ is observed for $K \approx 5\,\pi$ (see Fig. 3.8). The evolution of the growth rate with time has to be taken into account, which leads to a shift of the maximum growth rate to lower wavenumbers. Additionally, the growth rate stays positive for a longer time for lower wavenumbers (as the cutoff wavelength decreases with increasing time). Due to these non-linear effects, it is not possible to predict the disturbance growth rate, which leads to the highest film deformation or even film rupture, from the linear stability analysis. If the wavenumber is increased even more, to $K = 8\,\pi$, the disturbance growth rate is negative for all times and the film quickly presumes a flat interface shape.

3.4 Turbulent Shear Flow

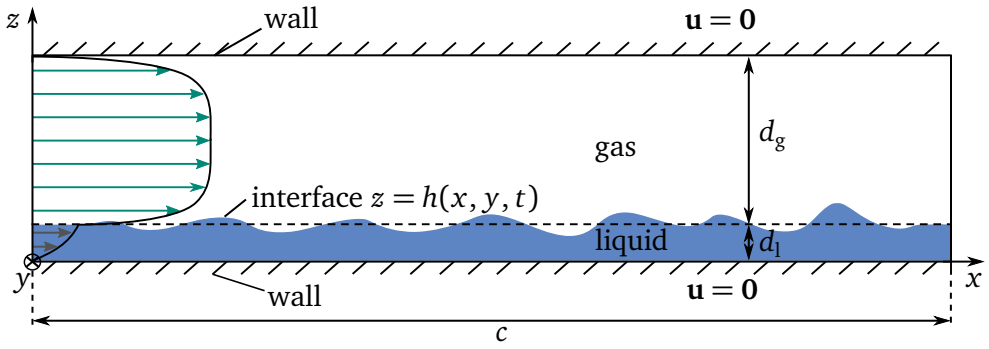

Figure 3.14: Domain for the simulation of a thin film sheared by a turbulent gas flow.

In this section, a thin film sheared by a turbulent gas flow is investigated. The turbulent shear stress at the liquid-gas interface has been shown to lead to film disturbances (see section 2.1.3). However, the effect of the turbulent shear stress fluctuations on the film evolution have been previously neglected, which is why it is the focus of this section. Some of the derivations, discussions, and results given in this section have been published by Bender *et al.* in [32].

3.4.1 Modeling Approach for Thin Films Driven by Turbulent Shear Flow

A flat channel of length c, bounded on the bottom and top by two parallel solid walls, is considered (see Fig. 3.14). The remaining boundaries are periodic (double periodic channel). The bottom wall is covered by a thin liquid film with a time- and position-dependent film thickness $h(x, y, t)$ (average film thickness d_l). The film initially possesses a flat interface. A turbulent gas flows in the remaining channel height of d_g. The turbulent gas flow exerts a shear stress on the liquid-gas interface, which sets the film in motion and leads to film deformation.

Generally, the turbulent fluctuations of the gas velocity and the resulting shear stress fields are three-dimensional, which is why a three-dimensional model is used. The liquid film is assumed to be thin,

isothermal, and non-volatile for simplicity. The film height disturbances resulting from the turbulent shear stress are assumed to have no influence on the turbulent gas flow. This assumption is justified as long as the interfacial deformations are limited to the viscous sublayer of the gas flow (amplitudes below $z^+ = (z\,u_\tau)/\nu_g = 5$, with the superscript plus sign denoting viscous scales). The liquid-gas interface is then perceived as hydraulically smooth for the gas flow [191].

The large viscosity difference between the liquid and the gas means that the turbulent fluctuations in the gas phase decay towards the liquid-gas interface in the same way, as if the interface were a solid wall [224]. Using this, the liquid and the gas flow problem can be separated and investigated individually. For the gas phase, a direct numerical simulation (DNS) and a large eddy simulation (LES) are conducted. The space- and time-dependent shear stress data at the lower stationary wall, representing the liquid-gas interface, of the gas channel with the height d_g is stored with a high temporal resolution so that the movement of the shear stress structures can be interpolated from the saved fields. The shear stress data are then used as a time- and position-dependent boundary condition for the numerical treatment of the liquid flow problem of the thin liquid film. This liquid problem is solved with LWT. The spatial resolution of the long-wave simulation in x- and y-direction is chosen identical to the numerical grid of the gas flow problem to avoid interpolation and to ensure the accuracy of the solution.

The long-wave model of the liquid problem is derived similarly to the two previous sections with the difference being that the evolution equation is two-dimensional in this case. The film is assumed to be periodic in streamwise (x) and spanwise (y) direction, which agrees with the boundary conditions from the DNS and LES (double periodic channel). The boundary condition at the lower wall is the no-slip, no-penetration condition

$$\mathbf{u} = \{0, 0, 0\}\,. \tag{3.64}$$

The dynamic boundary condition at the liquid-gas interface ($z = h(x, y, t)$) follows from a shear stress balance to

$$(\mathbf{T}\cdot\mathbf{n})_l = \sigma\,\kappa\,\mathbf{n} + (\mathbf{T}\cdot\mathbf{n})_g\ , \tag{3.65}$$

where $\mathbf{n}$ is the unit normal vector on the interface and κ ($\kappa = -\nabla\cdot\mathbf{n}$) is the interface curvature.

The second term on the right hand side of Eq. (3.65) is the time- and position-dependent stress vector exerted from the turbulent gas flow on the liquid film. This term is evaluated from the DNS solution and is written in the following form:

$$(\mathbf{T}\cdot\mathbf{n})_g = \{\tau_{\mathrm{int},x}, \tau_{\mathrm{int},y}, 0\}\,. \tag{3.66}$$

Assuming once again that the film is thin ($d_\mathrm{l} \ll c$), the non-dimensional variables are defined using viscous length scales and time scales and follow as

$$\epsilon = \frac{d_\mathrm{l}}{c}, \qquad H = \frac{h}{d_\mathrm{l}}, \qquad X = \frac{x}{c} = \frac{x\,\epsilon}{d_\mathrm{l}}, \qquad Y = \frac{y}{c} = \frac{y\,\epsilon}{d_\mathrm{l}}, \qquad Z = \frac{z}{d_\mathrm{l}},$$

$$U = \frac{u\, d_l}{\nu_l}, \qquad V = \frac{v\, d_l}{\nu_l}, \qquad W = \frac{v\, d_l}{\epsilon\, \nu_l} \qquad \tau = \frac{t\, \nu_l\, \epsilon}{d_l^2}, \qquad P = \frac{\epsilon\, p\, d_l^2}{\mu_l\, \nu_l},$$

where V is the non-dimensional velocity component in the non-dimensional Y-direction. The governing non-dimensional parameters are the non-dimensional surface tension $\widetilde{S}$, gravity $\widetilde{G}$, and interfacial shear stress vector $\mathbf{F}$,

$$\widetilde{S} = \epsilon^3 \frac{\sigma\, d_l}{3\mu_l\, \nu_l}, \qquad \widetilde{G} = \epsilon \frac{d_l^3\, g}{\nu_l^2}, \qquad \mathbf{F} = \frac{d_l^2}{\mu_l\, \nu_l}\{\tau_{\mathrm{int},x}, \tau_{\mathrm{int},y}\} = \{F_x, F_y\}.$$

A perturbation analysis in ϵ, applied to the non-dimensional governing equations and boundary conditions, results in a zeroth order evolution equation of the non-dimensional film height

$$\frac{\partial H}{\partial \tau} + \nabla \cdot \left\{ H^2 \left[H \nabla \left(\widetilde{S} \nabla^2 H - \frac{\widetilde{G}}{3} H \right) + \frac{1}{2}\mathbf{F} \right] \right\} = 0. \tag{3.67}$$

The second term on the left hand side of the evolution equation is the influence of surface tension, the third term represents the effect of gravity, and the last term on the left hand side is the effect of the interfacial shear stress. The shear stress varies with position and time so that $\mathbf{F}$ has to be left inside the brackets. The shear stress values from the gas flow problem are read into the solver at each iteration and are used to calculate the non-dimensional shear stress vector $\mathbf{F}$. The chosen time step of the liquid flow problem is lower than the storage time step of the shear stress fields from the gas flow problem to ensure the convergence of the solver. However, the storage time step from the DNS and LES is small enough that the instantaneous shear stress field for each solver iteration can be calculated through linear interpolation from the stored fields without compromising the accuracy of the solution.

An advantage of the separated approach is that the results of the DNS and LES can be used for a wide range of liquid properties and film thicknesses without having to reevaluate the gas flow problem. The results shown in the next sections are for a hexane film of a thickness of 100 µm, sheared by a turbulent air flow in a gas channel with a channel height $d_g = 2$ cm, length $c = 10$ cm, and width of 4 cm. This leads to the following non-dimensional parameters

$$\epsilon = 1 \cdot 10^{-3}, \qquad \widetilde{S} = 5.064 \cdot 10^{-6}, \qquad \widetilde{G} = 5.886 \cdot 10^{-2}.$$

Two different bulk Reynolds numbers of the gas flow are evaluated ($Re = 5660$ and $Re = 40005$), which, using the approximate relationship $Re_\tau \approx 0.09\, Re^{0.88}$ [172], result in friction Reynolds numbers of the gas flow of $Re_\tau \approx 180$ and $Re_\tau \approx 1000$, respectively.

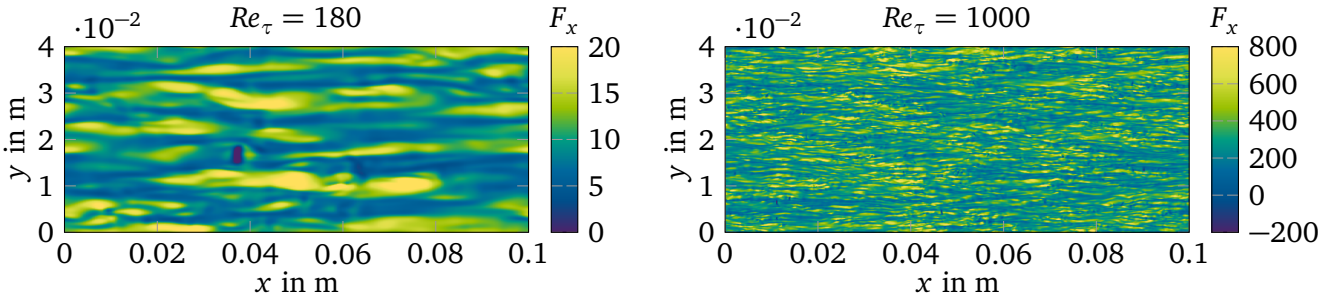

Figure 3.15: Snapshots of the instantaneous dimensionless shear stress from the DNS of the turbulent gas on the film surface at Re_τ = 180 (left) and Re_τ = 1000 (right).

Table 3.1: Results of the DNS.

Re_τ	Re	u_τ in m/s	δ_ν in m	$\overline{F}_x$	$F_{x,\mathrm{rms}}$	$\overline{F}_y$	$F_{y,\mathrm{rms}}$
180	5660	0.313	$5.556 \cdot 10^{-5}$	10.155	10.807	$9.357 \cdot 10^{-3}$	1.974
1000	40005	1.736	$1.000 \cdot 10^{-5}$	312.787	338.085	−0.073	82.274

3.4.2 Direct Numerical Simulation and Long-Wave Theory

The execution of the DNS to obtain the shear stress data is not covered in the scope of this work. The data are taken from [32], where the setup of the DNS and details on the used solver for the gas flow problem, as well as the simulation setup are also presented [I].

Exemplary snapshots of the X-component of the instantaneous shear stress distribution for both Reynolds numbers are shown in Fig. 3.15. It can bee seen that the shear stress magnitude increases considerably with the increase of the friction Reynolds number. Furthermore, the length scales of the shear stress fluctuations are much smaller for $Re_\tau = 1000$ compared to $Re_\tau = 180$ both in the main gas flow direction (streamwise or x-direction) and in the spanwise direction (y-direction). For both Reynolds numbers, the length scale of the shear stress structures is longer in streamwise direction than in spanwise direction, but the number of structures inside the domain are in the same order of magnitude for both directions. These shear stress results agree well with similar DNS results from Perrard *et al.* [169].

Some important flow parameters calculated from the DNS solution are shown in Tab. 3.1. The friction velocity u_τ is proportional to the friction Reynolds number and consequently increases by 5.56-fold from $Re_\tau = 180$ to $Re_\tau = 1000$. The viscous length scale $\delta_\nu = \nu_g / u_\tau$ decreases by the same factor as the friction Reynolds number is increased. It has been shown previously in the literature that streaks propagating in streamwise direction are characteristic for turbulent near wall flows. It was further shown that the spacing between these streaks is of $\mathcal{O}(100\,\delta_\nu)$ and that the length of the streaks is at least in $\mathcal{O}(1000\,\delta_\nu)$ [172]. This results in expected streak lengths of around 5.56 cm for $Re_\tau = 180$ and 1.00 cm for $Re_\tau = 1000$. The average values of the dimensionless shear stress components in streamwise and spanwise direction ($\overline{F}_x$ and $\overline{F}_y$), as well as the root mean square values of the shear stress components ($F_{x,\mathrm{rms}}$ and $F_{y,\mathrm{rms}}$) are also

[I] I would like to thank Dr. Alexander Stroh from Karlsruhe Institute of Technology for conducting the DNS. I also kindly acknowledge his help and guidance regarding the calculation of the correlations in this section.

given in Tab. 3.1. For both Reynolds numbers, the root mean square of the two components of the shear stress fluctuations are in the same order of magnitude. This means that the amplitudes of the fluctuations are similar in x- and y-direction. However, it can be seen that the mean of the shear stress component in x-direction is positive, which leads to the movement of the film in positive x-direction, while the mean of the shear stress in y-direction is close to zero. By increasing the friction Reynolds number from $Re_\tau = 180$ to $Re_\tau = 1000$, the mean shear stress increases by a factor of 30.8, which means that it scales with Re_τ^2, as predicted theoretically in [172], in a very good approximation.

The spatial one-time correlations in streamwise ($\mathscr{C}_x$) and spanwise direction ($\mathscr{C}_y$) for a quantity ϕ (where $\phi(x,y,t) = F_x(x,y,t)$ or $\phi(x,y,t) = H(x,y,t)$) are defined as

$$\mathscr{C}_x(\phi) = \frac{\overline{\phi'(x,y,t)\,\phi'(x+\Delta x,y,t)}}{\sqrt{\left(\overline{\phi'(x,y,t)^2}\cdot\overline{\phi'(x+\Delta x,y,t)^2}\right)}}, \tag{3.68}$$

$$\mathscr{C}_y(\phi) = \frac{\overline{\phi'(x,y,t)\,\phi'(x,y+\Delta y,t)}}{\sqrt{\left(\overline{\phi'(x,y,t)^2}\cdot\overline{\phi'(x,y+\Delta y,t)^2}\right)}}, \tag{3.69}$$

with the time-dependent deviation from the mean value ϕ'.

The temporal one-point correlation for ϕ is given by

$$\mathscr{C}_t(\phi) = \frac{\overline{\phi'(x,y,t)\,\phi'(x,y,t+\Delta t)}}{\overline{\phi'(x,y,t)^2}}. \tag{3.70}$$

The correlation functions indicate over which distance (Δx or Δy) or time (Δt) the field correlates with itself. A value of unity corresponds to a perfect correlation and a value of zero to no correlation. A negative value of the correlation indicates that an above average value of ϕ (a local maximum) is compared to a below average value (a local minimum) or vice versa. This can be used to deduce the length scales and time scales of the investigated field.

Spatial one-time correlations in the streamwise ($\mathscr{C}_x$, left picture) and spanwise direction ($\mathscr{C}_y$, middle picture) and temporal one-point correlations ($\mathscr{C}_t$, right picture) of the x-component of the turbulent shear stress (Eqs. (3.68) - (3.70) with $\phi(x,y,t) = F_x(x,y,t)$) are shown for both Reynolds numbers in Fig. 3.16. The spatial one-time correlations decay to zero faster for the higher Reynolds number, showing that the shear stress structures are about one order of magnitude smaller in both streamwise and spanwise direction for $Re_\tau = 1000$ compared to $Re_\tau = 180$. This confirms the qualitative observations from Fig. 3.15. The temporal one-point correlation also decays faster for the higher Reynolds number, which means that the time scales of the turbulent shear stress structures decrease substantially when the Reynolds number is increased (note the different range in Δt for the two Reynolds numbers). It can be seen that for $Re_\tau = 180$ the spatial one-time correlation in streamwise direction and the temporal

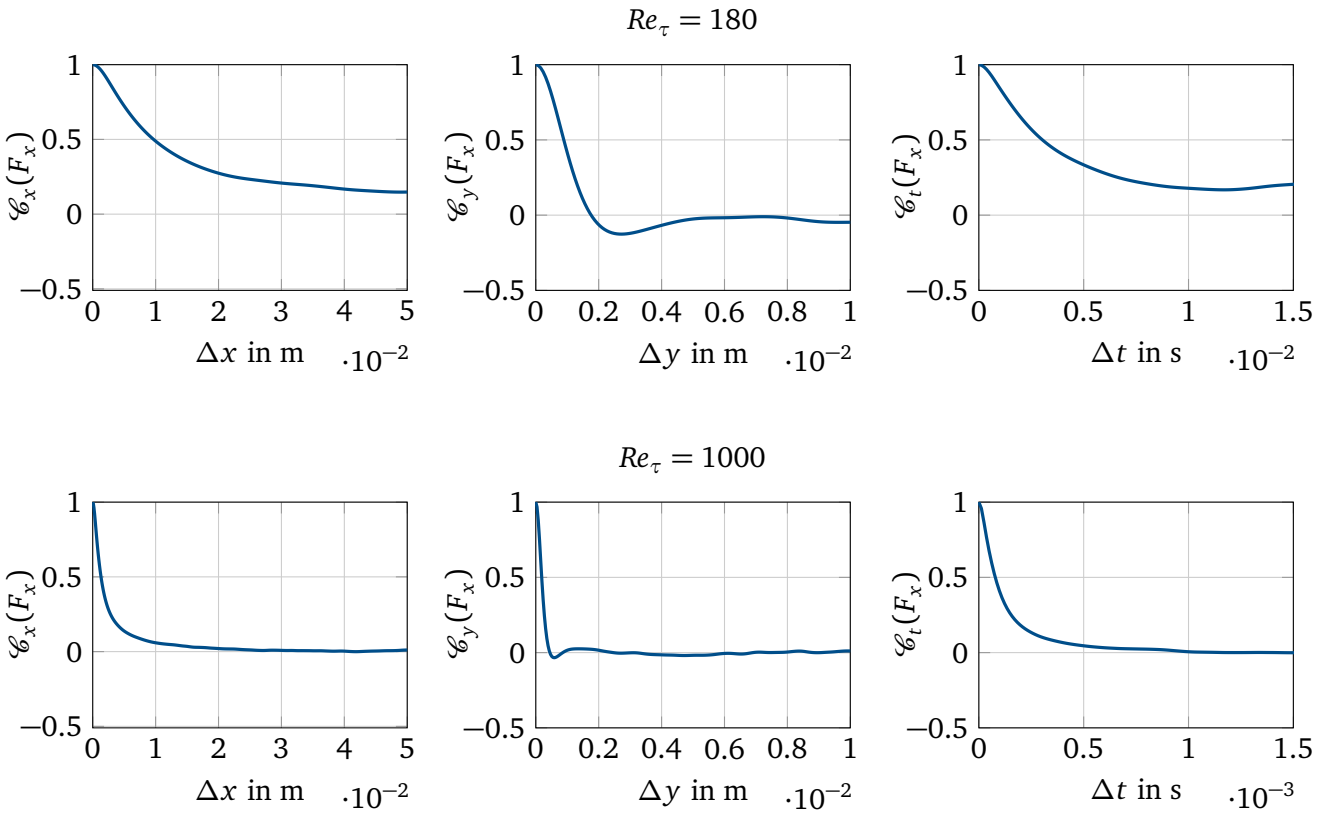

Figure 3.16: Streamwise (left), spanwise (middle), and temporal (right) correlation of the streamwise shear stress component F_x for $Re_\tau = 180$ and $Re_\tau = 1000$ from the DNS.

one-point correlation do not decay to zero in the observed intervals, due to the length of the streaks in streamwise direction, which – as discussed above – are expected to be more than half the domain length long.

The spatiotemporal correlation for a quantity ϕ (where $\phi(x,y,t) = F_x(x,y,t)$ or $\phi(x,y,t) = H(x,y,t)$) is given by

$$\mathscr{C}_{xt}(\phi) = \frac{\overline{\phi'(x,y,t)\,\phi'(x+\Delta x, y, t+\Delta t)}}{\sqrt{\left(\overline{\phi'(x,y,t)^2} \cdot \overline{\phi'(x+\Delta x, y, t+\Delta t)^2}\right)}}. \tag{3.71}$$

It is shown for the x-component of the shear stress structures ($\phi(x,y,t) = F_x(x,y,t)$) in Fig. 3.17. From these correlations, the convection velocity of the shear stress structures $u_{\text{wave,g}}$ can be calculated as

$$u_{\text{wave,g}} = \frac{\Delta x_{\max}}{\Delta t}, \tag{3.72}$$

where $\Delta x_{\max}$ marks the position at which the maximum of the spatiotemporal correlation occurs for a given temporal separation Δt. As the accuracy of this prediction depends on the choice of Δt, the convection velocity is based on $\Delta t^+ = 18$ (with $t^+ = 4Re_\tau^2\, \nu_g\, d_g^{-2}\, t$), which is recommended in the literature by Kim and Hussain [126] to reduce the error from interpolation and get a reasonable detection of the correlation peak on the used numerical grid. This corresponds to $\Delta t = 3.20 \cdot 10^{-3}$ s and $\Delta t = 1.04 \cdot 10^{-4}$ s for

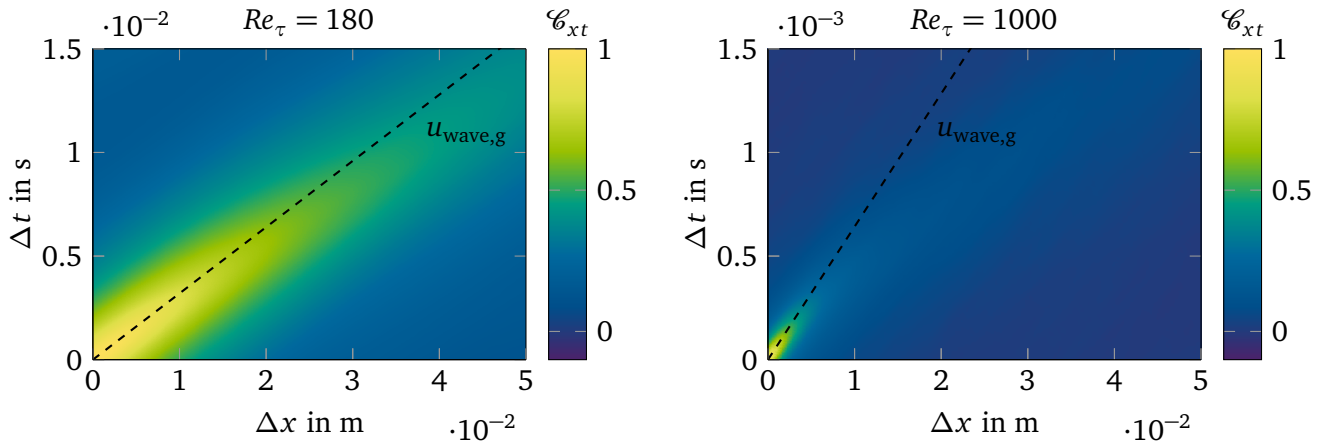

Figure 3.17: Spatiotemporal correlation $\mathscr{C}_{xt}$ of the streamwise shear stress component F_x for $Re_\tau = 180$ (left) and $Re_\tau = 1000$ (right) from the DNS.

$Re_\tau = 180$ and $Re_\tau = 1000$, respectively. The calculated convection velocities are represented in Fig. 3.17 by the dashed lines and are estimated to be around 3.127 m/s (or $U_{\text{wave,g}} = 765.95$ in dimensionless form) for $Re_\tau = 180$ and 15.577 m/s ($U_{\text{wave,g}} = 3815.55$) for $Re_\tau = 1000$. The values obtained for the convection velocity of the shear stress perturbations agree very well with the estimation $u_{\text{wave,g}} = 10\,u_\tau$ given in the literature [177].

From this analysis it can be followed that the turbulent shear stress structures are more intense but smaller in size (in both streamwise direction and spanwise direction) and lifetime as the Reynolds number is increased. Additionally, the convection speed of the shear stress structures in streamwise direction increases with the Reynolds number. The effect of these phenomena on the evolution of the liquid film is now investigated.

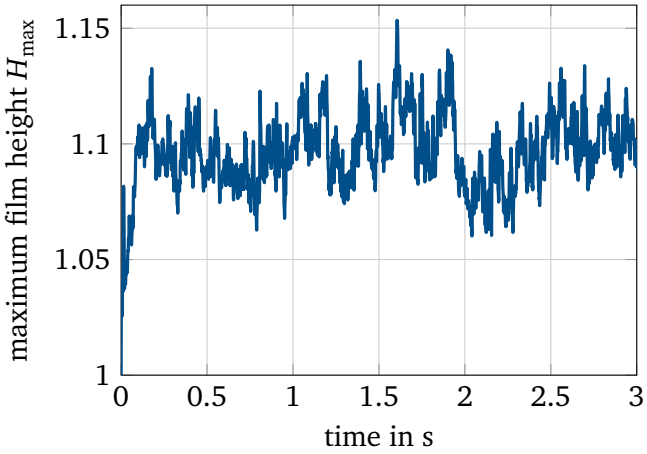

Figure 3.18: Time evolution of the film height maximum for $Re_\tau = 180$ from DNS and LWT.

The development of the maximum non-dimensional film thickness over time for the friction Reynolds number of $Re_\tau = 180$ is given in Fig. 3.18. As one can see, the maximum film thickness initially increases rapidly from the uniform film thickness ($H = 1$). However, after some time, the maximum film height fluctuates around a mean value, which does not change with time. The turbulent shear stress at the interface leads to the development of the film height minima and maxima and, as the shear stress

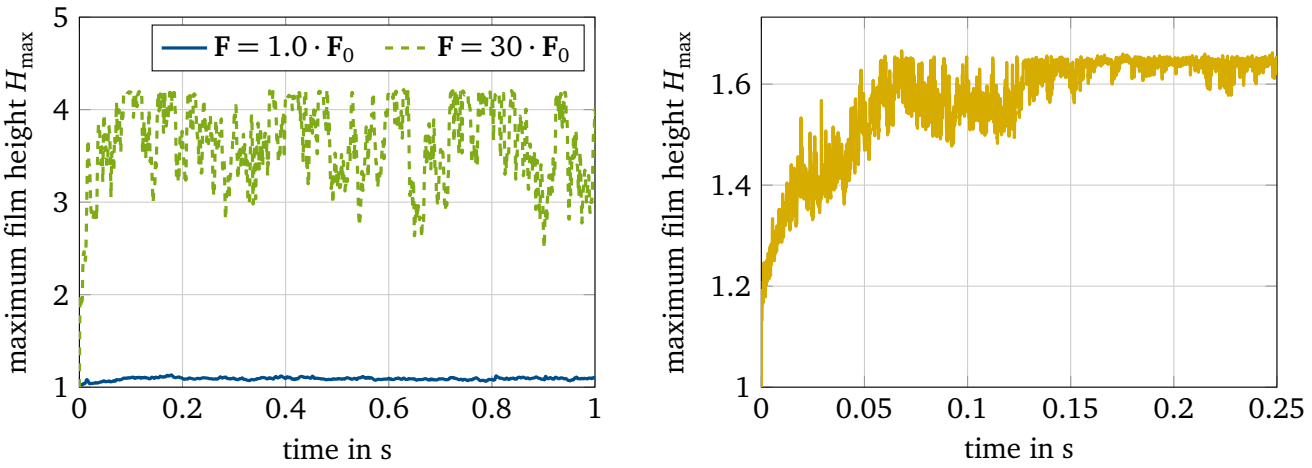

Figure 3.19: Time evolution of the film height maximum for Re_τ = 180 with 30-fold increased shear stress amplitude (left) and Re_τ = 1000 (right) from DNS and LWT.

structures vary with time, the position of the film height maximum changes with time and the magnitude of the maximum film height itself is fluctuating. The constant mean value results from a balance between destabilizing shear stress and stabilizing surface tension and gravity. The observed film height maxima are not very high (below 1.15) so that the film height disturbances are below 15 µm for the investigated film height of $d_l = 100\,\mu m$.

It has been shown earlier in this section that the instantaneous values of the shear stress fluctuations increase by a 30.8-fold factor when the friction Reynolds number is increased from $Re_\tau = 180$ to $Re_\tau = 1000$ (see Tab. 3.1). Consequently, if the influence of the changing length and time scales of the shear stress structures can be ignored (comparable to a RANS approach), a film exposed to a 30-fold increased shear stress field from the DNS with $Re_\tau = 180$ should show the same behavior as a film exposed to the shear stress field from $Re_\tau = 1000$. However, it follows from Fig. 3.19 that this assumption does not hold true. The maximum of the non-dimensional film height from $Re_\tau = 180$ with the shear stress amplitude increased by a 30-fold factor is shown on the left (with a plot of the response to the original shear stress field denoted as $\mathbf{F}_0$ for reference) and the maximum film height for $Re_\tau = 1000$ is given on the right.

It becomes clear that the film deforms very strongly in the left picture for the increased shear stress amplitude. For this set of parameters, film height maxima are observed that are four times higher than the average film height. These high film disturbances develop within the first 0.1 s. It can also be shown that the film is very close to rupture in other areas. It is shown in the right picture of Fig. 3.19, depicting the maximum film height over time for $Re_\tau = 1000$, that the maximum film thickness increases less rapidly and stays much below the values predicted from the left part of Fig. 3.19. The maximum film height increases initially and then again fluctuates around a mean value as, globally, a force balance is achieved. Compared to Fig. 3.18, the maximum film height increases much faster and reaches much higher values for $Re_\tau = 1000$ ($H_{max} \approx 1.65$, corresponding to an disturbance amplitude of 65 µm).

Perrard *et al.* [169] presented a qualitative evaluation for the increase of the film deformation amplitude with time. Starting from a flat interface, three regimes were identified. Initially, the film height amplitude increases very quickly in the so called ballistic response. This is followed by the diffusive response. In

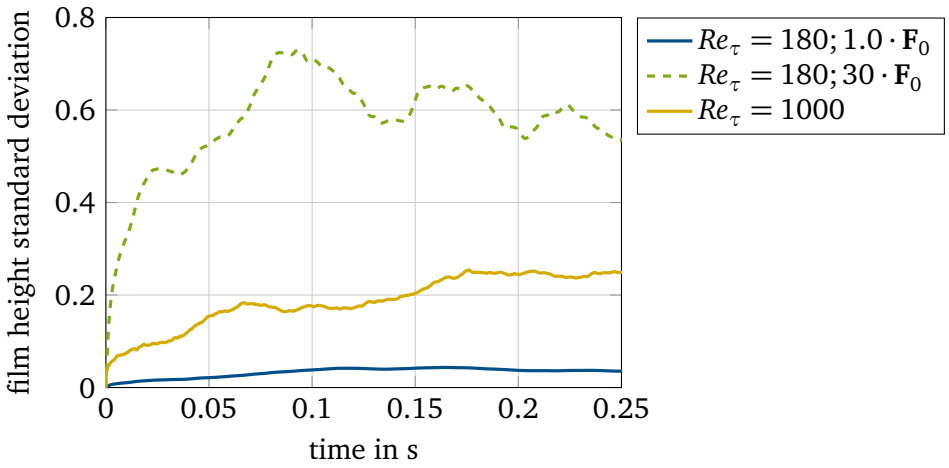

Figure 3.20: Standard deviation of the dimensionless film height over time for the three investigated scenarios from DNS and LWT.

this regime, the film height continues to increase but more slowly than in the first regime. Eventually, an asymptotic limit is reached and the average of film height amplitude over time does not increase anymore. This behavior agrees well with the observation made for both Reynolds numbers in this work.

The standard deviation of the non-dimensional film height can be used as a measure for the increase of the film surface area for a disturbed film (a flat interface having a standard deviation of zero). The interface area is an important quantity for the estimation of heat transport and mass transport from the liquid to the gas phase. As illustrated in Fig. 3.20, the standard deviation initially increases with time for all three investigated scenarios and then tends towards a plateau. The film surface increase is lower for $Re_\tau = 180$ without the enhanced shear stress magnitude than for $Re_\tau = 1000$, which in turn exhibits a lower increase than for $Re_\tau = 180$ with the 30-fold enhanced shear stress magnitude. For $Re_\tau = 1000$, one can observe a maximum of the standard deviation of the film height of about 0.24, which leads to a noticeable increase of the film interface area. The average peak-to-peak amplitude of the film height disturbances is estimated as twice the standard deviation and corresponds to $4.8\,z^+$ (48 µm). Consequently, the assumption that the effect of the film height variation on the turbulent flow field is negligible ($z^+ < 5$) is justified.

Snapshots of the liquid film thickness distribution from interaction with a turbulent gas flow of $Re_\tau = 1000$ for different times can be seen in Fig. 3.21. The initially flat film interface is disturbed by the shear stress, which leads to the development of local film height maxima and minima. These film height disturbances travel downstream. As larger structures are not leveled out as fast as smaller structures and higher film height disturbances travel faster compared to lower disturbances, merging of different film disturbances can be observed with time. From this, streaks in streamwise direction develop. Additionally, an increase of the magnitude of the film height disturbances over time is observed.

The spatial one-time and temporal one-point correlations of the film height distribution (Eqs. (3.68) - (3.70) with $\phi(x, y, t) = H(x, y, t)$) are shown in Fig. 3.22. The correlations are calculated from the state of H after approximately 25 ms. It can be seen that the streamwise correlations only decay to about 0.7 for $Re_\tau = 180$ and 0.45 for $Re_\tau = 1000$, indicating the presence of long coherent regions occupying the entire domain length. By comparing the streamwise correlation of the film height and the shear stress

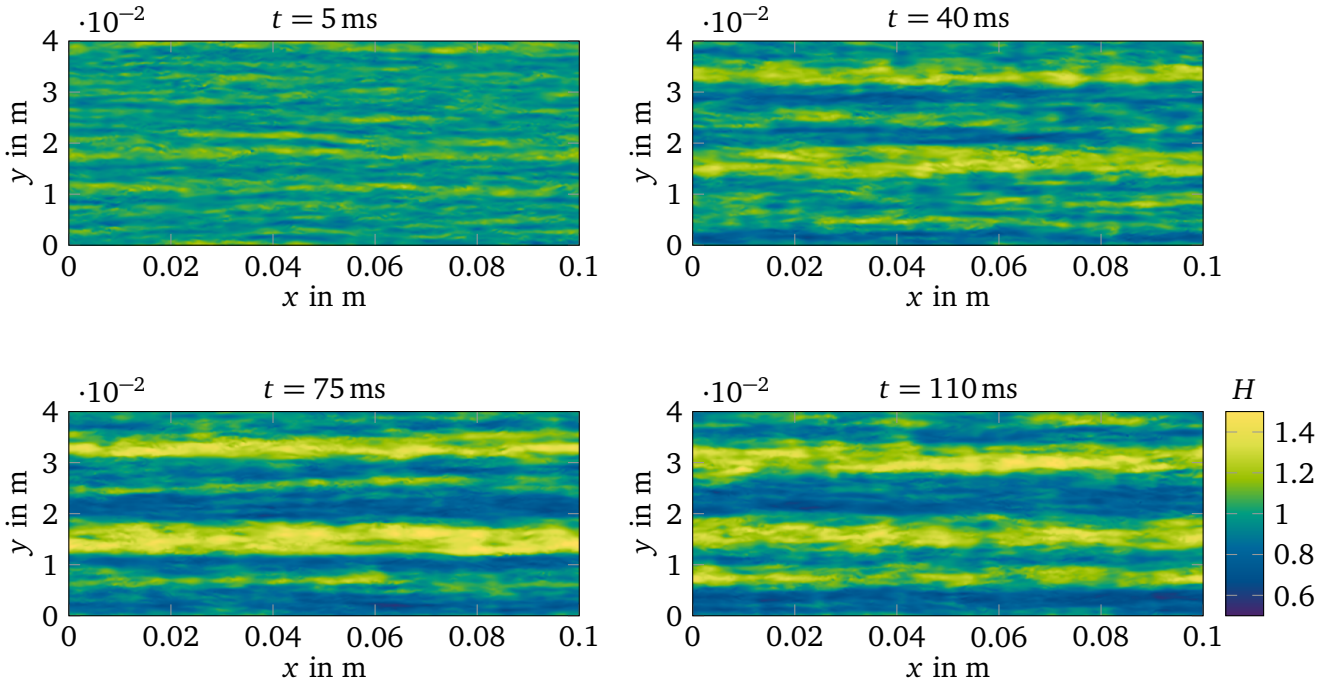

Figure 3.21: Snapshots of the dimensionless film height variation for $Re_\tau = 1000$ at various times from DNS and LWT.

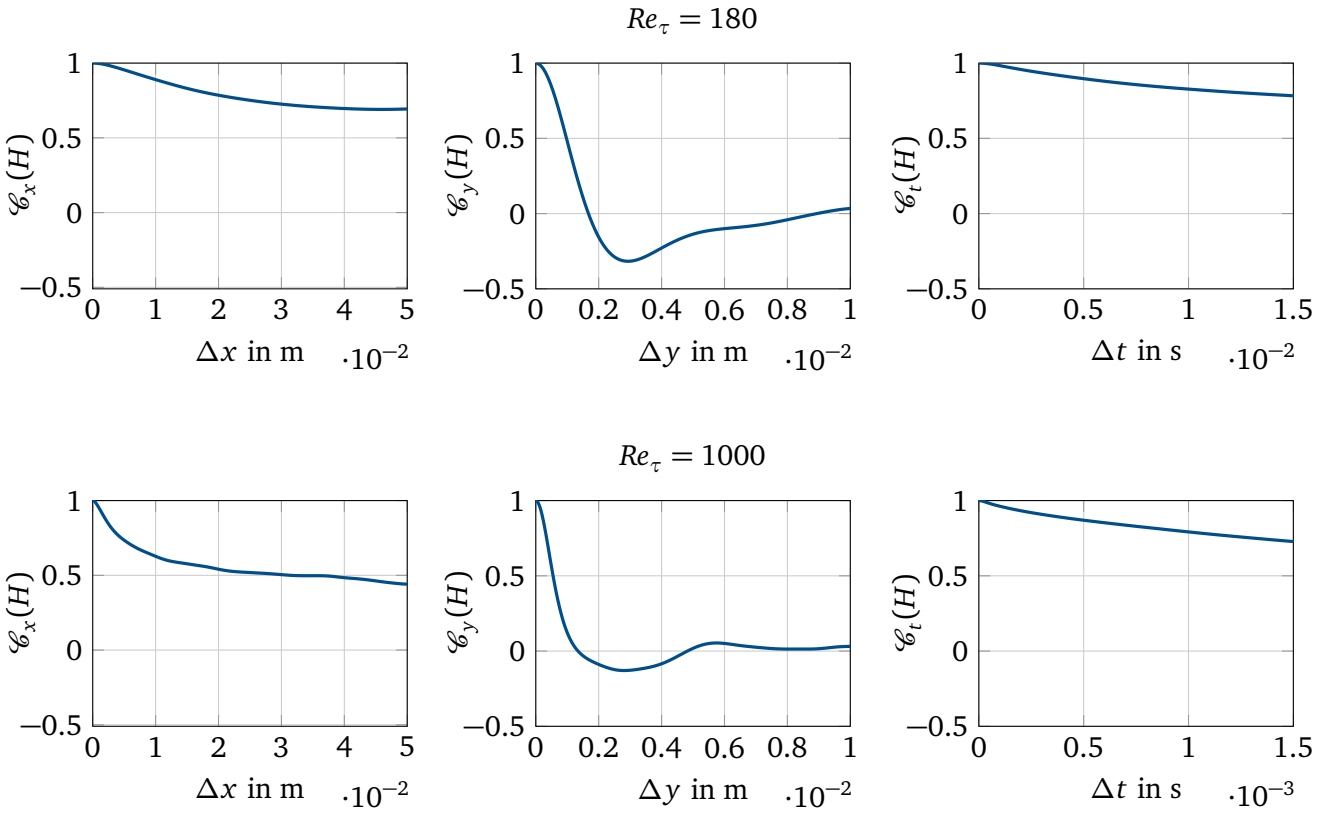

Figure 3.22: Streamwise (left), spanwise (middle), and temporal (right) correlation of the non-dimensional film height H for $Re_\tau = 180$ and $Re_\tau = 1000$ from DNS and LWT.

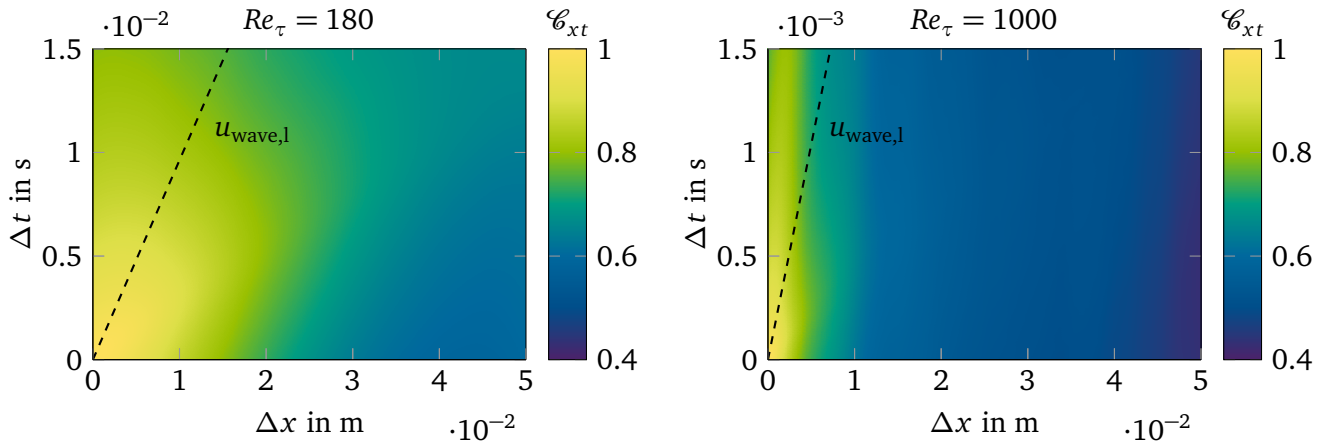

Figure 3.23: Spatiotemporal correlation $\mathscr{C}_{xt}$ of the non-dimensional film height H for Re_τ = 180 (left) and Re_τ = 1000 (right) from DNS and LWT.

(Fig. 3.16), it can be concluded that the structures in the film are much larger in streamwise direction than the structures of the turbulent shear stress. The spanwise correlation, contrarily, decays similarly to the correlation of the turbulent shear stress in Fig. 3.16. It can be seen that the spanwise extent of the film disturbance structures is similar in size for both Reynolds numbers in the developed state of H.

The temporal correlation of the film height decays much more slowly than the temporal correlation of the shear stress for both Reynolds numbers. This shows that the time scale of the film height perturbations is much larger than the time scale of the shear stress structures. By comparing the temporal correlations of the film height for both Reynolds numbers, one can see that the time scale is smaller for the higher Reynolds number of $Re_\tau = 1000$. In summary, it can be concluded from the streamwise and temporal correlations that, as the turbulent shear stress fluctuations are flowing downstream, they leave behind streaks of film height disturbances, which form due to the long lifetime of the film height perturbations. From the spanwise correlation, the wavy structure of the film height distribution is visible, with a negative correlation peak at $y = 2.9\,\text{mm}$ and $y = 2.8\,\text{mm}$ for $Re_\tau = 180$ and $Re_\tau = 1000$, respectively. It should be mentioned that the resulting length scales of the film surface fluctuation obtained from Fig. 3.22 – and in fact also the dominant length scales of the shear stress fluctuation (see Fig. 3.16) – are, for both Reynolds numbers, substantially larger than the film thickness so that the long-wave assumption stays valid.

The spatiotemporal correlation of the film height (Eq. (3.71) with $\phi(x,y,t) = H(x,y,t)$), which is presented in Fig. 3.23, allows an estimate of the convection velocity of the interface structures ($u_{\text{wave,l}}$). The convection velocity of the interface structures is calculated in the same way as the convection velocity of the shear stress structures. It should be noted, however, that there seems to be a wider range of convection velocities (areas with high values of $\mathscr{C}_{xt}$) that are present in the film (Fig. 3.23) compared to the clear convection velocity of the shear stress structures (Fig. 3.17).

The analysis shows that the interface structures travel downstream with a convection velocity of $u_{\text{wave,l}} = 1.039\,\text{m/s}$ ($U_{\text{wave,l}} = 254.45$) at $Re_\tau = 180$ and $u_{\text{wave,l}} = 4.812\,\text{m/s}$ ($U_{\text{wave,l}} = 1178.69$) at $Re_\tau = 1000$. These values are only about one third (33.22 % for $Re_\tau = 180$ and 30.89 % for $Re_\tau = 1000$) of the convection velocity of the shear stress structures (see Fig. 3.17). This is quite interesting, as the film surface speed is predominantly affected by the turbulent shear stress, but still the film height disturbances

show a much lower convection velocity than the turbulent shear stress structures. It is worth noting that, in agreement with the difference in the convection velocities, there is essentially no cross correlation between F_x and H.

A theory for the differences in the observed maximum film heights in Figs. 3.18 and 3.19 can now be developed. As shown in Fig. 3.17, the length and time scales of the wall shear stress reduce considerably when the Reynolds number is increased. This leads to a decrease in the characteristic wavelength of the disturbance on the film surface (see Fig. 3.22). One possible reason for the observed slow growth of the maximum of the film height amplitude is the action of surface tension. As has been shown in section 3.3.2, the surface tension force strongly depends on the curvature, suppressing film thickness fluctuations with shorter wavelength more effectively. Furthermore, it has been shown that the time scale of the turbulent fluctuation, which is proportional to δ_ν/u_τ, decreases with increasing Reynolds number even more strongly than the length scale of the turbulent structures. This suggests that a local shear stress maximum acts on every spot of the interface for a shorter period of time and the resulting film height maxima reduce. It can be concluded that the turbulent shear stress fluctuations with high convection velocity or small length scales do not influence the film as strongly as other shear stress fluctuations.

3.4.3 Linear Analysis of Turbulent Shear-Driven Liquid Films

In order to explicate the influence of the length and time scales of the turbulent gas flow on the film further, a linear stability analysis of a shear-driven film is performed. For this analysis, an infinitely extended liquid film resting on a planar wall is considered. To simplify the analysis, the problem is assumed to be two-dimensional so that the local film height h (average film height d_l) is only a function of the spatial coordinate x and time t. A fluctuating interfacial shear stress is subjected on the film. Employing the non-dimensionalizations introduced in section 3.4.1 and assuming that the interfacial shear stress has the form of a traveling wave, it can be written in the following non-dimensional form

$$F(X,\tau) = \overline{F}\left\{1 + A\exp\left[i\left(KX - \Omega\tau\right)\right]\right\} = \overline{F}\left\{1 + A\exp\left[iK\left(X - U_\mathrm{wave}\,\tau\right)\right]\right\}, \tag{3.73}$$

with the average shear stress $\overline{F}$, the relative amplitude of the shear stress fluctuations $A \ll 1$, the non-dimensional wavenumber $K = k_\mathrm{wave}\, d_\mathrm{l}/\epsilon$, the non-dimensional frequency $\Omega = \omega\, d_\mathrm{l}^2/(\epsilon\ \nu_\mathrm{l})$, and the non-dimensional wave speed $U_\mathrm{wave} = u_\mathrm{wave}\, d_\mathrm{l}/\nu_\mathrm{l}$. Additionally, k_wave, ω, and u_wave are the dimensional wavenumber, frequency, and speed, respectively. U_wave corresponds to the convective velocity of the shear stress.

The evolution equation (3.67) simplifies to the following form for a two-dimensional problem

$$\frac{\partial H}{\partial \tau} + \frac{\partial}{\partial X}\left(\widetilde{S}H^3\frac{\partial^3 H}{\partial X^3} + \frac{\widetilde{G}}{3}H^3\frac{\partial H}{\partial X} + \frac{1}{2}H^2 F\right) = 0\,. \tag{3.74}$$

The small parameter A is used to expand the solution of the one-dimensional evolution equation (3.74) in a series, which, utilizing that the film height fluctuates around unity, follows as

$$H(X,\tau) = 1 + AH_1(X,\tau) + A^2 H_2(X,\tau) + \dots . \tag{3.75}$$

This solution form of the non-dimensional film height is substituted into the evolution equation (3.74) together with the expected traveling wave form of the shear stress given in Eq. (3.73). Each term of the resulting equation is developed in series of the small parameter A ($\mathcal{O}(0), \mathcal{O}(A), \mathcal{O}(A^2), \dots$). Terms of order A^2 or higher are neglected to obtain the following equation for the first order of the non-dimensional film height $H_1(X,\tau)$:

$$\frac{\partial H_1}{\partial \tau} + \widetilde{S}\frac{\partial^4 H_1}{\partial X^4} + \frac{\widetilde{G}}{3}\frac{\partial^2 H_1}{\partial X^2} + \overline{F}\frac{\partial H_1}{\partial X} + \frac{1}{2}\overline{F}\, iK \exp\left[iK\left(X - U_{\text{wave}}\,\tau\right)\right] = 0 . \tag{3.76}$$

This equation is a linear non-homogeneous differential equation, which can be solved analytically. The resulting solution has the form of a traveling wave and reads

$$H_1(X,\tau) = \frac{\overline{F}}{2}\left[\left(\widetilde{S}K^3 + \frac{\widetilde{G}K}{3}\right)^2 + \left(U_{\text{wave}} - \overline{F}\right)^2\right]^{-\frac{1}{2}} \exp\left\{i\left[K\left(X - U_{\text{wave}}\,\tau\right) + \arctan\frac{3\widetilde{S}K^3 + \widetilde{G}K}{3\left(U_{\text{wave}} - \overline{F}\right)}\right]\right\} . \tag{3.77}$$

From this equation, a shift in the phase of the wave of the liquid film compared to the wave-like fluctuations of the shear stress can be identified.

Additionally, from Eq. (3.77), the amplitude B of the film thickness fluctuations in the first order is found as

$$B = \frac{A\overline{F}}{2}\left[\left(\widetilde{S}K^3 + \frac{\widetilde{G}K}{3}\right)^2 + \left(U_{\text{wave}} - \overline{F}\right)^2\right]^{-\frac{1}{2}} . \tag{3.78}$$

Using this analysis, the governing parameters for the influence of the fluctuating shear stress on the film evolution can be found. It follows directly from Eq. (3.78) that the maximum amplitude of the film height deformation B corresponds to fluctuations for which the sum of the terms inside the square brackets is minimal. The first term inside the square brackets shows that surface tension $\widetilde{S}$ and gravity $\widetilde{G}$ suppress film fluctuations, as expected. This influence is dependent on the wavenumber K, with fluctuations of higher wavenumber, or decreasing wavelength, being suppressed more effectively.

However, for the investigated Reynolds numbers of the gas phase and the chosen film parameters, the resulting wavenumbers of the film lead to the first term in the square brackets in Eq. (3.78) being $\mathcal{O}(10^{-3})$

and $\mathcal{O}(1)$ for $Re_\tau = 180$ and $Re_\tau = 1000$, respectively. As can bee seen in Tab. 3.1, the average streamwise shear stress component $\overline{F}_x$ is $\mathcal{O}(10)$ for $Re_\tau = 180$ and $\mathcal{O}(10^3)$ for $Re_\tau = 1000$. It can be concluded from this estimation that the second term in the square brackets in Eq. (3.78) is generally much larger than the first term and that the maximum film deformation can be found when this second term is minimized.

Consequently, the maximal amplitude of the film deformations corresponds to the fluctuations that satisfy $U_{\text{wave}} = \overline{F}$. These fluctuations are traveling with the velocity

$$u^*_{\text{wave}} = \frac{\overline{\tau}_{\text{int}}\, d_{\text{l}}}{\mu_l} = u_{\text{int}}\,, \tag{3.79}$$

where u_{int} is the velocity of the free surface of the liquid.

To summarize, the amplitude of the waves of the film height deviations depend primarily on the difference between the shear stress wave propagation and the velocity of the film surface. If one now further assumes for simplification that the amplitude of the fluctuating shear stress, which propagates with $U_{\text{wave,g}}$, is comparable with $F_{x,\text{rms}}$, the amplitudes of the film thickness distributions can be approximately predicted from the DNS results. Using the wave propagation velocities $U_{\text{wave,g}}$ from Fig. 3.17 and the DNS results summarized in Tab. 3.1, the ratio of the amplitudes of the film thickness fluctuation for $Re_\tau = 180$ ($B_{Re_\tau=180}$) and $Re_\tau = 1000$ ($B_{Re_\tau=1000}$) can be estimated as

$$\begin{aligned}\frac{B_{Re_\tau=1000}}{B_{Re_\tau=180}} \approx \left(\frac{A\overline{F}}{U_{\text{wave}} - \overline{F}}\right)_{Re_\tau=1000} \left(\frac{U_{\text{wave}} - \overline{F}}{A\overline{F}}\right)_{Re_\tau=180} \approx \\ \left(\frac{F_{x,\text{rms}}}{U_{\text{wave,g}} - \overline{F}_x}\right)_{Re_\tau=1000} \left(\frac{U_{\text{wave,g}} - \overline{F}_x}{F_{x,\text{rms}}}\right)_{Re_\tau=180} \approx 6.75\,.\end{aligned} \tag{3.80}$$

The value obtained from this approximate analysis is much smaller than the ratio of the values of the average wall shear stress in x-direction for $Re_\tau = 1000$ and $Re_\tau = 180$ ($\overline{F}_{x,Re_\tau=1000}/\overline{F}_{x,Re_\tau=180} \approx 30.8$) or the ratio of the root mean square of the streamwise component of the wall shear stress ($\mathrm{F}_{x,\text{rms},Re_\tau=1000}/F_{x,\text{rms},Re_\tau=180} \approx 31.3$). If one looks at the actual ratio of the maximum film height deviation, which can be obtained by dividing the quasi steady state film height amplitude from Fig. 3.18 and Fig. 3.19 (right) one obtains

$$\frac{\overline{H}_{\text{max},Re_\tau=1000} - 1}{\overline{H}_{\text{max},Re_\tau=180} - 1} \approx 6.59\,.$$

It can be seen that this value is reasonably close to the value obtained from Eq. (3.80), which indicates that this equation can be used to get an *a priori* estimation of the expected film height amplitudes utilizing only the wall shear stress statistics and its propagation velocity. Obviously, this can only lead to an approximate first guess for the film height amplitudes, but it is expected to be superior to an estimation based solely on the average streamwise shear stress.

However, as shown in the state of the art and in section 3.4.2, the fluctuating wall shear stress of a turbulent gas flow cannot be properly represented in the form of a single propagating wave. Instead, one can think of it as a superposition of numerous different waves with varying amplitudes, frequencies, and propagating velocities. The components of the turbulent shear stress possessing propagation velocities similar to the velocity of the film surface velocity lead to film thickness fluctuations with higher amplitude than components with faster or slower velocity, assuming all components of the turbulent shear stress possess the same amplitude. This can explain the earlier result that the dominant velocity of the disturbances of the film thickness is much smaller (or much closer to $\overline{F}_x$, as shown above) than the convection velocity of the turbulent shear stress structures.

The results of the DNS and LWT calculations and of the simplified linear analysis show that the dynamics of a thin liquid film, which is sheared by a turbulent gas flow, is not only determined by the average shear stress amplitude at the liquid-gas interface. The absolute values of the fluctuating turbulent shear stress, as well as the spatial and temporal scales of the fluctuations and their propagation velocity have to be considered. This means that classical RANS approaches, which do not resolve the turbulent shear stress, cannot be used to accurately simulate the turbulent two-phase flows considered here. LES could be suitable for the description of a thin liquid film sheared by a turbulent gas flow if the filtering limit is chosen such that those turbulent fluctuations, which have a strong influence on the liquid film, are resolved. Compared to DNS, a substantial reduction in computational costs could be achieved in this case. This approach is considered and analyzed in the following section.

3.4.4 Large Eddy Simulation and Long-Wave Theory

The LES is carried out for the double-periodic gas channel using the open-source CFD program OpenFOAM [110]. The wall-adapting local eddy viscosity (WALE) model [156] is used to determine the subgrid stress tensor. This model is more accurate at the wall compared to classical eddy viscosity approaches. The simulations are carried out for the same Reynolds numbers as in the DNS calculations and the shear stress at the lower wall is again stored with a high frequency to be used as the time-dependent boundary condition of the LWT simulation. Each simulation is run until a fully developed turbulent velocity profile is achieved, before the shear stress data are stored. The mesh is graded so that the mesh size reduces towards the two walls. Additionally, cells in the bottom eighth of the domain are split in half in each of the three dimensions to refine the mesh further at the lower wall. This means that, contrary to the DNS, the grid size in x- and y-direction is not uniform in the LES setup, to reduce the number of cells.

Table 3.2: Parameters of the numerical configuration of DNS and LES for Re_τ = 180 and Re_τ = 1000.

		Grid size				Resolution at the wall		
		$N_{x,\min}$	$N_{y,\min}$	N_z	number of cells	Δx^+	Δy^+	Δz^+
$Re_\tau = 180$	DNS	256	256	201	$13.173 \cdot 10^6$	7.03	2.81	0.02
	LES	500	200	49	$2.575 \cdot 10^6$	3.60	3.60	1.79
$Re_\tau = 1000$	DNS	1024	768	385	$302.776 \cdot 10^6$	9.77	5.21	0.03
	LES	500	200	49	$2.575 \cdot 10^6$	20	20	9.95

The resulting grid sizes and resolutions are given in Tab. 3.2 for the DNS and LES. It is evident that the total number of cells of the LES is lower than for the DNS for both Reynolds numbers, which directly translates into a much decreased simulation time. Additionally, the mesh is refined for the higher Reynolds number situation in the DNS but not for the LES. This is done in an attempt to further reduce the simulation time, especially for the computationally costly high Reynolds number situation. However, through the refinement of the cells at the lower wall, a good resolution of the stored shear stress field can be achieved in the LES for both Reynolds numbers in x- and y-direction.

The grid has been chosen such that these resolutions resemble typical values for a LES for the higher Reynolds number. The same grid was then also used for $Re_\tau = 180$. The resolution in z-direction is two orders of magnitude coarser in the LES compared to the DNS, which might affect the calculation of the velocity gradient and the resulting shear stress. The grid size at the bottom wall is chosen also as the grid size of the LWT calculations for both DNS and LES. This means that for $Re_\tau = 1000$ the computational effort of the LWT calculation is extensively decreased in the LES case compared to the DNS.

Selected flow parameters of the LES can be found in Tab. 3.3. Compared to the DNS results shown in Tab. 3.1, the average values of the non-dimensional shear stress from the LES are about 15.7 % lower for $Re_\tau = 180$ and 29.9 % lower for $Re_\tau = 1000$. The root mean squares of the streamwise shear stress component decrease in a similar manner, while the root mean square of the spanwise shear stress decreases by 24.2 % and 56.5 % for $Re_\tau = 180$ and $Re_\tau = 1000$, respectively. The much coarser resolution

in wall-normal direction (z-direction) in the LES, might result in an inaccurate calculation of the velocity gradients and, consequently, of the shear stress components.

Table 3.3: Results of the LES.

Re_τ	Re	u_τ in m/s	δ_ν in m	$\overline{F}_x$	$F_{x,\mathrm{rms}}$	$\overline{F}_y$	$F_{y,\mathrm{rms}}$
180	5668	0.313	$5.556 \cdot 10^{-5}$	8.560	9.105	$-1.689 \cdot 10^{-2}$	1.496
1000	40007	1.736	$1.000 \cdot 10^{-5}$	219.172	234.606	0.355	35.783

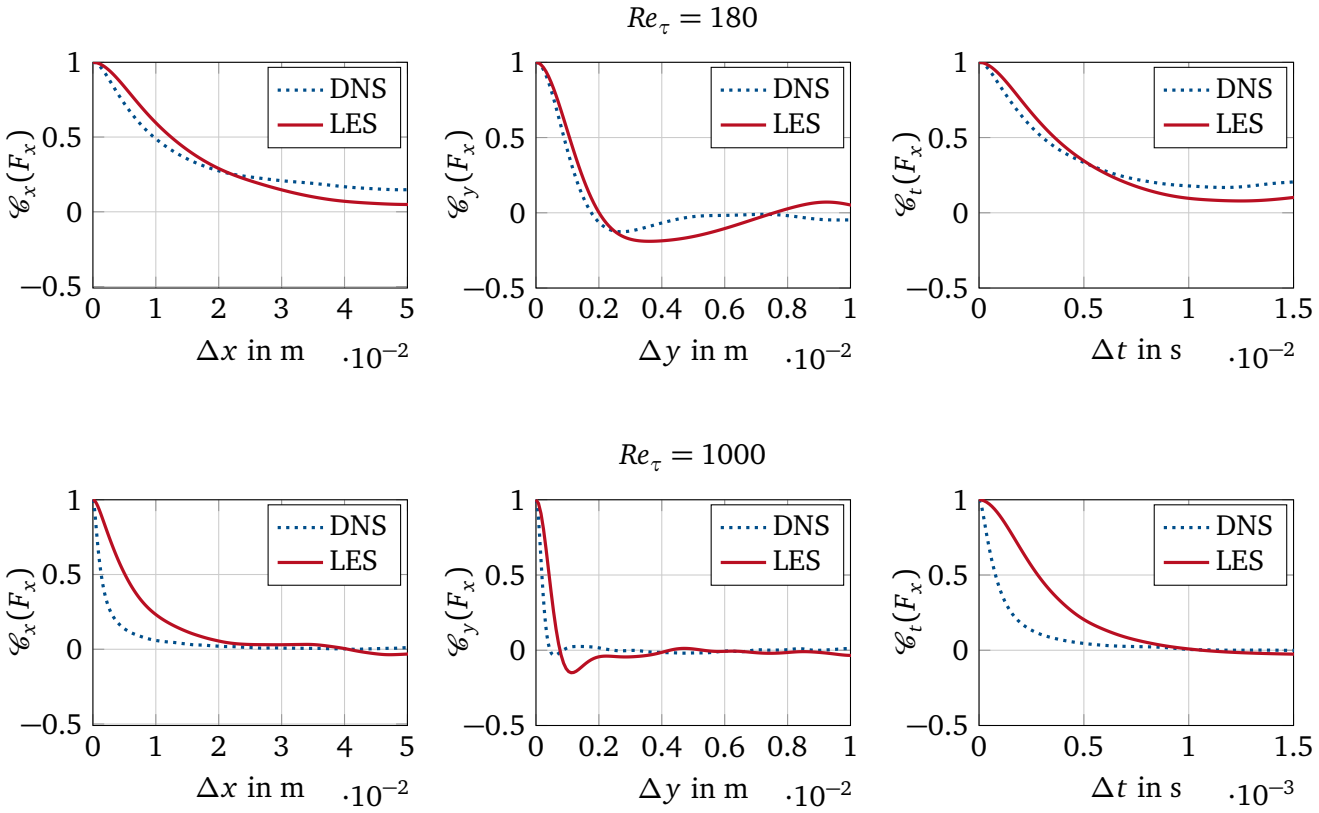

Figure 3.24: Streamwise (left), spanwise (middle), and temporal (right) correlation of the streamwise shear stress component F_x for $Re_\tau = 180$ and $Re_\tau = 1000$ from the LES compared to the DNS.

However, despite the inaccuracies of the shear stress data from the LES, the spatial one-time and temporal one-point correlations of the streamwise shear stress component of the LES, which are depicted in Fig. 3.24, agree well with the correlation data of the DNS (from Fig. 3.16). For $Re_\tau = 180$, the streamwise, spanwise, and temporal correlation plots of DNS and LES are very similar. Small differences in the slope can only be observed for larger values of Δx, Δy, and Δt, which shows that the length scales and time scales of the shear stress structures agree very well. The correlations also match well for $Re_\tau = 1000$. A slower decrease of the streamwise one-time correlation function can be found for the LES, which indicates that the streamwise structures are slightly larger in this case. Similarly, the temporal correlation of the LES also decays slower than for the DNS. These differences might result from the lower resolution in streamwise direction in the LES.

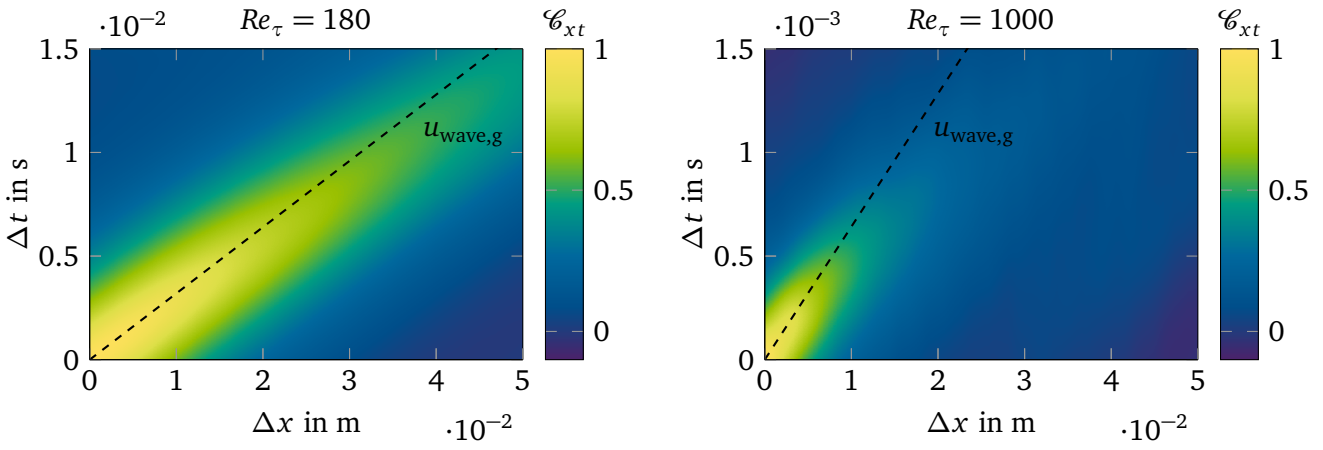

Figure 3.25: Spatiotemporal correlation $\mathscr{C}_{xt}$ of the streamwise shear stress component F_x for $Re_\tau = 180$ (left) and $Re_\tau = 1000$ (right) from the LES.

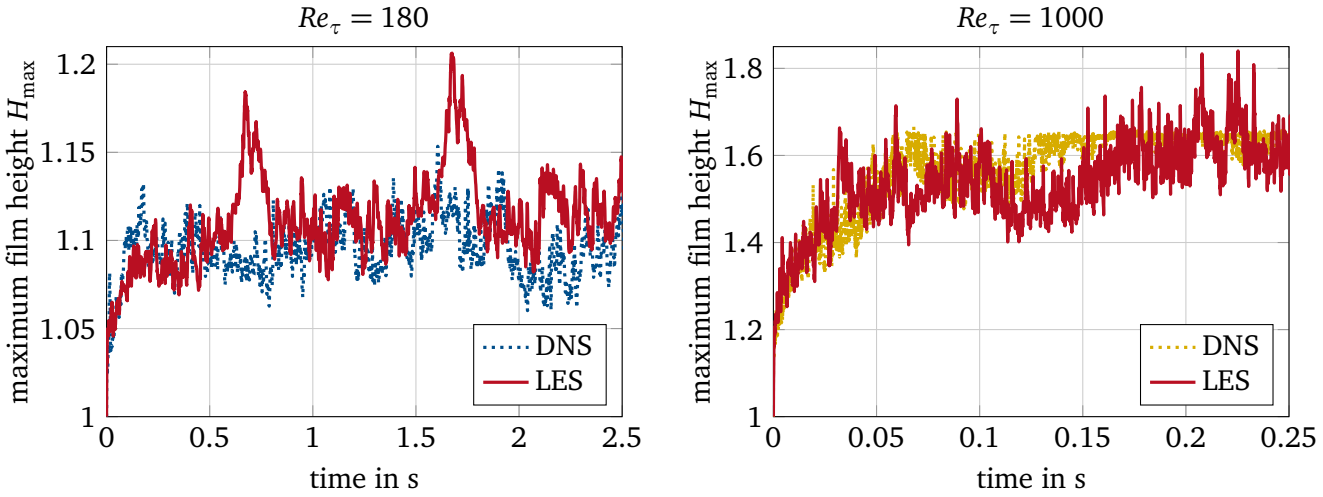

Figure 3.26: Time evolution of the film height maximum for $Re_\tau = 180$ (left) and $Re_\tau = 1000$ (right) with DNS and LES.

The spatiotemporal correlation of the horizontal shear stress is depicted in Fig. 3.25. The dashed line marks the convection velocity obtained from the DNS calculations (see Fig. 3.17). The convection velocity of the DNS results agrees very well with the spatiotemporal correlation of the LES results. This means that the velocity of the shear stress structures, which is an important factor, as shown in the linear analysis in section 3.4.3, is correctly represented in the LES. Compared to the DNS, there is a wider distribution of the velocity around the average value in the LES.

The evolution of the maximum non-dimensional film height over time for $Re_\tau = 180$ (on the left) and $Re_\tau = 1000$ (on the right) is presented in Fig. 3.26. For both Reynolds numbers, both the initial slope of the maximum film height growth and the quasi steady state value obtained for the maximum film height agree very well between the DNS and LES calculations. Differences can be observed in the fluctuations around the mean value for both Reynolds numbers. This is expected, as the turbulent gas flow is a statistical process and the exact location and size of the individual shear stress structures vary between the simulations. It is somewhat surprising that, despite the shortcomings of the LES in predicting the correct average shear stress and some of the length scales and time scales, the response of the maximum height

of the liquid film to the turbulent flow can be captured so well with the LES. A possible explanation for this phenomenon was already given in section 3.4.3, where it was stated that the shear stress structures, which travel with the velocity of the film interface velocity are most important for the response of the liquid film to the turbulent flow. If these structures have been correctly resolved in the LES, shortcomings in the resolution of other turbulent structures do not play an important role for the film evolution. The estimation of the ratio of the amplitudes of the film thickness fluctuations from Eq. (3.80) based on the LES results leads $B_{Re_\tau=1000}/B_{Re_\tau=180} \approx 5.43$, which is still well within 20 % of the numerically calculated ratio of the maximum film height deviation ($(\overline{H}_{\max,Re_\tau=1000}-1)/(\overline{H}_{\max,Re_\tau=180}-1) \approx 6.59$).

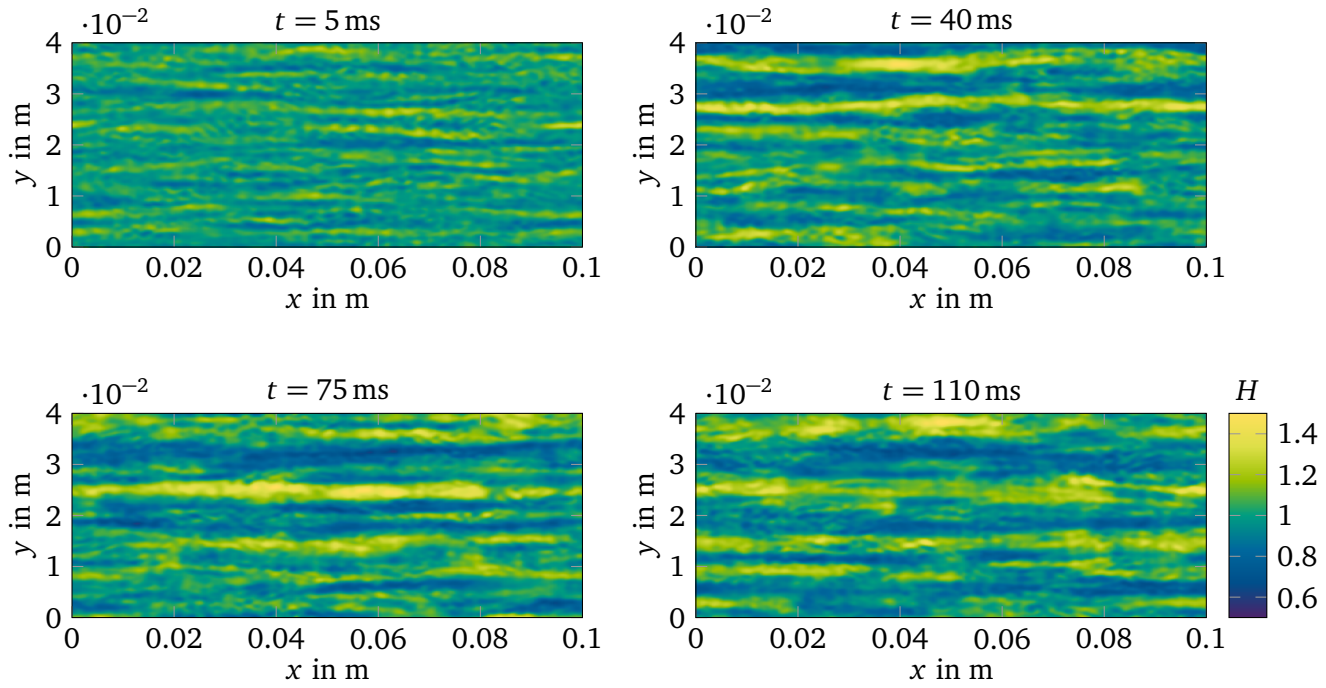

Figure 3.27: Snapshots of the dimensionless film height variation for Re_τ = 1000 at various times from LES and LWT.

This finding is further supported by looking at the snapshots of the dimensionless film height for $Re_\tau = 1000$ for different times in Fig. 3.27. The initially flat film is disturbed by the turbulent shear stress and develops maxima and minima. With increasing time, these film deformations merge as they travel downstream and form larger streaks. Again, these results look quite similar to the snapshots from the DNS calculations (see Fig. 3.21). The streaks evolving from the DNS seem to be a little longer in streamwise direction. This claim is supported by the spatial one-time correlations and the temporal one-point correlation of the non-dimensional film height from the LES given in Fig. 3.28. It is evident from the decay of the streamwise correlation function that the film height structures in streamwise direction are larger for the shear stress data from the DNS (slower decay of the correlation) than for the LES case. This could result from the numerical grid used in the LES. As discussed above, in the LES the grid is the same for both Reynolds numbers, despite the fact that a grid refinement is usually necessary if the Reynolds number is increased.

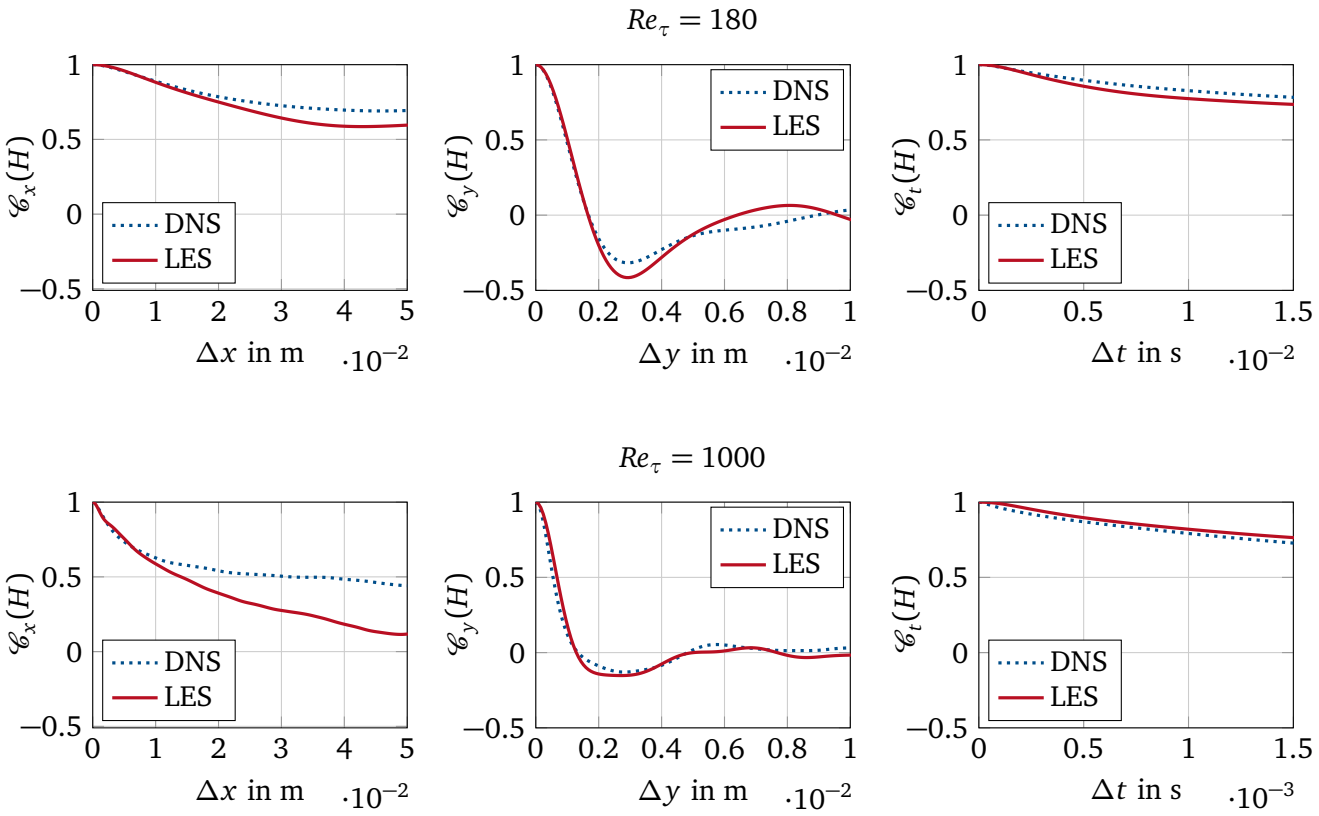

Figure 3.28: Streamwise (left), spanwise (middle), and temporal (right) correlation of the non-dimensional film height H for $Re_\tau = 180$ and $Re_\tau = 1000$ from LES and LWT compared to DNS and LWT.

Consequently, the effect of the numerical resolution can be investigated implicitly by comparing the simulations for the two Reynolds numbers. As the statistics for $Re_\tau = 180$ resemble the DNS values considerably better than for $Re_\tau = 1000$, an influence of the resolution on the results can be expected. A LES for $Re_\tau = 1000$ with a slightly finer grid would potentially lead to results closer to those obtained using the DNS. However, it is also possible that the deduced length scales of the film disturbance structures depend on the instantaneous shear stress values at the moment at which the film is analyzed. This is supported by the fact that the breaking of the large streaks and the formation of new structures can be observed both in the snapshots from the DNS (Fig. 3.21) and from the LES (Fig. 3.27) from 75 ms to 110 ms. A larger number of simulations for both the DNS and LES with different grid sizes and a statistical analysis would be necessary to shed more light on this issue. The spanwise correlation functions and the temporal correlation for both DNS and LES agree very well with each other for both Reynolds numbers. This shows that the width of the film height structures and their lifetime is captured very well in the LES.

Lastly, the spatiotemporal correlation of the non-dimensional film height based on the shear stress data from the LES results is given in Fig. 3.29. The dashed line corresponds to the convection velocity of the film disturbances calculated from the DNS results in section 3.4.2 (Fig. 3.23). It can be seen that the spatiotemporal correlations based on the DNS and LES look very similar to each other. Only for $Re_\tau = 1000$, the correlation function decreases slightly faster for increasing Δx in the LES case in accordance with the findings of the reduced length scale in streamwise direction (see Fig. 3.28).

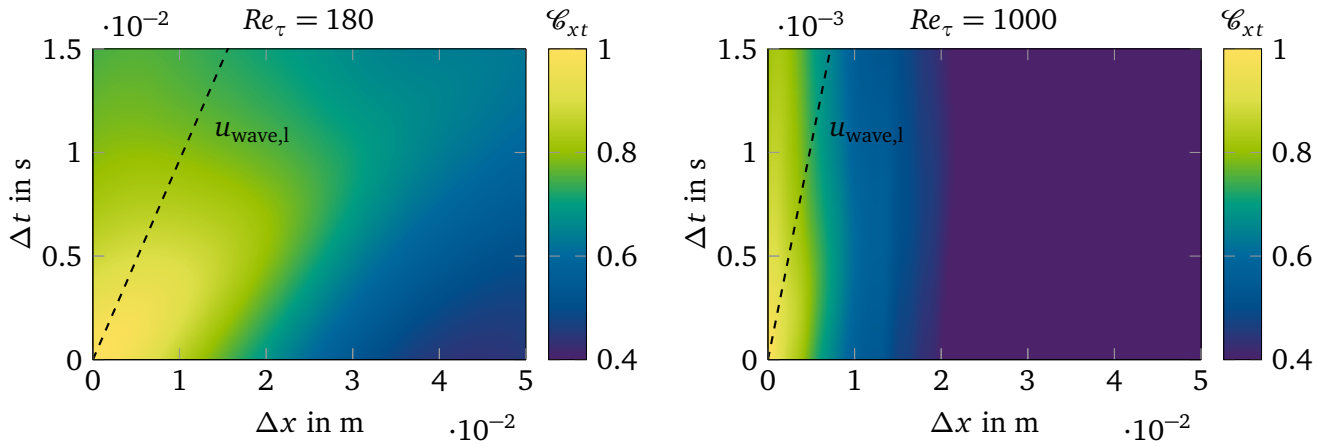

Figure 3.29: Spatiotemporal correlation $\mathscr{C}_{xt}$ of the non-dimensional film height H for Re_τ = 180 (left) and Re_τ = 1000 (right) from LES and LWT.

Additionally, the convection velocity from the DNS represents the correlation very well, indicating that the wave speed of the film height disturbances for DNS and LES are comparable.

The results of this section agree qualitatively with the experimental investigations mentioned in section 2.1.3, which show that the frequency and velocity of film height disturbances increase when the Reynolds number of the gas flow is increased [10, 23, 231]. However, since the flow regime maps obtained for falling films cannot be used for horizontal films [115] and flow regime maps cannot be transferred from different fluids, a quantitative comparison with experimental investigations is difficult. Moreover, film disturbances induced by the specific experimental setup cannot easily be identified and distinguished from the influence of the shear stress.

In summary, it was shown in this section that LES can be used instead of DNS for the simulation of the turbulent gas flow to substantially reduce the computational cost both for the gas and for the liquid simulations due to the decreased spatial resolution. Despite the resulting shortcomings in the turbulent shear stress fluctuations from the LES, there was no fundamental change in the evolution of the liquid film. In fact, the evolution of the liquid film could be calculated very well from the LES results. However, it seems that the results of the LES agree better with the DNS for $Re_\tau = 180$ than for $Re_\tau = 1000$, which indicates that the grid resolution of the LES has to be chosen carefully and fine enough to resolve all important shear stress structures.

3.5 Conclusions for Stage I

It was shown in chapter 1 that the complex process of multi-component films and drops evaporating and depositing on heated structured walls can be separated into two stages for the industrial applications considered in this thesis. The first stage of the problem consists of a thin liquid film on a substrate, which is affected by various physical-chemical processes. In this chapter, models for investigation of the film evolution and breakup for evaporating films on structured walls, films with chemical reactions, and films sheared by a turbulent gas flow were derived. LWT was used to solve the evolution equations for these scenarios. It was shown that all the phenomena considered in this chapter are, in fact, the key influencing

processes and, thus, have an important influence on the film evolution and breakup. Furthermore, there are complex interactions between the different phenomena. Their respective importance for the film evolution can be determined from solving the evolution equations for the individual relevant setups and ambient conditions. Therefore, LWT has proven to be a very suitable method to investigate the first stage of the technical problem and to deduce critical situations and parameter values, which will lead to film instability and breakup and, consequently, deposit formation at the then formed contact lines.

Chapter 4

Evaporation of Two-Component Drops and Deposit Formation

In this chapter, the second stage of the process described in section 1.2 is investigated. The liquid film has ruptured and formed pinned drops on the substrate, which evaporate and leave behind deposits. Some of the derivations, discussions, and results given in this section have been published by Bender *et al.* in [30].

4.1 The Arbitrary Lagrangian-Eulerian Method and its COMSOL Multiphysics Implementation

The process considered in this chapter is strongly influenced by the temperature and concentration values at the liquid-gas interface. Consequently, an interface resolving method with a sharp representation of the interface is needed. In this work, the arbitrary Lagrangian-Eulerian (ALE) method is used, which is a moving mesh interface tracking method [233]. This method was developed to combine the advantages of the Lagrangian and Eulerian descriptions [65]. In the classical Eulerian description, which is widely used for CFD, the mesh is fixed and the fluid moves with respect to the computational grid. With this approach, large deformations of the fluid can be computed, but the resolution of flow details and interfaces suffers. In the Lagrangian description, each node of the computational grid follows a fluid particle during the fluid motion, which has the advantage of an easy and accurate tracking of interfaces but at the cost of not being able to follow large distortions of the computational domain (for large fluid motion) without frequently remeshing the geometry. The associated coordinate systems (also referred to as frames) are the spatial and material systems, with the coordinates $\mathbf{x}$ and $\mathbf{x}_{\mathrm{mat}}$, respectively.

The basic idea of ALE is to introduce a third coordinate system, the so called mesh frame (coordinates $\mathbf{x}_{\mathrm{mesh}}$), which is defined independently from the other frames and defines the position of the mesh nodes [105]. Using this approach, it becomes possible to move the mesh nodes with the fluid flow as in a Lagrangian description, to keep the mesh fixed in time (Eulerian description) or to move the mesh based on another arbitrarily defined rule. This allows dividing the domain into areas with different descriptions to utilize the respective strengths as desired. Consequently, the interface can be resolved very finely and a

sharp interface representation can be achieved, without the need to use the Lagrangian description for the entire domain.

The governing equations in the ALE framework can be derived utilizing the so called convection velocity $\mathbf{u}_\mathrm{c}$ defined as

$$\mathbf{u}_\mathrm{c} = \mathbf{u} - \mathbf{u}_\mathrm{mesh} = \left.\frac{\partial \mathbf{x}}{\partial t}\right|_{\mathbf{x}_\mathrm{mat}} - \left.\frac{\partial \mathbf{x}}{\partial t}\right|_{\mathbf{x}_\mathrm{mesh}}, \tag{4.1}$$

with the velocity vector of the mesh $\mathbf{u}_\mathrm{mesh} = \mathbf{u}_\mathrm{mesh}(\mathbf{x}_\mathrm{mesh}, t)$ and the velocity vector of the material $\mathbf{u} = \mathbf{u}(\mathbf{x}_\mathrm{mat}, t)$. Using this definition, the governing equations for mass, momentum, energy, and species concentration can be written similarly to section 3.1.1 with replacing the velocity in the convective terms with $\mathbf{u}_\mathrm{c}$ and evaluating the time derivative with the mesh coordinate held fixed

$$\nabla \cdot \mathbf{u} = 0\,, \tag{4.2}$$

$$\rho \left[\left.\frac{\partial \mathbf{u}}{\partial t}\right|_{\mathbf{x}_\mathrm{mesh}} + (\mathbf{u}_\mathrm{c} \cdot \nabla)\,\mathbf{u} \right] = \rho\,\mathbf{g} + \nabla \cdot \mathbf{T}\,, \tag{4.3}$$

$$\left.\frac{\partial \left(\rho\, c_p\, T\right)}{\partial t}\right|_{\mathbf{x}_\mathrm{mesh}} + \nabla \cdot \left(\mathbf{u}_\mathrm{c}\, \rho\, c_p\, T\right) = \nabla \cdot (k\, \nabla T) + \Sigma_\mathrm{e}\,, \tag{4.4}$$

$$\left.\frac{\partial \xi}{\partial t}\right|_{\mathbf{x}_\mathrm{mesh}} + \nabla \cdot (\mathbf{u}_\mathrm{c}\, \xi) = \nabla \cdot (D_\mathrm{bin}\, \nabla \xi) + \Sigma_{\xi,\mathrm{ls}}\,. \tag{4.5}$$

In the above, $\Sigma_\mathrm{e} = \Sigma_\mathrm{e,lv} + \Sigma_\mathrm{e,ls}$ accounts for source terms due to evaporation (evaporative cooling) $\Sigma_\mathrm{e,lv}$ and deposition $\Sigma_\mathrm{e,ls}$ in the energy equation (with one energy equation solved for the liquid and the gas phase), while $\Sigma_{\xi,\mathrm{ls}}$ accounts for source terms due to deposit formation in the species transport equations. This methodology introduces the convection velocity $\mathbf{u}_\mathrm{c}$ as an additional degree of freedom if the mesh velocity is not prescribed explicitly. In the moving mesh framework, an additional equation for the mesh displacement is solved, which yields a smooth mesh deformation and a steady mesh velocity. In this work, a Yeoh smoothing method [240] is used to smoothly deform the mesh by utilizing constraints for the mesh displacement or mesh velocity at the domain boundaries. If the mesh movement at the boundary is known, a minimum for the mesh deformation energy $\mathscr{W}$ is searched, which is here defined as

$$\mathscr{W} = \frac{1}{2} \int_{\mathscr{D}} \left[(\mathscr{I} - 3) + 100\,(\mathscr{I} - 3)^2 + (\mathscr{J} - 1)^2 \right] \mathrm{d}V\,, \tag{4.6}$$

with the integration over the entire domain volume $\mathscr{D}$ and the substitutions

$$\mathscr{J} = \det\left(\nabla_{\mathbf{x}_{\text{mat}}}\mathbf{x}\right) \tag{4.7}$$

and

$$\mathscr{I} = \mathscr{J}^{-2/3}\text{tr}\left[\left(\nabla_{\mathbf{x}_{\text{mat}}}\mathbf{x}\right)^{\text{T}}\left(\nabla_{\mathbf{x}_{\text{mat}}}\mathbf{x}\right)\right]. \tag{4.8}$$

For two-phase flows (i.e. liquid and gas) the mass and momentum balance is defined individually for each of the phases, leading to a velocity vector of the liquid phase $\mathbf{u}_{\text{l}}$, a velocity vector of the gas phase $\mathbf{u}_{\text{g}}$, and the mesh velocity $\mathbf{u}_{\text{mesh}}$, which exists in both phases. At the liquid-gas interface, transition conditions for these quantities have to be defined. These are the normal and tangential stress balance (see section 3.2)

$$\mathbf{T}_{\text{l}} \cdot \mathbf{n} \cdot \mathbf{n} - \mathbf{T}_{\text{g}} \cdot \mathbf{n} \cdot \mathbf{n} + \sigma \nabla \cdot \mathbf{n} = 0\,, \tag{4.9}$$

$$\mathbf{T}_{\text{l}} \cdot \mathbf{n} \cdot \mathbf{t} - \mathbf{T}_{\text{g}} \cdot \mathbf{n} \cdot \mathbf{t} - \nabla\sigma \cdot \mathbf{t} = 0\,, \tag{4.10}$$

as well as the following transition conditions for the velocities

$$\mathbf{u}_{\text{l}} = \mathbf{u}_{\text{g}} + j_{\text{lv}}\left(\frac{1}{\rho_{\text{l}}} - \frac{1}{\rho_{\text{v}}}\right)\mathbf{n}\,, \tag{4.11}$$

$$\mathbf{u}_{\text{mesh}} = \left(\mathbf{u}_{\text{l}} \cdot \mathbf{n} - \frac{j_{\text{lv}}}{\rho_{\text{l}}}\right)\mathbf{n}\,. \tag{4.12}$$

The latter two equations account for the so called Stefan flow, which is introduced by the phase change of the material and the difference in the densities of the two phases.

In this thesis, the ALE formulation implemented in the CFD software *COMSOL Multiphysics* is used. The spatial discretization of the geometry is done with the finite element method (FEM). The so called *PARDISO*-solver [133] is used to solve the system of equations, which allows for parallel computation on multiple cores using distributed memory. Time integration is done using a method based on the implicit multi-step class of backward differentiation formula (BDF) [189], which changes freely and automatically between a first order method (backward Euler method) and a second order method. The time step is also chosen automatically by the solver so that the relative error is below 0.001, but the maximum allowed time step is defined by the user and set to $\Delta t_{\text{max}} = 0.5\,\text{s}$ throughout this chapter (see appendix A.3). The solver also allows tracing the deformation of the mesh induced by the mesh movement. Large mesh deformations affect the accuracy of the solution. If the mesh deformation exceeds a threshold value, the computation is stopped and a new mesh is automatically generated before the computation is resumed.

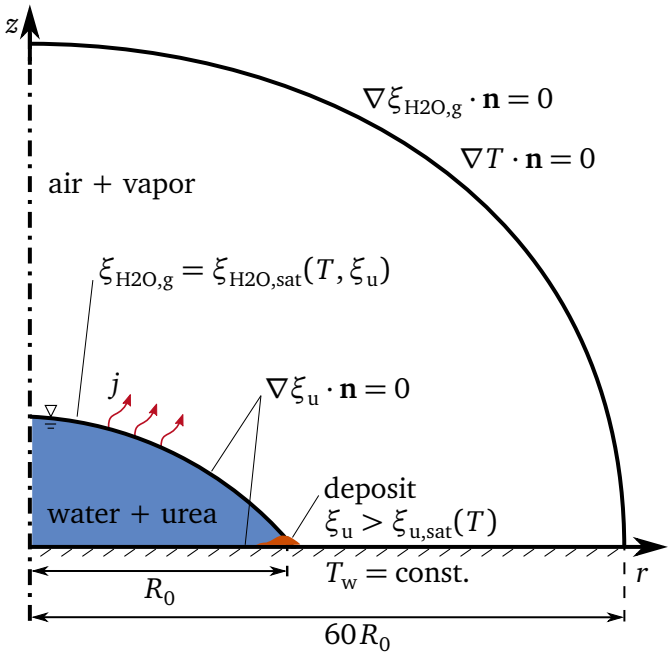

Figure 4.1: Domain for the simulation of deposit formation from evaporating drops.

4.2 Model Overview

A sketch of the computational domain is given in Fig. 4.1. The drop is assumed to be axially symmetric, making the problem two-dimensional. A urea-water drop with initial contact line radius R_0 sits on a hot wall with constant temperature T_w. The drop evaporates into the surrounding gas phase. It was shown in experimental works that the urea-water drop is pinned throughout the evaporation process [30, 192], which is also assumed in this model. Furthermore, it has been shown that evaporation of urea is negligible due to its low vapor pressures [70]. Consequently, only the water evaporates from the drop and is transported in the gas phase through convection and diffusion. It has been found that a radius of $60R_0$ for the surrounding gas phase is sufficient to eliminate boundary effects (appendix A.3). The urea remains in the drop and forms deposits on the hot wall as soon as the local urea concentration exceeds saturation. Only heterogeneous crystallization of urea on the wall is considered, as it can be assumed that the wall provides sufficient nucleation sites for crystal growth so that homogeneous crystallization, which usually requires a urea concentration well above the saturation, does not play an important role.

The drop radius R_0 is chosen to 1 mm in the reference setting and the initial contact angle was set to 80 degrees, which leads to a Bond number of

$$Bo = \frac{\rho_l g h_0 R_0}{\sigma_0} \approx 0.118\,. \tag{4.13}$$

It was mentioned earlier that the influence of gravity on the drop shape can be neglected if the Bond number is well below unity. As the value of the Bond number here is below unity but not by several orders of magnitude, calculations including gravitational volume forces and without gravitational volume forces

have been performed. The results showed that drop remains almost in exactly the same shape for both cases (the difference in the drop height is below 6 µm or 0.7 %), which is why gravity is not considered in the simulations shown in this chapter. Additionally, the capillary number resulting from Deegan flow is very small ($\mathcal{O}(Ca) = 1 \cdot 10^{-5}$). Natural convection in the drop is also neglected so that the drop shape follows a spherical cap in the absence of deposit formation.

To simulate this problem, an ALE method with a moving mesh is used for the drop and the gas phase. One energy equation (Eq. (4.4)) is solved covering both the drop and the surrounding gas phase. A species transport equation for the water vapor transport in the gas phase $\xi_{\mathrm{H2O,g}}$ and a species transport equation for the urea mass fraction ξ_{u} in the liquid are solved (Eq. (4.5)). The mass fraction of air in the gas phase is $\xi_{\mathrm{air,g}} = \left(1 - \xi_{\mathrm{H2O,g}}\right)$ and the mass fraction of water in the liquid is $\xi_{\mathrm{H2O,l}} = (1 - \xi_{\mathrm{u}})$. The computational mesh consists of triangular cells (see appendix A.3) and is refined towards the liquid-gas interface and towards the wall to accurately capture the thermal and concentration gradients, as well as the deposit shape.

4.2.1 Calculation of Material Properties

The material values used in the simulations are summarized in appendix A.1.2. The density of the urea-water solution is calculated as a function of the temperature and concentration of urea to account for density changes between different simulations. The surface tension at the liquid-gas interface is approximated according to Eq. (3.7) to include thermocapillarity. In a recent publication, it has been suggested that the surface tension of the UWS increases with the urea mass fraction [94]. However, these measurements were only done for one temperature so that reliable data for the surface tension of UWS as a function of temperature and composition are not yet available. Furthermore, as discussed in section 2.2, the importance of the thermal Marangoni effect on water drops is a debated topic. Therefore, in this work, the drop evaporation and deposit formation is first investigated in the absence of thermal and solutal Marangoni effect. Afterwards, the effect of thermocapillarity on the evaporation and deposit formation process is briefly discussed (section 4.4). The remaining material properties of the UWS are calculated for average values of temperature and composition.

The density in the gas is calculated assuming that the gas phase is a mixture of ideal gases consisting of air and water vapor

$$\rho_{\mathrm{g}} = \chi_{\mathrm{H20,g}}\, \rho_{\mathrm{H20}} + \left(1 - \chi_{\mathrm{H20,g}}\right) \rho_{\mathrm{air}}\,, \tag{4.14}$$

where $\chi_{\mathrm{H20,g}}$ is the volume fraction of water in the gas phase

$$\chi_{\mathrm{H20,g}} = \xi_{\mathrm{H20,g}} \frac{M_{\mathrm{g}}}{M_{\mathrm{H20}}} \tag{4.15}$$

and $M_{\mathrm{g}} = \chi_{\mathrm{H20,g}}\, M_{\mathrm{H2O}} + \left(1 - \chi_{\mathrm{H20,g}}\right) M_{\mathrm{air}}$ is the molar mass of the gas mixture. All other concentrations can be converted from mass fraction to volume fraction, analogously. The temperature-dependent values of air are used for the remaining properties in the gas phase to simplify the calculation.

The deposit is generally a porous substance, containing both crystalline urea and urea-water solution. The thermal conductivity k_{dep} and density ρ_{dep} of the deposit are calculated assuming a homogeneous porosity of the deposit λ_{dep} [232]

$$k_{\mathrm{dep}} = k_{\mathrm{l}}^{\lambda_{\mathrm{dep}}} k_{\mathrm{u}}^{\left(1-\lambda_{\mathrm{dep}}\right)}, \tag{4.16}$$

$$\rho_{\mathrm{dep}} = \lambda_{\mathrm{dep}} \rho_{\mathrm{l}} + \left(1-\lambda_{\mathrm{dep}}\right) \rho_{\mathrm{u}}, \tag{4.17}$$

where k_{u} and ρ_{u} denote the thermal conductivity and density of solid urea, respectively. The porosity of the deposit is set to $\lambda_{\mathrm{dep}} = 0.2$, which is estimated based on typical porosities for similar materials [26].

4.2.2 Modeling the Phase Change

The evaporative mass flux of water is calculated utilizing the assumption of local equilibrium at the liquid-gas interface, which means that every part of the interface is saturated with vapor in the gas phase $\xi_{\mathrm{H2O,int}} = \xi_{\mathrm{H2O,sat}}$. Generally, the saturation vapor pressure is temperature-dependent and follows from the Clausius-Clapeyron equation

$$\frac{\mathrm{d}p}{\mathrm{d}T} = \frac{h_{\mathrm{lv}} \rho_{\mathrm{v}} \rho_{\mathrm{l}}}{T\left(\rho_{\mathrm{l}} - \rho_{\mathrm{v}}\right)}. \tag{4.18}$$

However, to obtain the vapor pressure, the Clausius-Clapeyron equation has to be integrated and assumptions have to be made regarding the temperature dependence of the material values. This is why several ways have been reported to approximate the vapor pressure over a temperature range through fitting with experimental data [171]. In this work, the Wagner equation is utilized to calculate the temperature-dependent saturation vapor pressure $p_{\mathrm{H2O,sat}}$ for a pure water drop

$$\ln\left(\frac{p_{\mathrm{H2O,sat}}(T)}{p_{\mathrm{crit}}}\right) = \frac{C_1\left(1-T/T_{\mathrm{crit}}\right) + C_2\left(1-T/T_{\mathrm{crit}}\right)^{1.5} + C_3\left(1-T/T_{\mathrm{crit}}\right)^3 + C_4\left(1-T/T_{\mathrm{crit}}\right)^6}{T/T_{\mathrm{crit}}}, \tag{4.19}$$

where p_{crit} is the critical pressure, T_{crit} the critical temperature, and C_1-C_4 are tabulated material-specific constants used to approximate the vapor pressure curve.

Since the liquid is not pure water but a UWS, the saturation vapor pressure decreases as the concentration of urea at the interface increases. Using the mole fraction of urea χ_{u} in the liquid, the saturation vapor pressure can be calculated as (see [226])

$$p_{\mathrm{sat}}(T) = p_{\mathrm{H2O,sat}}(T)\left(1-\chi_{\mathrm{u}}\right). \tag{4.20}$$

When the saturation vapor pressure at every location of the interface is known, the saturation concentration follows as

$$\xi_{\mathrm{H2O,sat}} = \chi_{\mathrm{H2O,sat}} \frac{M_{\mathrm{H2O}}}{M_g} = \frac{p_{\mathrm{sat}}(T)}{p_\infty} \frac{M_{\mathrm{H2O}}}{M_g}, \tag{4.21}$$

where p_∞ is the pressure in the gas phase far away from the interface. The saturation concentration is prescribed as a boundary condition for the species transport equation of water vapor in the gas phase. The local evaporative mass flux at every interface position then follows by assuming pure diffusive species transport right at the interface:

$$j_{\mathrm{lv}} = -D_{\mathrm{bin}} \rho_g \nabla \left(\xi_{\mathrm{H2O}} - \xi_{\mathrm{H2O,sat}} \right) \cdot \mathbf{n}. \tag{4.22}$$

From this, the global evaporation rate of the drop can be computed by integrating over the liquid-gas interface length, which yields the volume rate of change of the drop. The mesh is then moved to follow the drop shape and to account for the Stefan flow according to Eqs. (4.11) and (4.12). The evaporation part of the source term in the energy equation (Eq. (4.4)) follows as $\Sigma_{\mathrm{e,lv}} = -j_{\mathrm{lv}} h_{\mathrm{lv}} / \delta_{\mathrm{lg}}$, where δ_{lg} is the cell volume divided by the surface area of the liquid-gas interface on every cell boundary. In the species transport equations for the water mass fraction in the gas phase and the urea mass fraction in the liquid, the liquid-gas interface is a boundary so that the evaporative mass flux j_{lv} can be prescribed as a boundary flux.

4.2.3 Modeling the Deposit Formation

As the water evaporates from the UWS drop, the urea concentration inside the drop increases. The urea concentration will be highest at the liquid-gas interface as this is where the water evaporates. However, due to diffusive and convective (Deegan or Marangoni flow) transport, the urea concentration increases inside the entire drop over time. As no urea evaporates or decomposes, all the urea inside the drop will eventually have to deposit. As stated above, heterogeneous crystallization at the wall is considered in this work as there are a large amount of crystallization nuclei present there and, hence, the deposition is expected to happen at the wall much more easily than anywhere else inside the drop. It is assumed that deposit formation starts at the wall as soon as the urea concentration exceeds the solubility of urea in water.

Calculation of the Reaction Source Term

The solubility of urea in water increases with temperature. The evaluation of literature values [226] shows that the solubility can be approximated as a linear function of temperature

$$\xi_{\mathrm{u,sat}} = 5.1687 \cdot 10^{-3} \mathrm{K}^{-1} \, T_{\mathrm{w}} - 1.0108, \tag{4.23}$$

which is evaluated based on the wall temperature T_{w}.

Once the saturation mass fraction is known, the crystallization mass flux can be calculated using a relaxation model. It is assumed that once formed, deposit does not go back into the solution even if the urea mass fraction falls below saturation for some reason. This yields for the deposition mass flux j_{ls} at the wall

$$j_{\mathrm{ls}} = \begin{cases} \rho_{\mathrm{l}} w_{\mathrm{ls}} \left(\xi_{\mathrm{u}} - \xi_{\mathrm{u,sat}} \right), & \text{for } \xi_{\mathrm{u}} > \xi_{\mathrm{u,sat}} \\ 0, & \text{otherwise}. \end{cases} \tag{4.24}$$

In the above, w_{ls} is a relaxation parameter, which ensures that the mass fraction at the wall is always very close to the saturation concentration. It can be interpreted as a deposition velocity and is set to $w_{\mathrm{ls}} = 0.1\,\mathrm{m\,s^{-1}}$ from a parametric study so that the urea mass fraction never considerably exceeds the saturation concentration. The deposition mass flux j_{ls} can then be defined as an outflow in the species transport equation of urea in the liquid. Additionally, crystallization leads to a temperature increase as the enthalpy of solution h_{ls} is released, which is considered in the energy equation (Eq. (4.4)) in the source term $\Sigma_{\mathrm{e,ls}} = j_{\mathrm{ls}} h_{\mathrm{ls}} / \delta_{\mathrm{ls}}$ (with δ_{ls} being the cell volume divided by the surface area of the liquid-solid interface on every cell boundary). The deposition source term in the species transport equation of urea in the liquid is therefore $\Sigma_{\xi,\mathrm{ls}} = -j_{\mathrm{ls}} / (\rho_{\mathrm{l}} \delta_{\mathrm{ls}})$

Calculation of Deposit Shape

As the deposit is created, the drop volume has to be decreased. This is achieved by deforming the wall to represent the deposit shape in the moving mesh framework. The position of the lower wall at each position in r can be explicitly defined, which also allows the inclusion of the feedback of the deposit on the drop.

In order to translate the deposition mass flux into a boundary condition for the moving mesh, the coordinate frame has to be changed. The deposit mass flux is calculated in the material frame. The deposit structure, however, is an integration of deposit mass flux over time and the shape of a once formed deposit is not supposed to change as the mesh moves. Consequently, the deposit structure has to be defined in the spatial frame. This is done by mapping the deposit mass flux in every time step onto a stationary one-dimensional grid, which represents the lower wall. The deposit shape is then evaluated on the stationary grid.

Once the local deposit mass flux j_{ls} for every position on the wall is calculated, the resulting growth of the deposit layer is obtained by solving an inhomogeneous Helmholtz equation for the deposit growth speed w_{dep} on every position of the wall

$$\frac{\partial}{\partial r} \left(\frac{\delta_{\mathrm{dep}}^2 R_0}{r+s} \frac{\partial w_{\mathrm{dep}}}{\partial r} \right) = w_{\mathrm{dep}} - \frac{j_{\mathrm{ls}}}{\rho_{\mathrm{dep}}}. \tag{4.25}$$

The above equation is similar to a diffusion equation. The total mass of deposit is conserved. The initially sharp deposit mass flux, which can theoretically be limited to one computational cell, is distributed over a range of cells. This is done for numerical reasons, as a sharp jump in the deposit height cannot

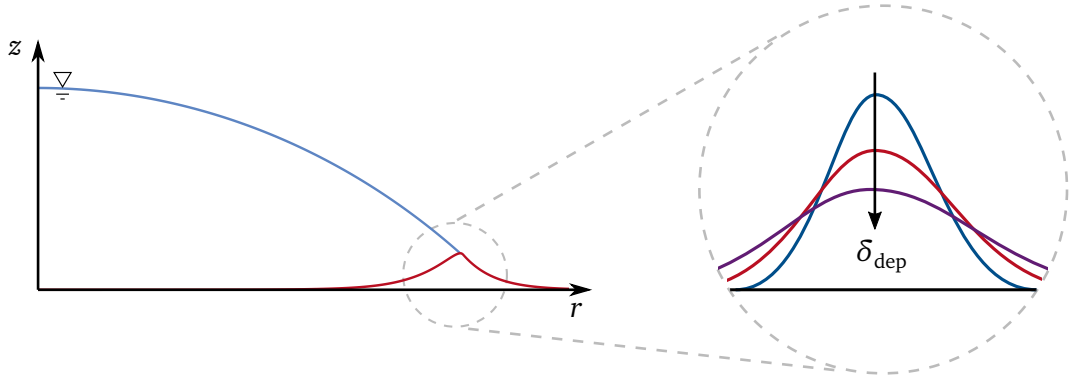

Figure 4.2: Sketch of the influence of δ_{dep} on the deposit shape. The arrow points in the direction of increasing δ_{dep}.

be followed by the moving mesh. However, this approach also allows reproducing the experimentally observed characteristics of porous crystal growth, which is not strictly limited to a well defined area and does also not show vertical flanks. With the chosen approach, the spreading decreases with increasing radial coordinate and the constant δ_{dep} determines the width over which the source term is distributed.

The influence of this numerical parameter on the deposit shape is shown in Fig. 4.2. With increasing δ_{dep}, the deposit width is increased as it is spread and the maxima of the deposit height are reduced. The parameter is chosen to $\delta_{dep}^2 = 5 \cdot 10^{-9}\mathrm{m}^2$ from numerical experiments, which are described in section 4.3.

The porosity of the deposit influences the deposition process through the deposit density ρ_{dep} in Eq. (4.25). Finally, $s = 1 \cdot 10^{-10}\mathrm{m}$ avoids division by zero at the symmetry axis.

With the known deposition speed, the deposit height z_{dep} at every time step can simply be calculated by integrating the deposition speed over time

$$z_{dep} = \int_{t_0}^{t} w_{dep}\,\mathrm{d}t\,. \tag{4.26}$$

The deposit height can then be prescribed as the condition for the mesh displacement at the lower wall. Consequently, the drop is affected by the presence of the deposit.

Influence on Heat Transfer

Once the deposit has formed, the interface between the drop and the solid (wall or deposit) is generally not of a uniform temperature, even if the wall temperature is constant. The deposit acts as a thermal resistance, which leads to a decrease of the drop temperature above the deposit that should be accounted for. However, with the moving mesh technique used to represent the deposit shape, the deposit is not actually part of the numerical discretization. The influence on the drop temperature has to be accounted for by an appropriate boundary condition. To do so, the boundary condition on the bottom – which is

initially just adjacent to the wall and later to the wall and deposit – is adjusted. Instead of a constant wall temperature $T = T_w$, a boundary condition of the third-type is set, which, using the heat flux $\dot{q}$ across the boundary, is formulated as

$$\dot{q} = \frac{-k_{dep}}{z_{dep} + s} (T - T_w) \,. \tag{4.27}$$

With this condition, a one-dimensional heat conduction in the deposit can be represented. It becomes clear from the equation that the heat flux always affects the liquid temperature in such a way that it tends towards the temperature of the wall. If the temperature is not equal to the wall temperature ($T \neq T_w$) and the deposit height at the current location is zero ($z_{dep} = 0$), a very high heat flux results, pushing the temperature almost instantly towards the wall temperature. However, if deposit is present $z_{dep} \neq 0$, the heat flux results from the thermal resistance of the deposit, which is calculated from the local deposit height and the thermal conductivity of the deposit.

4.3 Validation and Sensitivity Analysis

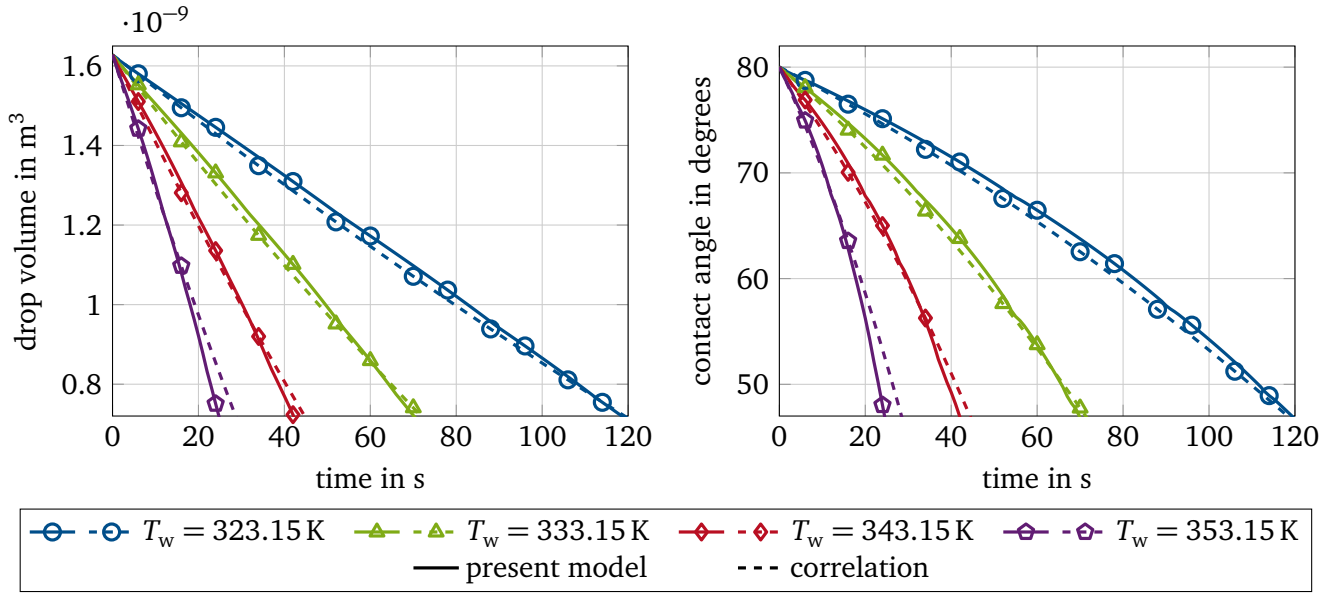

Figure 4.3: Drop volume (left) and contact angle (right) over time for various wall temperatures from the simulation and according to the correlation by Hu and Larson [107].

In order to validate the developed numerical model, the diffusion-driven evaporation of a pure water drop with a drop radius of 1 mm and an initial contact angle of 80 degrees is calculated with the model and compared to the correlation of Hu and Larson [107] (see Eq. (2.13)). The evolution of the drop volume over time on the left and of the contact angle on the right for various wall temperatures is given in Fig. 4.3. The contact angle for the correlation has been calculated from the drop volume at every time, assuming that the drop has the shape of a spherical cap (see Eq. (2.11) and Eq. (2.12)). It can bee seen that the drop volume decreases linearly over time for all temperatures. As expected, the evaporation rate and, consequently, the decrease of the drop volume is higher for higher wall temperatures. The decrease of the drop volume over time agrees very well with the correlation for lower wall temperatures. For higher

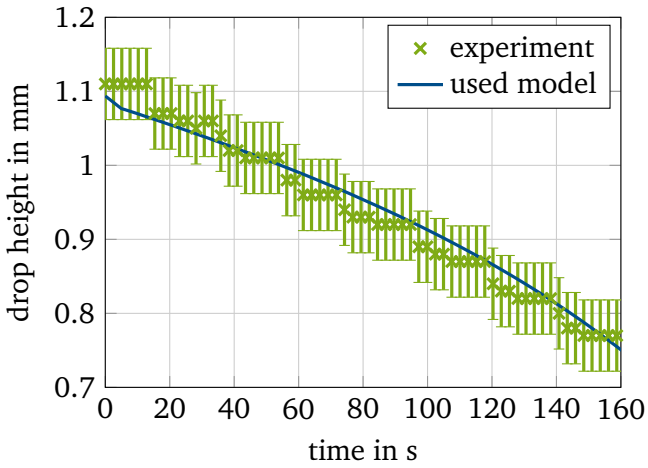

Figure 4.4: Comparison between experimental and numerical drop height evolution for an evaporating AdBlue drop on a wall with $T_w = 349\,\mathrm{K}$ (data from [30]).

wall temperatures ($T_w = 343.15\,\mathrm{K}$ and $T_w = 353.15\,\mathrm{K}$), small deviations between the correlation and the model results can be seen for larger times, but the agreement is still good with the maximum observed error for $T_w = 353.15\,\mathrm{K}$ below 10 %. These deviations might be due to the effect of the Stefan flow, which becomes more important compared to the diffusive vapor transport for higher wall temperatures and consequently higher evaporation rates. This effect was neglected in the numerical model used by Hu and Larson [107] to derive the correlation because slowly evaporating drops were considered in that work. The contact angles calculated in the model and predicted from the correlation assuming a spherical cap shape agree very well, as depicted in Fig. 4.3 (right). Again, the fit becomes worse for larger times if the evaporation rates are high. However, overall, the agreement of the model with the correlation is very good for all investigated wall temperatures.

Additionally, the model results for the evaporation of a urea-water drop on a hot wall are compared to experimental data [30] in Fig. 4.4 [I]. The decrease of the drop apex height over time from the experiment and the model agree very well over the entire duration. The numerical result is always within the measurement uncertainty of the experiment. Unfortunately, the experimental data do not cover the drop evolution during the deposit formation process so that the two-component evaporation can be successfully validated only until the beginning of the deposit formation.

The model contains the parameter δ_{dep}, which cannot be determined from the literature with good accuracy and which is necessary for the numerical stability of the problem. This parameter leads to spreading of the deposition source term over a small wall region to increase numerical stability and to predict the deposit shape resembling the growing behavior of crystals (see Fig. 4.2). The crystal growth is not restricted to the position corresponding to the computational cell right at the three phase contact line. The width of the deposit depends on the detailed chemical mechanism, governing the crystal growth, and on the liquid transport inside the porous deposit structure. The description of these phenomena are beyond the scope of the present work, which is why the exact extent of the deposit spread is approximated.

[I] Special thanks to my colleague Dr. Philipp Hänichen for conducting the experiment.

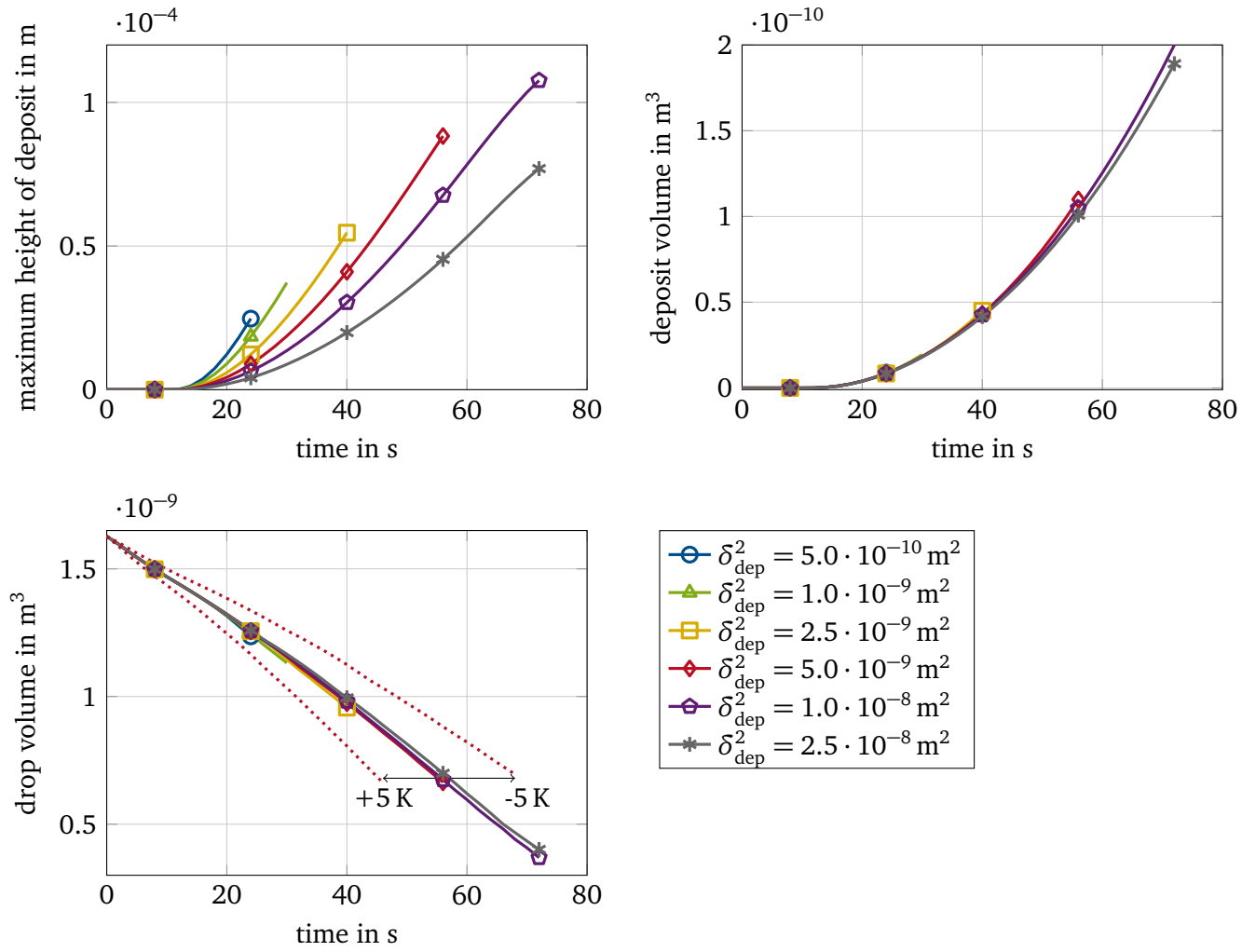

Figure 4.5: Deposit height (top left), deposit volume (top right) and drop volume (bottom) over time for various values of the parameter δ_{dep}.

Additionally, the model becomes more stable the more the source term is spread out, as the mesh can then more easily follow the deposit shape. Several numerical simulations have been conducted to make an optimal choice for the parameter and to study its influence on the simulation results.

The effect of δ_{dep} is illustrated in Fig. 4.5 in which the evolution of the maximum deposit height (top left), the deposit volume (top right), and the drop volume (bottom left) are shown for different values of δ_{dep} over time. The deposit formation was observed to happen around the three-phase contact line and the maximum deposit height in the simulations was found at the location of the three-phase contact line, which is discussed in more detail in the following section. As is evident from the plots of the maximum deposit height, an increase of δ_{dep} leads to lower maximum deposit heights because the deposition source term is spread over a wider area (see Fig. 4.2).

One can also see in that plot that not all simulations run for the same amount of time as the choice δ_{dep} affects the stability of the numerical simulation. For smaller values of δ_{dep}, corresponding to higher and thinner deposits, the moving mesh has to deform substantially within a few computational cells to follow the deposit shape. Errors then occur during the automatic remeshing procedure because the deposit shape cannot be accurately discretized with the computational mesh. This leads to stopping of the simulation at

the times where the lines in the plot end. For increasing values of δ_{dep}, the simulations run longer except for $\delta_{dep}^2 = 2.5 \cdot 10^{-8}\,m^2$, which again shows a decreased stability of the simulation.

Despite the large differences in the maximum deposit height, the overall deposit volume on the top right of Fig. 4.5 stays almost the same, independently of the choice of δ_{dep}. The maximum difference in the deposit volume between the smallest and largest considered value of δ_{dep} amounts to 7.15 %. This means that the deposit shape does not severely influence the deposition process. An even smaller influence of the value δ_{dep} is found by looking at the evolution of the drop volume, which can be seen in the bottom left plot of Fig. 4.5. The deposit shape can influence the overall drop evaporation by influencing the evaporation rate at the three-phase contact line or by lowering the drop temperature above the deposit through the thermal insulation effect of the deposit. The plots of the drop volume are lying almost on top of each other except for $\delta_{dep}^2 = 2.5 \cdot 10^{-8}\,m^2$, which shows a slightly slower volume decrease. Evidently, the influence of δ_{dep} on the drop evaporation process is very small. The dashed lines in the plot indicate evaporation of a drop on a wall, which is 5 K hotter or colder than for the solid lines. As one can easily see, the wall temperature has a much stronger effect on the evaporation process than the choice of δ_{dep}.

From these investigations, $\delta_{dep}^2 = 5.0 \cdot 10^{-9}\,m^2$ is chosen, corresponding to the red lines in Fig. 4.5. With the chosen parameter, a good numerical stability can be achieved through spreading of the deposit source terms over a wide enough area. At the same time, the resulting deposit shape is still limited to the area close to the three-phase contact line and follows the expected shape of a deposit growth through crystallization. The resulting drop and deposit shape for the chosen value of δ_{dep} after 52 s of evaporation are shown in the left part of Fig. 4.2.

4.4 Results for Drop Evaporation and Deposit Formation

Table 4.1: Initial conditions of the reference simulation.

R_0 in mm	θ_0 in deg	$\xi_{u,0}$	T_w in K	$T_{l,0}$ in K	$T_{g,0}$ in K	$\xi_{H2O,g,0}$	p_∞ in bar
1.0	80	0.325	338.15	298.15	298.15	0.0127	1.0

The initial conditions for the simulation are summarized in Tab. 4.1. The parameters are typical for experimental laboratory conditions to make them easily comparable to future laboratory experiments. The initial composition of the UWS drop of 32.5 % urea mass fraction is the industry standard for SCR applications [39]. The temperature and concentration fields inside the drop and the gas phase are initially uniform. The water mass fraction in the gas phase corresponds to a relative humidity of 63 % for the chosen ambient temperature $T_{g,0}$ and ambient pressure of p_∞.

4.4.1 General Observations

The general behavior of the solution regarding evaporation and deposit formation is discussed in this section for the reference configuration from Tab. 4.1. For simplicity, the temperature dependence of the surface tension is neglected. This dependence is discussed in detail in section 4.4.3.

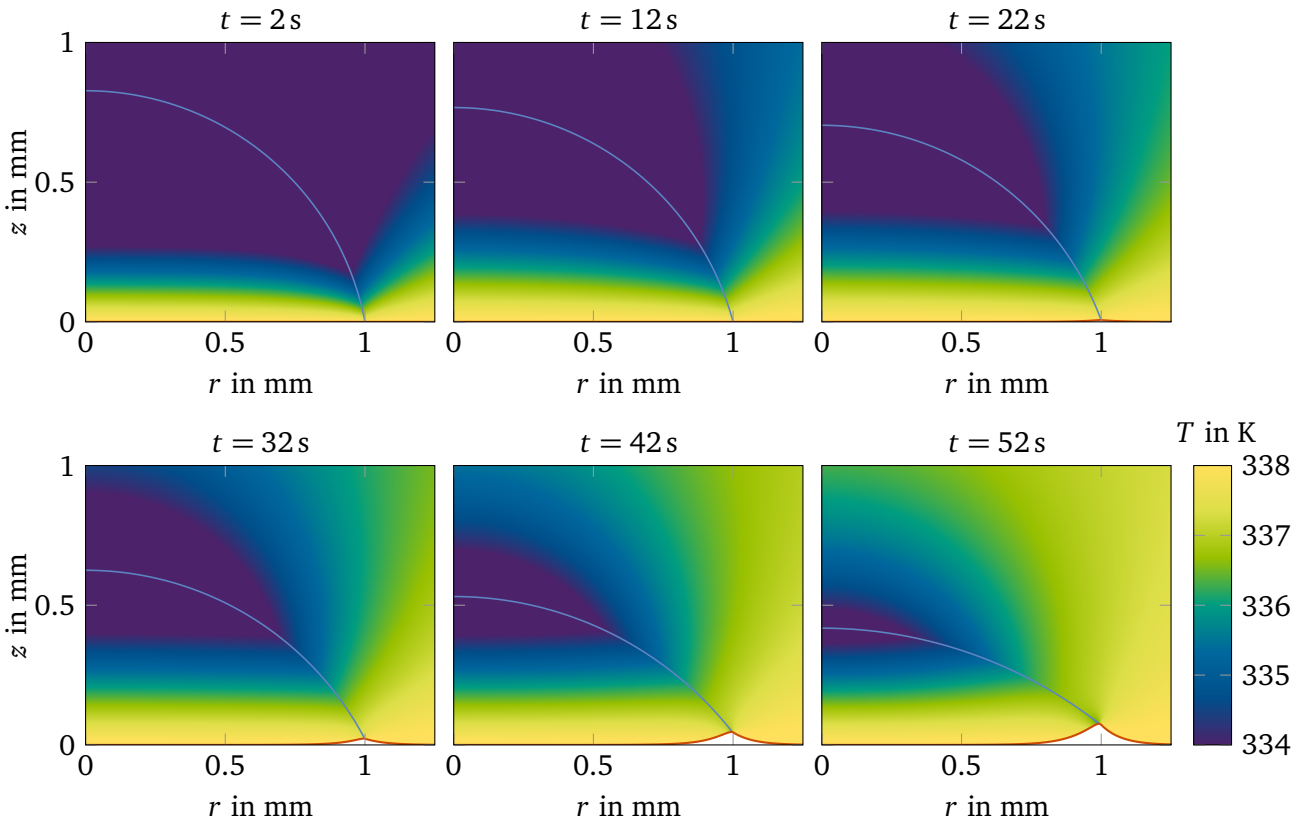

Figure 4.6: Time evolution of the temperature field in the drop and in the gas. Note that, due to the scaling, values below 334 K are not resolved.

The temperature field inside the drop and the gas phase in the vicinity of the drop at various times is presented in Fig. 4.6. The liquid-gas interface is highlighted for clarity in every picture. The decrease of the drop volume over time can be observed. As the drop radius stays the same, the contact angle and drop height decrease with time. Initially, the drop and gas phase have a homogeneous temperature of 298.15 K. The first picture shows that the hot wall ($T_w = 338.15\,\mathrm{K}$) leads to the development of a thermal boundary layer inside the drop and gas. As the thermal diffusivity of the liquid is two orders of magnitude lower than the one of the gas phase, the thermal boundary layer in the gas phase grows faster, which can be seen in the pictures for $t = 2\,\mathrm{s}$ and $t = 12\,\mathrm{s}$. The evaporative cooling of the liquid-gas interface can be clearly observed. Temperature isolines in the drop are not horizontal but bend down as they approach the interface – for $t = 2\,\mathrm{s}$, for example – as long as no deposit is present. The maximum of the interface temperature is located near the three-phase contact line and the minimum interface temperature is at the drop apex. Consequently, from the temperature field (and the contact angle below 90°), the highest evaporation rates are expected at the three-phase contact line. Starting from $t = 32\,\mathrm{s}$ the formation of deposit can be observed at the wall in the vicinity of the contact line. The height of the deposit increases with time and it spreads towards the center of the drop.

An influence of the enthalpy of solidification on the temperature field cannot be identified. The temperature above the deposit does not show a noticeable peak when the deposition starts (for $t = 22\,\mathrm{s}$). The temperature increase due to the enthalpy of solidification increases with time but always stays below 0.05 K. This is contrary to the observations made by Schmid *et al.* [192], who found a very sharp

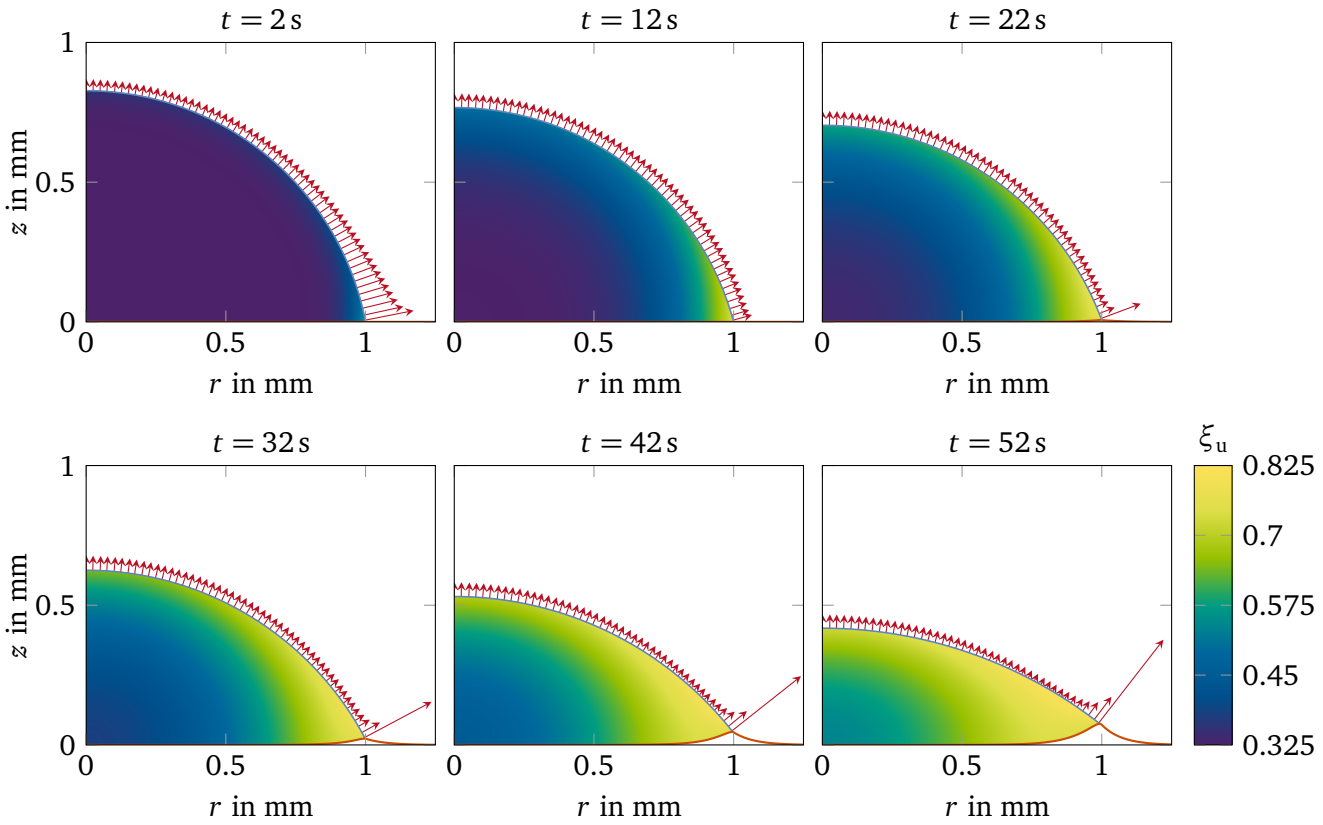

Figure 4.7: Time evolution of the urea mass fraction inside the drop and the local evaporation rate.

temperature peak with an amplitude of up to 40 K right at the moment of first deposition, which was attributed to the enthalpy of solution. Soon after the first deposition, the temperature was found to reduce again to the previous value. However, both in the literature and in the present model the deposition rate increases with time, which means that there should be a continuous effect on the temperature during the deposit formation process. The model shows this behavior but suggests that the influence of the enthalpy of the solution on the temperature field is negligible. This difference might be due to a substantial (local) supersaturation being achieved in the experiment before the onset of deposition, which would lead to a very high crystallization rate at the beginning of deposit formation.

Not negligible, however, is the effect of the deposit layer on the heat transport from the wall to the drop. The growing deposit layer has an insulating effect, shielding the drop above it from the hot wall. This can be clearly seen in the last image ($t = 52\,\mathrm{s}$). Here, the three-phase contact line has a lower temperature than the wall due to the heat conduction through the deposit layer and the evaporative cooling of the interface. The temperature at the three-phase contact line is about 2.3 K below the wall temperature for $t = 52\,\mathrm{s}$.

The urea mass fraction inside the drop for various times is depicted in Fig. 4.7. Additionally, the local evaporation rate is highlighted by the red arrows in every picture. As the water evaporates from the drop, the urea mass fraction at the liquid-gas interface increases. Diffusive mass transport in the drop can be observed, which homogenizes the urea mass fraction in the drop for larger times. The Deegan flow leads to convective fluid transport from the drop bulk to the contact line and acts in the opposite direction of the diffusive transport along the wall. In the first picture, the evaporation rate has a maximum at the

three-phase contact line, which leads to a maximum of the urea concentration at that position. However, the evaporation rate decreases with increasing urea concentration (see Eq. (4.20)), which is evident from the second picture ($t = 12\,\mathrm{s}$). Here, the evaporation rate at the three-phase contact line is lower than in the remaining drop. Eventually, the urea concentration reaches the saturation concentration and deposits start to form. The deposits first form at the three-phase contact line as this is the location of the highest urea mass fraction. With increasing time, the deposit also begins to form closer to the drop center as the saturation concentration is reached over a wider area due to the diffusive mass transport.

As soon as the deposits start to form (starting from $t = 22\,\mathrm{s}$), the evaporation rate at the three-phase contact line begins to increase again, while the evaporation rate at the rest of the liquid-gas interface continuously declines due to the still increasing urea mass fraction. The increase of the evaporation rate at the three-phase contact line during deposition is caused by the increase of space available to which the water vapor can diffuse. Before deposition starts, the solid wall prevents diffusion, but for $t = 42\,\mathrm{s}$, for example, the gas to the right of the deposit is an available space to which water vapor can be moved. This additional space can be thought of as a virtual decrease of the contact angle for the calculation of the evaporation rate. At the same time, the urea mass fraction in the drop does not increase anymore at the contact line because, as soon as saturation is reached, all excess urea forms deposit.

The resulting ring-shaped deposit qualitatively agrees well with experimental investigations [30, 41, 192] (see Fig. 2.3). These works also showed that the deposition starts at the three-phase contact line as it does in the model. Unfortunately, no experimental investigations are able to track the growing deposit layer inside the liquid urea-water drop due to the difficult accessibility, and no works are known that specify after what evaporation time the deposit formation has started. With the model, however, influencing factors on the start of the deposition, its growth rate, and shape can be easily identified, which is done in a parametric study.

4.4.2 Parametric Study

In the following, the wall temperature, initial urea concentration, and the drop radius are varied to study their effect on the evaporation and deposit formation process. Except for the varied parameter, all other initial conditions are kept as defined in Tab. 4.1 for the reference simulation. The setup corresponding to Tab. 4.1, which was thoroughly discussed in the previous section, is given by the yellow lines in every figure throughout the parametric study.

Influence of Wall Temperature

The wall temperature of an exhaust pipe can dramatically change depending on the ambient and engine operating conditions. This parametric study is limited to relatively low wall temperatures, far from the melting point of urea, which is at approximately 406 K. Experimental investigations have found that these low wall temperatures, which arise shortly after the engine start up or after a high dosage of the solution, are especially critical for deposit formation [216]. Additionally, in this regime, the deposit is driven by crystallization of urea and not by chemical decomposition [207, 243].

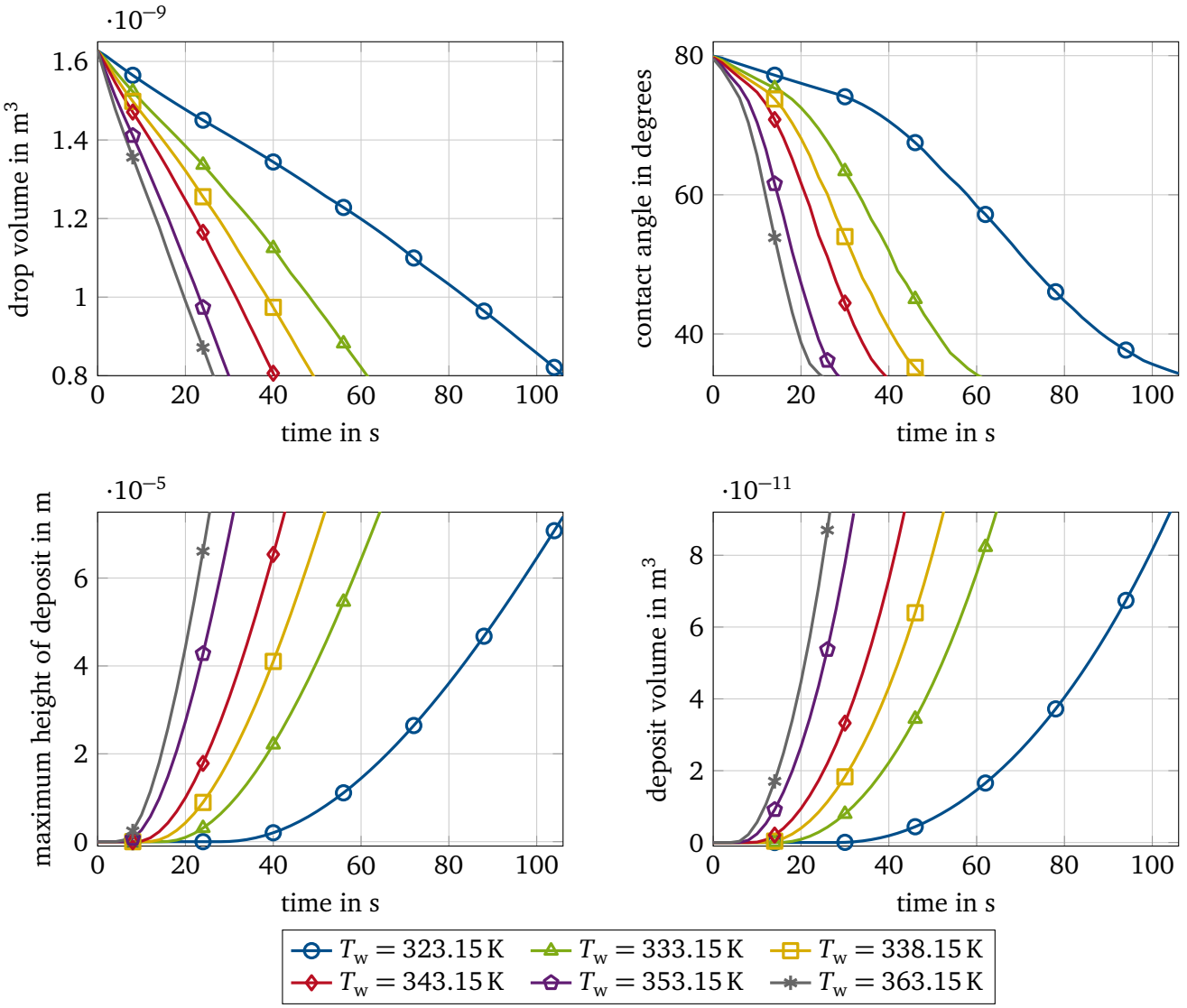

Figure 4.8: Drop volume (top left), contact angle (top right), maximum deposit height (bottom left), and deposit volume (bottom right) over time for different wall temperatures.

The results of six different simulations with wall temperatures ranging from 323.15 K to 363.15 K are summarized in Fig. 4.8. The evolution of the drop volume is shown in the top left figure. As expected, the drop volume decreases almost linearly with time and the drop evaporation is faster for higher wall temperatures. It follows from the contact angle evolution in the top right plot of Fig. 4.8 that the contact angle initially decreases identical to a cap-shaped drop (see Fig. 4.3). For higher times, an influence of the deposit on the contact angle can be identified, resulting in an inflection point, which leads to a slower decrease of the contact angle. This is caused by the growing deposit at the three-phase contact line, which pushes the liquid upwards and consequently reduces the rate of the contact angle decrease.

The maximum height of the deposit over time, which is the deposit height at the three-phase contact line, is depicted in the bottom left part of Fig. 4.8. In the early stages of evaporation, no deposit formation is observed for all wall temperatures because the urea concentration inside the drop has not reached saturation. It can be clearly seen that the beginning of deposit formation depends strongly on the wall temperature. As the wall temperature is increased, the deposit formation starts earlier, despite the increase

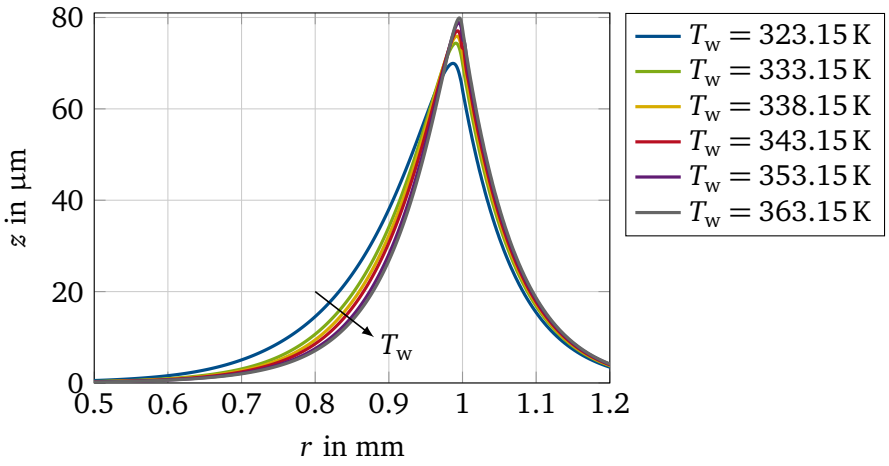

Figure 4.9: Deposit shape on the wall for various wall temperatures for a formed deposit volume of $9 \cdot 10^{-11}$ m^3. The three-phase contact line is at $r = 1$ mm. The arrow points in the direction of increasing wall temperature.

of the urea solubility in water with increasing temperature. This is due to the higher evaporation rates for higher wall temperatures, which lead to a faster increase of the urea concentration. The beginning of deposit formation is quite sensitive to the wall temperature. For example, a temperature increase of only 15 K (from $T_w = 323.15$ K to $T_w = 338.15$ K) shifts the beginning of deposition by 18 s. The increase in evaporation time before the onset of deposit formation grows as the wall temperature is decreased. Furthermore, it can be seen that the deposit growth rate increases with time as soon as the deposit formation has started, which is indicated by the nonlinear growth of the deposit volume in the bottom right plot of Fig. 4.8. As a result, the time at which a certain deposit volume has formed depends strongly on the temperature. For higher temperatures, the same deposit volume is reached much more quickly than for lower temperatures. It can be seen that the time, until a certain amount of deposit has formed, increases non-linearly with decreasing temperature.

The shape of the resulting deposit is exemplarily shown for all investigated wall temperatures in Fig. 4.9. As the beginning of the deposit formation and the deposit growth rate depends on the wall temperature, the deposit shape is evaluated after a deposit volume of $9 \cdot 10^{-11}$ m^3 has formed. This corresponds to evaporation times between 26 s and 103 s (see Fig. 4.8). In Fig. 4.9, the three-phase contact line is located at $r = 1$ mm, which is the position of the maximum deposit height, as expected. It was discussed previously that the exact shape of the deposit depends on the choice of δ_{dep} so that only qualitative influences of the wall temperature on the deposit shape can be assessed. As one can see, the maximum height of the deposit slightly decreases with decreasing wall temperature, while the width of the deposit towards the drop center simultaneously increases. This indicates that the diffusive mass transport in the drop, which leads to a homogenization of the urea concentration and so to deposit formation at a later time but over a wider area of the wall, becomes more important when the wall temperature is low. Indeed, the deposit shape for $T_w = 323.15$ K deviates the most from the other deposit shapes, which is due to the considerably longer time until the deposit is formed compared to the other wall temperatures (103 s compared to 64 s for $T_w = 333.15$ K; see Fig. 4.8).

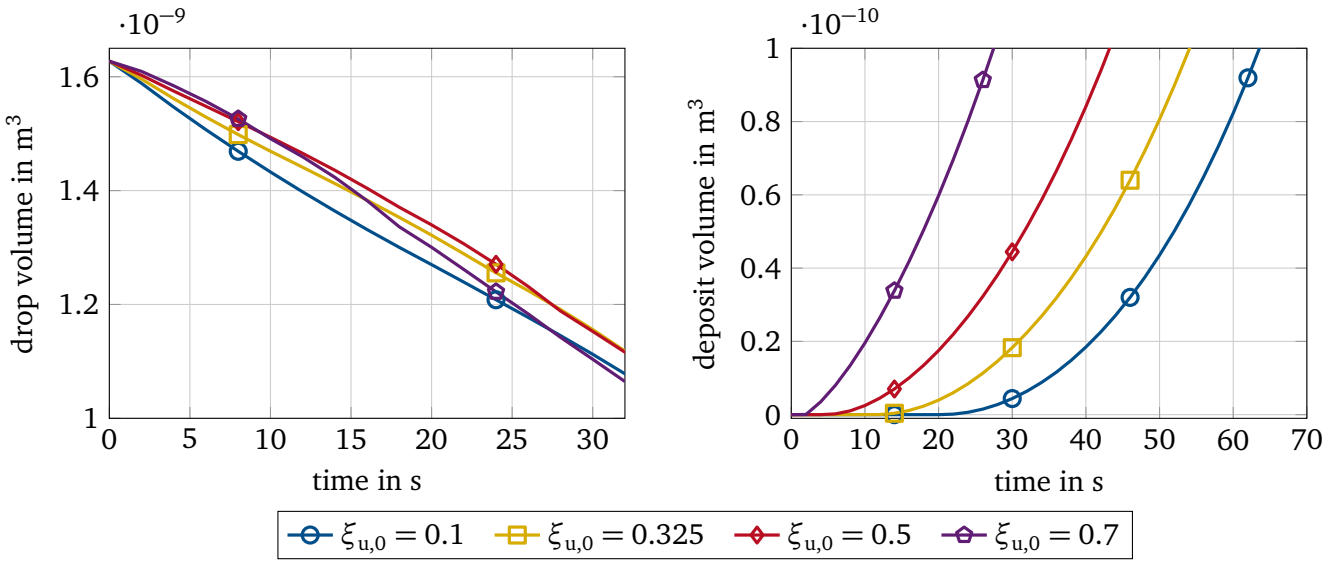

Figure 4.10: Drop volume (left) and deposit volume (right) over time for different initial urea concentrations.

Influence of Initial Drop Composition

As soon as the urea-water spray is injected into the exhaust pipe, the water begins to evaporate. By the time the drop impingement has happened and suspended drops have formed, the concentration in the drops might substantially deviate from the initial concentration. Furthermore, the concentration of the UWS filled into the tank might also vary.

The evolution of the drop volume in the initial stages of evaporation for various initial urea mass fractions inside the drop is given in the left part of Fig. 4.10. It is evident that the urea concentration does not affect the drop evaporation rate as strongly as the wall temperature (see Fig. 4.8). However, in the initial stages of evaporation the drop volume decreases faster for a drop with lower urea mass fraction. This behavior can be explained by the fact that the saturation vapor pressure reduces with increasing urea concentration (Eq. (4.20)). But for $t \approx 10\,\mathrm{s}$ the drop volume for $\xi_{u,0} = 0.7$ begins to decrease faster than for the other urea concentrations. A similar behavior can be observed for $\xi_{u,0} = 0.5$ at around 25 s. This behavior is related to the deposit formation. It was shown in Fig. 4.7 that the evaporation rate at the three-phase contact line increases during the deposit formation process. As confirmed in the right part of Fig. 4.10, the deposit formation starts earlier for a higher initial urea concentration. For $\xi_{u,0} = 0.7$, the deposition starts very shortly after the beginning of evaporation, since the initial urea concentration is close to the saturation concentration. With decreasing initial urea mass fraction, the deposit formation process starts considerably later. Again, the speed of the deposit formation process increases with time after the first deposit was formed for all investigated mass fractions.

The resulting shape of the formed deposit after a deposit volume of $9 \cdot 10^{-11}\,\mathrm{m}^3$ was reached is shown in Fig. 4.11. The deposit shape is almost identical for urea concentrations $\xi_{u,0} = 0.1 - 0.5$ for the chosen value of δ_{dep}. Only for $\xi_{u,0} = 0.7$ can a deviation from the other deposit shapes be observed. In this case, the deposit height is reduced and more deposit is found on the left flank of the deposit towards the drop center. This is again attributed to the influence of diffusion inside the drop, which only affects the deposit

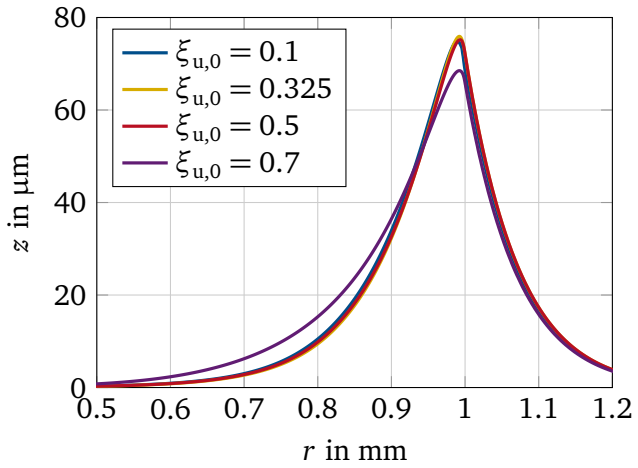

Figure 4.11: Deposit shape on the wall for various initial urea mass fractions for a formed deposit volume of $9 \cdot 10^{-11}$ m^3. The three-phase contact line is at $r = 1$ mm.

shape when the urea concentration in the drop bulk is already close to saturation. Then, a small increase of the urea mass fraction through diffusive mass transport from the three-phase contact line means that the saturation concentration is exceeded and deposition begins.

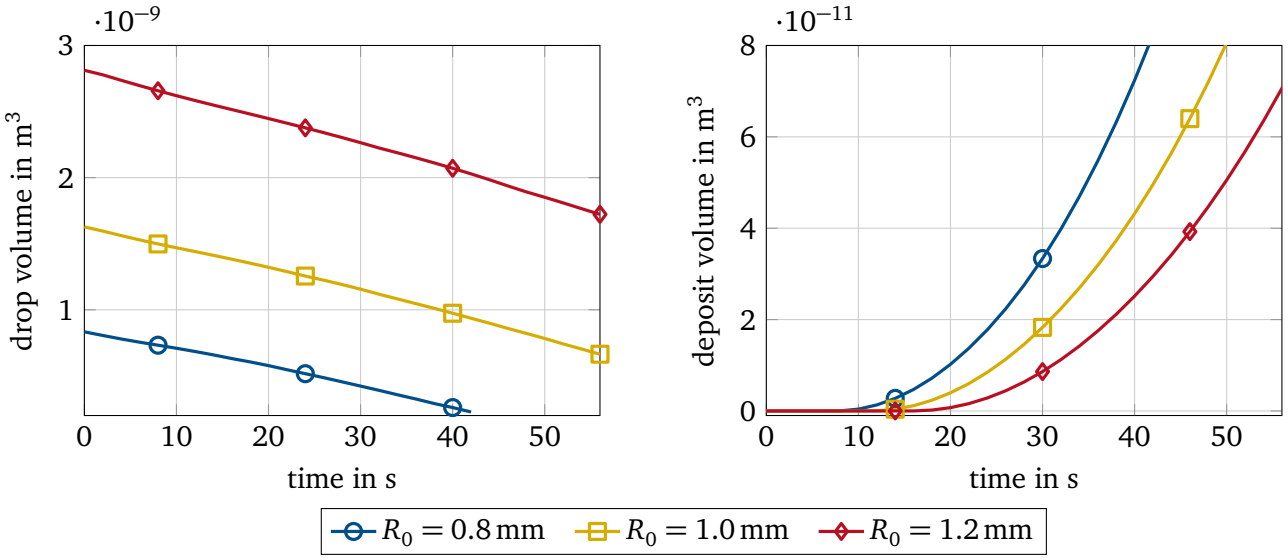

Figure 4.12: Drop volume (left) and deposit volume (right) over time for different initial drop radii.

Influence of Initial Drop Radius

The injection through the injector nozzle does not result in a spray of drops with identical volume but rather in a multitude of different drop sizes. This drop size distribution eventually results in suspended drops of different radii evaporating on the hot wall. Similarly, the breakup of the wall film is influenced by many parameters, as discussed earlier in this work, which results in different drop sizes.

The evaporation process for drops of three different radii is summarized in Fig. 4.12. It can be suggested from the left side of Fig. 4.12 that all three drops evaporate at a similar rate. The volume of the formed deposit over time for varied drop radius is given in the right plot of Fig. 4.12. It can be seen that the

deposit formation starts earlier when the initial drop radius decreases. Once the deposit formation has started, all three drops show a very similar increase of the deposit growth rate over time, which is expected from the similar evaporation rates of the drops. The shape of the resulting deposit is similar for all investigated radii and resembles the shape of the reference configuration, which is why it is not shown again here.

Deduction of a Correlation for the Beginning of Deposit Formation

An important parameter for the industrial application is the beginning of first deposit formation. Based on the simulations shown in this section, a first correlation for the start time of the deposition $t_{\mathrm{dep},0}$ can be deduced. This correlation has to depend on the wall temperature, the initial urea concentration, and the initial drop radius, based on the results of this section. The wall temperature is made non-dimensional with the initial temperature of the drop and the drop radius is non-dimensionalized utilizing the capillary length $\sqrt{\sigma_0/(\rho_\mathrm{l} g)}$. A linear regression is used to calculate the parameters of the correlation, which follows as

$$t_{\mathrm{dep},0} = 2.72\,\mathrm{s}\left(\frac{T_\mathrm{w}-T_{\mathrm{l},0}}{T_{\mathrm{l},0}}\right)^{-1.76}\left(1-\xi_{\mathrm{u},0}\right)^{2.18}\left[\frac{R_0}{\sqrt{\sigma_0/(\rho_\mathrm{l} g)}}\right]^{1.74}. \tag{4.28}$$

The simulation results are compared with the correlation in Fig. 4.13. The correlation fits the simulation results with a coefficient of determination of approximately 0.991. The maximum deviation observed for any individual simulation is around 12 %. It can be concluded that the correlation can be used to obtain a first guess for the start time of deposit formation through crystallization from urea-water drops. However, the number of simulations used to deduce this correlation is not very large. The correlation should be checked against further numerical or experimental results. Furthermore, other parameters, such as the initial contact angle of the drop and the relative humidity in the gas phase, are expected to influence the beginning of deposit formation so that the correlation will have to be extended.

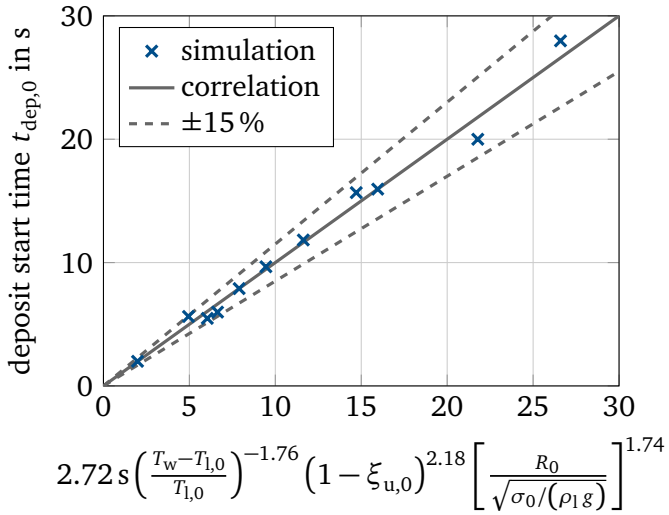

Figure 4.13: Beginning of deposit formation from the simulations and predicted with the correlation.

4.4.3 Influence of Thermocapillarity

Up to this point, both solutocapillarity and thermocapillarity inside the drop were neglected. This is partly due to the high computational demand, which follows from the inclusion of the Marangoni effect into the model. Additionally, no reliable data for the surface tension of urea as a function of both temperature and urea mass fraction are known. Even without considering the Marangoni effect, good qualitative agreement with the experimentally observed deposit shapes was already achieved. Nonetheless, the influence of both solutocapillarity and thermocapillarity on the evaporation and deposit formation of evaporating urea-water drops is a very interesting question.

The solutocapillarity, on the one hand, is induced by gradients of the urea mass fraction along the interface. The available literature data suggest that the surface tension of the urea-water mixture increases with urea concentration [94]. Since the highest evaporation rates are found at the three-phase contact line, the resulting Marangoni flow leads to a flow from the drop apex along the liquid-gas interface towards the three-phase contact line, then along the wall towards the drop center, and then upwards at the drop center line back towards the drop apex.

The thermocapillarity, on the other hand, is caused by temperature gradients along the drop interface. The maximum of the interface temperature is found at the three-phase contact line. The surface tension decreases with increasing temperature. Consequently, the resulting flow is exactly reversed compared to the solutocapillarity so that the two effects will partly cancel each other out. Additionally, the Deegan flow continuously supplies liquid to the pinned three-phase contact line, which leads to a flow from the drop center to the contact line. The Deegan flow has been taken into account throughout this chapter. The final flow field inside the drop results from a superposition of the three effects. This flow again influences the temperature and concentration fields inside the drop, which affects the evaporation and deposit formation process.

Unfortunately, due to computational restrictions of the model, the inclusion of both thermocapillarity and solutocapillarity into the model is not easily possible. Additionally, the computational times increase extensively, when the Marangoni flow is considered because of the large increase in the flow velocities inside the drop. For this reason, only the effect of thermocapillarity on the evaporation and deposit formation of the drop is considered here. This limits the applicability of the results for the industrial application but is interesting nonetheless as it has been shown experimentally that thermocapillarity might result in a drastic change of the deposition pattern [108].

The flow fields inside the evaporating drop without Marangoni effect and with thermocapillarity are shown in Fig. 4.14. In the absence of Marangoni convection, Deegan flow can be observed, supplying the three-phase contact line with liquid. If thermocapillarity is included, the resulting flow field transports liquid along the liquid-gas interface as described above. The temperature dependence of the surface tension $\sigma_{T,0}$ was chosen identical to the one of pure water. The scaling of the arrows in both plots is not identical. The ratio of the arrow scaling between the two plots is 4000. In fact, the average flow velocity in the absence of the Marangoni effect is $\mathcal{O}(10^{-5}\,\mathrm{m/s})$ and if thermocapillarity is included $\mathcal{O}(10^{-2}\,\mathrm{m/s})$.

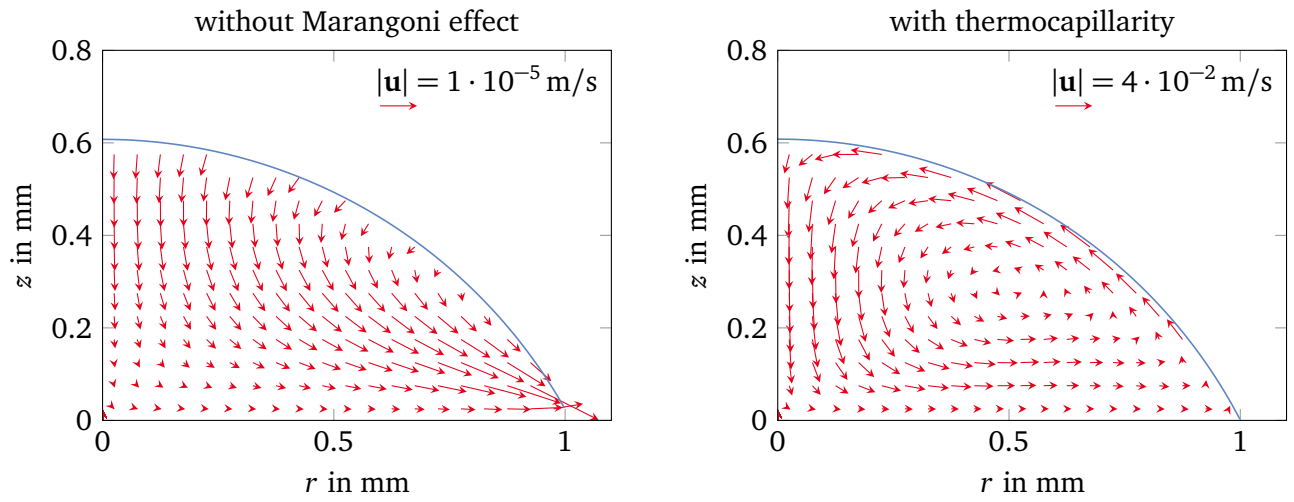

Figure 4.14: Velocity vectors in a drop without Marangoni flow (left) and with thermocapillarity (right).

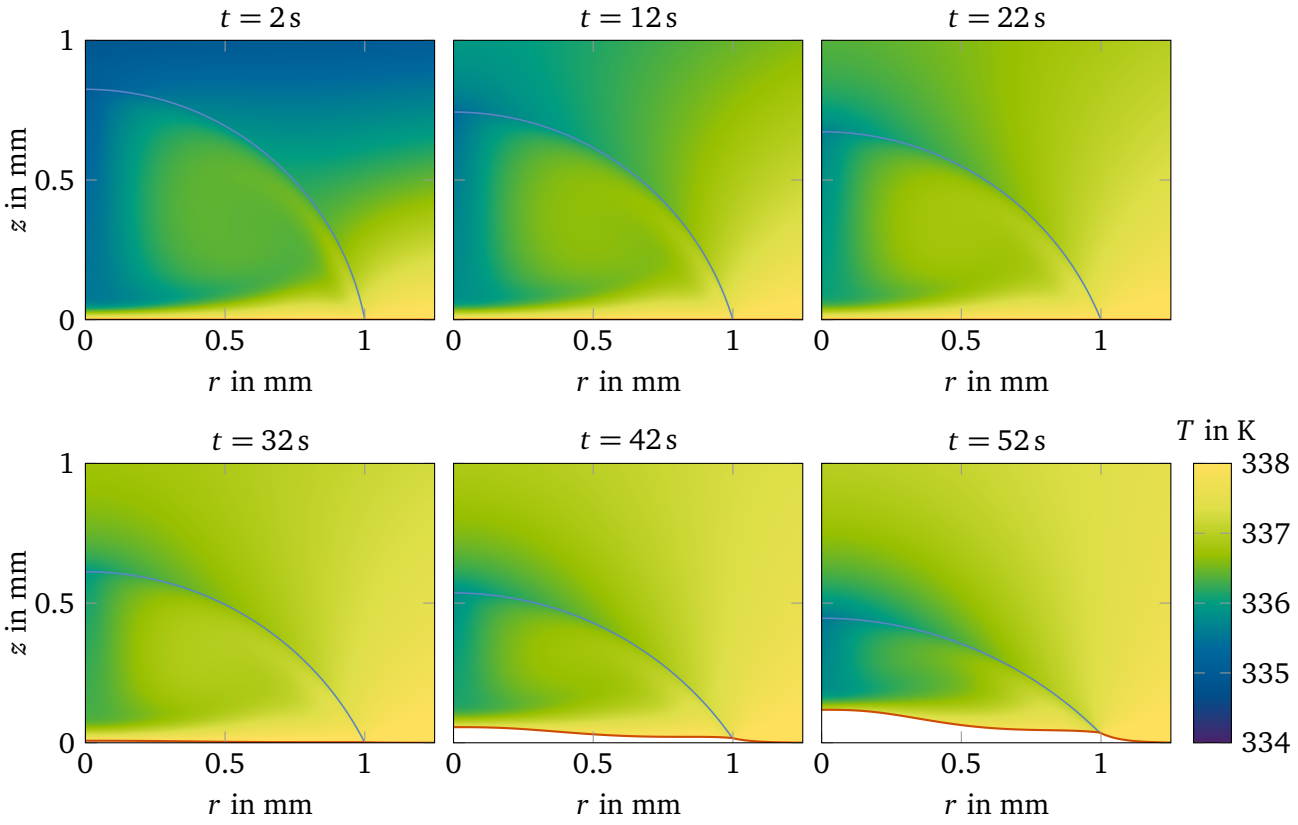

Figure 4.15: Time evolution of the temperature field in the drop and in the gas with thermal Marangoni effect.

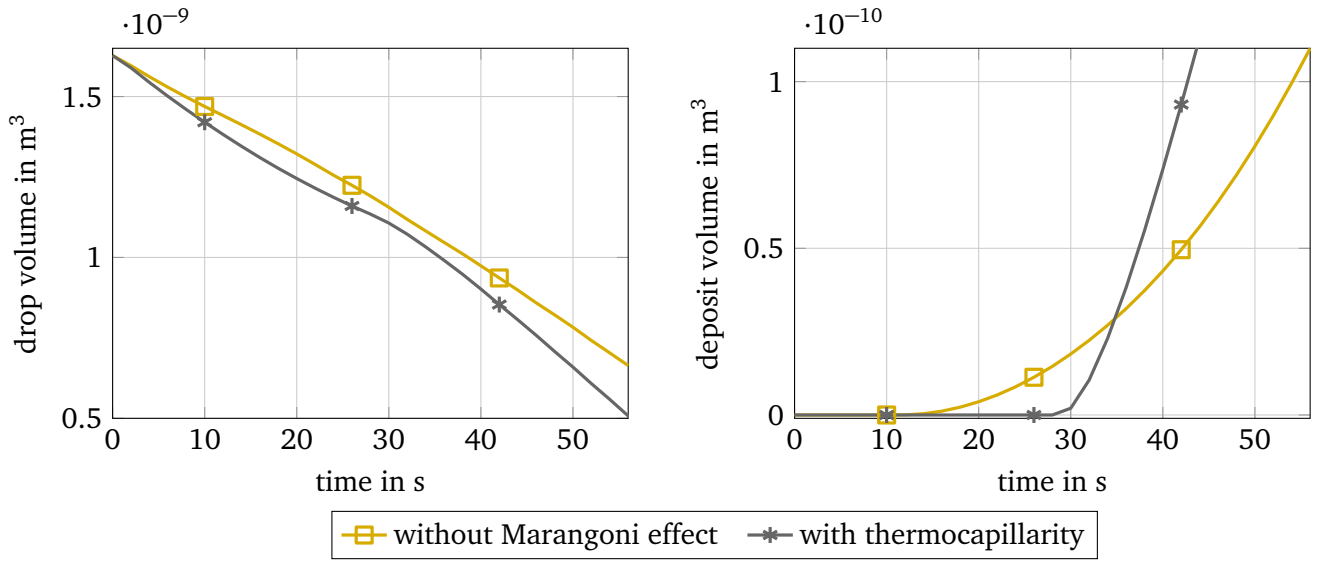

Figure 4.16: Drop volume (left) and deposit volume (right) over time with and without thermocapillarity.

The temperature profile inside the drop and the gas phase for the case when the thermal Marangoni effect is included is shown in Fig. 4.15. It is evident that the thermocapillary flow inside the drop leads to a better mixing inside the drop and to a more homogeneous temperature distribution compared to a drop without Marangoni effect (Fig. 4.6). The temperature differences in the drop are smaller and the average temperature inside the drop is higher if thermocapillarity is accounted for. Similarly, the urea mass fraction inside the drop is then more uniform. The thermocapillary flow transports the urea away from the contact line, along the interface towards the drop apex, and eventually to the drop center. This leads to the deposit growth not only in the region of the three-phase contact line but on the entire wetted area. The maximum of the deposit height can now be observed at the drop center. The deposit shape resembles a cap, which is fundamentally different from the ring-shaped deposit found without thermocapillarity.

The decrease of the drop volume over time with and without consideration of thermocapillarity is depicted in the left part of Fig. 4.16. If thermocapillarity is present, the drop evaporates faster initially, which can be explained with the faster temperature increase inside the drop and the transport of urea away from the interface through the thermocapillary flow. The evolution of the deposit height is given in the right part of Fig. 4.16. It can bee seen that the deposit formation starts earlier when no Marangoni flow is present. This is due to the peak urea mass fraction at the three-phase contact line, which is not present in the case of thermocapillarity. When the drop in the presence of Marangoni effect starts to form deposits, the deposit growth rate is much higher than for a drop without Marangoni effect so that the overall deposit volume for $t > 35\,\mathrm{s}$ is larger for the drop where thermocapillarity is present.

The deposit formation process can now explain the further progress of the drop evaporation in the left part of Fig. 4.16. When deposits are formed in the drop without Marangoni effect, the evaporation rate increases. At the same time, the urea mass fraction along the interface continuously increases for the drop with thermocapillary so that the evaporation rate declines. This is visible between $t \approx 10\,\mathrm{s}$ and $t \approx 30\,\mathrm{s}$. Finally, for $t > 30\,\mathrm{s}$ the drop subject to thermocapillarity begins to form deposits, which leads to

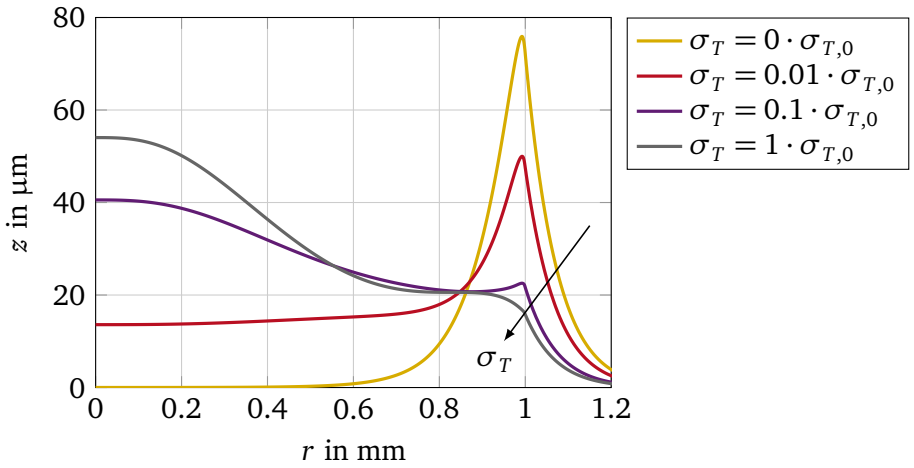

Figure 4.17: Deposit shape on the wall for varying thermocapillarity for a formed deposit volume of $9 \cdot 10^{-11}$ m^3. The three-phase contact line is at $r = 1$ mm. The arrow points in the direction of increasing thermocapillarity.

an increase of its evaporation rate. For larger times, the drop with thermocapillary evaporates faster and forms more deposits due to the higher average drop interface temperature.

It was stated above that the influence of thermocapillarity in water drops varies across experimental investigations. For this reason, the slope of the surface tension with temperature is varied in the model so that the effect of the strength of thermocapillarity on the formed deposit structure can be analyzed. The deposit shape after $9 \cdot 10^{-11}$ m^3 deposit has formed is depicted in Fig. 4.17 for varied thermocapillarity. This deposit volume is reached after between 41.5 s and 54.5 s of evaporation time. The Marangoni effect is varied between no thermocapillarity ($\sigma_T = 0 \cdot \sigma_{T,0}$) and the value observed for a pure water drop in ideal conditions ($\sigma_T = 1 \cdot \sigma_{T,0}$). The case without thermocapillarity ($\sigma_T = 0 \cdot \sigma_{T,0}$) shows the discussed ring-shaped deposit from the parametric study. As the influence of thermocapillarity is increased to $\sigma_T = 0.01 \cdot \sigma_{T,0}$, which is the fitting factor reported by Hu and Larson [108] for water drops, an influence of the Marangoni flow can already be observed. The peak of the deposit height at the three-phase contact line has decreased and deposit can be found over the entire wetted area. However, the maximum deposit height is still at the contact line. Further increasing the thermocapillarity to $\sigma_T = 0.1 \cdot \sigma_{T,0}$ and $\sigma_T = 1 \cdot \sigma_{T,0}$ leads to a continuous decrease of the deposit height at the contact line and an increase at the drop center. The deposit is now cap-shaped. This result agrees nicely with the experimental findings from Hu and Larson [108] for particle deposition, who showed that a ring-shaped deposit transitions to a uniform deposit layer and eventually to a cap-shaped deposit with increasing thermocapillarity.

The drop volume (on the left) and the deposit volume (on the right) over time is shown in Fig. 4.18 for varying wall temperatures including thermocapillarity ($\sigma_T = 1 \cdot \sigma_{T,0}$). The drop volume decreases faster with increasing wall temperatures. For all wall temperatures, the evaporation rate first decreases with time up to a certain point at which the evaporation rate suddenly increases. From this time onward, an almost linear decrease of the drop volume over time can be observed. The time at which the evaporation rate increases corresponds to the beginning of the deposit formation process, as is visible from Fig. 4.18 (right). The deposit formation begins earlier with increasing wall temperatures, similarly to a drop without accounting for thermocapillarity. Compared to a drop without thermocapillarity (Fig. 4.8), however, the

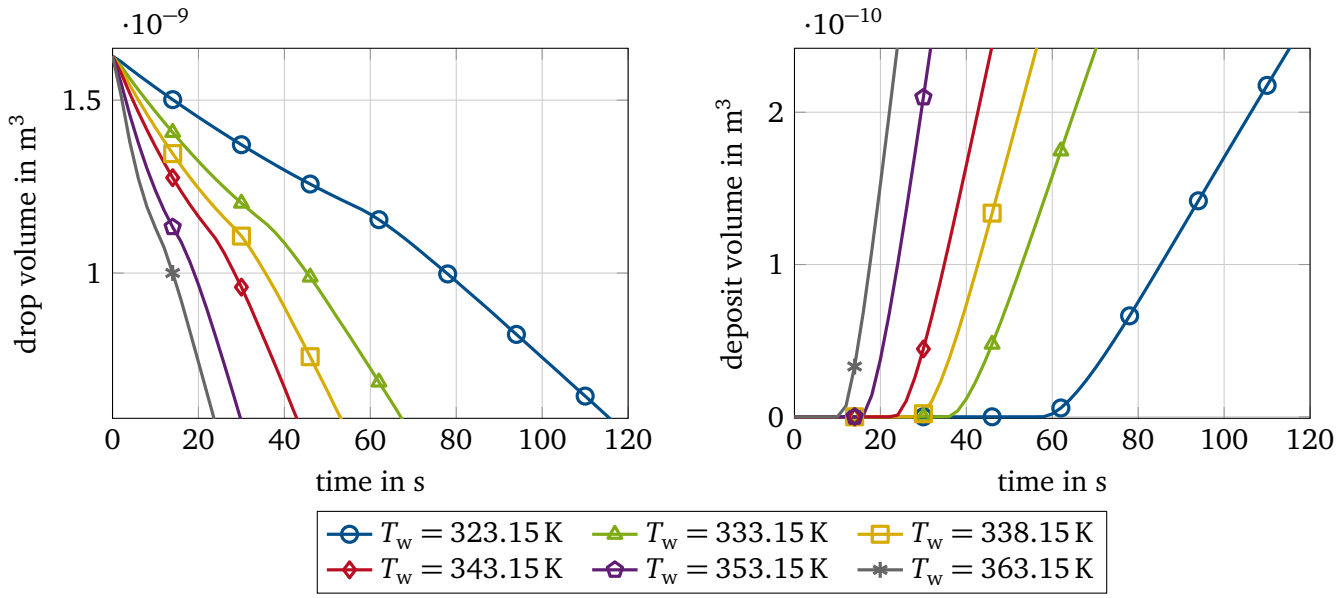

Figure 4.18: Drop volume (left) and deposit volume (right) over time for different wall temperatures and accounting for thermocapillarity ($\sigma_T = 1 \cdot \sigma_{T,0}$).

deposit formation begins later for all wall temperatures if the thermal Marangoni effect is accounted for. The speed of the deposit formation increases with time in all plots. Compared to drops without thermocapillarity, the evolution of the deposit growth rate with time is more similar for the different wall temperatures. This can be seen if the evaporation time before the deposit formation starts is subtracted for each curve, meaning that the curves are shifted relative to each other according to the onset of deposit formation. The resulting deposit shape is almost identical across all wall temperatures and resembles the cap-shaped deposit shown in Fig. 4.17. Molecular diffusion inside the drop now has no substantial influence on the deposit shape anymore. This is due to the high Péclet numbers resulting from the thermocapillary flow. The convective transport from the Marangoni flow leads to a more uniform urea concentration inside the drop – compared to a drop without thermocapillarity – and, consequently, a similar deposit shape.

4.5 Conclusions for Stage II

It was previously mentioned that the complex process of multi-component films and drops evaporating and depositing on heated structured walls can be separated into two stages for the industrial applications considered in this thesis. After the initially present thin film (stage I) has reduced to individual drops, these drops evaporate on the hot substrate and form deposits (stage II). In this chapter, a model to describe the evaporation and deposit formation process for evaporating binary drops was derived. By using an ALE method, the exact position of the interface is known and the temperature and concentration fields can be resolved in both vertical and radial direction. This allowed the studying of the influence of key parameters (wall temperature, initial drop composition, drop size) and the thermocapillarity on the evaporation and deposit formation process and on the final deposit shape. Consequently, this method is well suited to investigate the second stage of the technical problem and to deduce critical conditions and parameter ranges, which lead to the formation of deposits.

Chapter 5

Summary and Conclusions

The evaporation and deposit formation from evaporating multi-component drops and liquids is an important topic in many industrial applications. Specifically, in the automotive industry, deposit formation is found from fuel films in the combustion chamber of internal combustion engines and in the SCR exhaust gas treatment from UWS. An improved basic understanding of the process in both scenarios is desirable to increase the engine efficiency and decrease the emission of pollutants.

The evaporation and deposition process of multi-component liquid films and drops is a complex multiscale physical-chemical process. Various different phenomena influence and interact with each other and determine the overall heat and mass transfer, which makes the development of a numerical model for the entire process difficult. The approach taken in this thesis is to investigate the film stability and evolution separately from the deposit formation process since experimental investigations have shown that these two stages happen on different time scales. In the first stage (stage I), the thin liquid film evolution is investigated, until, eventually, film breakup is observed. In the second stage (stage II), which happens over longer time scales compared to the first stage, the liquid film has been reduced to individual drops evaporating on the hot surface and forming deposits. The advantage of this approach lies in the reduced complexity of the individual models, and this approach also enables picking the best suited numerical method for each stage.

Long-wave theory has proven to be a suitable method to investigate the evolution and breakup of thin liquid films (**stage I**). Evolution equations describing the identified key influences on film evolution and breakup for the industrial application were derived. These equations describe an evaporating liquid film on a heated or cooled structured wall, a film with a time-dependent chemical reaction sheared by a laminar shear stress, and a film sheared by a turbulent shear stress field. A finite difference solver was developed to solve the evolution equation for a two- or three-dimensional domain.

The results showed that high evaporation rates can be the main driver of film rupture and dominate over the influence of the Marangoni effect. However, even in the absence of evaporation, a film on a structured (or deposit covered) wall can be unstable when the film is heated from below by the hot wall. This is due to temperature gradients developing at the liquid-gas interface, which lead to thermocapillary

flow. The interactions between wall structure and evaporation are non-linear. A critical wall structure wavelength can be identified, which leads to the fastest rupture times. This critical wavelength depends on the evaporative mass flux, which makes the numerical solution of the system necessary. The point at which the rupture occurs also depends on both wall structure and phase change. If the film is heated by the ambient gas phase, the main driver of film rupture is evaporation and the film either assumes a flat interface shape or follows the shape of the structured wall, depending on the importance of the Marangoni effect.

If a chemical reaction is present in the film, stability is also affected by the heat released or consumed by the reaction. An exothermic reaction has a stabilizing effect on the film, whereas an endothermic reaction is destabilizing and might lead to film rupture. However, as the reaction rate decays while more and more educt is consumed, not every endothermic reaction leads to film breakup. It was found that the growth rate of the film height disturbances depends on the wavelength of the initial film disturbance and on time. In combination with an existing film disturbance, a laminar shear stress at the interface can affect the film evolution.

A new model was developed to investigate the response of a thin liquid film to turbulent shear stress fluctuations. The turbulent gas flow was simulated with a DNS and the time- and position-dependent shear stress field was stored with a high resolution. This was then used as the boundary condition to evaluate the response of the film to the turbulent flow with LWT. It was found that the film height maximum initially increases quickly with time before a force balance is reached and the film height maximum fluctuates around a mean value. The length and time scales of the turbulent structures play an important role and the response of the liquid film cannot be accurately deduced just from average shear stress values. Additionally, it was found that the film height disturbances form streaks in streamwise direction with increasing time, while the extent of the disturbances perpendicular to the main flow direction is similar to the shear stress structures. Interestingly, the interface structures travel downstream at a much slower velocity than the convection velocity of the turbulent shear stress. A linear analysis revealed that the amplitude of the waves of the film height deformations depends primarily on the velocity difference between the propagating shear stress wave and the interface velocity. This makes an accurate resolution of the fluctuating shear stress fields necessary. It was shown that LES can be used together with LWT instead of DNS and LWT to compute the film response to the turbulent shear stress field with a substantial reduction in computational cost if attention is paid that the turbulent shear stress field in the vicinity of the liquid film is accurately resolved.

Overall, the analysis of the first stage of the process shows that the various physical parameters, which influence the film, interact strongly with each other and that their interplay makes it necessary to calculate a numerical solution of the evolution equation in order to deduct the response of the liquid film. LWT was found to be a very suitable method for this stage. The time scale of the observed film deformation and rupture times for the investigated scenarios is $\mathcal{O}(10^{-2} - 10^{0}\,\mathrm{s})$.

The evaporation and deposit formation from suspended drops, which form after the previously considered film has ruptured, was investigated in the second step (**stage II**). A numerical model was developed to simulate evaporation and heterogeneous crystallization of a binary drop. Specifically, the model was applied to drops of UWS. An ALE method with a moving mesh was used to track the interface position and

deposit shape. This, together with a fine spatial discretization, allowed the resolution of the temperature and concentration fields at the interface and around the deposit. The computational domain was deformed to follow the deposit shape and to include the influence of the deposit layer on the drop. The drop evaporation model was validated against correlations and experimental results.

The results showed that, if thermocapillarity can be neglected, the maximum of the evaporation rate at the three-phase contact line leads to an increase of the urea mass fraction in this area. Consequently, when the saturation concentration is exceeded, the three-phase contact line is the position where the deposit formation begins and a ring-shaped deposit results. The evaporation rate of the drop depends both on the urea concentration at the interface and on the presence of deposits. The enthalpy of solution was found to have a negligible influence on the temperature field inside the drop, while the heat conduction through the deposit affects the liquid temperature above the deposit.

A parametric study showed that the wall temperature has a strong influence on the drop evaporation and deposition. With increasing wall temperature and increasing evaporation rates, the deposit formation process starts earlier. The deposit growth rate was found to increase with time as soon as the first deposit was formed. The shape of the resulting deposit also depends on the wall temperature. Diffusive mass transport inside the drop becomes more important with decreasing wall temperature and leads to a wider and lower deposit ring. With rising initial urea mass fraction, an earlier start of deposition is found. However, as soon as the first deposits are formed, the deposit growth rates and resulting deposit shapes are very similar, unless the initial urea mass fraction is very close to the saturation mass fraction. The initial drop radius also affects the deposit formation process, which makes a detailed numerical investigation of each specific configuration necessary. Still, a first correlation to predict the starting time of deposit formation was derived. The time scales of the drop evaporation process and the beginning of deposit growth are in the range of $\mathcal{O}(10^1 - 10^2\,\mathrm{s})$.

Thermocapillary flow inside the evaporating drop leads to more uniform temperature and concentration fields inside the drop compared to a drop without accounting for the Marangoni effect. If thermocapillary flow is present, the overall higher interface temperature causes an increase of the evaporation rate. The uniform distribution of urea results in the initial deposit growth almost simultaneously over the entire wetted area. The more uniform concentration field also leads to a later beginning of the deposit formation process compared to a drop without consideration for thermocapillarity. The deposit shape transitions from the ring-shaped deposit through an almost uniform deposit layer to a cap-shaped deposit with increasing importance of the thermal Marangoni effect. It was shown that the wall temperature is still a major influence on the beginning of the deposit formation, in this case.

In conclusion, the analysis of the two stages has confirmed the complexity of the problem and the importance of including all key influencing parameters and their interactions. However, suitable models were developed in this work for both stages and used to enhance the general understanding of the physical-chemical process.

Chapter 6

Outlook

Future research based on the results of this work and with the developed models will be conducted. The separation of the process into the two stages deducted and described in this thesis can be kept to include further physical phenomena and to conduct parametric studies.

The evolution equation for investigation of the stability and evolution of thin liquid films can be extended to include more physical processes and their interactions. This includes the effect of turbulent pressure fluctuations. Additionally, when the reaction mechanism leading to deposit formation is clear, it can be included into the long-wave model and its impact can be evaluated. The effect of the deposit porosity on the film flow can also be examined. The influence of diffusive mass transport within the film and of solutocapillarity on the film stability should be considered for multi-component mixtures. Parametric studies can also be performed for different fuels, including e-fuels, as well as urea-water solutions.

The investigation of the deposit formation process from evaporating drops can be extended to deposition not only from crystallization but also from polymerization and chemical reactions. This will allow the investigation of the deposit formation for fuel drops. However, the challenge remains that a large number of drops are necessary to form a relevant deposit structure in these circumstances. Additionally, the reaction mechanism, which leads to deposit formation, has to be known for each fuel. The effect of solutocapillarity on the evaporation process and the resulting deposit shape should also be considered, in this stage.

Critical conditions and parameter ranges, which lead to the formation of deposits, follow from parametric studies. Eventually, when the influence of the individual parameters on the deposit formation process for each fluid is sufficiently evaluated for both stages, an overall model for the evaporation and deposit formation process from multi-component films can be developed. This model will then only need to include the physical phenomena and interactions, which were found to be relevant from the parametric studies of the individual stages. LWT could be used for this overall model, as it makes the inclusion and variation of physical processes easy and is not too costly in terms of computational effort.

With the gained understanding of the process through the parameter studies and with the developed models, correlations for the influence of local parameters on the process can be developed. Combining the insight from experimental investigations and the numerical model, guidelines and strategies to control and potentially avoid deposit formation can be deduced. This will help with increasing the efficiency and decreasing the amounts of pollutants emitted from internal combustion engines. The general understanding of the underlying physical processes, however, will also be beneficial for other industrial applications.

Bibliography

[1] M. Ait Saada, S. Chikh, and L. Tadrist. Numerical investigation of heat and mass transfer of an evaporating sessile drop on a horizontal surface. *Physics of Fluids*, 22(11):112115, 2010.

[2] M. Ait Saada, S. Chikh, and L. Tadrist. Evaporation of a sessile drop with pinned or receding contact line on a substrate with different thermophysical properties. *International Journal of Heat and Mass Transfer*, 58(1):197–208, 2013.

[3] V. S. Ajaev, T. Gambaryan-Roisman, and P. Stephan. Static and dynamic contact angles of evaporating liquids on heated surfaces. *Journal of Colloid and Interface Science*, 342(2):550–558, 2010.

[4] V. S. Ajaev, J. Klentzman, T. Gambaryan-Roisman, and P. Stephan. Fingering instability of partially wetting evaporating liquids. *Journal of Engineering Mathematics*, 73(1):31–38, 2012.

[5] S. P. Aktershev and S. V. Alekseenko. Influence of condensation on the stability of a liquid film moving under the effect of gravity and turbulent vapor flow. *International Journal of Heat and Mass Transfer*, 48(6):1039–1052, 2005.

[6] M. Al Qubeissi, N. Al-Esawi, S. S. Sazhin, and M. Ghaleeh. Ethanol/Gasoline Droplet Heating and Evaporation: Effects of Fuel Blends and Ambient Conditions. *Energy and Fuels*, 32(6):6498–6506, 2018.

[7] S. Alekseenko, V. Antipin, A. Cherdantsev, S. Kharlamov, and D. Markovich. Two-wave structure of liquid film and wave interrelation in annular gas-liquid flow with and without entrainment. *Physics of Fluids*, 21(6):061701, 2009.

[8] S. V. Alekseenko and V. E. Nakoryakov. Instability of a liquid film moving under the effect of gravity and gas flow. *International Journal of Heat and Mass Transfer*, 38(11):2127–2134, 1995.

[9] S. V. Alekseenko, D. M. Markovich, S. M. Kharlamov, and A. V. Cherdantsev. Experimental Study of the Linear Stability of a Falling Liquid Film in the Presence of a Turbulent Gas Stream. *Fluid Dynamics*, 39(4):612–620, 2004.

[10] S. V. Alekseenko, S. P. Aktershev, A. V. Cherdantsev, S. M. Kharlamov, and D. M. Markovich. Primary instabilities of liquid film flow sheared by turbulent gas stream. *International Journal of Multiphase Flow*, 35(7):617–627, 2009.

[11] American Society of Heating, Refrigerating and Air-Conditioning Engineers. *ASHRAE Handbook–Fundamentals*. Atlanta, Ga, 1993. ISBN 978-1939200570.

[12] O. Andersson and R. G. Ross. Phase behavior and thermal conductivity of urea at pressures up to 1 GPa and at temperatures in the range 50-370 K. *International Journal of Thermophysics*, 15(3): 513–524, 1994.

[13] A. A. Aradi, B. Imoehl, N. L. Avery, P. P. Wells, and R. W. Grosser. The Effect of Fuel Composition and Engine Operating Parameters on Injector Deposits in a High-Pressure Direct Injection Gasoline (DIG) Research Engine. In *SAE Technical Paper, 1999-01-3690*. SAE International, 1999.

[14] C. D. Argyropoulos and N. C. Markatos. Recent advances on the numerical modelling of turbulent flows. *Applied Mathematical Modelling*, 39(2):693–732, 2015.

[15] Y. M. Arifin and M. Arai. Deposition characteristics of diesel and bio-diesel fuels. *Fuel*, 88(11): 2163–2170, 2009.

[16] Y. M. Arifin and M. Arai. The effect of hot surface temperature on diesel fuel deposit formation. *Fuel*, 89(5):934–942, 2010.

[17] Y. M. Arifin, T. Furuhata, M. Saito, and M. Arai. Diesel and bio-diesel fuel deposits on a hot surface. *Fuel*, 87(8-9):1601–1609, 2008.

[18] D. C. Arters and M. J. Macduff. The Effect on Vehicle Performance of Injector Deposits in a Direct Injection Gasoline Engine. In *SAE Technical Paper, 2001-02-2021*. SAE International, 2000.

[19] D. C. Arters, E. A. Bardasz, E. A. Schiferl, and D. W. Fisher. A Comparison of Gasoline Direct Injection and Port Fuel Injection Vehicles; Part I–Fuel System Deposits and Vehicle Performance. In *SAE Technical Paper, 1999-01-1498*. SAE International, 1999.

[20] T. Ashida, Y. Takei, and H. Hosi. Effects of Fuel Properties on SIDI Fuel Injector Deposit. In *SAE Technical Paper, 2001-01-3694*. SAE International, 2001.

[21] A. Askounis, D. Orejon, V. Koutsos, K. Sefiane, and M. E. R. Shanahan. Nanoparticle deposits near the contact line of pinned volatile droplets: size and shape revealed by atomic force microscopy. *Soft Matter*, 7:4152–4155, 2011.

[22] A. A. Ayati, P. S. C. Farias, L. F. A. Azevedo, and I. B. de Paula. Characterization of linear interfacial waves in a turbulent gas-liquid pipe flow. *Physics of Fluids*, 29(6):062106, 2017.

[23] B. J. Azzopardi. Disturbance wave frequencies, velocities and spacing in vertical annular two-phase flow. *Nuclear Engineering and Design*, 92(2):121–133, 1986.

[24] H. D. Baehr and K. Stephan. *Heat and Mass Transfer*. Springer-Verlag Berlin Heidelberg, third edition, 2011. ISBN 978-3642200205.

[25] S. Z. Bai, S. G. Lang, K. P. Yuan, Y. Liu, and G. X. Li. Experimental Study of Urea Depositions in Urea-SCR System. *Advanced Materials Research*, 937:74–79, 2014.

[26] A. Basit, P. Siwayanan, K. KuShaari, L. K. Keong, and B. Azeem. An investigation on dissolutive wetting of porous urea surface. *The Canadian Journal of Chemical Engineering*, 96(12):2690–2699, 2018.

[27] Ü. Bayram, E. Öztürk, S. Aksöz, and N. Maraşlı. Measurements of Thermal Conductivity Variations with Temperature for the Organic Analog of the Nonmetal–Nonmetal System: Urea–4-Bromo-2-Nitroaniline. *Metallurgical and Materials Transactions A*, 44(9):4051–4058, 2013.

[28] A. Bender, P. Stephan, and T. Gambaryan-Roisman. Thin liquid films with time-dependent chemical reactions sheared by an ambient gas flow. *Physical Review Fluids*, 2(8):084002, 2017.

[29] A. Bender, P. Stephan, and T. Gambaryan-Roisman. Numerical investigation of stability and evolution of an evaporating liquid film on a heated structured wall. In *Proceedings of CHT-17 ICHMT International Symposium on Advances in Computational Heat Transfer, Napoli, Italy, May 28 – June 1*. Begell House, 2017.

[30] A. Bender, P. Hänichen, P. Stephan, and T. Gambaryan-Roisman. Modeling crystallization and heat transfer in an evaporating urea-water drop. In *Proceedings of the International Heat Transfer Conference 16, Beijing, China, August 10–15*. Begell House, 2018.

[31] A. Bender, P. Stephan, and T. Gambaryan-Roisman. Numerical investigation of the evolution and breakup of an evaporating liquid film on a structured wall. *International Journal of Heat and Fluid Flow*, 70:104–113, 2018.

[32] A. Bender, A. Stroh, B. Frohnapfel, P. Stephan, and T. Gambaryan-Roisman. Combined direct numerical simulation and long-wave simulation of a liquid film sheared by a turbulent gas flow in a channel. *Physics of Fluids*, 31(2):022103, 2019.

[33] F. Birkhold, U. Meingast, P. Wassermann, and O. Deutschmann. Analysis of the Injection of Urea-Water-Solution for Automotive SCR DeNOx-Systems: Modeling of Two-Phase Flow and Spray/Wall-Interaction. In *SAE Technical Paper, 2006-01-0643*. SAE International, 2006.

[34] F. Birkhold, U. Meingast, P. Wassermann, and O. Deutschmann. Modeling and simulation of the injection of urea-water-solution for automotive SCR DeNOx-systems. *Applied Catalysis B: Environmental*, 70(1-4):119–127, 2007.

[35] D. Bonn, J. Eggers, J. Indekeu, J. Meunier, and E. Rolley. Wetting and spreading. *Reviews of Modern Physics*, 81:739–805, 2009.

[36] P. A. M. Boomkamp and R. H. M. Miesen. Classification of instabilities in parallel two-phase flow. *International Journal of Multiphase Flow*, 22:67–88, 1996.

[37] M. Börnhorst, S. Langheck, H. Weickenmeier, C. Dem, R. Suntz, and O. Deutschmann. Characterization of solid deposits from urea water solution injected into a hot gas test rig. *Chemical Engineering Journal*, 377:119855, 2019.

[38] W. Bou Zeid and D. Brutin. Influence of relative humidity on spreading, pattern formation and adhesion of a drying drop of whole blood. *Colloids and Surfaces A: Physicochemical and Engineering Aspects*, 430:1–7, 2013.

[39] W. Brack. *Untersuchung der Ablagerungsbildung durch Harnstofffolgeprodukte im Abgasstrang*. PhD thesis, Karlsruher Institut für Technologie, 2016.

[40] W. Brack, B. Heine, F. Birkhold, M. Kruse, G. Schoch, S. Tischer, and O. Deutschmann. Kinetic modeling of urea decomposition based on systematic thermogravimetric analyses of urea and its most important by-products. *Chemical Engineering Science*, 106:1–8, 2014.

[41] W. Brack, B. Heine, F. Birkhold, M. Kruse, and O. Deutschmann. Formation of Urea-Based Deposits in an Exhaust System: Numerical Predictions and Experimental Observations on a Hot Gas Test Bench. *Emission Control Science and Technology*, 2(3):115–123, 2016.

[42] R. J. Braun, B. T. Murray, W. J. Boettinger, and G. B. McFadden. Lubrication theory for reactive spreading of a thin drop. *Physics of Fluids*, 7(8):1797–1810, 1995.

[43] M. Brocchini and D. H. Peregrine. The dynamics of strong turbulence at free surfaces. Part 1. Description. *Journal of Fluid Mechanics*, 449:225–254, 2001.

[44] D. Brutin. *Droplet Wetting and Evaporation: From Pure to Complex Fluids*. Elsevier, 2015. ISBN 978-0128007228.

[45] D. Brutin and V. Starov. Recent advances in droplet wetting and evaporation. *Chemical Society Reviews*, 47:558–585, 2018.

[46] D. Brutin, B. Sobac, B. Loquet, and J. Sampol. Pattern formation in drying drops of blood. *Journal of Fluid Mechanics*, 667:85–95, 2011.

[47] M. Budakli. *Hydrodynamics and Heat Transfer in Gas-Driven Liquid Film Flows*. PhD thesis, Technische Universität Darmstadt, 2015.

[48] J. P. Burelbach, S. G. Bankoff, and S. H. Davis. Nonlinear stability of evaporating/condensing liquid films. *Journal of Fluid Mechanics*, 195:463–494, 1988.

[49] F. Carle, S. Semenov, M. Medale, and D. Brutin. Contribution of convective transport to evaporation of sessile droplets: Empirical model. *International Journal of Thermal Sciences*, 101:35–47, 2016.

[50] I. B. Celik, U. Ghia, P. J. Roache, H. W. Coleman, and P. E. Raad. Procedure for Estimation and Reporting of Uncertainty Due to Discretization in CFD Applications. *Journal of Fluids Engineering*, 130(7):078001, 2008.

[51] S.-w. S. Cheng. The Impacts of Engine Operating Conditions and Fuel Compositions on the Formation of Combustion Chamber Deposits. In *SAE Technical Paper, 2000-01-2025*. SAE International, 2000.

[52] S.-w. S. Cheng and C. Kim. Effect of Engine Operating Parameters on Engine Combustion Chamber Deposits. In *SAE Technical Paper, 902108*. SAE International, 1990.

[53] J. R. E. Christy, K. Sefiane, and E. Munro. A Study of the Velocity Field during Evaporation of Sessile Water and Water/Ethanol Drops. *Journal of Bionic Engineering*, 7(4):321–328, 2010.

[54] P. Colinet, J. C. Legros, and M. G. Velarde. *Nonlinear Dynamics of Surface-Tension-Driven Instabilities*. John Wiley & Sons, Ltd, first edition, 2001. ISBN 978-3527402915.

[55] Collaborative Research Centre/Transregio 150. Turbulent, chemically reactive, multi-phase flows near walls. *https://www.trr150.tu-darmstadt.de/der_sonderforschungsbereich/CRC.en.jsp*, (opened on 04.10.2019).

[56] B. Cox, C. L. Mutel, C. Bauer, A. Mendoza Beltran, and D. P. van Vuuren. Uncertain Environmental Footprint of Current and Future Battery Electric Vehicles. *Environmental Science & Technology*, 52 (8):4989–4995, 2018.

[57] R. V. Craster and O. K. Matar. Dynamics and stability of thin liquid films. *Reviews of Modern Physics*, 81(3):1131–1198, 2009.

[58] X. Cui, X. Li, H. Sui, and H. Li. Computational fluid dynamics simulations of direct contact heat and mass transfer of a multicomponent two-phase film flow in an inclined channel at sub-atmospheric pressure. *International Journal of Heat and Mass Transfer*, 55(21):5808–5818, 2012.

[59] Z. Dagan and L. M. Pismen. Marangoni Waves Induced by a Multistable Chemical Reaction on Thin Liquid Films. *Journal of Colloid and Interface Science*, 99(1):215–225, 1984.

[60] B. A. Davis and M. A. Figliozzi. A methodology to evaluate the competitiveness of electric delivery trucks. *Transportation Research Part E: Logistics and Transportation Review*, 49(1):8–23, 2013.

[61] R. D. Deegan, O. Bakajin, T. F. Dupont, G. Huber, S. R. Nagel, and T. A. Witten. Capillary flow as the cause of ring stains from dried liquid drops. *Nature*, 389:827–829, 1997.

[62] R. D. Deegan, O. Bakajin, T. F. Dupont, G. Huber, S. R. Nagel, and T. A. Witten. Contact line deposits in an evaporating drop. *Physical Review E*, 62(1):756–765, 2000.

[63] B. Derby. Inkjet Printing of Functional and Structural Materials: Fluid Property Requirements, Feature Stability, and Resolution. *Annual Review of Materials Research*, 40(1):395–414, 2010.

[64] M. Dondlinger, J. Margerit, and P. C. Dauby. Weakly nonlinear study of Marangoni instabilities in an evaporating liquid layer. *Journal of Colloid and Interface Science*, 283:522–532, 2005.

[65] J. Donea, A. Huerta, J.-P. Ponthot, and A. Rodríguez-Ferran. *Arbitrary Lagrangian–Eulerian Methods*, chapter 14. American Cancer Society, 2004. ISBN 978-0470091357.

[66] F. Doumenc and B. Guerrier. Self-patterning induced by a solutal Marangoni effect in a receding drying meniscus. *EPL (Europhysics Letters)*, 103(1):14001, 2013.

[67] M. C. Drake, T. D. Fansler, A. S. Solomon, and G. A. Szekely Jr. Piston Fuel Films as a Source of Smoke and Hydrocarbon Emissions from a Wall-Controlled Spark-Ignited Direct-Injection Engine. In *SAE Technical Paper, 2003-01-0547*. SAE International, 2003.

[68] P. G. Drazin. *Introduction to Hydrodynamic Stability*. Cambridge Texts in Applied Mathematics. Cambridge University Press, 2002. ISBN 978-0511809064.

[69] G. J. Dunn, S. K. Wilson, B. R. Duffy, S. David, and K. Sefiane. The strong influence of substrate conductivity on droplet evaporation. *Journal of Fluid Mechanics*, 623:329–351, 2009.

[70] V. Ebrahimian, A. Nicolle, and C. Habchi. Detailed modeling of the evaporation and thermal decomposition of urea-water solution in SCR systems. *AIChE Journal*, 58(7):1998–2009, 2012.

[71] R. Eötvös. Ueber den Zusammenhang der Oberflächenspannung der Flüssigkeiten mit ihrem Molecularvolumen. *Annalen der Physik*, 263:448–459, 1886.

[72] H. Y. Erbil. Evaporation of pure liquid sessile and spherical suspended drops: A review. *Advances in Colloid and Interface Science*, 170(1-2):67–86, 2012.

[73] M. H. Eres, D. E. Weidner, and L. W. Schwartz. Three-Dimensional Direct Numerical Simulation of Surface-Tension-Gradient Effects on the Leveling of an Evaporating Multicomponent Fluid. *Langmuir*, 15(5):1859–1871, 1999.

[74] P. Forooghi, A. Weidenlener, F. Magagnato, B. Böhm, H. Kubach, T. Koch, and B. Frohnapfel. DNS of momentum and heat transfer over rough surfaces based on realistic combustion chamber deposit geometries. *International Journal of Heat and Fluid Flow*, 69:83–94, 2018.

[75] A. M. Frank. Shear driven solitary waves on a liquid film. *Physical Review E*, 74:065301, 2006.

[76] L. Frastia, A. J. Archer, and U. Thiele. Dynamical Model for the Formation of Patterned Deposits at Receding Contact Lines. *Physical Review Letters*, 106:077801, 2011.

[77] Ľ. Fraštia, A. J. Archer, and U. Thiele. Modelling the formation of structured deposits at receding contact lines of evaporating solutions and suspensions. *Soft Matter*, 8(44):11363, 2012.

[78] M. Fulgosi, D. Lakehal, S. Banerjee, and V. De Angelis. Direct numerical simulation of turbulence in a sheared air-water flow with a deformable interface. *Journal of Fluid Mechanics*, 482:319–345, 2003.

[79] D. Gallez, A. De Wit, and M. Kaufman. Dynamics of a Thin Liquid Film with a Surface Chemical Reaction. *Journal of Colloid and Interface Science*, 180(2):524–536, 1996.

[80] T. Gambaryan-Roisman. Modulation of Marangoni convection in liquid films. *Advances in Colloid and Interface Science*, 222:319–331, 2015.

[81] T. Gambaryan-Roisman and P. Stephan. Analysis of Falling Film Evaporation on Grooved Surfaces. *Journal of Enhanced Heat Transfer*, 10(4):445–457, 2003.

[82] T. Gambaryan-Roisman and P. Stephan. Interface Dynamics and Heat Transfer in Evaporating Liquid Films on Microstructured Surfaces. In *Proceedings of the International Heat Transfer Conference 13, Sydney, Australia, August 13–18*. Begell House, 2006.

[83] T. Gambaryan-Roisman, A. Alexeev, and P. Stephan. Effect of the microscale wall topography on the thermocapillary convection within a heated liquid film. *Experimental Thermal and Fluid Science*, 29:765–772, 2005.

[84] P. H. Gaskell, P. K. Jimack, M. Sellier, and H. M. Thompson. Flow of evaporating, gravity-driven thin liquid films over topography. *Physics of Fluids*, 18(1):013601, 2006.

[85] M. Gerendas and S. Wittig. Experimental and Numerical Investigation on the Evaporation of Shear-Driven Multicomponent Liquid Wall Films. *Journal of Engineering for Gas Turbines and Power*, 123(3):580–588, 2001.

[86] F. Girard, M. Antoni, and K. Sefiane. On the Effect of Marangoni Flow on Evaporation Rates of Heated Water Drops. *Langmuir*, 24(17):9207–9210, 2008.

[87] F. Girard, M. Antoni, and K. Sefiane. Infrared Thermography Investigation of an Evaporating Sessile Water Droplet on Heated Substrates. *Langmuir*, 26(7):4576–4580, 2010.

[88] H. M. Gorr, J. M. Zueger, D. R. McAdams, and J. A. Barnard. Salt-induced pattern formation in evaporating droplets of lysozyme solutions. *Colloids and Surfaces B: Biointerfaces*, 103:59–66, 2013.

[89] B. S. Greensfelder, H. H. Voge, and G. M. Good. Catalytic and Thermal Cracking of Pure Hydrocarbons: Mechanisms of Reaction. *Industrial and Engineering Chemistry*, 41(11):2573–2584, 1949.

[90] M. Gryta. Fouling in direct contact membrane distillation process. *Journal of Membrane Science*, 325(1):383–394, 2008.

[91] O. Güralp, M. Hoffman, D. N. Assanis, Z. Filipi, T.-W. Kuo, P. Najt, and R. Rask. Characterizing the Effect of Combustion Chamber Deposits on a Gasoline HCCI Engine. In *SAE Technical Paper, 2006-01-3277*. SAE International, 2006.

[92] O. Güralp, P. Najt, and Z. S. Filipi. Method for Determining Instantaneous Temperature at the Surface of Combustion Chamber Deposits in an HCCI Engine. *Journal of Engineering for Gas Turbines and Power*, 135(8):081501, 2013.

[93] P. W. Guthrie. A Review of Fuel, Intake and Combustion System Deposit Issues Relevant to 4-Stroke Gasoline Direct Fuel Injection Engines. In *SAE Technical Paper, 2001- 01-1202*. SAE International, 2001.

[94] S. Halonen, T. Kangas, M. Haataja, and U. Lassi. Urea-Water-Solution Properties: Density, Viscosity, and Surface Tension in an Under-Saturated Solution. *Emission Control Science and Technology*, 3 (2):161–170, 2017.

[95] Y. Hamamoto, J. R. E. Christy, and K. Sefiane. The Flow Characteristics of an Evaporating Ethanol Water Mixture Droplet on a Glass Substrate. *Journal of Thermal Science and Technology*, 7(3): 425–436, 2012.

[96] P. Hänichen, M. van Eyk, and P. Stephan. Experimental investigations of fuel film evaporation with deposit formation. *International Journal of Heat and Fluid Flow*, 70:125–130, 2018.

[97] P. Hänichen, A. Bender, B. Voß, T. Gambaryan-Roisman, and P. Stephan. Drop evaporation of hydrocarbon fluids with deposit formation. *International Journal of Heat and Mass Transfer*, 128: 115–124, 2019.

[98] B. Haut and P. Colinet. Surface-tension-driven instabilities of a pure liquid layer evaporating into an inert gas. *Journal of Colloid and Interface Science*, 285:296–305, 2005.

[99] K. Helbig. *Messung zur Hydrodynamik und zum Wärmetransport bei der Filmverdampfung*. PhD thesis, Technische Universität Darmstadt, 2007.

[100] K. Helbig, A. Alexeev, T. Gambaryan-Roisman, and P. Stephan. Evaporation of Falling and Shear-Driven Thin Films on Smooth and Grooved Surfaces. *Flow, Turbulence and Combustion*, 75:85–104, 2005.

[101] L. Hentschel, K. Michels, T. Garbe, and M. Hönig. E-fuels – a central module for future engine design? In *Proceedings of Internationaler Motorenkongress 2018*. Springer Fachmedien Wiesbaden, 2018.

[102] M. Herrmann and M. Gorokhovski. A Large Eddy Simulation Subgrid Model for Turbulent Phase Interface Dynamics. In *Proceedings of the 11th Triennial International Annual Conference on Liquid Atomization and Spray Systems, Vail, CO, USA, July 26–30*, 2009.

[103] G. F. Hewitt. *Measurement of Two Phase Flow Parameters*. Academic Press, New York, 1978. ISBN 978-0123462602.

[104] G. F. Hewitt and P. M. C. Lacey. The breakdown of the liquid film in annular two-phase flow. *International Journal of Heat and Mass Transfer*, 8(5):781–791, 1965.

[105] C. W. Hirt, A. A. Amsden, and J. L. Cook. An Arbitrary Lagrangian-Eulerian Computing Method for All Flow Speeds. *Journal of Computational Physics*, 14:227–253, 1974.

[106] A. B. Hopwood, S. Chynoweth, and G. T. Kalghatgi. A Technique to Measure Thermal Diffusivity and Thickness of Combustion Chamber Deposits In-Situ. In *SAE Technical Paper, 982590*. SAE International, 1998.

[107] H. Hu and R. G. Larson. Evaporation of a Sessile Droplet on a Substrate. *The Journal of Physical Chemistry B*, 106(6):1334–1344, 2002.

[108] H. Hu and R. G. Larson. Marangoni Effect Reverses Coffee-Ring Depositions. *The Journal of Physical Chemistry B*, 110(14):7090–7094, 2006.

[109] J. N. Israelachvili. *Intermolecular And Surface Forces: With Applications To Colloidal And Biological Systems*. Academic Press, London, 1992. ISBN 978-0123751812.

[110] H. Jasak. *Error Analysis and Estimation for the Finite Volume Method with Applications to Fluid Flows*. PhD thesis, University of London, 1996.

[111] L. A. Jurman and M. J. McCready. Study of waves on thin liquid films sheared by turbulent gas flows. *Physics of Fluids A: Fluid Dynamics*, 1(3):522–536, 1989.

[112] O. A. Kabov. Interfacial Thermal Fluid Phenomena in Thin Liquid Films. In *Proceedings of the 14th International Heat Transfer Conference, Washington, DC, USA, August 8–13*, volume 8. ASME, 2010.

[113] O. A. Kabov, Y. V. Lyulin, I. V. Marchuk, and D. V. Zaitsev. Locally heated shear-driven liquid films in microchannels and minichannels. *International Journal of Heat and Fluid Flow*, 28(1):103–112, 2007.

[114] O. A. Kabov, E. Y. Gatapova, and D. V. Zaitsev. Cooling technique based on evaporation of thin and ultra thin liquid films. In *Proceedings of the 11th Intersociety Conference on Thermal and Thermomechanical Phenomena in Electronic Systems, Orlando, FL, USA, May 28–31*, pages 520–527. IEEE, 2008.

[115] O. A. Kabov, D. V. Zaitsev, V. V. Cheverda, and A. Bar-Cohen. Evaporation and flow dynamics of thin, shear-driven liquid films in microgap channels. *Experimental Thermal and Fluid Science*, 35 (5):825–831, 2011.

[116] Y. Kabova, V. V. Kuznetsov, O. Kabov, T. Gambaryan-Roisman, and P. Stephan. Evaporation of a thin viscous liquid film sheared by gas in a microchannel. *International Journal of Heat and Mass Transfer*, 68:527–541, 2014.

[117] Y. O. Kabova, A. Alexeev, T. Gambaryan-Roisman, and P. Stephan. Thermocapillarity-induced vortexes and liquid film dynamics on structured heated walls. *Journal of Non-Equilibrium Thermodynamics*, 30(3):225–241, 2005.

[118] Y. O. Kabova, A. Alexeev, T. Gambaryan-Roisman, and P. Stephan. Marangoni-induced deformation and rupture of a liquid film on a heated microstructured wall. *Physics of Fluids*, 18(1):012104, 2006.

[119] G. Kalghatgi. *Fuel/Engine Interactions*. SAE International, Warrendale, Pennsylvania, USA, 2013. ISBN 978-0768064582.

[120] G. T. Kalghatgi. Combustion Chamber Deposits in Spark-Ignition Engines: A Literature Review. In *SAE Technical Paper, 952443*. SAE International, 1995.

[121] G. Karapetsas, K. C. Sahu, and O. K. Matar. Evaporation of Sessile Droplets Laden with Particles and Insoluble Surfactants. *Langmuir*, 32(27):6871–6881, 2016.

[122] K. Kawahara and C. Tanford. Viscosity and Density of Aqueous Solutions of Urea and Guanidine Hydrochloride. *Journal of Biological Chemistry*, 241(13):3228–3232, 1966.

[123] D. Kaya, V. A. Belyi, and M. Muthukumar. Pattern formation in drying droplets of polyelectrolyte and salt. *The Journal of Chemical Physics*, 133(11):114905, 2010.

[124] S. Ketterl and M. Klein. A-priori assessment of subgrid scale models for large-eddy simulation of multiphase primary breakup. *Computers & Fluids*, 165:64–77, 2018.

[125] C. Kim, S.-W. S. Cheng, and S. A. Majorski. Engine Combustion Chamber Deposits: Fuel Effects and Mechanisms of Formation. In *SAE Technical Paper, 912379*. SAE International, 1991.

[126] J. Kim and F. Hussain. Propagation velocity of perturbations in turbulent channel flow. *Physics of Fluids A: Fluid Dynamics*, 5(3):695–706, 1993.

[127] M. Kinoshita, A. Saito, M. Souchi, H. Shibata, and Y. Niwa. A Method for Suppressing Formation of Deposits on Fuel Injector for Direct Injection Gasoline Engine. In *SAE Technical Paper, 1999-01-3656*. SAE International, 1999.

[128] Y. Kita, A. Askounis, M. Kohno, Y. Takata, J. Kim, and K. Sefiane. Induction of Marangoni convection in pure water drops. *Applied Physics Letters*, 109(17):171602, 2016.

[129] J. Klentzman and V. S. Ajaev. The effect of evaporation on fingering instabilities. *Physics of Fluids*, 21(12):122101, 2009.

[130] M. Koebel, M. Elsener, and M. Kleemann. Urea-SCR: a promising technique to reduce NOx emissions from automotive diesel engines. *Catalysis Today*, 59:335–345, 2000.

[131] K. S. Kolegov and L. Y. Barash. Joint effect of advection, diffusion, and capillary attraction on the spatial structure of particle depositions from evaporating droplets. *Physical Review E*, 100:033304, 2019.

[132] N. I. Kolev. *Multiphase Flow Dynamics 2*. Springer-Verlag Berlin Heidelberg, third edition, 2007. ISBN 978-3540221074.

[133] D. Kourounis, A. Fuchs, and O. Schenk. Toward the Next Generation of Multiperiod Optimal Power Flow Solvers. *IEEE Transactions on Power Systems*, 33(4):4005–4014, 2018.

[134] D. Lakehal, M. Fulgosi, S. Banerjee, and G. Yadigaroglu. Turbulence and heat exchange in condensing vapor-liquid flow. *Physics of Fluids*, 20(6):065101, 2008.

[135] H. Lan, M. Friedrich, B. F. Armaly, and J. A. Drallmeier. Simulation and measurement of 3D shear-driven thin liquid film flow in a duct. *International Journal of Heat and Fluid Flow*, 29(2): 449–459, 2008.

[136] R. G. Larson. Transport and deposition patterns in drying sessile droplets. *AIChE Journal*, 60(5): 1538–1571, 2014.

[137] G. Lavalle, J.-P. Vila, G. Blanchard, C. Laurent, and F. Charru. A numerical reduced model for thin liquid films sheared by a gas flow. *Journal of Computational Physics*, 301:119–140, 2015.

[138] M. Lecompte, J. Obiols, J. Cherel, and S. Raux. The Benefits of Diesel Exhaust Fluid (DEF) Additivation on Urea-Derived Deposits Formation in a Close-Coupled Diesel SCR on Filter Exhaust Line. In *SAE Technical Paper, 2017-01-2370*. SAE International, 2017.

[139] J. Leiterer, F. Emmerling, U. Panne, W. Christen, and K. Rademann. Tracing Coffee Tabletop Traces. *Langmuir*, 24(15):7970–7978, 2008.

[140] H. Y. Li, Y. F. Yap, J. Lou, J. C. Chai, and Z. Shang. Conjugate heat transfer in stratified two-fluid flows with a growing deposit layer. *Applied Thermal Engineering*, 113:215–228, 2017.

[141] Y.-F. Li, Y.-J. Sheng, and H.-K. Tsao. Evaporation Stains: Suppressing the Coffee-Ring Effect by Contact Angle Hysteresis. *Langmuir*, 29(25):7802–7811, 2013.

[142] A. M. Liaquat, H. H. Masjuki, M. A. Kalam, and I. M. Rizwanul Fattah. Impact of biodiesel blend on injector deposit formation. *Energy*, 72:813–823, 2014.

[143] M.-Y. Lin, C.-H. Moeng, W.-T. Tsai, P. P. Sullivan, and S. E. Belcher. Direct numerical simulation of wind-wave generation processes. *Journal of Fluid Mechanics*, 616:1–30, 2008.

[144] C. Liu, E. Bonaccurso, and H.-J. Butt. Evaporation of sessile water/ethanol drops in a controlled environment. *Physical Chemistry Chemical Physics*, 10:7150–7157, 2008.

[145] S. Liu, A. Kermani, L. Shen, and D. K. P. Yue. Investigation of coupled air-water turbulent boundary layers using direct numerical simulations. *Physics of Fluids*, 21(6):062108, 2009.

[146] M. C. Lopes, E. Bonaccurso, T. Gambaryan-Roisman, and P. Stephan. Influence of the substrate thermal properties on sessile drop evporation: Effect on transient heat transport. *Colloids and Surfaces, A: Physicochemical and Engineering Aspects*, 432:64–70, 2013.

[147] J. R. Marati. *Two-Phase CFD Simulation of Turbulent Gas-Driven Liquid Film Flows on Heated Walls*. PhD thesis, Technische Universität Darmstadt, 2016.

[148] J. R. Marati, M. Budakli, T. Gambaryan-Roisman, and P. Stephan. Heat transfer in shear-driven thin liquid film flows. *Computational Thermal Sciences*, 5(4):303–315, 2013.

[149] O. K. Matar and P. D. M. Spelt. Dynamics of thin free films with reaction-driven density and viscosity variations. *Physics of Fluids*, 17(12):122102, 2005.

[150] S. A. McBride, S. Dash, and K. K. Varanasi. Evaporative Crystallization in Drops on Superhydrophobic and Liquid-Impregnated Surfaces. *Langmuir*, 34(41):12350–12358, 2018.

[151] J. McGarry. Correlation and Prediction of the Vapor Pressures of Pure Liquids over Large Pressure Ranges. *Industrial and Engineering Chemistry Process Design and Development*, 22:313–322, 1983.

[152] R. J. McSherry, K. V. Chua, and T. Stoesser. Large eddy simulation of free-surface flows. *Journal of Hydrodynamics, Ser. B*, 29(1):1–12, 2017.

[153] G. P. Merker, C. Schwarz, and R. Teichmann. *Grundlagen Verbrennungsmotoren*, chapter Zukunft des Verbrennungsmotors, pages 735–778. Vieweg+Teubner Verlag, 2012. ISBN 978-3834819888.

[154] A. Nakayama and S. Yokojima. LES of open-channel flow with free-surface fluctuation. *Proceedings of Hydraulic Engineering*, 46:373–378, 2002.

[155] A. Nakayama and S. Yokojima. Modeling Free-Surface Fluctuation Effects for Calculation of Turbulent Open-Channel Flows. *Environmental Fluid Mechanics*, 3:1–21, 2003.

[156] F. Nicoud and F. Ducros. Subgrid-Scale Stress Modelling Based on the Square of the Velocity Gradient Tensor. *Flow, Turbulence and Combustion*, 62(3):183–200, 1999.

[157] K. Norinaga and O. Deutschmann. Detailed Kinetic Modeling of Gas-Phase Reactions in the Chemical Vapor Deposition of Carbon from Light Hydrocarbons. *Industrial and Engineering Chemistry Research*, 46(11):3547–3557, 2007.

[158] D. A. Notter, M. Gauch, R. Widmer, P. Wäger, A. Stamp, R. Zah, and H.-J. Althaus. Contribution of Li-Ion Batteries to the Environmental Impact of Electric Vehicles. *Environmental Science & Technology*, 44(19):7744–7744, 2010.

[159] L. Ó Náraigh, P. D. M. Spelt, O. K. Matar, and T. A. Zaki. Interfacial instability in turbulent flow over a liquid film in a channel. *International Journal of Multiphase Flow*, 37:812–830, 2011.

[160] L. Ó Náraigh, P. D. M. Spelt, and S. J. Shaw. Absolute linear instability in laminar and turbulent gas–liquid two-layer channel flow. *Journal of Fluid Mechanics*, 714:58–94, 2013.

[161] D. Orejon, K. Sefiane, and M. E. R. Shanahan. Stick–Slip of Evaporating Droplets: Substrate Hydrophobicity and Nanoparticle Concentration. *Langmuir*, 27(21):12834–12843, 2011.

[162] A. Oron and S. G. Bankoff. Dewetting of a Heated Surface by an Evaporating Liquid Film under Conjoining/Disjoining Pressures. *Journal of Colloid and Interface Science*, 218:152–166, 1999.

[163] A. Oron, S. H. Davis, and S. G. Bankoff. Long-scale evolution of thin liquid films. *Reviews of Modern Physics*, 69(3):931–979, 1997.

[164] A. Paquier, F. Moisy, and M. Rabaud. Surface deformations and wave generation by wind blowing over a viscous liquid. *Physics of Fluids*, 27(12):122103, 2015.

[165] M. Parsa, R. Boubaker, S. Harmand, K. Sefiane, M. Bigerelle, and R. Deltombe. Patterns from dried water-butanol binary-based nanofluid drops. *Journal of Nanoparticle Research*, 19(8):268, 2017.

[166] M. Parsa, S. Harmand, and K. Sefiane. Mechanisms of pattern formation from dried sessile drops. *Advances in Colloid and Interface Science*, 254:22–47, 2018.

[167] A. Pereira, P. M. J. Trevelyan, U. Thiele, and S. Kalliadasis. Thin Films in the Presence of Chemical Reactions. *Fluid Dynamics and Materials Processing*, 3(4):303–316, 2007.

[168] A. Pereira, P. M. J. Trevelyan, U. Thiele, and S. Kalliadasis. Interfacial instabilities driven by chemical reactions. *European Physical Journal Special Topics*, 166(1):121–125, 2009.

[169] S. Perrard, A. Lozano-Durán, M. Rabaud, M. Benzaquen, and F. Moisy. Turbulent windprint on a liquid surface. *Journal of Fluid Mechanics*, 873:1020–1054, 2019.

[170] R. G. Picknett and R. Bexon. The evaporation of sessile or pendant drops in still air. *Journal of Colloid and Interface Science*, 61(2):336–350, 1977.

[171] B. E. Poling, J. N. Prausnitz, and J. P. O'Connel. *The Properties of Gases and Liquids*. McGrawHill, fifth edition, 2001. ISBN 978-0070116825.

[172] S. B. Pope. *Turbulent Flows*. Cambridge University Press, seventh edition, 2010. ISBN 978-0521598866.

[173] Y. O. Popov. Evaporative deposition patterns: Spatial dimensions of the deposit. *Physical Review E*, 71:036313, 2005.

[174] C. Poulard, G. Guéna, and A. M. Cazabat. Diffusion-driven evaporation of sessile drops. *Journal of Physics: Condensed Matter*, 17(49):4213–4227, 2005.

[175] S. S. Prabhu, N. S. Nayak, N. Kapilan, and V. Hindasageri. An experimental and numerical study on effects of exhaust gas temperature and flow rate on deposit formation in Urea-Selective Catalytic Reduction (SCR) system of modern automobiles. *Applied Thermal Engineering*, 111:1211–1231, 2017.

[176] Q. Qi and R. E. Johnson. Gravity-Driven Reactive Coating Flow Down an Inclined Plane. *AIChE Journal*, 40(1):2–10, 1994.

[177] M. Quadrio and P. Luchini. Integral space–time scales in turbulent wall flows. *Physics of Fluids*, 15 (8):2219–2227, 2003.

[178] Y. Ra and R. D. Reitz. A vaporization model for discrete multi-component fuel sprays. *International Journal of Multiphase Flow*, 35:101–117, 2009.

[179] D. Rettenmaier. *Numerical Simulation of Shear Driven Wetting*. PhD thesis, Technische Universität Darmstadt, 2019.

[180] B. Richter. *Charakterisierung der Tropfen-Wand-Interaktion im Parameterbereich von Ottomotoren mit Direkteinspritzung*. PhD thesis, Universität Karlsruhe (TH), 2007.

[181] B. Richter, S. Crusius, U. Schümann, and H. Harndorf. Charakterisierung interner Ablagerungen in Common-Rail-Injektoren. *MTZ–Motorentechnische Zeitschrift*, 74(10):796–803, 2013.

[182] W. D. Ristenpart, P. G. Kim, C. Domingues, J. Wan, and H. A. Stone. Influence of Substrate Conductivity on Circulation Reversal in Evaporating Drops. *Physical Review Letters*, 99:234502, 2007.

[183] E. Roohi, A. P. Zahiri, and M. Passandideh-Fard. Numerical simulation of cavitation around a two-dimensional hydrofoil using VOF method and LES turbulence model. *Applied Mathematical Modelling*, 37(9):6469–6488, 2013.

[184] H. Rosskamp, M. Willmann, and S. Wittig. Heat up and evaporation of shear driven liquid wall films in hot turbulent air flow. *International Journal of Heat and Fluid Flow*, 19(2):167–172, 1998.

[185] P. J. Sáenz, P. Valluri, K. Sefiane, G. Karapetsas, and O. K. Matar. On phase change in Marangoni-driven flows and its effects on the hydrothermal-wave instabilities. *Physics of Fluids*, 26(2):024114, 2014.

[186] P. J. Sáenz, K. Sefiane, J. Kim, O. K. Matar, and P. Valluri. Evaporation of sessile drops: a three-dimensional approach. *Journal of Fluid Mechanics*, 772:705–739, 2015.

[187] G. Saliba, R. Saleh, Y. Zhao, A. A. Presto, A. T. Lambe, B. Frodin, S. Sardar, H. Maldonado, C. Maddox, A. A. May, G. T. Drozd, A. H. Goldstein, L. M. Russell, F. Hagen, and A. L. Robinson. Comparison of Gasoline Direct-Injection (GDI) and Port Fuel Injection (PFI) Vehicle Emissions: Emission Certification Standards, Cold-Start, Secondary Organic Aerosol Formation Potential, and Potential Climate Impacts. *Environmental Science and Technology*, 51(11):6542–6552, 2017.

[188] S. S. Sazhin. Modelling of fuel droplet heating and evaporation: Recent results and unsolved problems. *Fuel*, 196:69–101, 2017.

[189] M. Schäfer. *Computational Engineering: Introduction to Numerical Methods*. Springer-Verlag Berlin Heidelberg, 2006. ISBN 978-3540306856.

[190] K. Schintzel. *Kohlenwasserstoff-Emissionen eines Motors mit Benzin-Direkteinspritzung und wandgeführtem Brennverfahren*. PhD thesis, Otto-von-Guericke-Universität Magdeburg, 2005.

[191] H. Schlichting and K. Gersten. *Boundary-Layer Theory*. Springer-Verlag Berlin Heidelberg, ninth edition, 2017. ISBN 978-3662529171.

[192] J. Schmid, I. Zarikos, A. Terzis, N. Roth, and B. Weigand. Crystallization of urea from an evaporative aqueous solution sessile droplet at sub-boiling temperatures and surfaces with different wettability. *Experimental Thermal and Fluid Science*, 91:80–88, 2018.

[193] P. Schmidt, L. Ó Náraigh, M. Lucquiaud, and P. Valluri. Linear and nonlinear instability in vertical counter-current laminar gas-liquid flows. *Physics of Fluids*, 28(4):042102, 2016.

[194] F. Schönfeld, K.-H. Graf, S. Hardt, and H.-J. Butt. Evaporation dynamics of sessile liquid drops in still air with constant contact radius. *International Journal of Heat and Mass Transfer*, 51(13–14): 3696–3699, 2008.

[195] R. W. Schrage. *A theoretical study of interphase mass transfer*. PhD thesis, Columbia University, New York, 1953.

[196] T. Schütte. *Ablagerungs- und Alterungsverhalten wässriger Harnstofflösung bei selektiver katalytischer Reduktion von Stickoxidemissionen*. PhD thesis, Leuphana Universität Lüneburg, 2010.

[197] K. Sefiane. Patterns from drying drops. *Advances in Colloid and Interface Science*, 206:372–381, 2014.

[198] K. Sefiane and R. Bennacer. An expression for droplet evaporation incorporating thermal effects. *Journal of Fluid Mechanics*, 667:260–271, 2011.

[199] K. Sefiane, L. Tadrist, and M. Douglas. Experimental study of evaporating water–ethanol mixture sessile drop: influence of concentration. *International Journal of Heat and Mass Transfer*, 46(23): 4527–4534, 2003.

[200] K. Sefiane, S. David, and M. E. R. Shanahan. Wetting and Evaporation of Binary Mixture Drops. *The Journal of Physical Chemistry B*, 112(36):11317–11323, 2008.

[201] S. Semenov, V. M. Starov, and R. G. Rubio. Evaporation of pinned sessile microdroplets of water on a highly heat-conductive substrate: Computer simulations. *The European Physical Journal Special Topics*, 219(1):143–154, 2013.

[202] M. E. R. Shanahan, K. Sefiane, and J. R. Moffat. Dependence of Volatile Droplet Lifetime on the Hydrophobicity of the Substrate. *Langmuir*, 27(8):4572–4577, 2011.

[203] L. Shen and D. K. P. Yue. Large-eddy simulation of free-surface turbulence. *Journal of Fluid Mechanics*, 440:75–116, 2001.

[204] E. Shirani, A. Jafari, and N. Ashgriz. Turbulence Models for Flows with Free Surfaces and Interfaces. *AIAA Journal*, 44(7):1454–1462, 2006.

[205] S. Shklyaev and A. Nepomnyashchy. *Longwave Instabilities and Patterns in Fluids*. Springer Science + Business Media, first edition, 2017. ISBN 978-1493975884.

[206] P. Singer and J. Rühe. On the mechanism of deposit formation during thermal oxidation of mineral diesel and diesel/biodiesel blends under accelerated conditions. *Fuel*, 133:245–252, 2014.

[207] H. Smith, T. Lauer, V. Schimik, and K. Gabel. Evaluation and Prediction of Deposit Severity in SCR Systems. *SAE International Journal of Engines*, 9(3):1735–1750, 2016.

[208] M. K. Smith. Instability mechanisms in dynamic thermocapillary liquid layers. *The Physics of Fluids*, 29(10):3182–3186, 1986.

[209] B. Sobac and D. Brutin. Triple-Line Behavior and Wettability Controlled by Nanocoated Substrates: Influence on Sessile Drop Evaporation. *Langmuir*, 27(24):14999–15007, 2011.

[210] B. Sobac and D. Brutin. Thermal effects of the substrate on water droplet evaporation. *Physical Review E*, 86:021602, 2012.

[211] J. M. Stauber, S. K. Wilson, B. R. Duffy, and K. Sefiane. On the lifetimes of evaporating droplets. *Journal of Fluid Mechanics*, 744:R2, 2014.

[212] R. Steinhagen, H. Müller-Steinhagen, and K. Maani. Problems and Costs due to Heat Exchanger Fouling in New Zealand Industries. *Heat Transfer Engineering*, 14(1):19–30, 1993.

[213] P. Stephan, T. Gambaryan-Roisman, M. Budakli, and J. R. Marati. *Experimental and Numerical Investigation of Shear-Driven Film Flow and Film Evaporation*, chapter 2, pages 29–54. Fluid Mechanics and Its Applications. Springer Science + Business Media Dordrecht, 2013. ISBN 978-9400753198.

[214] P. C. Stephan and C. A. Busse. Analysis of the heat transfer coefficient of grooved heat pipe evaporator walls. *International Journal of Heat and Mass Transfer*, 35:383–391, 1992.

[215] M. Still. *Temperaturmessungen und Analyse von Wärme- und Stofftransportvorgängen bei verdunstenden Tropfen*. PhD thesis, Technische Universität Darmstadt, 2016.

[216] V. O. Strots, S. Santhanam, B. J. Adelman, G. A. Griffin, and E. M. Derybowski. Deposit Formation in Urea-SCR Systems. *SAE International Journal of Fuels and Lubricants*, 2:283–289, 2009.

[217] P. Takhistov and H.-C. Chang. Complex Stain Morphologies. *Industrial and Engineering Chemistry Research*, 41(25):6256–6269, 2002.

[218] H. Tan, C. Diddens, P. Lv, J. G. M. Kuerten, X. Zhang, and D. Lohse. Evaporation-triggered microdroplet nucleation and the four life phases of an evaporating Ouzo drop. *Proceedings of the National Academy of Sciences USA*, 113(31):8642–8647, 2016.

[219] S. Taniewska-Osińska, B. Piestrzyńska, and R. Łogwinienko. The enthalpy of solution of NaI, NaCl, NaClO4, and urea in water–tetrahydrofuran mixtures at 298.15 K. *Canadian Journal of Chemistry*, 58(15):1584–1588, 1980.

[220] U. Thiele. Patterned deposition at moving contact lines. *Advances in Colloid and Interface Science*, 206:399–413, 2014.

[221] P. M. J. Trevelyan and S. Kalliadasis. Dynamics of a reactive falling film at large Péclet numbers. I. Long-wave approximation. *Physics of Fluids*, 16(8):3191–3208, 2004.

[222] P. M. J. Trevelyan, S. Kalliadasis, J. H. Merkin, and S. K. Scott. Dynamics of a vertically falling film in the presence of a first-order chemical reaction. *Physics of Fluids*, 14(7):2402–2421, 2002.

[223] P. M. J. Trevelyan, A. Pereira, and S. Kalliadasis. Dynamics of a Reactive Thin Film. *Mathematical Modelling of Natural Phenomena*, 7(4):99–145, 2012.

[224] D. Tseluiko and S. Kalliadasis. Nonlinear waves in counter-current gas–liquid film flow. *Journal of Fluid Mechanics*, 673:19–59, 2011.

[225] P. Valluri, L. Ó Náraigh, H. Ding, and P. D. M. Spelt. Linear and nonlinear spatio-temporal instability in laminar two-layer flows. *Journal of Fluid Mechanics*, 656:458–480, 2010.

[226] VDI-Gesellschaft Verfahrenstechnik und Chemieingenieurwesen. *VDI Heat Atlas*. Springer-Verlag Berlin Heidelberg, second edition, 2010. ISBN 978-3540778769.

[227] R. Vellingiri, D. Tseluiko, N. Savva, and S. Kalliadasis. Dynamics of a liquid film sheared by a co-flowing turbulent gas. *International Journal of Multiphase Flow*, 56:93–104, 2013.

[228] R. Vellingiri, D. Tseluiko, and S. Kalliadasis. Absolute and convective instabilities in counter-current gas-liquid film flows. *Journal of Fluid Mechanics*, 763:166–201, 2015.

[229] F. K. von Gottberg, T. A. Hatton, and K. A. Smith. Surface Instabilities Due to Interfacial Chemical Reaction. *Industrial and Engineering Chemistry Research*, 34:3368–3379, 1995.

[230] A. Weidenlener, J. Pfeil, H. Kubach, T. Koch, P. Forooghi, B. Frohnapfel, and F. Magagnato. The influence of operating conditions on combustion chamber deposit surface structure, deposit thickness and thermal properties. *Automotive and Engine Technology*, 3(3):111–127, 2018.

[231] S. Wittig, J. Himmelsbach, B. Noll, H. J. Feld, and W. Samenfink. Motion and Evaporation of Shear-Driven Liquid Films in Turbulent Gases. In *Volume 3: Coal, Biomass and Alternative Fuels; Combustion and Fuels; Oil and Gas Applications; Cycle Innovations, Cologne, Germany, June 1–4*. ASME, 1992.

[232] W. Woodside and J. H. Messmer. Thermal Conductivity of Porous Media. I. Unconsolidated Sands. *Journal of Applied Physics*, 32(9):1688–1699, 1961.

[233] M. Wörner. Numerical modeling of multiphase flows in microfluidics and micro process engineering: a review of methods and applications. *Microfluidics and Nanofluidics*, 12(6):841–886, 2012.

[234] H. Xu, C. Wang, X. Ma, A. K. Sarangi, A. Weall, and J. Krueger-Venus. Fuel injector deposits in direct-injection spark-ignition engines. *Progress in Energy and Combustion Science*, 50:63–80, 2015.

[235] X. Xu, J. Luo, and D. Guo. Criterion for Reversal of Thermal Marangoni Flow in Drying Drops. *Langmuir*, 26(3):1918–1922, 2010.

[236] T. A. Yakhno, O. A. Sedova, A. G. Sanin, and A. S. Pelyushenko. On the existence of regular structures in liquid human blood serum (plasma) and phase transitions in the course of its drying. *Technical Physics*, 48(4):399–403, 2003.

[237] T. A. Yakhno, V. G. Yakhno, A. G. Sanin, O. A. Sanina, A. S. Pelyushenko, N. A. Egorova, I. G. Terentiev, S. V. Smetanina, O. V. Korochkina, and E. V. Yashukova. The informative-capacity phenomenon of drying drops. *IEEE Engineering in Medicine and Biology Magazine*, 24(2):96–104, 2005.

[238] T. A. Yakhno, V. V. Kazakov, O. A. Sanina, A. G. Sanin, and V. G. Yakhno. Drops of biological fluids drying on a hard substrate: Variation of the morphology, weight, temperature, and mechanical properties. *Technical Physics*, 55(7):929–935, 2010.

[239] K. Yang, F. Hong, and P. Cheng. A fully coupled numerical simulation of sessile droplet evaporation using Arbitrary Lagrangian–Eulerian formulation. *International Journal of Heat and Mass Transfer*, 70:409–420, 2014.

[240] O. H. Yeoh. Some Forms of the Strain Energy Function for Rubber. *Rubber Chemistry and Technology*, 66(5):754–771, 1993.

[241] C.-S. Yih. Instability due to viscosity stratification. *Journal of Fluid Mechanics*, 27(2):337–352, 1967.

[242] P. J. Yunker, T. Still, M. A. Lohr, and A. G. Yodh. Suppression of the coffee-ring effect by shape-dependent capillary interactions. *Nature*, 476:308–311, 2011.

[243] H. Zhang, Y. Xi, C. Su, and Z. G. Liu. Lab Study of Urea Deposit Formation and Chemical Transformation Process of Diesel Aftertreatment System. In *SAE Technical Paper, 2017-01-0915*. SAE International, 2017.

[244] J. Zhang, M. K. Borg, K. Sefiane, and J. M. Reese. Wetting and evaporation of salt-water nano-droplets: A molecular dynamics investigation. *Physical Review E*, 92:052403, 2015.

[245] L. Zhang, J. Cai, T. Zhang, and F. Qi. Kinetic modeling study of toluene pyrolysis at low pressure. *Combustion and Flame*, 157(9):1686–1697, 2010.

[246] F. Zhao, M.-C. Lai, and D. L. Harrington. Automotive spark-ignited direct-injection gasoline engines. *Progress in Energy and Combustion Science*, 25(5):437–562, 1999.

[247] F. Zonta, A. Soldati, and M. Onorato. Growth and spectra of gravity–capillary waves in counter-current air/water turbulent flow. *Journal of Fluid Mechanics*, 777:245–259, 2015.

[248] F. Zonta, M. Onorato, and A. Soldati. Decay of gravity-capillary waves in air/water sheared turbulence. *International Journal of Heat and Fluid Flow*, 61:137–144, 2016.

List of Figures

List of Tables

CHAPTER A

Appendix

A.1 Material Properties

A.1.1 Properties Used in the Finite Difference Simulations

Table A.1: Properties of hexane at $T_0 = 313.15\,\mathrm{K}$ and $p_0 = 1\,\mathrm{bar}$ (based on [226]).

property	symbol	value liquid	value vapor
density	ρ	$643.658\,\mathrm{kg\,m^{-3}}$	$3.3101\,\mathrm{kg\,m^{-3}}$
dynamic viscosity	μ	$2.6278 \cdot 10^{-4}\,\mathrm{kg\,m^{-1}\,s^{-1}}$	
specific heat capacity	c_p	$2.3393 \cdot 10^{3}\,\mathrm{J\,kg^{-1}\,K^{-1}}$	
thermal conductivity	k	$0.1143\,\mathrm{W\,m^{-1}\,K^{-1}}$	
molar mass	M	$8.6180 \cdot 10^{-2}\,\mathrm{kg\,mol^{-1}}$	
enthalpy of vaporization	h_{lv}	$3.555 \cdot 10^{5}\,\mathrm{J\,kg^{-1}}$	
surface tension	σ	$1.6297 \cdot 10^{-2}\,\mathrm{N\,m^{-1}}$	
	σ_T	$-1.062 \cdot 10^{-4}\,\mathrm{N\,m^{-1}\,K^{-1}}$	
binary diffusion coefficient in air	D_{bin}	$8.4578 \cdot 10^{-6}\,\mathrm{m^2\,s^{-1}}$	
condensation coefficient	f	0.5	
gradient of saturation concentration with temperature	$\frac{\mathrm{d}\xi_{\mathrm{sat}}}{\mathrm{d}T}$	$1.3945 \cdot 10^{-2}\,\mathrm{K^{-1}}$	

Table A.2: Properties of aluminum (from [226]).

property	symbol	value
thermal conductivity	k	$236\,\mathrm{W\,m^{-1}\,K^{-1}}$

Table A.3: Properties of air at $T_0 = 313.15\,\mathrm{K}$ and $p_0 = 1\,\mathrm{bar}$ (based on [226]).

property	symbol	value
density	ρ	$1.1123\,\mathrm{kg\,m^{-3}}$
dynamic viscosity	μ	$1.9311 \cdot 10^{-5}\,\mathrm{kg\,m^{-1}\,s^{-1}}$
specific heat capacity	c_p	$1.0076 \cdot 10^{3}\,\mathrm{J\,kg^{-1}\,K^{-1}}$
thermal conductivity	k	$0.0273\,\mathrm{W\,m^{-1}\,K^{-1}}$
molar mass	M	$2.8958 \cdot 10^{-2}\,\mathrm{kg\,mol^{-1}}$

A.1.2 Properties Used in the Finite Element Simulations

Table A.4: Computation rules for the properties of air (from [11]).

property	symbol	value
density	$\rho(T)$	$\left(348.448\,\mathrm{kg\,m^{-3}\,K}\right)/T$
dynamic viscosity	$\mu(T)$	$\left[-8.38278 \cdot 10^{-7} + 8.35717 \cdot 10^{-8}\,T/\mathrm{K} - 7.69430 \cdot 10^{-11}\,(T/\mathrm{K})^2 + 4.64373 \cdot 10^{-14}\,(T/\mathrm{K})^3 - 1.06586 \cdot 10^{-17}\,(T/\mathrm{K})^4\right]\mathrm{kg\,m^{-1}\,s^{-1}}$
specific heat capacity	$c_p(T)$	$\left[1047.64 - 0.372589\,(T/\mathrm{K}) + 9.45304 \cdot 10^{-4}\,(T/\mathrm{K})^2 - 6.02409 \cdot 10^{-7}\,(T/\mathrm{K})^3 + 1.28590 \cdot 10^{-10}\,(T/\mathrm{K})^4\right]\mathrm{J\,kg^{-1}\,K^{-1}}$
thermal conductivity	$k(T)$	$\left[-2.27584 \cdot 10^{-3} + 1.15480 \cdot 10^{-4}\,(T/\mathrm{K}) - 7.90253 \cdot 10^{-8}\,(T/\mathrm{K})^2 + 4.11703 \cdot 10^{-11}\,(T/\mathrm{K})^3 - 7.43864 \cdot 10^{-15}\,(T/\mathrm{K})^4\right]\mathrm{W\,m^{-1}\,K^{-1}}$
molar mass	M	$2.8958 \cdot 10^{-2}\,\mathrm{kg\,mol^{-1}}$

Table A.5: Properties of water vapor (based on [151, 226]).

property	symbol	value
density	$\rho(T)$	$\left(216.732\,\mathrm{kg\,m^{-3}\,K}\right)/T$
binary diffusion coefficient of vapor in air	$D_{\mathrm{bin}}(T)$	$1.1856 \cdot 10^{-9}\,(T/\mathrm{K})^{1.75}\ \mathrm{m^2\,s^{-1}}$
molar mass	M	$1.8015 \cdot 10^{-2}\,\mathrm{kg\,mol^{-1}}$
enthalpy of vaporization	h_{lv}	$2.200 \cdot 10^{6}\,\mathrm{J\,kg^{-1}}$
critical temperature	T_{crit}	$647.10\,\mathrm{K}$
critical pressure	p_{crit}	$220.64\,\mathrm{bar}$
Wagner equation coefficients	C_1	-7.76451
	C_2	1.45838
	C_3	-2.77580
	C_4	-1.23303

Table A.6: Properties of urea-water solution. The density is calculated as a function of concentration and temperature, while the other parameters are evaluated for characteristic values of $T_0 = 343.15\,\mathrm{K}$ and $\xi_{\mathrm{u},0} = 0.325$ (based on [27, 94, 122, 226]).

property	symbol	value
density	$\rho(T, \xi_\mathrm{u})$	$[-0.3009\,\xi_\mathrm{u}\,(T/\mathrm{K}) - 0.4653\,(T/\mathrm{K}) + 374.52\,\xi_\mathrm{u} + 1134.1]\,\mathrm{kg\,m^{-3}}$
dynamic viscosity	μ	$5.61 \cdot 10^{-4}\,\mathrm{kg\,m^{-1}\,s^{-1}}$
specific heat capacity	c_p	$3.478 \cdot 10^{3}\,\mathrm{J\,kg^{-1}\,K^{-1}}$
thermal conductivity	k	$0.716\,\mathrm{W\,m^{-1}\,K^{-1}}$
binary diffusion coefficient of urea in water	D_bin	$2.4041 \cdot 10^{-9}\,\mathrm{m^2\,s^{-1}}$
surface tension	σ	$7.430 \cdot 10^{-2}\,\mathrm{N\,m^{-1}}$
	$\sigma_{T,0}$	$-1.938 \cdot 10^{-4}\,\mathrm{N\,m^{-1}\,K^{-1}}$

Table A.7: Properties of crystalline urea (from [12, 219]).

property	symbol	value
density	ρ	$1320\,\mathrm{kg\,m^{-3}}$
thermal conductivity	k	$1.05\,\mathrm{W\,m^{-1}\,K^{-1}}$
molar mass	M	$6.006 \cdot 10^{-2}\,\mathrm{kg\,mol^{-1}}$
enthalpy of solution	h_ls	$2.562 \cdot 10^{5}\,\mathrm{J\,kg^{-1}}$

A.2 Estimation of the Discretization Error for the Finite Difference Solvers

To evaluate the error of the spatial and temporal discretization, several simulations for varying number of grid points or time step sizes are conducted. From these simulations, the convergence order and the estimated grid-independent solution ϕ_{ind} of the characteristic parameter (e.g. the maximum film height at the end of the simulation) is calculated using the Richardson extrapolation [189]. With this grid-independent solution, the error ε of each individual simulation i can be calculated as follows

$$\varepsilon_i = \frac{|\phi_i - \phi_{\text{ind}}|}{\phi_{\text{ind}}}, \tag{A.1}$$

where ϕ_i refers to the value of the characteristic parameter of the i-th simulation.

A.2.1 Thin Film Evaporating on a Structured Wall

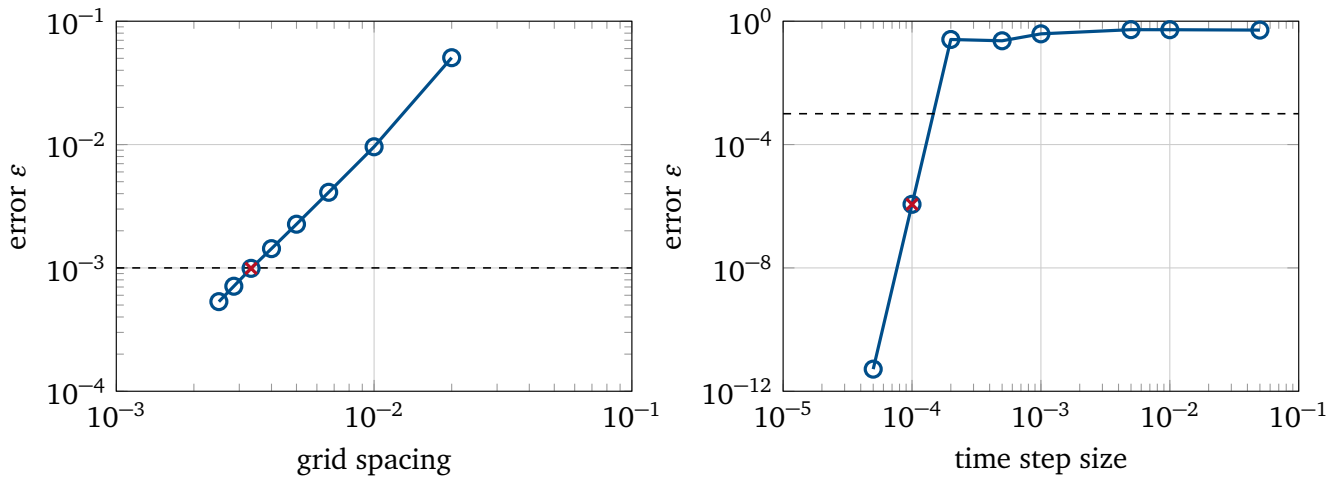

Figure A.1: Error of the maximum film height over grid spacing (for a time step size of $1 \cdot 10^{-4}$) (left) and over time step size (for 300 grid points) (right) for an evaporating film on a structured wall. The dashed line represents the error limit. The red crosses are the chosen spatial and temporal discretization.

The maximum film height H_{max} at the moment of rupture is chosen as the characteristic parameter for the calculation of the error. After the grid-independent solution is calculated both for the spatial and temporal discretization, the relative error is evaluated. The evolution of the error of the spatial discretization for different grid spacing is shown in Fig. A.1 (left) and the error of the temporal discretization for different time step sizes is given in Fig. A.1 (right) in double logarithmic diagrams. The convergence order of the spatial discretization, which can be identified as the average slope of Fig. A.1 (left), is calculated to 2.09. This value is very close to the expected convergence order of two for second order central differences. The convergence order of the temporal discretization is estimated to approximately 17.8, which is very high. However, as one can see in Fig. A.1 (right), for the small time step sizes the error is very low and the numerical simulation yields values very close to the grid-independent simulation, which affects the

estimation of the convergence order [189]. The dashed line represents a relative error of 0.001 in both figures, which is chosen as a measure for an "accurate enough" simulation in order to have cost effective simulations that do not require too much calculation resources and time. The relative error falls below this threshold for a spatial resolution of 300 grid points and a time step size of $1 \cdot 10^{-4}$, which are the values chosen for all simulations and marked in Fig. A.1 with the red cross.

A.2.2 Reacting Thin Film Sheared by Constant Shear Stress

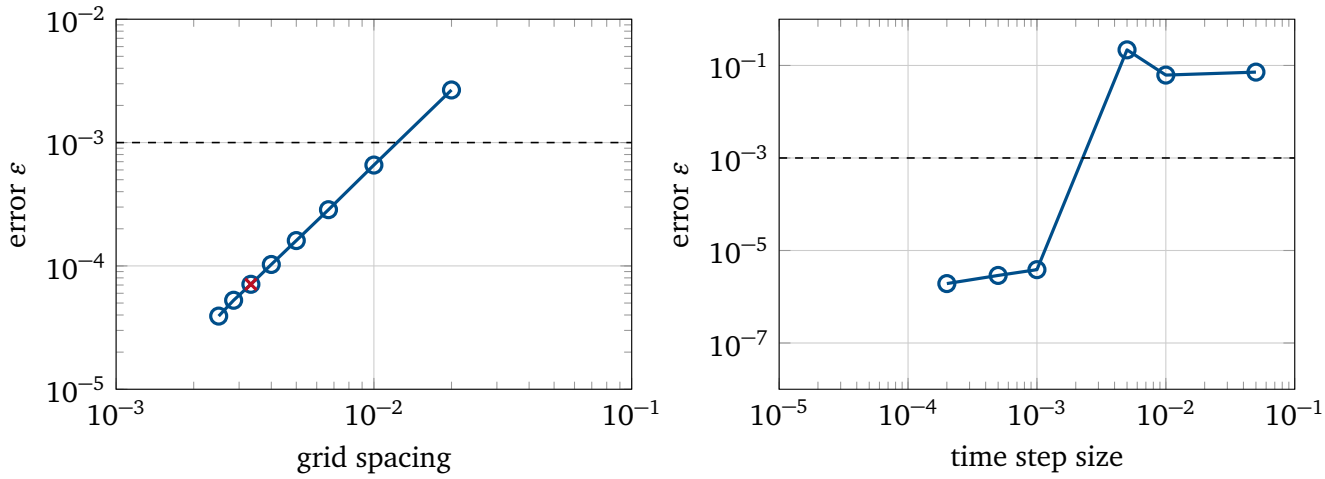

Figure A.2: Error of the maximum film height over grid spacing (for a time step size of $1 \cdot 10^{-4}$) (left) and over time step size (for 300 grid points) (right) for a reacting film sheared by a gas flow. The dashed line represents the error limit. The red cross is the chosen spatial discretization.

The maximum film height $H_{\max}$ at the end of the simulation ($\tau = 6$) is chosen as the characteristic parameter for the calculation of the error. The error of the spatial discretization is shown in Fig. A.2 (left) and the error of the temporal discretization is given in Fig. A.2 (right). The dashed line again represents an error of 0.001. The error falls below this threshold for a spatial resolution of 100 grid points and a time step size of $2 \cdot 10^{-3}$. The errors of the temporal discretization of the time step sizes $1 \cdot 10^{-4}$ and $5 \cdot 10^{-5}$ do not show up in the diagram, as the estimated error is zero, indicating that the grid-independent solution is reached. The convergence order of the spatial discretization is 2.02, which is again very close to the expected value. In order to have an easier setup of the two-dimensional finite difference solver, the spatial resolution is chosen to 300 grid points (marked by the red cross in Fig. A.2 (left)) and the time step size is set to $1 \cdot 10^{-4}$, which are the values obtained from the previous section. This can be done as the simulation times for the reactive film sheared by a constant shear stress are still only in the order of minutes for this spatial and temporal resolution.

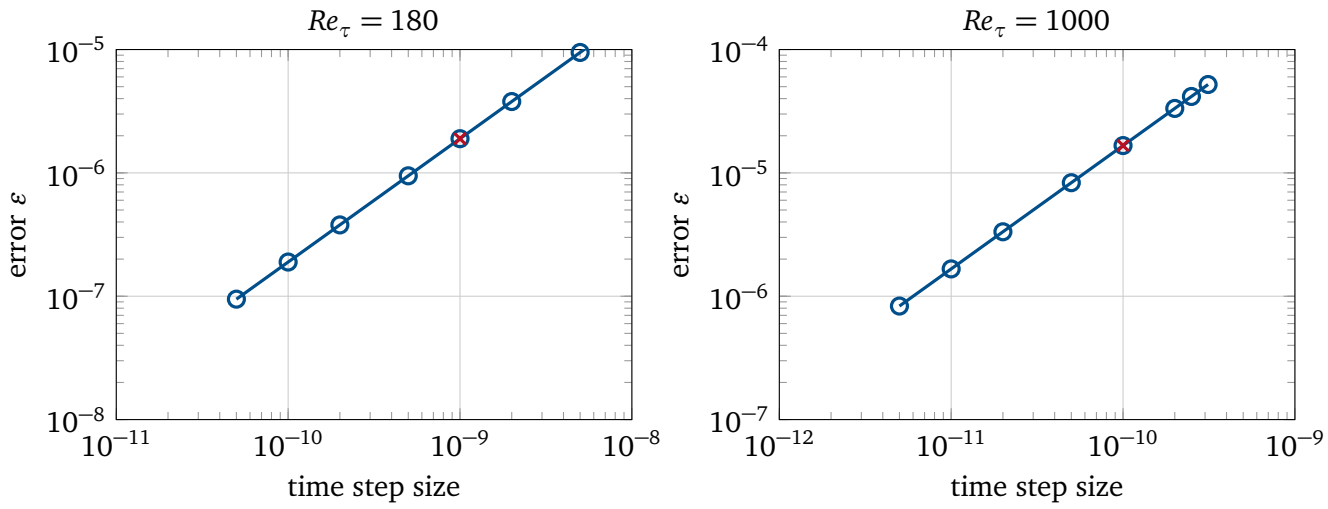

Figure A.3: Error of the standard deviation of the film height over time-step size for Re_τ = 180 (left) and Re_τ = 1000 (right). The red crosses are the chosen temporal discretization.

The error of the temporal discretization for the standard deviation of the film height after $\tau = 1 \cdot 10^{-6}$ is shown in Fig. A.3 for $Re_\tau = 180$ on the left and $Re_\tau = 1000$ on the right. The spatial resolution of the long-wave simulation has been chosen identical to the resolution of the DNS, which is why the convergence plots are different for the two Reynolds numbers and also why the error of the spatial discretization is not computed. One can see that the error decreases with a convergence order of almost exactly unity for both Reynolds numbers, which is expected for the explicit Euler method. Additionally, it can be seen that the error is very small for all displayed time step sizes. Consequently, the time step size is chosen so that the shear stress data from the DNS and LES can be calculated easily (with about ten iterations of the finite difference solver between each storage time step of the shear stress). Based on this, the time step size is chosen to $1 \cdot 10^{-9}$ for $Re_\tau = 180$ and $1 \cdot 10^{-10}$ for $Re_\tau = 1000$, which is marked by the red crosses in Fig. A.3.

A.3 Domain Size Influence and Discretization Error for the Finite Element Method

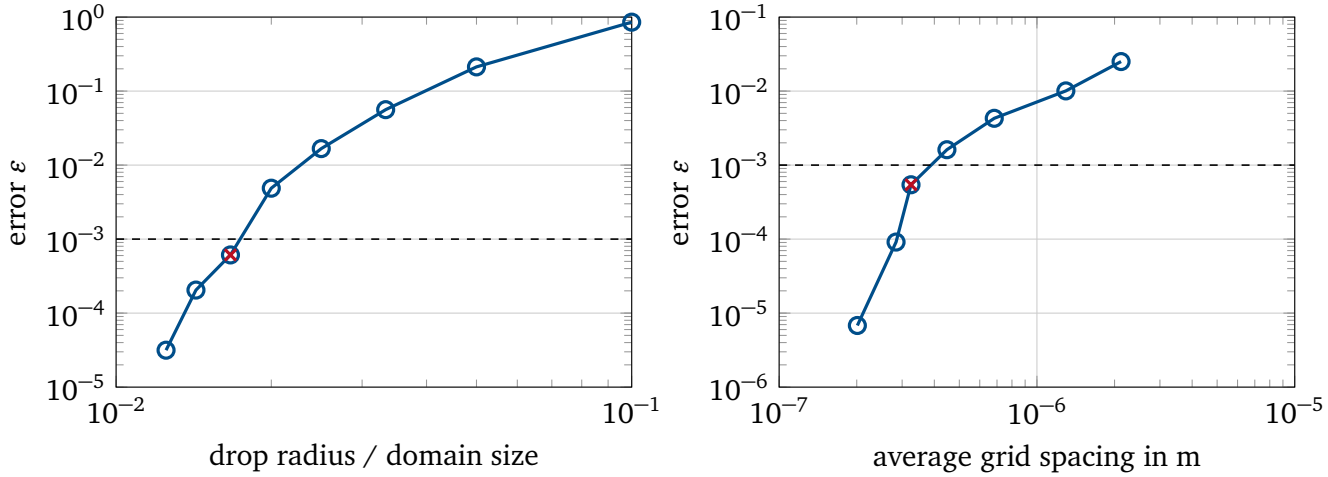

Figure A.4: Error of the global evaporation rate over domain sizes – expressed as multitudes of the drop radius R – (left) and over number of cells (right). The dashed line represents the error limit. The red crosses are the chosen domain size and spatial discretization.

The convergence order and the estimated grid-independent solution is calculated using the grid convergence method outlined in [50]. This method is based on the Richardson expansion but allows the grid refinement factor to deviate from the factor of two. This is necessary, as the mesh is created by *COMSOL Multiphysics* and locally refined in the simulations towards the deposit and the interface so that the exact number of cells cannot be explicitly defined. The grid refinement factor chosen in this section is between 1.33 and 1.57. After the grid-independent solution is obtained, the error is calculated using Eq. (A.1). The overall evaporative mass flux is chosen as the characteristic parameter to compare the simulations as it is influenced by the length of the liquid-gas interface, the temperature field, and the concentration field in the drop and the gas phase. All simulations are run for the reference configuration defined in Tab. 4.1 for 36 s, which is when some deposit has already formed, but most of the very time consuming remeshing has not happened, yet.

To evaluate the influence of the boundary conditions far away from the drop in the gas phase, simulations for varying domain sizes (expressed as drop radius divided by the domain size) are conducted. The development of the error for different domain sizes is given in Fig. A.4 (left). The error decreases with increasing domain size and falls below the chosen threshold value of 0.001 for a domain size of $60\,R_0$ (marked by the red cross). Consequently, this domain size is chosen for all simulations. It should be noted that the resulting domain is three times larger than the domain size used by Hu and Larson [107] ($20\,R_0$) in their benchmark simulations.

In the second step, the error from the spatial discretization is considered. Again, the global evaporative mass flux after 36 s is used as the characteristic parameter. The relative error over the average grid spacing can be seen in Fig. A.4 (right). The error decreases with increasing grid resolution with a convergence order of approximately 7.5 and falls below 0.001 for the mesh with approximately $1.45 \cdot 10^5$ triangular cells, which is marked by the red cross in the figure and is the resolution chosen for all the simulations. A

part of the resulting mesh, showing the drop and a fraction of the surrounding gas phase with formed deposit, can be seen in Fig. A.5. It is evident that the mesh is refined towards the liquid-gas interface and then even further refined around the formed deposit and the three-phase contact line. The minimum mesh size is at the three-phase contact line and is equal to $1.25 \cdot 10^{-7}$ m. The maximum mesh size in the bulk of the drop is set to $1.0 \cdot 10^{-5}$ m.

The time step size is chosen automatically by the program so that the relative error is below 0.001. The maximum allowed time step is set to 0.5 s.

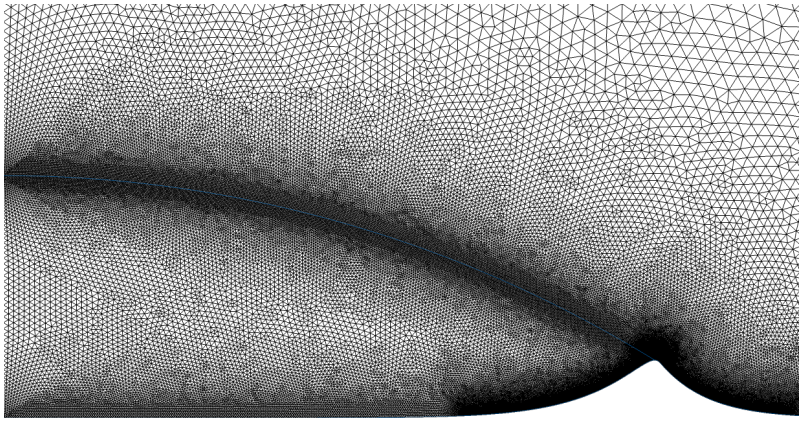

Figure A.5: Part of the numerical mesh of the FEM simulation.

Publications

Peer reviewed journal papers

A. Bender, P. Stephan, and T. Gambaryan-Roisman. Thin liquid films with time-dependent chemical reactions sheared by an ambient gas flow. *Physical Review Fluids*, 2:084002, 2017.

A. Bender, P. Stephan, and T. Gambaryan-Roisman. Numerical investigation of the evolution and breakup of an evaporating liquid film on a structured wall. *International Journal of Heat and Fluid Flow*, 70:104 – 113, 2018.

P. Hänichen, **A. Bender**, B. Voß, T. Gambaryan-Roisman, and P. Stephan. Drop evaporation of hydrocarbon fluids with deposit formation. *International Journal of Heat and Mass Transfer*, 128:115 – 124, 2019.

A. Bender, A. Stroh, B. Frohnapfel, P. Stephan, and T. Gambaryan-Roisman. Combined direct numerical simulation and long-wave simulation of a liquid film sheared by a turbulent gas flow in a channel. *Physics of Fluids*, 31:022103, 2019.

Peer reviewed papers in conference proceedings

A. Bender, P. Stephan, and T. Gambaryan-Roisman. Numerical investigation of stability and evolution of an evaporating liquid film on a heated structured wall. *Proceedings of 7^{th} International Symposium on Advances in Computational Heat Transfer*, Napoli, Italy, 2017.

A. Bender, P. Hänichen, T. Gambaryan-Roisman, and P. Stephan. Modeling crystallization and heat transfer in an evaporating urea water drop. *Proceedings of the 16^{th} International Heat Transfer Conference*, Beijing, China, 2018.

A. Bender, A. Stroh, B. Frohnapfel, P. Stephan, and T. Gambaryan-Roisman. A novel two-step model to investigate turbulent gas flows shearing thin liquid films. *Proceedings in Applied Mathematics and Mechanics*, Vienna, Austria, 2019.

Further conference contributions (non reviewed or abstracts only)

A. Bender and T. Gambaryan-Roisman. Numerical investigation of chemical reactions in thin liquid film flows sheared by an outer gas. *International Combustion Institute Summer School on Near-Wall Reactive Flows*, Bensheim, Germany, 2016.

A. Bender, P. Stephan, and T. Gambaryan-Roisman. Thin films with time-dependent chemical reactions. *8^{th} Conference of the International Marangoni Association*, Bad Honnef, Germany, 2016.

A. Bender and T. Gambaryan-Roisman. Numerical simulation of dynamics and stability of a liquid film evaporating on a heated structured wall. *2^{nd} International Workshop on Near-Wall-Reactive Flows*, Darmstadt, Germany, 2017.

A. Bender, T. Gambaryan-Roisman, and P. Stephan. Numerical investigation of deposit formation in an evaporating urea-water drop. *2017 ASME 15^{th} International Conference on Nanochannels, Microchannels and Minichannels*, Cambridge, MA, USA, 2017.

A. Bender, P. Stephan, and T. Gambaryan-Roisman. Numerische Untersuchung der Ablagerungsbildung aus verdunstenden Harnstoff-Wasser-Tropfen. *Tagung der Fachgruppen Wärme- und Stoffübertragung, Mehrphasenströmung und Computational Fluid Dynamics, ProcessNet VDI/Dechema*, Bremen, Germany, 2018.

A. Bender, P. Stephan, and T. Gambaryan-Roisman. Einfluss der Marangoni-Konvektion und Lösungsenthalpie auf die Ablagerungsbildung aus verdunstenden Harnstoff-Wasser-Tropfen. *Tagung der Fachgruppen Wärme- und Stoffübertragung, Trocknungstechnik und Mischvorgänge, ProcessNet VDI/Dechema*, Essen, Germany, 2019.

A. Bender, A. Stroh, B. Frohnapfel, P. Stephan, and T. Gambaryan-Roisman. Influence of shear stress fluctuations on dynamics of waves on a liquid film sheared by a turbulent gas flow. *8^{th} International Symposium on Bifurcations and Instabilities in Fluid Dynamics*, Limerick, Ireland, 2019.

A. Bender, P. Stephan, and T. Gambaryan-Roisman. Modeling film evolution, stability, and deposit formation for internal combustion engines and exhaust gas treatment. *International Workshop on "Clean Combustion: Principles and Applications" 2019*, Darmstadt, Germany, 2019.

A. Bender, P. Stephan, and T. Gambaryan-Roisman. Numerical model for deposit formation from evaporating sessile drops. *10^{th} Conference of the International Marangoni Association*, Iaşi, Romania, 2020, accepted.